Spring 5-15-2019

The effect of depositional environment and early marine diagenesis on carbonate-associated sulfate

Jocelyn Ann Richardson
Washington University in St. Louis

Recommended Citation

Richardson, Jocelyn Ann, "The effect of depositional environment and early marine diagenesis on carbonate-associated sulfate" (2019). *Arts & Sciences Electronic Theses and Dissertations*. 1854.
https://openscholarship.wustl.edu/art_sci_etds/1854

WASHINGTON UNIVERSITY IN ST. LOUIS
Department of Earth and Planetary Sciences

Dissertation Examination Committee:
David A. Fike, Chair
Alexander S. Bradley
Jeffrey G. Catalano
Michael J. Krawczynski
Samuel M. Webb

The Effect of Depositional Environment and Early Marine Diagenesis on Carbonate-Associated Sulfate

by
Jocelyn Ann Richardson

A dissertation presented to
The Graduate School
of Washington University in
partial fulfillment of the
requirements for the degree
of Doctor of Philosophy

May 2019
St. Louis, Missouri

Table of Contents

List of Figures

List of Tables

Acknowledgments

First and foremost, I would like to thank my advisor, David Fike. David's curiosity, excitement, and genuine passion for science and learning is unparalleled. I cannot thank you enough, David, for the opportunity to work with you, your support, encouragement, and freedom to discover my scientific interests, and everything you have taught me over the past five years. It has been a true pleasure to learn from you. I am excited for our continued collaborations making advances in our field.

I would like to thank my committee members, Alex Bradley, Jeff Catalano, Mike Krawczynski and Sam Webb for being available to answer my questions, for your interest, and thought-provoking discussions on my research. Sam, thank you for taking the time to teach me in depth about the magic of 14-3, your software and for the delicious wine. I look forward to continuing these things in California. I would also like to thank my collaborators: Olle Hints, Aivo Lepland, Colin Keating, Matt Newville, Tony Lanzirotti, Catherine Rose, Clive Jones and Bill Gilhooly for your comments, discussion and support.

To the members, past and present, of the Fike and Bradley lab groups; the support you have shown has helped more than you know. From Friday chalk talks, to detailed slide-by-slide editing and to the many beers; each moment has impacted the scientist I have become and made my time at Wash U more enjoyable. To Wil, Derek, Maya, Harry and Jen thank you for always pushing me to become the best scientist I can be. Steph, thank you for all your analytical help and data collection. Thank you to the office staff in EPSc for keeping on top of the forms and policies that make being a graduate student possible.

My time at WashU has been greatly impacted by my fellow graduate students and friends that were always there during times of stress and happiness, and continually provided encouragement. Specifically; Ryan Nickerson, Kat Powell, Michael Bouchard, Xiaochen Mao, Mike Sly, Robert 'Bobby Joe' Kupper, Kaushik Mitra, Torin O'Brien and Tabb Prissel. I could not have asked for better friends than Kelsey and Melody who were there for me through the toughest of times. I cannot thank you enough for your support, advice and true friendship. To my friends from the Manor, the Trap and the Shed thank you for the constant laughs and conversations.

I would not be the geologist I am without the incredible geology program at the University of St. Andrews. I'd like to thank Tony Prave for being an incredible mentor, for the many letters of recommendation and, of course, for pointing me in the direction of David. Tony, I will always remember the first lecture of your Earth History course and how it impacted my decision to choose this field of research. Thank you to Mark Claire, Aubrey Zerkle and Gareth Izon for teaching me isotope geochemistry, helping to start my research career and for encouraging me to pursue a PhD. I am incredibly grateful to Catherine Rose for the past few years of mentorship. Your encouragement and conversations have helped to shape my career and the type of scientist I aspire to be.

I would like to thank my family for the amazing amount of support they have shown me from 4,000 miles away. Thank you for helping me to visit home often and for always being available to talk. Thank you, Mum, for being the first person to navigate the St. Louis roads with me to help make my house feel like a home. And to my Dad, your words of encouragement and mindfulness helped to make tough times more manageable and to helped me to thoroughly enjoy my work. To Kevin, Tessa, Hannah and Lucas; thank you for making the 4,000 miles seem shorter.

I could not have asked for better office mates or friends than Scott and Roger. The past four years in our office have been truly enjoyable. Your constant support, encouragement and discussion throughout chalk talks, orals, conference presentations and manuscript preparation has helped me become the scientist I am today. I will always maintain the official Scott Beeler coffee hours and use it as a time to relax from work or to send you both some science questions.

Lastly, I would like to thank Joseph. The love and support you have shown me helped make the final few months of writing more manageable and less stressful. Thank you for the countless meals, for help doing simple tasks when I was exhausted and for always making me smile. You are the most caring and thoughtful person I have ever met.

Jocelyn Richardson

Washington University in St. Louis

May 2019

This work is dedicated to Dr. Tony Prave, without whom I would not have found my passion.

ABSTRACT OF THE DISSERTATION

The effect of depositional environment and early marine diagenesis on carbonate-associated sulfate

by

Jocelyn A. Richardson

Doctor of Philosophy in Earth and Planetary Sciences

Washington University in St. Louis, 2019

Professor David A. Fike, Chair

The long-term redox state of Earth's surface environments is governed by the relative burial proportions of redox-sensitive carbon and sulfur species throughout geologic time. The sulfur isotopic signature of seawater sulfate ($\delta^{34}S_{SO4}$) traces the relative proportions of sulfur buried as sulfide (commonly pyrite) and sulfate (as evaporites, barite or carbonate-associated sulfate) and weathering source to the ocean. Thus, $\delta^{34}S_{SO4}$ is a powerful tool to understand the evolution of redox conditions and the marine biogeochemical sulfur cycle. Due to the spatial and temporal extent of carbonates in the rock record, carbonate-associated sulfate ($\delta^{34}S_{CAS}$) is a common proxy for the isotopic composition of ancient seawater sulfate. However, deep-time $\delta^{34}S_{CAS}$ datasets are inherently variable and many paired $\delta^{34}S_{CAS}$-$\delta^{34}S_{pyr}$ records display discordant signals that cannot be reconciled by established interpretations of the sulfur cycle. Here we investigate the effects of depositional and diagenetic controls on CAS by combining sedimentologic observations, bulk isotopic records and micron-scale investigations using µ-X-ray Fluorescence imaging (µ-XRF) and X-ray Absorption Near Edge Structure (XANES) spectroscopy into the abundance and speciation of sulfur in ancient carbonates.

We demonstrate the effect of shallow- vs. deep-water depositional processes that generate heavier and more variable vs. lighter and more stable bulk $\delta^{34}S_{CAS}$-$\delta^{34}S_{pyr}$ records over timescales considered too short to reflect perturbations to the marine sulfate reservoir from early Silurian carbonates. Shallow-water environments have higher (more variable) sedimentation rates that limit the exchange of pore fluid sulfate with seawater sulfate. Due to microbial sulfate reduction in the sediment, and lack of connectivity to seawater, pore fluid sulfate evolves under closed-system conditions. However, site-specific depositional environment information is important to constrain, as these effects differ across a platform, depending on the energy of the environment, where high energy (paleoshoreline) and low sedimentation (deep water) environments record the most seawater-like values. Combined with $\delta^{18}O_{CAS}$, ancient $\delta^{34}S_{SO4}$ can be determined based on the least evolved $\delta^{34}S_{CAS}$-$\delta^{18}O_{CAS}$ and most stable $\delta^{34}S_{CAS}$-$\delta^{34}S_{pyr}$ values.

Micron-scale investigations of carbonate petrographic thin sections using µ-XRF and XANES spectroscopy demonstrate the variable abundance and speciation of sulfur between carbonate components (fossils, grains, cement and micrite). Sulfate is present in all carbonate components but, based on the timing and location of precipitation, is variable within a sample. Micron-sized sulfide minerals are present in micrite and are often partially oxidized. The relative proportions of fossils, grains, cement and micrite, and thus the abundance and source of sulfate, therefore, varies between different depositional settings. The sulfate in extant and well-preserved fossil brachiopods is inorganic sulfate (as CAS) with little contribution from organic sulfate esters suggesting epifaunal brachiopods are a relatively robust archive of local seawater $\delta^{34}S_{SO4}$. Depositional and early marine diagenetic conditions inherently impact $\delta^{34}S_{CAS}$-$\delta^{34}S_{pyr}$ values and must be assessed for all carbonate successions prior to interpreting sulfur isotopes, in order to disentangle local signal from global trends.

1. Introduction

1.1 Motivation

Long-term global biogeochemical cycles are important for regulating Earths atmospheric composition. The timing and concentration of atmospheric oxygen fluctuations, as well as carbon dioxide, is central to understanding the driving mechanism behind large-scale biological evolutionary changes such as the origin of life, diversification and radiation of macrofauna at the Cambrian explosion, body complexity and extinction events. Geologic transformations play a central role in regulating the relative abundance of gases in the atmosphere. The precipitation of carbonate in the ocean sequesters CO_2 during the carbonate-silicate cycle and the burial of organic carbon and reduced sulfide (as pyrite) dictates the accumulation of atmospheric oxygen over geologic timescales (Berner, 2001; Berner and Canfield, 1989). Understanding the relative amount, rates, and controls on organic carbon and pyrite burial over time is essential for reconstructing past O_2 concentrations since there are no direct measurements for atmospheric oxygen for a majority of Earth history. The rock record retains information on the relative burial ratio of organic carbon to carbonate carbon and pyrite to sulfate (as evaporites or carbonate-associated sulfate; CAS) through the preservation of these reservoirs in marine sedimentary successions. To infer changes in the burial ratio of organic carbon and pyrite, stable isotopic ratios of carbon and sulfur phases from the reduced and oxidized reservoirs are measured and compared to mass-balance models from key intervals throughout Earth history. However, there is a limitation to understanding global processes from individual sections based on the complexity of site-specific processes occurring during deposition, which ultimately impact the isotopic signature of carbon and sulfur preserved in these sediments. In this dissertation we provide a detailed description of the numerous depositional and early diagenetic controls on the abundance, speciation and isotopic composition of sulfur in ancient carbonate rocks, acting as a cautionary tale for the over-interpretation of sulfur isotopes from carbonate successions.

1.2 The Biogeochemical Sulfur Cycle

1.2.1 Fluxes and Reservoirs

Biogeochemical interactions between carbon, sulfur, oxygen and iron play a major role in regulating Earth's surface redox conditions. Microbial sulfate reduction (MSR) is intimately linked to the carbon cycle through organic carbon remineralization during sulfate reduction, and residual sulfide reacts with available iron to form pyrite (and other iron sulfide minerals). Over time, the relative proportion of sulfur buried as sulfide minerals and burial of organic carbon in marine sediments regulates marine and, consequently, atmospheric oxygen levels (Berner, 1989; Garrels and Lerman, 1981).

The global sulfur cycle has three main reservoirs; dissolved seawater sulfate, sedimentary sulfate and sedimentary sulfide minerals. Seawater sulfate is the largest reservoir of sulfur in the modern ocean at 28 mM, corresponding to a 13 Myr residence time (Berner, 2001; Canfield, 2004). However, it is thought that the size of the marine sulfate reservoir has fluctuated throughout Earth history based on changes to the input and outputs of sulfur to the ocean (Canfield, 2004; Crowe et al., 2014; Habicht et al., 2000; Horita et al., 2002a; Kah et al., 2004; Lowenstein et al., 2003). Inputs to the dissolved marine sulfate reservoir include riverine weathering, volcanic and hydrothermal outgassing, re-oxidation of sulfide and intermediate sulfur species, and dust. Sulfate is removed from the dissolved reservoir as sulfate minerals (either evaporite minerals or barite) or as carbonate-associated sulfate (CAS), or as sulfide minerals (Canfield, 2004) and sulfurization of organic compounds (Sinninghe-Damste and de Leeuw, 1990). During MSR, microbes discriminate against ^{34}S resulting in a kinetic isotope fractionation that causes the product sulfide to be isotopically depleted in ^{34}S relative to the source sulfate (Harrison and Thode, 1958). Depending on the availability of reactive iron, this isotopically depleted sulfide may form pyrite, resulting in an isotopic offset between coeval sulfates and sulfides in marine sedimentary rocks.

Paired δ^{34}S of co-occurring sulfates and sulfides from the rock record are frequently used to the determine the operation and evolution of the marine sulfur cycle throughout geologic time. Steady-state mass balance models of the marine sulfur cycle assume that the δ^{34}S of sulfates and sulfides will change synchronously during a global perturbation by:

$$\delta_{SO4} = \delta_{in} + f_{pyr} * \varepsilon_{pyr} \tag{1.1}$$

where δ_{SO4} is the δ^{34}S of the sedimentary sulfate reservoir, δ_{in} is the δ^{34}S of the riverine input, f_{pyr} is the relative proportion of sulfur buried as sulfides and ε_{pyr} is the isotopic offset between coeval sulfate and pyrite records (Canfield, 2004, 2001a; Fike et al., 2015). Based on this description for the steady-state sulfur cycle, the main drivers responsible for synchronous excursions to the δ^{34}S of coeval sulfates and sulfides are: changes to the relative amount of pyrite burial, changes to the isotopic value of the input (i.e. weathering more pyrite than evaporite or carbonate), and/or a changing biological fractionation.

1.2.2 Isotope Notation

Traditional sulfur isotope analyses measure the ratio of the two most abundant sulfur isotopes (^{32}S and ^{34}S, 95% and 4.2%, respectively) of a sample, relative to the same ratio in the internationally recognized Vienna-Canyon Diablo Troilite (V-CDT) standard (Canfield 2001), expressed in per mil (parts per thousand, ‰), as follows:

$$\delta^{34}S = [(^{34/32}S_{sample}/^{34/32}S_{VCDT})-1]*1000 \quad (1.2)$$

If $\delta^{34}S_{sample}$ is greater than the standard, the sample is said to be heavy or enriched in ^{34}S, whereas if it is lower than the standard (i.e., $\delta^{34}S < 0$) it is light or depleted in ^{34}S. The main process that fractionates sulfur isotopes in the marine sulfur cycle is MSR, by up to 70‰. The magnitude of this fractionation is dependent on the initial sulfate concentration, the cell-specific sulfate reduction rate (csSRR) and, therefore, electron donor availability (Leavitt et al., 2013; Sim et al., 2011). Other processes that fractionate sulfur include sulfur disproportionation and oxidative sulfur cycling (see Gomes and Johnston, 2017). In comparison, the magnitude of the fractionation that may occur during the incorporation of sulfate into CAS or other sulfate minerals is much smaller (~ 0-2‰) (Balan et al., 2014; Holser and Kaplan, 1966; Raab and Spiro, 1991; Rennie et al., 2018; Thode et al., 1974).

1.2.3 Sulfate proxies

Direct measurements of ancient seawater sulfate is limited to a small number of halite fluid inclusions in the rock record (Horita et al., 2002a; Lowenstein et al., 2003). Due to the close agreement between modern seawater and evaporite minerals, $\delta^{34}S_{evap}$ has been widely used to reconstruct $\delta^{34}S_{SO4}$ since the 1960's (Claypool et al., 1980; Holser and Kaplan, 1966; Schidlowski et al., 1977; Strauss, 1997a; Thode et al., 1974). However, the episodic nature of evaporite deposition creates an intermittent record of seawater sulfate. Sedimentary barite forms in the water column, is deposited in deep sea sediments and lacks any fractionation during incorporation of sulfate (Paytan, 1998). Screening of barite crystal morphology is required to ensure it is sedimentary and not metamorphic and/or hydrothermal (Cecile et al., 1983; Paytan et al., 1998, 1993). Although $\delta^{34}S_{barite}$ data were supposed to supplement the intermittent evaporite record, the most continuous record of sedimentary barite exists for the Cenozoic and Cretaceous (Paytan, 1998; Paytan et al., 2004). Additionally, barite is deposited in deep-sea sediments and thus will not be able to generate high-resolution continuous datasets in older successions. A similarly sporadic proxy is sulfate bound in marine phosphorite, which is generally more abundant in the Ediacaran and Cambrian (Shields et al., 1999).

The identification of sulfate in carbonate minerals revealed an uninterrupted archive of marine sulfate $\delta^{34}S$ throughout geologic time (Burdett et al., 1989; Takano, 1985) and has been widely used in carbonates from the Archean to the Cenozoic (Bottrell and Newton, 2006; Burdett et al., 1989; Gellatly and Lyons, 2005; Gill et al., 2008; Hurtgen et al., 2006; Jones and Fike, 2013; Kah et al., 2016; Kampschulte and Strauss, 2004, 1998; Osburn et al., 2015; Paris et al., 2014; Rennie et al., 2018; Sim et al., 2015; Young et al., 2016b). CAS became a common proxy for seawater sulfate, albeit one without adequate investigations into the mechanisms of sulfate incorporation, processes controlling incorporation and the processes that control local $\delta^{34}S$ variation, irrespective of global trends. Because of this, some more recent investigations have studied the impact of meteoric diagenesis (Gill et al., 2008), pyrite oxidation (Marenco et al., 2008a) and non-CAS sulfur phases (Wotte et al., 2012a) on bulk $\delta^{34}S_{CAS}$ records.

1.3 Carbonate-associated sulfate

1.3.1 Definition of CAS

Carbonate-associated sulfate is a SO_4^{2-} ion that has substituted for a CO_3^{2-} ion within the carbonate crystal lattice, determined via raman, IR and X-ray Absorption Near Edge Structure (XANES) spectroscopies (Pingitore et al., 1995; Takano, 1985; Takano et al., 1980). Unlike evaporite minerals and barite, CAS is generally a trace component in all carbonate minerals, including dolomite. CAS ranges in abundance from 10's to 100's ppm in ancient carbonate and 100's to 1000's ppm in modern carbonate. The variability of CAS abundance in ancient vs. modern carbonate is attributed to loss of sulfate during diagenesis over time (Staudt and Schoonen, 1995). The abundance of CAS in various carbonate components and the suite of processes that could variably affect this abundance reflect a composite of the changing size of the sulfate reservoir, biological and abiotic effects on incorporation, and local sulfate concentration.

Early studies on the mechanisms controlling trace ion incorporation into calcite indicate a growth-rate dependence of sulfate incorporation, such that an increase in crystal growth rate increases the partition coefficient of sulfate into carbonate (Busenberg and Plummer, 1985). Growth rate however, is a dependent variable and is influenced by local seawater/porewater chemistry, mineral surface interactions and mineral structural controls (Staudt et al., 1994). In turn, local seawater chemistry influences carbonate mineralogy, where a greater abundance of dissolved sulfate favors aragonite precipitation over calcite, but sulfate substitution into calcite is more favorable than into aragonite or vaterite (Fernández-Díaz et al., 2010; Kitano et al., 1975). In addition, sulfate abundance increases with increasing Mg and Mn incorporation in the carbonate mineral (Staudt et al., 1993; Takano, 1985). Lastly, the dissolved SO_4^{2-}:CO_3^{2-} ratio linearly impacts the resultant mineral S:Ca molar ratio (Fernández-Díaz et al., 2010). Together these complex controls, which are likely impacted by depositional environment and pore fluid evolution during early marine diagenesis, are seldom considered in $\delta^{34}S$ chemostratigraphic studies. The impact of biology on the abundance and $\delta^{34}S$ of CAS is even less well understood.

1.3.2 Bulk $\delta^{34}S_{CAS}$ records

Due to the relatively low abundance of CAS, particularly in ancient carbonate rocks, a large initial sample size (30 to 80 g, depending on carbonate content) of homogenized carbonate powder is required for bulk extraction of sulfate. Although the extraction protocol has changed over time, and varies between research groups, the protocols follow similar steps including; (1) leaching of non-CAS free sulfate or reduced sulfur that may be sorbed onto the carbonate minerals (by a combination of NaCl brine, NaOCl brine, bleach and/or deionized water), (2) dissolution of carbonate to liberate CAS and (3) addition of $BaCl_2$ to react with sulfate and form $BaSO_4$ for analyses (Burdett et al., 1989; Fike and Grotzinger, 2008; Gill et al., 2008; Hurtgen et al., 2002; Loyd et al., 2012; Richardson et al., 2019; Rose et al., 2019; Thompson and Kah, 2012; Wotte et al., 2012a). These protocols focus on removing non-CAS sulfur contaminants during the leaching process, and limit the potential oxidation of pyrite during carbonate dissolution (Marenco et al., 2008a). Despite this, there is a characteristic sample-to-sample variability in many deep-time CAS records which could be due to variations in leaching or acidification, or variations in the proportion of different carbonate components that are homogenized prior to the extraction.

The inherent sample-to-sample variability (up to 10‰ in some sections) (Edwards et al., 2018; Jones and Fike, 2013; Kozik et al., 2019; Riccardi et al., 2006; Rose et al., 2019) exhibited in most CAS records is often accompanied by discordant, in magnitude and/or direction, isotope excursions between coeval CAS and pyrite (Jones and Fike, 2013; Rose et al., 2019; Young et al., 2016b). Such high-frequency stratigraphic variability and the increasing number of discordant isotope records cannot be easily resolved by canonical explanations to the global sulfur cycle, questioning the fidelity of these proxies as archives for the global sulfur cycle. Instead, some research has suggested that both CAS and pyrite isotopes are predominantly controlled by local depositional processes, imprinting a local signature on top of the global records (Claypool, 2004; Goldberg et al., 2005; Liu et al., 2019; Pasquier et al., 2017; Present, 2018; Rose et al., 2019).

1.3.3 Component-specific $\delta^{34}S_{CAS}$ records

The composition of carbonate rocks differs depending on the environment in which they precipitate, termed facies, which ultimately determines the relative proportions of the carbonate components (fossils, abiotic grains, cement and micrite). It is suggested that the changing abundance of components, which form in different environments from one another, could be the source of observed sample-to-sample variability in $\delta^{34}S_{CAS}$ (Present et al., 2015). To reduce 'noise' in bulk $\delta^{34}S_{CAS}$ datasets, protocols have been developed to use a much smaller sample size (Paris et al., 2014, 2013) and/or to target specific carbonate components, such as micrite (Gellatly and Lyons, 2005; Kampschulte and Strauss, 2004; Present et al., 2015; Riccardi et al., 2006; Wotte et al., 2012a) and biogenic carbonate (Gill et al., 2011; Kampschulte et al., 2001; Kampschulte and Strauss, 1998; Present et al., 2015). A comparison of the $\delta^{34}S_{CAS}$ values of micro-drilled cement, fossils and micrite from a single Ordovician carbonate sample show 20‰ variability, where micrite is the most depleted in ^{34}S, brachiopods closely approximate time-correlative evaporite $\delta^{34}S$ values and other fossils and cements are variably enriched in ^{34}S (Present et al., 2015). Integrating over this internal sample variability, together with the frequency at which the relative proportions of carbonate components changes in a given section, can give rise to the observed $\delta^{34}S_{CAS}$ variability in the rock record. A detailed investigation into the processes affecting CAS abundance and $\delta^{34}S_{CAS}$ under different depositional environments and during early marine diagenesis is required to understand the source of component-specific isotope variability, to interpret discordant changes in paired $\delta^{34}S_{CAS}$-$\delta^{34}S_{pyr}$ and to determine how to tease apart, if possible, depositional signatures vs. global trends in $\delta^{34}S_{CAS}$.

1.4 Chapter Summaries

1.4.1 Chapter 2: Effect of depositional environment on bulk carbon and sulfur isotopes

The early Silurian is a key interval of environmental variation with numerous global sea level fluctuations, climate change, perturbations to the global carbon cycle and biological turnover. Previous reports of sulfur isotope signatures during the early Silurian indicate conflicting paired $\delta^{34}S_{CAS}$-$\delta^{34}S_{pyr}$ that cannot be readily interpreted using current models of the biogeochemical S-cycle. We present bulk isotope ($\delta^{13}C_{carb,}$ $\delta^{13}C_{org,}$ $\delta^{18}O_{carb}$, $\delta^{34}S_{CAS}$ and $\delta^{34}S_{pyr}$) and elemental abundance (Ca, Mg, Fe, Sr, Mn) data from the Viki drill core in the Baltoscandian basin. Carbon isotopes indicate that there is a basin-wide, and potentially global, perturbation to the carbon cycle. In contrast, the sulfur isotope records do not display synchronous changes with temporally correlative samples from Gotland, Sweden. In the Viki drill core, trends in paired $\delta^{34}S_{CAS}$-$\delta^{34}S_{pyr}$ correlate with depositional environment such that heavier and more variable $\delta^{34}S_{CAS}$ and $\delta^{34}S_{pyr}$ occur in shallow-water depositional environments owing to increased sedimentation rate, sediment reworking, iron and labile organic carbon availability. This results in closed-system isotope behavior that causes distillation of porewater sulfate resulting in isotopic enrichments in residual sulfate and sulfide produced during MSR. During deep-water carbonate precipitation, $\delta^{34}S_{CAS}$ and $\delta^{34}S_{pyr}$ are lighter and more stable, reflecting more open-system isotope behavior where seawater sulfate is exchanged more readily with porewater sulfate.

1.4.2 Chapter 3: Evidence of closed-system conditions on paired bulk sulfur and oxygen isotopes of CAS

To further investigate basin-wide sulfur isotope variability and depositional effects, we measured bulk $\delta^{13}C_{carb,}$ $\delta^{13}C_{org,}$ $\delta^{18}O_{carb}$, $\delta^{34}S_{CAS}$, $\delta^{34}S_{pyr}$ and $\delta^{18}O_{CAS}$ from the Paatsalu drill core, a time-correlative section to the Viki drill core within the Baltoscandian basin. Paired $\delta^{34}S_{CAS}$ and $\delta^{18}O_{CAS}$ corroborate our previous interpretations from the Viki drill core, where samples enriched in $\delta^{18}O_{CAS}$ and $\delta^{34}S_{CAS}$ preserve distilled isotope values due to MSR. This enrichment is observed in both shallow-water and deep-water carbonate facies, contrary to our earlier suggestion that deep-water carbonates are more likely to preserve a seawater-like signature. However, Mn/Sr ratios indicate that deep-water carbonate samples precipitated and/or recrystallized in an anoxic fluid that overprinted primary $\delta^{34}S_{CAS}$ and $\delta^{18}O_{CAS}$ values.

The difference in relative sea level during carbonate precipitation between the Paatsalu and Viki core sites results in differences between absolute $\delta^{34}S_{CAS}$, $\delta^{34}S_{pyr}$ and $\delta^{18}O_{CAS}$ values, such that the more proximal settings experienced increased wave and tidal action that likely disrupted the isotope distillation. The observed relationships show that depositional controls on $\delta^{34}S$ values may overprint or mask basin-wide or global S-cycle signals. Global sea level change, typical of times of environmental change such as during the early Silurian, can differentially affect sedimentary basins and, as such, depositional factors must be assessed for any section in which these proxies will be applied prior to reconstructing the operation of the ancient sulfur cycle.

1.4.3 Chapter 4: Micron-scale analysis of sulfur speciation in carbonate components

Marine carbonate rocks are composed of cement, micrite, fossils and grains that form in different locations (e.g. water column vs. pore space) at different times and occur in varying abundance based on depositional facies. We used μ-X-ray Fluorescence imaging (μ-XRF) and X-ray Absorption Near Edge Structure (XANES) spectroscopy within a petrographic context to determine the speciation and abundance of sulfur in independent components within a given sample, as well as between lithofacies. μ-XRF imaging indicates that sulfate abundance is highest within unaltered, low-Mg fossil fragments and lowest within equant marine calcite cements. However, sulfate abundance in pore-filling cements is variable due to changes in pore fluid sulfate composition and carbonate precipitation rates during early marine diagenesis. Disseminated sulfide is the predominant S-species in all micrite and co-occurs with sulfate indicating partial *in situ* oxidation from diagenetic fluids over time, resulting in a sulfate signal that does not represent primary CAS. This suggests CAS sourced from micrite of shallow-water depositional facies is not necessarily expected to be a faithful record of ancient seawater sulfate. Our research highlights the micron-scale sulfate variability that bulk CAS records are masking, where the small-scale variability in sulfate abundance is due to variably closed-system conditions during shallow-water carbonate deposition and early marine diagenesis.

1.4.4 Chapter 5: Micron-scale sulfur speciation in brachiopods

Brachiopods frequently retain the highest abundance of sulfate of most biomineralizers throughout the rock record. Due to the robust nature of their low-Mg calcite and the multi-layered shell of articulate brachiopods that form in contact with seawater, ancient brachiopods may be a more faithful archive of seawater sulfate. XANES spectroscopy and μ-XRF imaging of extant and fossil brachiopods show that inorganic sulfate is the major sulfur species, with low contributions from organic sulfur compounds (including thiols, thioether, sulfoxide and esters). This finding is contrary to previous literature that suggests sulfate esters are the predominant sulfate species in biomineralizers as opposed to inorganic sulfate. Combined with bulk and micro-drilled brachiopod specific $\delta^{34}S_{CAS}$, our findings are consistent with well-preserved brachiopods acting as a robust recorder of local seawater $\delta^{34}S_{SO4}$.

2. Silurian Records of Carbon and Sulfur Cycling from Estonia: The Importance of Depositional Environment on Isotopic Trends

Jocelyn A. Richardson[1*], Colin Keating[1], Aivo Lepland[2,3], Olle Hints[3], Alexander S. Bradley[1] and David A. Fike[1*]

[1]Department of Earth and Planetary Sciences, Washington University, St. Louis, MO 63130 USA
[2]Geological Survey of Norway, 7491 Trondheim, Norway
[3]Department of Geology, Tallinn University of Technology, Ehitajate 5, 19086 Tallinn, Estonia

Published as:
Richardson, J.A., Keating, C., Lepland, A., Hints, O., Bradley, A.S., Fike, D.A., 2019. Silurian records of carbon and sulfur cycling from Estonia: The importance of depositional environment on isotopic trends. Earth Planet. Sci. Lett. 512, 71–82.
https://doi.org/10.1016/J.EPSL.2019.01.005

2.1 Abstract

The Llandovery-Wenlock carbonate-marl succession of the Baltoscandian Basin has been analyzed in the Viki drill core, western Estonia, for carbonate carbon ($\delta^{13}C_{carb}$), organic carbon ($\delta^{13}C_{org}$), carbonate-associated sulfate ($\delta^{34}S_{CAS}$) and pyrite ($\delta^{34}S_{pyr}$) isotopes, along with trace element concentrations. Following the End-Ordovician glaciation and the Hirnantian carbon isotope excursion, $\delta^{13}C_{carb}$ values rise to an early Llandovery carbon isotope maximum (+2‰). Subsequently, $\delta^{13}C_{carb}$ and coeval $\delta^{13}C_{org}$ record a large ~ +4.5‰ excursion in the early Wenlock, associated with a regression and biotic turnover known as the Ireviken bioevent (IBE). Overall, $\delta^{34}S_{CAS}$ values generally fall within a range (25‰ to 35‰) similar to that reported in other sections of comparable age. Two distinct trends are observed: low and stable $\delta^{34}S_{CAS}$ values are associated with deep-water facies, while $\delta^{34}S_{CAS}$ becomes higher and more variable in the shallow-water facies. Similarly, $\delta^{34}S_{pyr}$ values are low and invariant (~ -15‰) in deep-water facies but become higher and more variable (ranging between -35‰ and 16‰) in shallow-water deposits. Despite abundant recrystallization, no obvious evidence for large-scale alteration of proxies is apparent in concentrations of Fe, Sr, Mn and Mg, or in isotopic correlations, although increased variability and lower values of $\delta^{34}S_{CAS}$ are observed where CAS abundance is low. A large, well-resolved positive excursion in $\delta^{34}S_{CAS}$ observed during the IBE from a time-correlative section on Gotland (Sweden) is absent in the data presented here. This difference demonstrates that, counter to general understanding, local environmental variations can give rise to divergent $\delta^{34}S_{CAS}$ profiles in coeval sections. The S-isotope fluctuations in CAS and pyrite in the Viki drill core can be explained by local processes involving facies changes, early diagenetic processes and associated open vs. closed system behavior that can overprint and potentially mask basin or global signals.

2.2 Introduction

Sedimentary phases of carbon (inorganic and organic carbon) and sulfur (pyrite and sulfate) are routinely analyzed for their concentration and isotopic composition ($\delta^{13}C$, $\delta^{34}S$) with the data used to constrain ancient biogeochemical cycling and the redox evolution of Earth's surface environments (Berner, 1989; Garrels and Lerman, 1981). Coupled C-isotope records are used to infer global changes in the amount of organic carbon burial or carbonate weathering (Kump and Arthur, 1999). Similarly, coupled S-isotope records are used to determine the pyrite burial flux and source of sulfur inputs to the ocean (Fike and Grotzinger, 2008; Halevy et al., 2012). Steady-state models used to interpret paired isotope data implicitly assume both oxidized and reduced species will change synchronously under a global forcing.

Carbonate-associated sulfate (CAS; Burdett et al., 1989) is an increasingly common proxy for the $\delta^{34}S$ value of ancient seawater sulfate. CAS forms via substitution of a sulfate ion for a carbonate ion during carbonate precipitation where the S-isotopic composition of CAS is interpreted to correspond to that of sulfate in seawater at the time of carbonate precipitation (Gill et al., 2008; Lyons et al., 2004a). However, numerous discordant and/or highly variable $\delta^{34}S$ chemostratigraphic sections have raised concerns regarding the fidelity of CAS and pyrite as representing global signatures (e.g. Aller et al., 2010; Jones and Fike, 2013; Pasquier et al., 2017; Present et al., 2015; Ries et al., 2009; Rose et al., 2019). In addition to these studies, numerous isotopic studies of Paleozoic strata reveal excursions in $\delta^{13}C$, $\delta^{18}O$, and $\delta^{34}S$ that occur in association with facies changes and/or local variation in sea level (Munnecke et al., 2003; Rose et al., 2019; Saltzman et al., 2000a; Yan et al., 2009). Further, deep-time $\delta^{34}S_{CAS}$ datasets often display inherent variability, or 'noise', (Jones and Fike, 2013; Kampschulte and Strauss, 2004; Present et al., 2015; Ries et al., 2009) that is challenging to reconcile with global changes in the marine sulfate pool due to the short time scales (<< 1 Myr) over which such variations are expressed. Unlike other traditional isotope proxies (e.g., $\delta^{13}C_{carb}$), CAS is a trace component that may be more susceptible to alteration, contributing to this characteristic variability. These observations indicate that we must investigate the local depositional and diagenetic processes that contribute to the final isotopic composition of carbonate strata.

In this study we report bulk $\delta^{13}C_{carb}$, $\delta^{13}C_{org}$, $\delta^{34}S_{CAS}$, and $\delta^{34}S_{pyr}$ records in carbonate strata from Estonia. These strata span the earliest Silurian through mid-Wenlock and include the well-defined global C-cycle perturbation at the Llandovery-Wenlock boundary coincident with the Ireviken bioevent (IBE; Munnecke et al., 2003). The IBE is characterized by biotic turnover through step-wise extinction events associated with facies changes that suggest a global cooling climate (Lehnert et al., 2010; Munnecke et al., 2003). Carbonate strata on Gotland Island, Sweden, record the IBE, the $\delta^{13}C$ excursions, and synchronous positive excursions in both $\delta^{34}S_{CAS}$ and $\delta^{34}S_{pyr}$, although of vastly different magnitudes (Rose et al., 2019). In contrast to many reports of parallel isotopic excursions in Earth history, these data were interpreted to be the result of local, facies-dependent processes. Here we test this hypothesis by comparing two time-equivalent records from the same Baltoscandian basin (Figure 2.1).

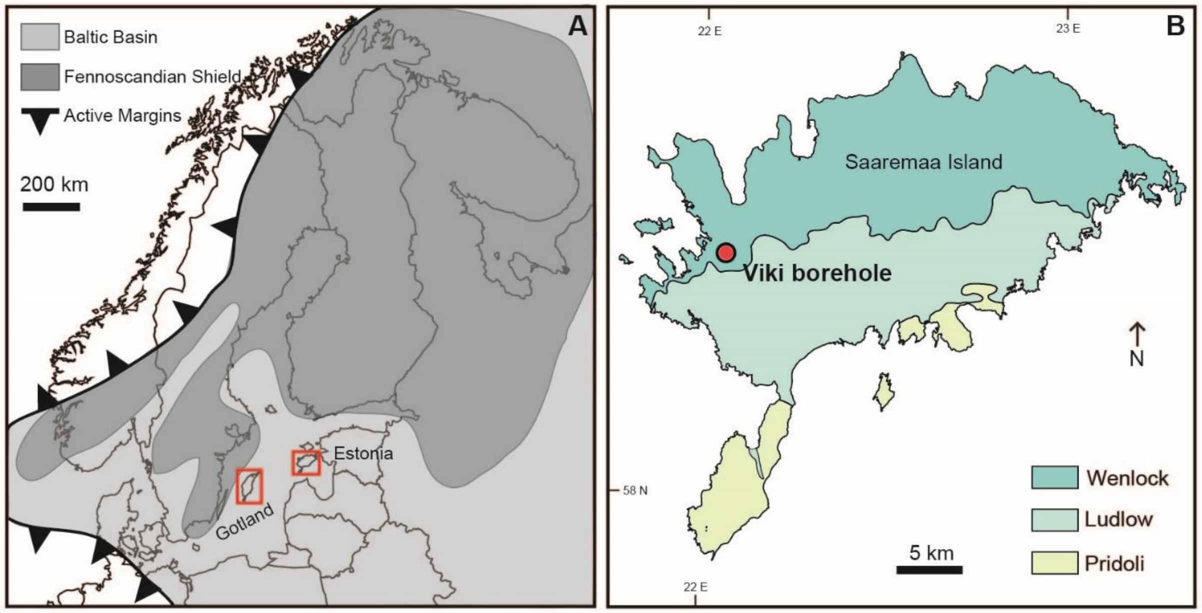

Figure 2.1 – A) Map of Northern Europe. Light gray shaded area represents the extent of the Baltoscandian Basin during the Silurian sea level maximum and the dark gray shaded area reflects the Fennoscandian Shield. Saaremaa Island, Estonia, and Gotland are outlined in red. Modified from Calner (2005) B) Close up of Saaremaa Island showing location of the Viki borehole and Silurian outcrop areas.

2.3 Geologic Setting

Samples in this study were collected in 2015 from the Viki reference drill core, Saaremaa Island, western Estonia (Figure 2.1; see Põldvere, 2010 for details and core description). The Viki drill core is archived at the Department of Geology, Tallinn University of Technology (http://geokogud.info/locality/1464). The analyzed samples date from the basal Juuru to Jaagarahu Baltoscandian regional stages (~ 444 Ma to ~ 427 Ma; Figure 2.2). Silurian stratigraphy of the Viki core is well constrained by conodont and chitinozoan biostratigraphy (e.g. Jeppsson and Männik, 1993; Nestor, 2010) chemostratigraphy (Hints et al., 2014; Munnecke and Männik, 2009), and K-bentonites (Kiipli et al., 2001). The studied interval of the Viki drill core records the peritidal to distal shelf facies of a carbonate platform where the lower strata record a shallowing sequence of mixed siliciclastics and bioturbated wackestones from proximal shelf to backreef

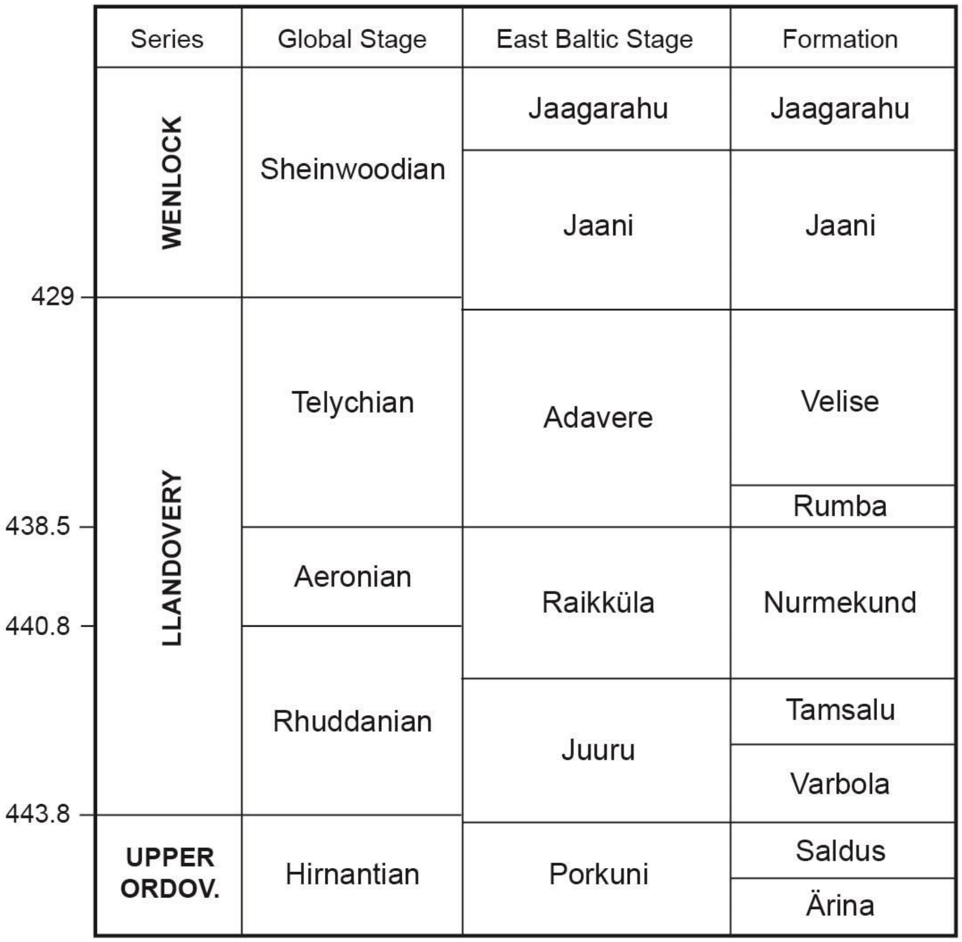

	Series	Global Stage	East Baltic Stage	Formation
	WENLOCK	Sheinwoodian	Jaagarahu	Jaagarahu
			Jaani	Jaani
429	LLANDOVERY	Telychian	Adavere	Velise
				Rumba
438.5		Aeronian	Raikküla	Nurmekund
440.8		Rhuddanian	Juuru	Tamsalu
				Varbola
443.8	UPPER ORDOV.	Hirnantian	Porkuni	Saldus
				Ärina

Figure 2.2 – Baltic regional stages and formations of the Viki core aligned with the global stage and series. Modified from Kaljo and Martma (2000).

facies, capped by an unconformity. This is overlain by a deepening upward succession of marlstones and mudstones with the deepest lithofacies at approximately 140 m. This is followed by a shallowing upward sequence of reef and shoal facies to marginal marine facies represented by partially dolomitized wackestone-packstones with coral-stromatoporoid bioherms and pyritized hardgrounds (Figure 2.4). The strata have not experienced significant thermal/burial alteration (Marshall et al., 1997) and have undergone minimal tectonic alteration. They are generally flat-lying with slight dip to the south.

The lowest strata examined come from the Varbola Formation (241.33 to 224.2 m). These strata are wavy bedded fine to micro-crystalline wackestones with calcitic marlstone beds (Figure

2.3a) with a diverse fossil content including brachiopods, trilobites, rugose and tabulate corals, stromatoporoids and crinoids, that varies from ~10 to 50%. The overlying Tamsalu Fm. (224.2 to 221.5 m) has similar lithology and fossil content and is distinguished by increased pyrite and clastic content. The Nurmekund Formation (221.5 to 190.7 m) is a finely crystalline brachiopodal wackestone marked by pyritized limestone at its top (Figure 2.3b). The upper part of the Nurmekund Formation (upper Aeronian) is missing on Saaremaa Island and represents an erosional surface and unconformity in the Viki core (Nestor and Einasto, 1997). These formations are interpreted to reflect a moderate- to low-energy shallowing basin, from proximal shelf facies of the Varbola Fm. to backreef facies of the Tamsalu and Nurmekund Fms. These correspond to the Rhuddanian and Aeronian global stages, spanning no more than 5.3 Myr of deposition (Figure 2.2).

The Rumba Formation (190.7 to 183.5 m) marks a change in lithology with a decrease in fossil content and increase in marlstone, claystone and dolomite content. The Velise Formation (183.5 to 121.1 m) is predominantly marlstone with some partially dolomitized mudstone beds (Figure 2.3c) and a fossil content < 10%, reflecting distal shelf facies. The Rumba and Velise Fms. correspond to a majority of the Telychian in the Viki core (5.1 Myr; Figure 2.2). The Rumba and Velise Formations are interpreted as a rapid deepening of the Baltoscandian basin (Nestor and Einasto, 1997), where the depositional environment is low-energy distal shelf facies.

The Jaani Formation (121.1 to 87.6 m) includes the Llandovery-Wenlock boundary at 113.5 m. The lowermost Jaani beds are marlstone and have an increase in partially dolomitic mudstone compared to the Velise Fm. below, while the upper Jaani Formation marks an increase in carbonate content (e.g. stromatoporoid packstones; Figure 2.3d). Strongly recrystallized and partially dissolved fossils and bioclasts (Figures 3e and 3f) are present. The datum points (extinction events) comprising the IBE are identified by conodont biostratigraphy in the Viki core from 114 to 108 m (Lehnert et al., 2010). These datum points allow precise correlation with the succession on Gotland (Jeppsson and Männik, 1993) and elsewhere where the IBE is recorded. The overlying Jaagarahu Formation (87.6 to 49.5 m) consists of partially dolomitic limestone, particularly in the basal ~10 m. A 5 m thick, partially dolomitized coral biohermal boundstone (Figure 2.3g) overlies this, followed by partially dolomitized coral-stromatoporoid packstone from 72 to 54.5 m. These packstones have a similar fossil groups to the Varbola Fm. Hardgrounds throughout the Jaagarahu Fm. are commonly pyritized (Figure 2.3h). The sampled Jaani and Jaagarahu Fms. sorrespond to the Sheinwoodian stage and thus records less than 3 Myr (Figure 2.2). The inferred depositional environment is moderate-energy shallow, reef and shoal mid-shelf to marginal marine facies.

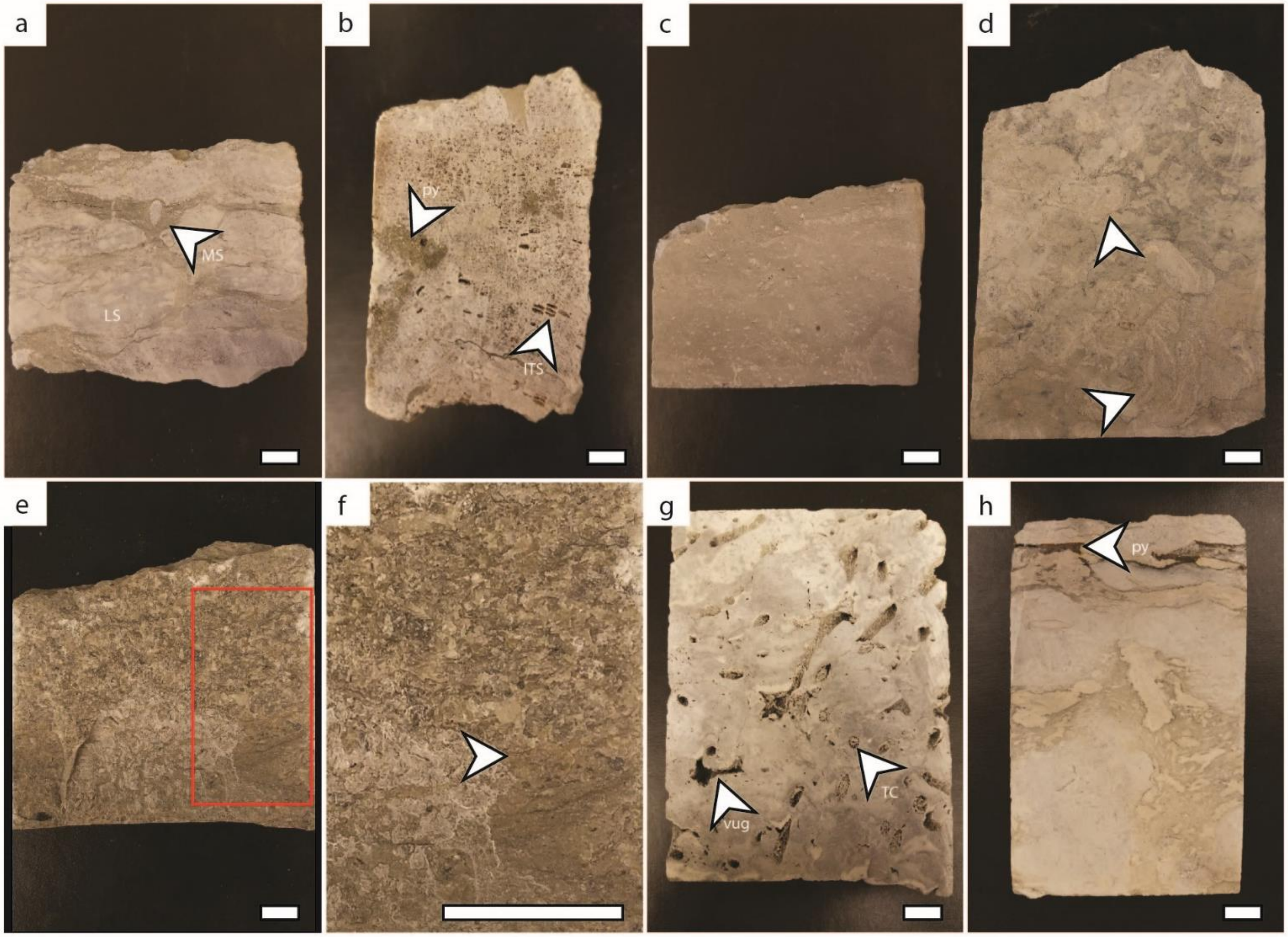

Figure 2.3 – Samples representative of the main lithologies of the Viki core. py = pyrite, vug = vuggy pore, TC = tabulate coral, ITS = inter-tabulae space, LS = limestone, MS = marlstone. White arrows point to locations of these features in a given sample. Scale bar on each image corresponds to 1 cm. a.) 232.46 m – dolomitized limestone with calcitic marlstone interbeds and patches. b.) 192.7 m – *Favosites. sp.* c.) 139.32 m – dolomitic and calcitic marlstone, d.) 93.9 m – packstone with arrows pointing to stromatoporoids, e.) 87.6 m – wackestone showing differential recrystallization f.) 87.6 m – close up of area outlined in e, arrow points to change from microcrystalline to crystalline carbonate due to diagenetic recrystallization, g.) 71.61 m – biohermal dolostone, and, h.) 53.5 m - limestone with dolomite patches and films, and a pyritized discontinuity surface indicated by the white arrow.

2.4 Methods

Approximately 70 to 100 grams of rock was powdered using a Spex 8515 shatterbox in an alumina ceramic vessel for 3 minutes. All analyses were performed at Washington University.

2.4.1 Carbon and Oxygen Isotopes

Carbonate carbon and oxygen isotopes were prepared by dissolving ~100 μg in 100% phosphoric acid (H_3PO_4) for at least 4 hours at 70°C. Sample vials were subsequently flushed with He and the evolved CO_2 was measured on a Thermo Finnigan Gasbench II coupled to a Delta V Advantage Isotope Ratio Mass Spectrometer.

Insoluble residues were obtained for organic carbon analyses by acidifying 4–5 g of rock powder with 6M HCl for 10 to 20 minutes, for at least 3 rinses. This was repeated until there was no visible reaction when HCl was added. Insoluble residues were analysed for organic carbon isotope composition on a Flash 2000 Organic Elemental Analyzer, coupled via a ConFlo IV to a Delta V Isotope Ratio Mass Spectrometer. Total organic carbon (TOC) abundance was determined from the area of the resulting CO_2 peak upon combustion. Carbon and oxygen isotopes are expressed in standard delta notation ($\delta^{13}C$, $\delta^{18}O$) in permil (‰) as a deviation from the Vienna-Pee Dee Belemnite (V-PDB) standard. From standard and replicate measurements, the 1σ error on $\delta^{13}C_{carb}$ is 0.19‰, $\delta^{18}O_{carb}$ is 0.15‰ (reported relative to calcite) and for $\delta^{13}C_{org}$ is 0.15‰.

2.4.2 Sulfur Isotopes

Preparation for sulfur isotope determination of CAS follows a modified method from Burdett et al. (1989) and (Wotte et al., 2012a). Approximately 30–50 g of powder was rinsed 3 times in a

10% brine (NaCl) solution for 30 minutes. After the third brine rinse, the supernatant was filtered and checked for sulfate by adding ~1 ml of saturated $BaCl_2$ solution. Brine rinses were repeated until no sulfate precipitate appeared in the supernatant. This was followed by 3 deionized H_2O rinses. To liberate CAS, 6M HCl was gradually added to each sample. Samples were stirred at a pH of ~2 for no longer than 3 hours. An excess of saturated $BaCl_2$ solution was added to the acidic supernatant and left for 5 days to precipitate $BaSO_4$. CAS abundance (ppm) is calculated from the sulfate yield relative to the initial carbonate content in the sample.

Pyrite was extracted from insoluble residues. Samples were heated to 186°C (± 10°C) under N_2 gas and constant stirring for 4 hours with 6N HCl and 2M chromium (II) chloride solution. Evolved gas was passed through a water trap before bubbling into a test tube containing silver nitrate solution in deionized H_2O, precipitating silver sulfide. Whole-rock pyrite abundance (wt % S) was calculated from the CRS precipitate yield relative to the initial mass used for the extraction.

Approximately 350 μg of silver sulfide or barium sulfate (combined with 1–3 mg of vanadium pentoxide) were combusted using a Costech ECS 4010 elemental analyzer coupled to a Thermo Finnigan Delta V Plus mass spectrometer. S-isotopes are expressed in standard delta notation ($\delta^{34}S$) in permil (‰) as a deviation from the Vienna-Canyon Diablo Troilite (V-CDT) standard. From standard and replicate measurements, the 1σ error on $\delta^{34}S_{CAS}$ is 0.3‰ and for $\delta^{34}S_{pyr}$ is 0.2‰.

2.4.3 Elemental Abundance

Preparation of samples for cation analysis by inductively coupled plasma optical emission spectroscopy (ICP-OES) analyses followed the method by Husson et al., (2015) where only the carbonate fraction is dissolved. Analyses were conducted using a PerkinElmer Optima 7300DV ICP-OES. Calcium, magnesium, iron, strontium and manganese, given in ppm, were standardized to the Sigma Multi-element Standard Solution 5.

2.5 Results

2.5.1 Carbon and Oxygen Isotopes

The Viki drill core records three positive $\delta^{13}C_{carb}$ isotope excursions (Figure 2.4). The peak in $\delta^{13}C_{carb}$ between ~246 and 243 m reflects the global Hirnantian carbon isotope excursion that approximates the Ordovician-Silurian boundary (Hints et al., 2014), here characterized by a long falling limb continuing in the lower Varbola Fm. From a minimum of -1.3‰ at 237.47 m, $\delta^{13}C_{carb}$ steadily increases throughout the Varbola Fm. reaching 2.5‰ at 208 m in the lower Nurmekund Fm. $\delta^{13}C_{carb}$ values are generally stable throughout the Nurmekund (with one outlier of 4.8‰). Across the unconformity between the Nurmekund and Rumba Fms., $\delta^{13}C_{carb}$ values decline to ~0.3‰ for a short interval before increasing to 2.5‰ in the basal Velise Fm. (175 m). Variability in $\delta^{13}C_{carb}$ decreases and values fall to 1‰ at 141.27 m. Near the base of the Jaani Fm., $\delta^{13}C_{carb}$ values increase from 1.8‰ to 4‰ at 110 m. The $\delta^{13}C_{carb}$ values increase again at 101 m to 5‰ and remain invariant into the Jaagarahu Fm., except for an outlier of 1.5‰ at the Jaani-Jaagarahu contact (87.6 m). At the 73 m, $\delta^{13}C_{carb}$ begins to decline toward -2‰ at the top of the section (49.5 m).

Carbonate oxygen isotopes vary more widely than carbonate carbon isotopes (Figure 2.4). Basal $\delta^{18}O_{carb}$ values are ~ -5‰. There is a shift to lower (-5.8‰) values at the base of the Nurmekund Fm. Above this, $\delta^{18}O_{carb}$ is relatively invariant around -5‰, until 130 m where values steadily increase towards -3.5‰ at 100 m. From 99 to 83.6 m, values are the most variable, before clustering around -3.5‰ until 69 m, at which point $\delta^{18}O_{carb}$ decreases to -5‰ at the top of the section.

Overall, $\delta^{13}C_{org}$ displays similar stratigraphic trends to $\delta^{13}C_{carb}$ (Figure 2.4). The lowermost samples, 241.33 to 222.75 m, record $\delta^{13}C_{org}$ of approximately -31‰. The $\delta^{13}C_{org}$ values increase to -29‰ in the Tamsalu and Nurmekund Fms. (194.77 m; with two outliers of ~-26.5‰ at 210.68 and 200.7 m). In the Rumba Fm. $\delta^{13}C_{org}$ values decrease to -31.2‰ at 190.57 m before transiently increasing to -26.4‰ at the base of the Velise Fm. (183.4 m). Up to 151.17 m, $\delta^{13}C_{org}$ varies between -26.5‰ and -27.9‰; above this, values decrease but remain variable (-27‰ to -28.5‰). In the Jaani and Jaagarahu Fms., a positive excursion from -28‰ to -24.7‰ appears to lag $\delta^{13}C_{carb}$ by ~ 4 m; however, variability in $\delta^{13}C_{org}$ makes it difficult to precisely identify the onset of increased $\delta^{13}C_{org}$ values. The overlying strata record a drop in $\delta^{13}C_{org}$ to -31‰, paralleling that observed in $\delta^{13}C_{carb}$.

2.5.2 Sulfur Isotopes

$\delta^{34}S_{CAS}$ data have an isotopic range of ~17‰ (20‰ to 37‰) with three outliers falling below 20‰ in the Rumba and Velise Fms. (Figure 2.4). At the base of the section, values sharply decline from 32.8 to 24.8‰ over 15 m, then increase to 37‰ in the lower Nurmekund Fm. (216.6 m). Values decrease slightly from ~35 to 33.8‰ through to the top of the Nurmekund Fm. In the Rumba Fm. and the base of the Velise Fm. (190.57 to 164.07 m), $\delta^{34}S_{CAS}$ becomes highly variable (with values as low as 8.2‰). This interval has few data points due to low sulfate abundance and low carbonate content, which frequently precluded sufficient CAS yield for isotopic analysis (Figure 2.5). At 160.25 m, $\delta^{34}S_{CAS}$ returns to 30.2‰ and then decreases to 24‰ at 145.26 m, where it remains relatively steady until 126 m. Above this point, $\delta^{34}S_{CAS}$ slowly increases, reaching 30‰ in the basal Jaani Fm. Throughout the Jaani Fm. and the Jaagarahu Fm., $\delta^{34}S_{CAS}$ values oscillate between 28 and 36.2‰.

Basal Hirnantian strata show a large positive $\delta^{34}S_{pyr}$ excursion from -20 to 40‰ (Figure 2.4; Hints et al., 2014) which rapidly decreases to -28‰ at the base of the Varbola Fm. $\delta^{34}S_{pyr}$ values increase to 14.9‰ throughout the Varbola Fm. (241.33 to 224.6 m). At the base of the Nurmekund Fm. (214.65 m), there is an abrupt transition to more negative $\delta^{34}S_{pyr}$ values (-35‰), followed by an increase to 18.4‰ (at 190.57 m) at the Nurmekund-Rumba contact. The Rumba and basal Velise Fm. are marked by a transition to more negative $\delta^{34}S_{pyr}$ values (~ -22‰ at 180.2 m), which are stable throughout the Velise Fm., before increasing toward 1.8‰ in the lowermost Jaani Fm. (112.65 m). From 103.6 to 96.82 m, $\delta^{34}S_{pyr}$ declines to -28.7‰ and then return to -21‰ in the upper Jaani Fm. at 89.64 m. The Jaagarahu Fm. (87.6 to 61.7 m) marks an increase in the variability and average value of $\delta^{34}S_{pyr}$ (reaching 17.1‰), although $\delta^{34}S_{pyr}$ returns to lower values (-25‰) in the uppermost part of the formation (54.7 to 49.9 m).

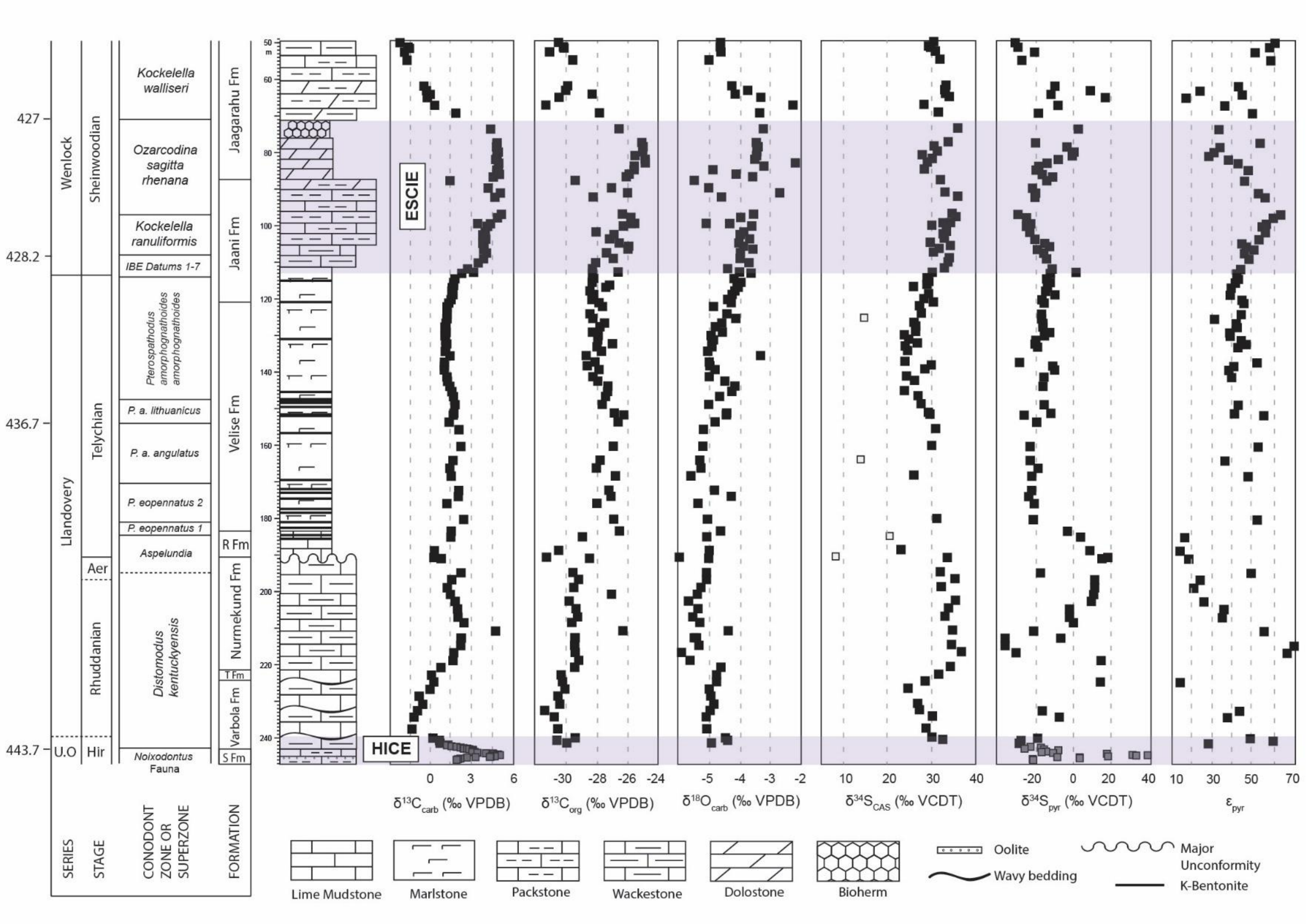

Figure 2.4 – Isotope data plotted against Viki core litho- and biostratigraphy. From left to right: $\delta^{13}C_{carb}$, $\delta^{13}C_{org}$, $\delta^{18}O_{carb}$, $\delta^{34}S_{CAS}$, $\delta^{34}S_{pyr}$ and ε_{pyr}. Included in $\delta^{13}C_{carb}$ and $\delta^{34}S_{pyr}$ is data from Hints et al., (2014) as grey squares reflecting the Hirnantian isotope excursion. Shaded regions correspond to the globally recognized Hirnantian positive carbon isotope excursion (HICE) and Ireviken/early Sheinwoodian carbon isotope excursion (ESCIE). In $\delta^{34}S_{CAS}$ plot, empty squares are samples suspected to have undergone alteration.

2.5.3 Lithologic data

From the base of the core to the top of the Nurmekund Fm. (185 m), carbonate content increases from 45% to 96.6% (Figure 2.5). Carbonate content is mostly < 40% in the Velise Fm., with a trend of increasing % carbonate throughout the Velise Fm. An increase in % carbonate occurs in the lower Jaani Fm., where it varies between 65-100% throughout the Jaagarahu Fm. Combined with the lithofacies interpretation, % carbonate tracks trends in reconstructed local sea level (higher % carbonate in shallow-water facies; lower % carbonate in deep-water facies). Total organic carbon (TOC, wt %) is highest in the Varbola Fm. at 0.9%. There is a strong trend of decreasing and less variable TOC throughout the Varbola, Nurmekund and Rumba Fms., and into the base of the Velise Fm. (~175 m) to < 0.2% where they remain for the rest of the core (Figure 2.5). CAS abundance varies between 0 and 590 ppm in the lowermost formations. In the Velise Fm., CAS values are mostly between 400 and 1200 ppm (with an outlier of 2950 ppm at 151.17 m). CAS abundances remain variable, up to 1800 ppm in the Jaani Fm., but trend towards lower values at the top of the section. Pyrite abundance (wt % S) is < 1% in the Varbola and Nurmekund Fms. In the Velise Formation and into the Jaani Formation, between 175.85 and 110 m, pyrite content is more variable reaching 3.2%. Above 110 m, pyrite abundance is generally < 0.6 % with a few outliers up to 1.7%.

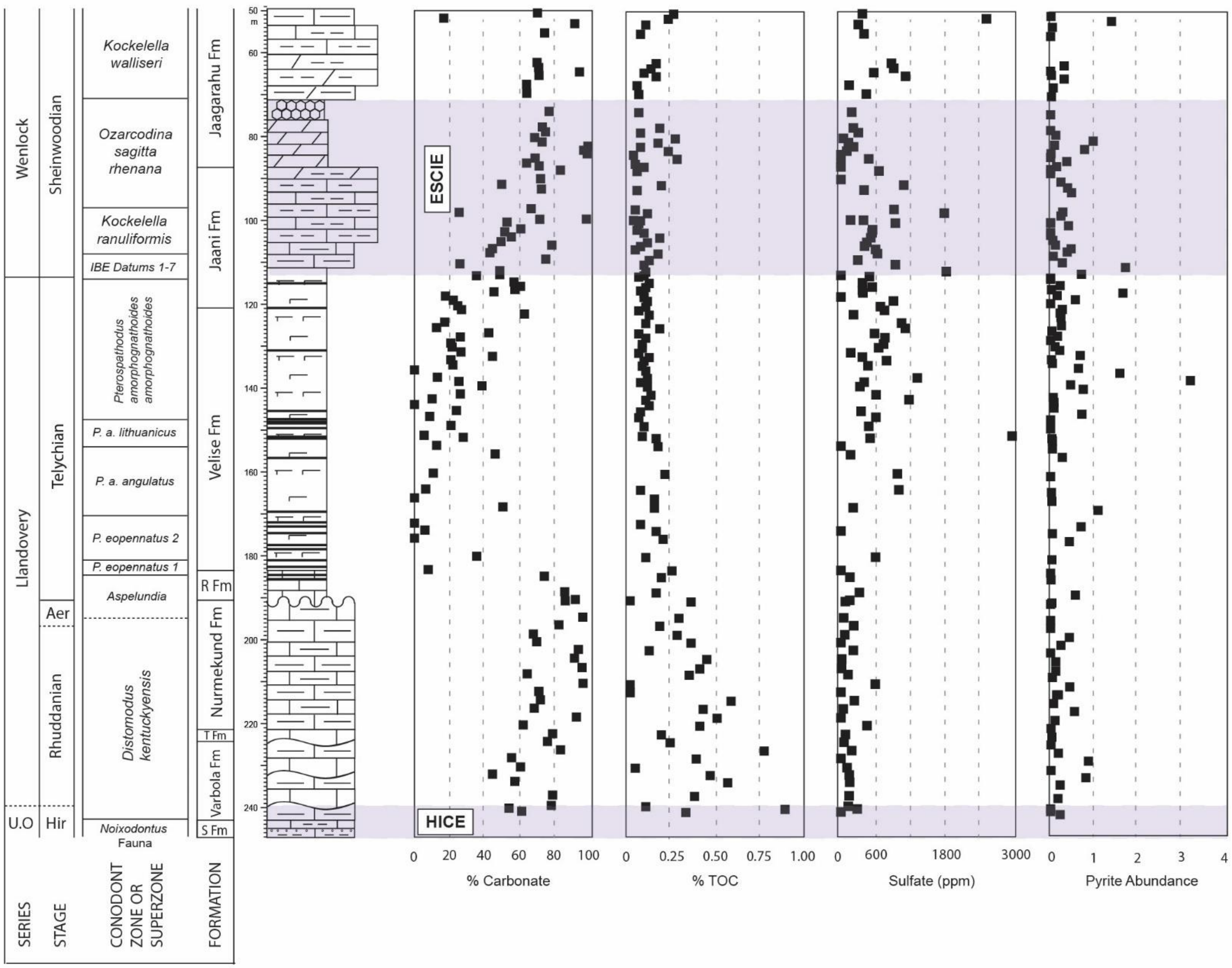

Figure 2.5 – Lithologic data plotted against Viki core stratigraphy. From left to right: % carbonate, % TOC, CAS (ppm) and pyrite abundance (wt. % S)

2.5.4 Elemental Concentrations

The Viki drill core has undergone variable degrees of dolomitization. The Varbola and Nurmekund formations have relatively invariant molar Mg/Ca ratios generally < 0.05 (Figure 2.6). The Velise Fm. (190 m) marks a transition of elevated and more variable Mg/Ca, up to 0.5. This variability decreases to ~ 0.1 between 121 m and 97.73 m. In the upper Jaani Fm. (96.82 to 87.6 m), Mg/Ca ratios are < 0.2. The Jaagarahu Fm. marks an abrupt increase in Mg/Ca to 0.5 for ~16 m, before declining to < 0.1 at the top of the core. From the lowermost samples of the Varbola Fm., to the middle of the Jaani Fm., Sr/Ca increases from 1 to 4 mmol/mol, where the greatest variability occurs in the Velise Fm. Above 110.8m, values decline to < 1 mmol/mol where they remain for the rest of the section.

Iron concentrations display the greatest variability of all trace components, ranging from 25 to 1187 ppm. Generally, up to 190.88 m, iron concentrations are less than 200 ppm (with few samples reaching ~450 ppm). The average content of iron increases in the Velise Fm. to a maximum of 1187 ppm at 168.35 m. This variability continues into the lower Jaani Fm., where iron concentrations range from 90 to 775 ppm, before declining to 125 ppm at 92.15 m. Iron concentrations increase to 915 ppm at the base of the Jaagarahu Fm. (86.6 m), followed by a decrease to ~70 ppm at the top of the core. Mn concentrations are mostly below 200 ppm with little stratigraphic variation, except for 3 samples between 170 and 180 m that reach values between 401 and 997 ppm.

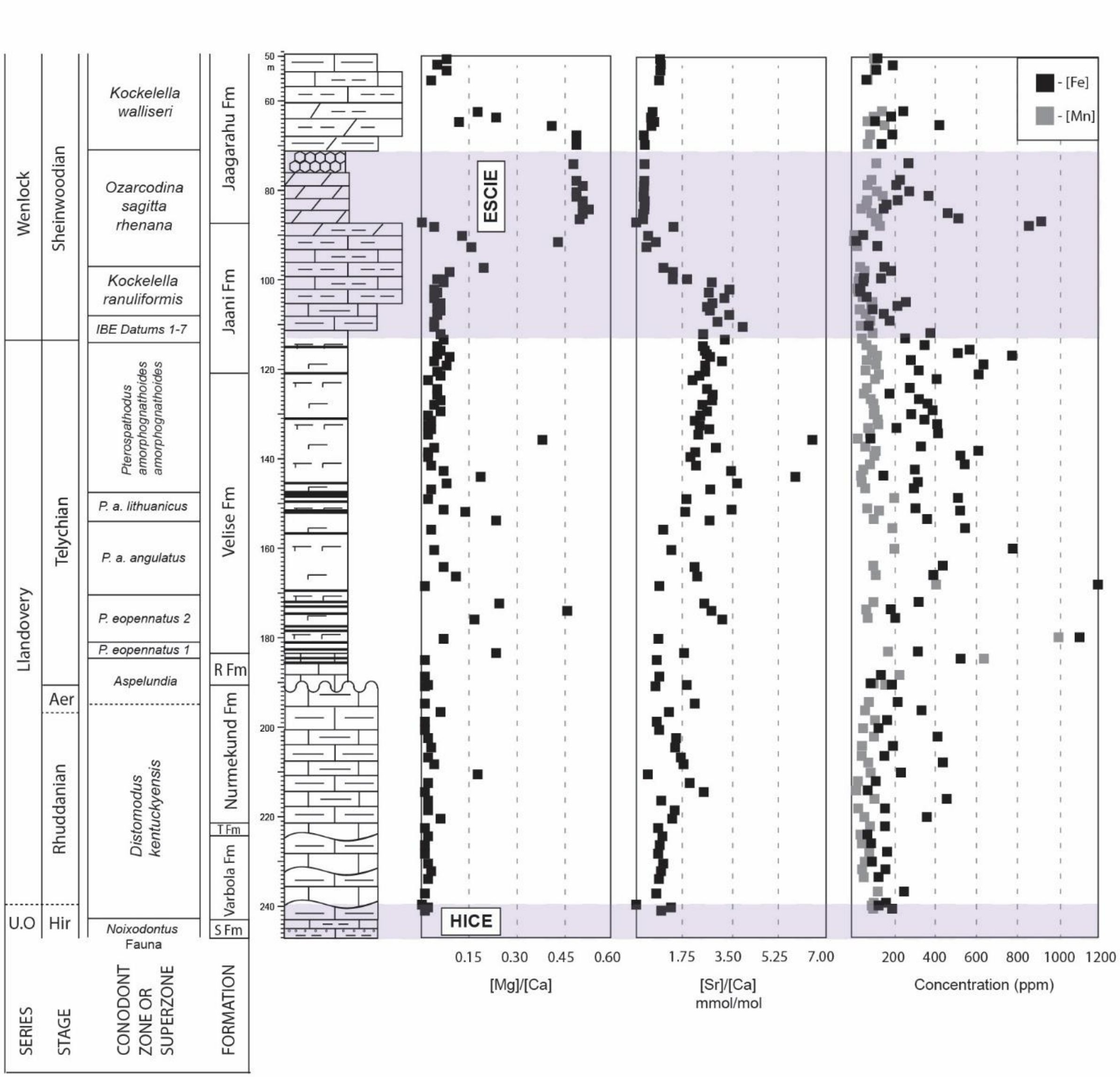

Figure 2.6 – Trace element data plotted against Viki core stratigraphy. From left to right: molar Mg/Ca, Sr/Ca in mmol/mol and [Mn], [Fe] in ppm.

2.6 Controls on Carbon and Sulfur Isotope Signals

2.6.1 Global Forcings

Traditionally, transient variations in carbon or sulfur isotope ratios throughout a stratigraphic section have been attributed to perturbations to the global carbon and sulfur cycles. Steady-state isotope mass-balance models invoke similar parameters to explain isotope excursions in carbon or sulfur (Canfield, 2004; Kump and Arthur, 1999):

$$\delta_{\mathrm{reservoir}} = \delta_{\mathrm{in}} + f * \varepsilon$$

where $\delta_{\mathrm{reservoir}}$ represents the isotopic composition of the (oxidized) marine reservoir (DIC or sulfate, respectively), δ_{in} represents the isotopic composition of DIC or sulfate entering the ocean, f represents the relative burial of the reduced reservoir exported from the ocean (organic carbon or pyrite), and ε represents the isotopic fractionation between the oxidized and reduced reservoirs. These variables are used alone or combined to explain stratigraphic isotope trends, particularly trends in which both isotope species co-vary in their timing and relative magnitude of excursion (Canfield 2004; Kump and Arthur 1999). Parallel co-variation is observed in the C-isotope, but not the S-isotope, data presented here.

The studied strata of the Viki drill core span ~ 15 Myr. The δ^{13}C manifestation of the IBE is estimated to last ~1 Myr (Lehnert et al., 2010). These timescales are long enough for the global C-cycle to respond to a perturbation (residence time of carbon in the modern ocean-atmosphere is 10^5 years; Kump and Arthur, 1999). However, it is unlikely that the global S-cycle can respond on such short time scales. The residence time is the ratio of the size of the reservoir, to the input or output flux, which are equal at steady state. Modern marine sulfate concentrations of 28 mM corresponds to a 13 Myr residence time for sulfate (Berner, 2001; Canfield, 2004). Based on estimated Silurian seawater sulfate (5-12 mM; (Lowenstein et al., 2003), a multi-million-year residence time of seawater sulfate in the Silurian is anticipated. Thus, S-isotope variability in the Viki core is unlikely to reflect changes to the global S-cycle.

2.6.2 Local Effects

Sea Level, Gradients and Chemocline Migration

There is evidence for multiple global sea level changes throughout the early Silurian (Munnecke et al., 2010). The effect of these on individual basins will differ; therefore, it is imperative to include local depositional context in interpretations of isotope records. Areas undergoing shallowing may experience an increase in $\delta^{13}C$ of the local dissolved inorganic carbon ($\delta^{13}C_{DIC}$) pool as the location of sedimentation changes relative to the $\delta^{13}C$ gradient associated with the biological pump (Holser, 1997). Generally, the biological pump increases the relative ^{13}C content in surface waters while lowering ^{13}C in deep waters. This is due to isotopic fractionation during DIC-fixation in surface waters, and remineralization of ^{13}C-depleted organic carbon in deep water.

Sea level fluctuations may also be extremely important to sedimentary $\delta^{34}S$ records due to both chemical and physical processes. In shallow environments, sediment reworking, sedimentation rate, Fe availability, and labile organic carbon availability will increase relative to deeper water (Aller et al., 2010; Fike et al., 2015; Toth and Lerman, 1977). These factors suggest that in shallow-water environments, pore waters generally evolve under more closed-system conditions. In this model, sulfate is consumed by microbial sulfate reduction (MSR) faster than it is replenished from the overlying water column. As progressive MSR occurs, the $\delta^{34}S$ of porewater sulfate increases, resulting in a parallel increase in $\delta^{34}S_{pyr}$ of any newly formed pyrite at any given time and in $\delta^{34}S_{CAS}$, as predicted by a Rayleigh-type distillation model (e.g. Pasquier et al., 2017).

In shallow environments, tidal or storm forcings can result in pulsed sedimentation and reworking events that can disturb the natural isotope stratification within previously anoxic sediments (Aller et al., 2010; Fike et al., 2015; Pasquier et al. 2017). These processes, as well as bioturbation, can result in $\delta^{34}S_{pyr}$ values that may be highly variable over short spatial and temporal scales. These effects are expected to be minimized during high local sea level. In deep-water settings, sea water exchange with pore water is not generally limited by sedimentation rate, which may result in lower and less variable $\delta^{34}S_{pyr}$. Due to more open-system isotope systematics, the $\delta^{34}S_{CAS}$ in deep-water carbonate has the potential to more faithfully record basinal $\delta^{34}S_{CAS}$ values.

A model for pyrite formation impacted by local closed-system conditions within sediments explains the decoupling of $\delta^{34}S_{pyr}$ and $\delta^{34}S_{CAS}$ records, that reflect adjacent, yet distinct environments. Generally, pyrite forms within the sediment from pore waters, however carbonate, especially the shallow-water facies that dominate during the early Llandovery and the early Wenlock (proximal, backreef, reef, and shoal; respectively), are precipitated within seawater and may not be affected by the distilling pore water (Lyons et al., 2004b; Rennie and Turchyn, 2014). Such carbonates from the water column and surficial sediments above the chemocline are more likely to capture sulfate with a $\delta^{34}S_{CAS}$ value similar to the local seawater. However, cements forming below the chemocline in the region of distillation may record a CAS signal divergent from ambient seawater (i.e., lower [CAS]; higher $\delta^{34}S_{CAS}$). These cements will comprise only a portion of a given sample, dampening any aberrant signal from these cements during homogenization prior to bulk extraction.

A series of cross-plots were made to assess any potential facies dependence on carbon and sulfur isotopes results (Figure 2.7). $\delta^{13}C_{carb}$ vs. % carbonate shows no correlation (Figure 2.7a), but $\delta^{13}C_{org}$ vs. TOC shows that high TOC correlates with relatively invariant $\delta^{13}C_{org}$ (~ -30‰)

(Figure 2.7b). Samples with high TOC and lower $\delta^{13}C_{org}$ are from the top of the Jaagarahu Fm. and are 2‰ heavier than the anticipated offset relative to $\delta^{13}C_{carb}$, indicative of a local control on these signals. $\delta^{34}S_{CAS}$ and $\delta^{34}S_{pyr}$ vs. % carbonate (Figure 2.7c, d) indicate that both $\delta^{34}S_{CAS}$ and $\delta^{34}S_{pyr}$ are heavier at higher % carbonate, and $\delta^{34}S_{pyr}$ is more variable under these conditions, which further highlights the depositional dependence on these proxies.

Variable ε_{pyr}

A changing biological fractionation during microbial sulfur cycling (ε_{bio}; fractionation occurring during sulfate reduction or other microbial processes), usually results in a change in the product sulfide $\delta^{34}S$. Holding other parameters constant, changes in ε_{bio} should be inherited in the pyrite record and mirrored in ε_{pyr} (isotopic offset between coeval sulfate and pyrite records). A decrease in ε_{bio} can arise during a decrease in sulfate concentrations or an increase in cell-specific sulfate reduction rates (csSRR; Leavitt et al., 2013; Sim et al., 2011). Increases in csSRR usually results from increased electron donor availability, such as organic carbon. Variations in ε_{bio} can also result from changing the dominant metabolism(s) within a microbial community; MSR, sulfide oxidation and sulfur disproportionation. MSR imparts a fractionation of up to ~ 70‰ (Leavitt et al., 2013; Sim et al., 2011; Wing and Halevy, 2014) and its isotopic fractionation is thought to dominate most sedimentary systems. However, sulfur disproportionation could result in an increase in ε_{bio} (Canfield and Teske, 1996), while abiotic sulfide oxidation could shift net ε_{bio} toward lower values (Fry et al., 1988).

Closed-system effects can drive changes in ε_{pyr} irrespective of any change in ε_{bio}. Such effects can arise from variations in sedimentation rate or other environmental parameters (e.g., organic carbon loading, bottom water oxygen availability) that can impact the proximity of the chemocline to the sediment-water interface and therefore the connectivity between the overlying water column and the porewaters where pyrite is forming.

2.6.3 Diagenesis

Geochemical Characteristics

Cross-plots of isotope and elemental concentrations (Figure 2.7) are often used to assess the extent and magnitude of alteration and/or overprinting of geochemical data, resulting from water-rock interaction. Diagenetic fluids could be meteoric, marine (including pore-water), and/or brines. A correlation between $\delta^{13}C_{carb}$ and $\delta^{18}O_{carb}$ often reflects diagenetic water-rock interaction, where alteration by meteoric fluids that contain DIC with some component from respiration are associated with depletion in both $\delta^{18}O_{carb}$ and $\delta^{13}C_{carb}$ (Banner and Hanson, 1990; Brand and Veizer, 1980). In Figure 2.7e, there is minimal correlation ($r^2 = 0.2$) between $\delta^{13}C_{carb}$ and $\delta^{18}O_{carb}$, providing no (obvious) evidence for diagenetic fluid interaction that impacted these signals.

Similar to changes anticipated in diagenetic $\delta^{13}C_{carb}$ and $\delta^{18}O_{carb}$, strontium in calcite should decrease during progressive water-rock interaction, while manganese and iron concentrations will increase under these conditions in an anoxic environment (Banner and Hanson, 1990). Comparing strontium and manganese concentrations, many samples fall between 20 and 200 ppm manganese over a wider range in strontium (60 to 486 ppm), with 3 outliers containing low (< 200 ppm) strontium and high manganese concentration (> 400 ppm) (Figure 2.7f). The anomalous samples come from the base of the Velise Fm. where $\delta^{34}S_{CAS}$ is also low and variable. The plot of strontium vs. iron concentrations shows more variability in Fe concentration (Figure 2.7g). Samples higher in iron but low in manganese occur in mudstone-marlstone units of the upper Velise and lower Jaani Formations (Figure 2.6). Due to the similar behavior of manganese and iron in diagenetic fluids, it is likely that different trends in enrichment of Mn and Fe here are correlated with different detrital sources during deposition, as opposed to a redox difference during diagenesis.

To discern potential effects of dolomitization on $\delta^{34}S_{CAS}$, Mg/Ca is plotted against $\delta^{34}S_{CAS}$, (Figure 2.7h). Two patterns are observed: samples with Mg/Ca < 0.1 are spread over the entire range of observed $\delta^{34}S_{CAS}$; in contrast samples with Mg/Ca > 0.1 are characterized by a narrower $\delta^{34}S_{CAS}$ range (28-36.2‰). Samples with the greatest dolomitization (i.e. Mg/Ca > 0.5) are from shallow-water facies in the early Wenlock. These data indicate that dolomitization, in this case, does not substantially alter $\delta^{34}S_{CAS}$ – and, if anything, suggests that early dolomitization can aid in the preservation of a depositional signal with minimal subsequent alteration, consistent with previous observations (Marenco et al., 2008b).

Recrystallization in contact with meteoric fluids would likely strip carbonate of sulfate (Gill et al., 2008), whereas a brine fluid may increase sulfate content in recrystallized carbonates. Figure 2.7i indicates samples with CAS abundance less than 200ppm have more variable $\delta^{34}S_{CAS}$ and may have undergone alteration, most likely during early diagenesis, due to the lack of evidence of late stage fluid alteration. The absence of correlation between [CAS] and $\delta^{34}S_{CAS}$ is consistent with a lack of contamination from pyrite oxidation (Marenco et al., 2008a). Although the carbonates are variably dolomitized and visibly recrystallized throughout the core, creating the potential for alteration of primary geochemical signals, the record of $\delta^{34}S_{CAS}$ presented (excluding 188.7 to 164 m) is overall less variable (sample-to-sample variability is generally ≤ 4‰, with a maximum of 5.8‰), than other comparable sections (e.g. maximum of ~ 8‰; Jones and Fike 2013; maximum of ~ 7.5‰; Rose et al., 2019).

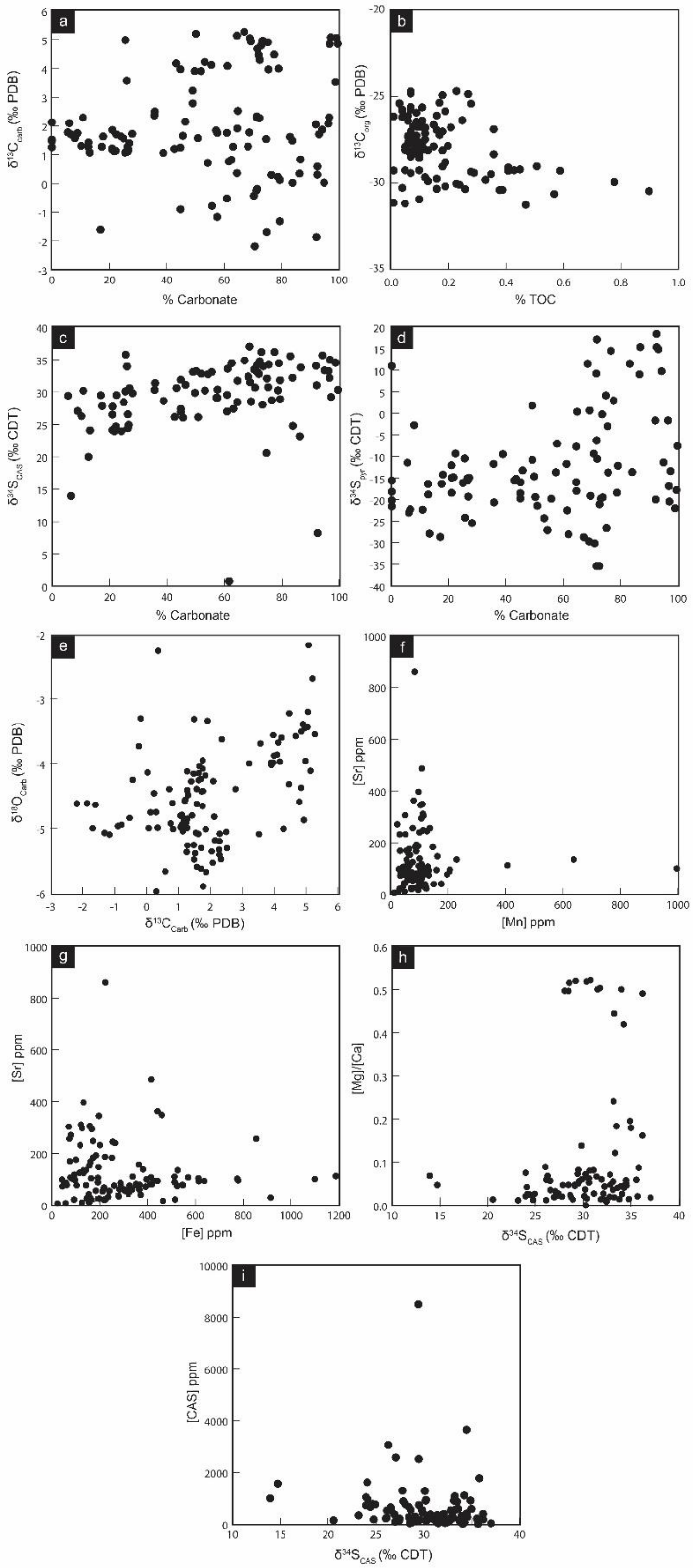

Figure 2.7 – Geochemical cross-plots a.) % carbonate vs. $\delta^{13}C_{carb}$, b.) % TOC vs. $\delta^{13}C_{org}$, c.) % carbonate vs. $\delta^{34}S_{CAS}$, d.) % carbonate vs. $\delta^{34}S_{pyr}$ e.) $\delta^{18}O_{carb}$ vs. $\delta^{13}C_{carb}$ f.), [Sr] vs. [Mn], g.) [Sr] vs. [Fe], h.) [Mg]/[Ca] vs. $\delta^{34}S_{CAS}$, and i.) [CAS] vs $\delta^{34}S_{CAS}$.

Early Marine Diagenesis: Composition and Abundance of Carbonate Components

In order to make credible interpretations of $\delta^{34}S_{CAS}$, we must understand what contributes to the bulk $\delta^{34}S_{CAS}$ records in ancient carbonates. Carbonates are composed, in varying abundances, of cement, micrite, fossils and abiotic grains. These components can have different $\delta^{34}S_{CAS}$ and sulfate concentrations (Present et al., 2015), which may be masked when using bulk methods. Although the bulk chemistry here suggests no large-scale resetting of proxies, early diagenesis influencing CAS on a small scale may not be reflected in these parameters, e.g. dissolution-reprecipitation of cement. Shallow-water carbonates contain a higher abundance of fossils, grains and cement than deep-water carbonates. Cements precipitate in a range of environments and are prone to several dissolution and re-precipitation events meaning the $\delta^{34}S_{CAS}$ of cements will be more variable (see section 2.6.2) because of the variable sulfate compositions of diagenetic fluids. Detrital micrite is likely to contain a higher abundance of pyrite than cement, due to a higher porosity and surface area. The oxidation of sulfide in pore space (e.g. during bioturbation and/or reworking) is one mechanism that could decrease $\delta^{34}S_{CAS}$ in deep-water environments (e.g. lower Velise Fm.).

Shallow-water environments analyzed here have a greater diversity and abundance of fossils than deep-water settings. Aragonite and high-Mg calcite fossils are prone to micritization or dissolution and subsequent cement precipitation, thus many (recrystallized) fossils may reflect secondary $\delta^{34}S_{CAS}$ components (Present et al., 2015). Biological controls on the incorporation of sulfate into biogenic carbonate are not well constrained; however, it has been suggested that brachiopods may be among the most faithful archives for CAS (Kampschulte and Strauss, 2004; Present et al., 2015). This is due to the multi-layered, low-Mg calcite structure of brachiopod shells that are less likely to recrystallize during diagenesis. Changes in the abundance of carbonate components, each with their own susceptibility to alteration, throughout a section, could introduce variability in the $\delta^{34}S_{CAS}$ record. These factors require further investigation to understand how individual components may affect the ultimate $\delta^{34}S_{CAS}$ value in a given sample.

2.7 Interpreting the Viki Isotope Record

2.7.1 End-Hirnantian

The coeval positive $\delta^{13}C_{carb}$ and $\delta^{34}S_{pyr}$ excursion at the end of the Hirnantian have been interpreted to reflect perturbations to the global C and S-cycles, by increased carbonate weathering or organic carbon burial, and an increase in pyrite burial respectively (Hints et al., 2014; Kump et al., 1999; Yan et al., 2009). The short duration and absence of a co-occurring $\delta^{34}S_{CAS}$ excursion on Anticosti Island (Jones and Fike, 2013), suggests that a global perturbation is unlikely to explain the $\delta^{34}S_{pyr}$ excursion. The similarity of end-Hirnantian $\delta^{34}S_{pyr}$ record to the overlying chemostratigraphy and lithofacies in the Rhuddanian-Aeronian, indicate similar (i.e., local depositional) mechanisms can explain these data, discussed in section 2.7.2.

2.7.2 Rhuddanian – Aeronian

From the Varbola to the top of the Nurmekund Fm., there is a positive $\delta^{13}C_{carb}$ excursion up to 2.5‰. Simultaneously, there is a stepwise increase in $\delta^{13}C_{org}$ by ~ 1.5‰. These trends appear to be coincident with the fall and rise of global sea level associated with early Silurian glacial maxima (Kaljo and Martma 2000), where weathering of carbonate or an increase in f_{org} could be drivers for this C-isotope excursion. Alternatively, changing local sea level (and the relative position of sedimentation with respect to the biological pump) could contribute to this signal. However, the absence of a correlation between $\delta^{13}C_{carb}$ and % carbonate does not provide a clear fingerprint for this mechanism to be the cause of the C-isotope changes through the Rhuddanian and Aeronian.

Initially, $\delta^{34}S_{CAS}$ declines from 33‰ to 25‰ but then increases and remains steady through the Aeronian at ~ 35‰. Simultaneously, $\delta^{34}S_{pyr}$ is variable, ranging from -35 to 15‰, where higher $\delta^{34}S_{pyr}$ values are associated with higher carbonate content and shallower depositional facies. This behavior likely reflects increased closed-system conditions. The low abundance of fossils relative to cement and micrite in these samples means that much of the carbonate was forming within the sediment pore space. Here, $\delta^{34}S_{CAS}$ is relatively heavy with respect to suggested Silurian seawater $\delta^{34}S_{SO4}$ of 27‰ (Kampschulte and Strauss, 2004). This heavy $\delta^{34}S_{CAS}$ could reflect the high and episodic sedimentation rate in shallow-water environments, resulting in (variably) closed-system isotope behavior. Progressive MSR in pore space increases carbonate alkalinity, therefore diagenetic carbonate formation is likely, and would capture residual pore water sulfate with elevated ^{34}S. The likelihood of observing these signals depends on the abundance of these components relative to those that formed in the water column (see section 2.6.3).

Decreases in ε_{pyr} occur in both the Varbola and Nurmekund formations, which could be tracking a change in ε_{bio}. TOC values are the highest at the base of the core where there is greater potential for increased csSRR. However, corresponding $\delta^{13}C_{org}$ values increase from the Rhuddanian into the Aeronian, which is the opposite trend anticipated when there is more metabolizable organic matter, implying there may not have been sufficient labile organic matter available to increase csSRR. This suggests that other factors contribute to the observed variability in ε_{pyr}; given the relationship between facies and $\delta^{34}S_{pyr}$ we infer these factors are depositional conditions that modulate the onset and degree of closed-system conditions during deposition.

2.7.3 Telychian

Carbon isotopes in the Telychian are comparatively more stable. There is a small, gradual decrease in $\delta^{13}C_{carb}$ of ~ 1‰, known as the "Rumba Low" (Kaljo and Martma, 2000). The facies indicate a deepening from the Rumba to Velise formations, immediately following an unconformity (Nestor, 2010). This is consistent with high global sea level estimates during the Telychian (Munnecke et al., 2010). As such, the observed decline in $\delta^{13}C_{carb}$ may be attributed to the local $\delta^{13}C$ gradient changing with depth and is unlikely to reflect a regional or global perturbation to the C-cycle.

With the exception of $\delta^{34}S_{CAS}$ values between 188.7 and 164 m, both $\delta^{34}S_{CAS}$ and $\delta^{34}S_{pyr}$ are relatively stable with respect to the formations below. The deeper environment results in a more open system, in which sulfur isotopes are less variable and minimally impacted by porewater distillation. As such, these $\delta^{34}S_{CAS}$ could be more representative of ambient seawater $\delta^{34}S_{SO4}$ values, while the $\delta^{34}S_{pyr}$ values, minimally impacted by closed-system effects, may more closely approximate ε_{bio}. Samples between 188.7 and 164 m are generally characterized by low CAS abundance (most below the threshold needed for isotopic analysis) and are suspected to have undergone substantial post-depositional alteration.

2.7.4 Sheinwoodian

Early Wenlock strata show a 4‰ positive excursion in $\delta^{13}C_{carb}$, with a 3‰ excursion in $\delta^{13}C_{org}$, coincident with the IBE. The onset of the excursion is associated with a facies change in the Jaani Fm. and an increase in carbonate content (Figure 2.5), reflecting marine regression. The synchronous excursion in carbon isotopes during an extinction event suggests a perturbation to the local DIC pool. Such a perturbation could arise from changes in the depth that the carbonates sample DIC along the biological pump gradient. Based on the modern $\delta^{13}C_{DIC}$ gradient, this could account for approximately 2 ‰ of the excursion (Holser, 1997); as such, unless the Silurian $\delta^{13}C_{DIC}$ gradient was greatly different, a change in depth would be insufficient to explain the observed excursion. Further, this $\delta^{13}C$ signal is globally correlative (Cramer and Saltzman, 2005; Munnecke et al., 2003; Rose et al., 2019), which suggests a perturbation to the global DIC reservoir (e.g. decrease in organic carbon burial) possibly enhanced by globally modulated changes to sea level associated with glacioeustatic sea level change (Munnecke et al., 2010; Jones and Fike, 2013).

S-isotopes, both $\delta^{34}S_{CAS}$ and $\delta^{34}S_{pyr}$, become heavier and increasingly more variable throughout the Sheinwoodian. As seen during the Rhuddanian and Aeronian, an increase in carbonate content and a change to shallow, reefal carbonate lithofacies favors a shift to more closed-system isotope behavior, which is likely driving the variation in $\delta^{34}S_{pyr}$ (and in ε_{pyr}). Again, $\delta^{34}S_{CAS}$ is heavier than anticipated for seawater sulfate (as in the Rhuddanian-Aeronian) and the data show two transient decreases in $\delta^{34}S_{CAS}$ of ~8‰. The abruptness of these trends in CAS are unlikely to reflect global seawater sulfate, and instead may be a result of the shallow depositional environment as discussed in section 2.7.2.

2.8 Comparison to other C and S excursions

While the carbon isotope trends observed here are consistent with previous records, the sulfur isotope proxies in the Viki core show different patterns to coeval data from outcrop on Gotland (Rose et al., 2019). Gotland $\delta^{34}S_{CAS}$ and $\delta^{34}S_{pyr}$ show positive excursions during the IBE of ~ 7‰ and 30‰ respectively. These excursions in are absent ($\delta^{34}S_{CAS}$) or muted and shortened in duration ($\delta^{34}S_{pyr}$) in the coeval interval from the Viki core. This distinction between the two datasets is important as it highlights that S-isotope systematics can vary significantly within an individual depositional basin. While not unexpected for pyrite (which inherently is locally controlled), it is a surprising and important result for CAS. This result exemplifies the need to better understand the controls and mechanisms of incorporation of sulfate into carbonate before it can be most effectively utilized as a proxy to constrain the ancient sulfur cycle.

The stratigraphic record across the IBE presented here is strikingly similar to trends in End-Ordovician carbonate strata from on Anticosti Island (Jones and Fike 2013), where coeval positive isotope excursions in $\delta^{13}C_{carb}$, $\delta^{13}C_{org}$ and $\delta^{34}S_{pyr}$ are recorded without an accompanying excursion in $\delta^{34}S_{CAS}$. Numerous records of the End-Ordovician, and throughout much of the Phanerozoic, show paired $\delta^{13}C_{org}$ and $\delta^{34}S_{pyr}$ excursions that were interpreted to reflect a coupled increase in organic carbon and pyrite burial (Yan et al., 2009; Hints et al., 2014). The addition of paired sulfate data indicated that the linkages between the carbon and sulfur cycles were more complex, with the S response likely resulting from local depositional changes during the Hirnantian glaciation (Jones and Fike, 2013; Rose et al., 2019), akin to those observed in Pleistocene glacial-interglacial transitions (Pasquier et al. 2017). Similar depositional controls are likely the source of the analogous trends during the IBE observed in the Viki core. Combined, these results demonstrate that a greater understanding is needed of the spatial variation and facies-dependence of these isotope proxies that are often used to reconstruct global biogeochemical cycling.

2.9 Conclusions

Paired $\delta^{13}C_{carb}$-$\delta^{13}C_{org}$ and $\delta^{34}S_{CAS}$-$\delta^{34}S_{pyr}$ data spanning the early Silurian from the Viki drill core, Estonia provide unique insights into local C and S cycling, as well as the impact of depositional conditions on these isotope proxies. Paired $\delta^{34}S_{CAS}$-$\delta^{34}S_{pyr}$ do not co-vary and changes in sulfur isotopes cannot be explained by established interpretations of perturbations to the global S-cycle. Both $\delta^{34}S_{CAS}$ and $\delta^{34}S_{pyr}$ values are elevated and more variable in shallow-water marine facies.

The $\delta^{34}S_{CAS}$ and $\delta^{34}S_{pyr}$ isotope fluctuations in this succession can be explained by local processes involving facies changes and open vs. closed system isotope behavior. Comparing the Wenlock chemostratigraphy to a time-equivalent section on Gotland indicates that these localities recorded distinct signals in $\delta^{34}S_{CAS}$ and $\delta^{34}S_{pyr}$. This relationship is independent from global perturbations to the sulfur cycle, such that depositional controls on $\delta^{34}S$ values may overprint or mask basinal or global S-cycle signals. The sedimentary lithofacies recorded in the Viki drill core and on Gotland indicate basin-wide sea level regression when $\delta^{34}S_{CAS}$-$\delta^{34}S_{pyr}$ are heavy and variable and corresponds to global eustatic sea level fall in the early Silurian. Global sea level fall may differentially affect basins; thus, these depositional factors must be assessed for any given section in which these proxies will be applied to reconstruct details of the ancient sulfur cycle.

2.10 Acknowledgements

Acknowledgment is made to the donors of the American Chemical Society Petroleum Research Fund (#57548-ND2) for partial support of this research and from the Estonian Research Council (#PUT611) to O.H. We thank the Geological Survey of Estonia, the Department of Geology at Tallinn University of Technology, and the Department of Geology at Tartu University. T. Avila and S. Rodriguez helped with sample preparation and S. Moore conducted stable isotope and ICP-OES measurements at Washington University. We thank Ted Present for a helpful review that improved this manuscript.

2.11 Supplementary Data

Table S2.1 – isotope data for the Viki drill core

Sample ID	Age	Stratigraphy	Depth (m)	$\delta^{13}C_{carb}$	$\delta^{13}C_{org}$	$\delta^{18}O_{carb}$	$\delta^{34}S_{CAS}$	$\delta^{34}S_{pyr}$	ε_{pyr}
DF15-86	Sheinwoodian	Jaagarahu Fm.	49.9	-2.19	-30.36	-4.62	30.69	-30.11	60.80
DF15-85	Sheinwoodian	Jaagarahu Fm.	51.12	-1.60	-30.04	-4.63	29.49	-28.66	58.15
DF15-84	Sheinwoodian	Jaagarahu Fm.	52.48	-1.86	-30.95	-4.61	31.06	-19.96	51.02
DF15-82	Sheinwoodian	Jaagarahu Fm.	54.7	-1.68	-29.43	-5.00	32.10	-26.60	58.70
DF15-77	Sheinwoodian	Jaagarahu Fm.	61.77	-0.43	-29.76	-4.25	33.49	-9.31	42.81
DF15-76	Sheinwoodian	Jaagarahu Fm.	63	-0.24	-29.89	-3.73	33.18	9.21	23.97
DF15-75	Sheinwoodian	Jaagarahu Fm.	64.03	0.03	-28.16	-4.14	33.35	-11.36	44.71
DF15-74	Sheinwoodian	Jaagarahu Fm.	64.9	-0.18	-30.33	-3.30	34.24	17.13	17.12
DF15-72	Sheinwoodian	Jaagarahu Fm.	67.02	0.36	-31.19	-2.25	28.44	-7.67	36.11
DF15-70	Sheinwoodian	Jaagarahu Fm.	69.15	1.92	-27.68	-3.34	31.74	-17.96	49.70
DF15-67	Sheinwoodian	Jaagarahu Fm.	73.5	4.48	-26.4	-3.22	36.19	2.95	33.24
DF15-65	Sheinwoodian	Jaagarahu Fm.	77.25	4.96	-24.91	-3.45	34.00	-19.46	53.46
DF15-64	Sheinwoodian	Jaagarahu Fm.	78.4	4.91	-24.82	-3.39	30.75	-3.01	33.77
DF15-63	Sheinwoodian	Jaagarahu Fm.	79.79	5.05	-24.85	-3.43	31.50	0.68	30.83
DF15-62	Sheinwoodian	Jaagarahu Fm.	80.82	4.96	-25.35	-3.44	28.06	-0.22	28.28
DF15-61	Sheinwoodian	Jaagarahu Fm.	81.82	4.86	-24.69	-3.50	30.36	-7.54	37.90
DF15-60	Sheinwoodian	Jaagarahu Fm.	82.82	5.08	-24.68	-2.17	29.23	-13.40	42.63
DF15-59	Sheinwoodian	Jaagarahu Fm.	83.7	5.06	-25.4	-3.20	-	-17.77	-
DF15-58	Sheinwoodian	Jaagarahu Fm.	84.7	4.94	-25.41	-4.87	28.53	-19.11	47.64
DF15-57	Sheinwoodian	Jaagarahu Fm.	85.9	5.14	-25.74	-4.11	-	-15.92	-
DF15-56	Sheinwoodian	Jaani Fm.	87.6	1.49	-29.27	-5.48	32.22	-13.60	45.82
DF15-54	Sheinwoodian	Jaani Fm.	89.64	4.30	-26.89	-5.01	-	-21.06	-
DF15-53	Sheinwoodian	Jaani Fm.	91	5.20	-25.84	-2.68	33.26	-19.37	52.64
DF15-52	Sheinwoodian	Jaani Fm.	92.15	4.80	-28.09	-4.59	36.18	-19.74	55.91
DF15-47	Sheinwoodian	Jaani Fm.	96.82	5.28	-26.18	-3.54	34.89	-28.70	63.59

DF15-46	Sheinwoodian	Jaani Fm.	97.73	4.99	-25.62	-3.96	35.79	-24.15	59.94
DF15-44	Sheinwoodian	Jaani Fm.	99.36	3.53	-25.38	-5.09	34.54	-21.99	56.53
DF15-45	Sheinwoodian	Jaani Fm.	99.4	4.47	-25.6	-4.32	32.80	-	-
DF15-43	Sheinwoodian	Jaani Fm.	100.8	4.23	-26.12	-3.60	30.24	-24.27	54.51
DF15-42	Sheinwoodian	Jaani Fm.	101.7	4.09	-27.9	-3.86	33.60	-22.46	56.06
DF15-41	Sheinwoodian	Jaani Fm.	102.4	3.91	-26.73	-3.98	32.83	-	-
DF15-40	Sheinwoodian	Jaani Fm.	103.6	4.13	-27.02	-3.67	33.11	-19.79	52.90
DF15-39	Sheinwoodian	Jaani Fm.	104.73	3.91	-26.39	-4.02	29.88	-14.64	44.52
DF15-38	Sheinwoodian	Jaani Fm.	105.6	4.00	-25.77	-3.87	34.48	-12.12	46.60
DF15-37	Sheinwoodian	Jaani Fm.	106.4	3.97	-25.81	-3.56	31.91	-18.49	50.40
DF15-36	Sheinwoodian	Jaani Fm.	107.4	4.18	-27.22	-3.97	30.61	-15.16	45.77
DF15-35	Sheinwoodian	Jaani Fm.	108.95	3.97	-26.78	-3.98	34.27	-13.69	47.96
DF15-34	Sheinwoodian	Jaani Fm.	110.08	3.57	-27.93	-3.69	33.96	-	-
DF15-33	Sheinwoodian	Jaani Fm.	111.72	2.79	-28.14	-4.39	33.12	-10.78	43.90
DF15-32	Sheinwoodian	Jaani Fm.	112.65	3.23	-26.46	-4.00	-	1.78	-
DF15-31	Sheinwoodian	Jaani Fm.	112.94	2.36	-28.14	-3.62	30.35	-11.71	42.06
DF15-30	Telychian	Jaani Fm.	114.43	1.85	-28.06	-4.18	29.15	-13.65	42.80
DF15-29	Telychian	Jaani Fm.	115.45	1.76	-28.16	-3.95	29.57	-11.72	41.29
DF15-28	Telychian	Jaani Fm.	116.23	1.76	-27.02	-4.08	29.11	-	-
DF15-27	Telychian	Jaani Fm.	116.81	1.66	-27.26	-4.04	26.05	-13.21	39.26
DF15-26	Telychian	Jaani Fm.	117.81	1.63	-28.3	-4.15	-	-14.21	-
DF15-25	Telychian	Jaani Fm.	118.78	1.71	-28.06	-4.24	29.51	-9.29	38.80
DF15-24	Telychian	Jaani Fm.	120.14	1.57	-28.18	-4.39	28.43	-16.10	44.54
DF15-23	Telychian	Jaani Fm.	121.04	1.40	-27.71	-4.27	30.60	-14.92	45.52
DF15-22	Telychian	Velise Fm.	122.07	1.28	-27.48	-4.85	27.43	-	-
DF15-21	Telychian	Velise Fm.	124.06	1.28	-28.3	-4.41	27.85	-16.34	44.19
DF15-20	Telychian	Velise Fm.	125.35	1.27	-28.11	-4.12	14.73	-16.34	31.07
DF15-19	Telychian	Velise Fm.	126.59	1.20	-27.35	-4.58	26.16	-15.56	41.72
DF15-18	Telychian	Velise Fm.	127.6	1.12	-27.65	-4.79	26.57	-15.59	42.16
DF15-17	Telychian	Velise Fm.	129.09	1.21	-28.14	-4.56	26.53	-12.02	38.55
DF15-16	Telychian	Velise Fm.	130	1.12	-27.76	-4.93	23.95	-14.81	38.76

DF15-15	Telychian	Velise Fm.	131.2	1.17	-27.79	-4.85	24.94	-19.28	44.22
DF15-14	Telychian	Velise Fm.	132.24	1.25	-26.83	-4.91	26.93	-19.71	46.64
DF15-13	Telychian	Velise Fm.	133.08	1.18	-27.84	-4.90	24.15	-18.41	42.55
DF15-12	Telychian	Velise Fm.	134.3	1.14	-27.55	-5.04	24.69	-	-
DF15-11	Telychian	Velise Fm.	135.48	1.49	-28.55	-3.31	-	-	-
DF15-10	Telychian	Velise Fm.	137.25	1.08	-27.97	-4.99	24.09	-27.87	51.96
DF15-9	Telychian	Velise Fm.	138.25	1.08	-28.48	-4.97	30.12	-10.45	40.57
DF15-8	Telychian	Velise Fm.	139.32	1.07	-27.71	-4.80	28.64	-9.45	38.09
DF15-7	Telychian	Velise Fm.	141.27	1.27	-28.11	-4.99	24.44	-15.06	39.50
DF15-6	Telychian	Velise Fm.	142.46	1.31	-27.79	-4.48	26.28	-	-
DF15-5	Telychian	Velise Fm.	143.8	1.48	-27.13	-4.15	-	-15.57	-
DF15-4	Telychian	Velise Fm.	145.26	1.63	-27.15	-4.25	23.96	-	-
DF15-3	Telychian	Velise Fm.	146.65	1.75	-27.28	-4.65	27.07	-	-
DF15-2	Telychian	Velise Fm.	148.82	1.86	-27.5	-5.01	27.77	-14.92	42.69
DF15-1	Telychian	Velise Fm.	151.17	1.78	-26.71	-4.42	29.44	-11.43	40.87
DF15-228	Telychian	Velise Fm.	151.68	1.73	-26.09	-4.43	29.83	-25.44	55.27
DF15-227	Telychian	Velise Fm.	153.6	1.43	-26.46	-4.80	-	-18.81	-
DF15-226	Telychian	Velise Fm.	155.65	2.15	-	-5.18	31.12	-	-
DF15-224	Telychian	Velise Fm.	160.25	2.29	-26.78	-5.20	30.21	-22.31	52.52
DF15-222	Telychian	Velise Fm.	164.07	1.71	-27.64	-5.30	13.95	-22.23	36.18
DF15-221	Telychian	Velise Fm.	166.2	1.48	-27.88	-5.26	-	-18.14	-
DF15-220	Telychian	Velise Fm.	168.35	1.58	-26.63	-5.59	26.13	-21.41	47.54
DF15-218	Telychian	Velise Fm.	172.27	2.13	-27.06	-4.82	-	-21.52	-
DF15-217	Telychian	Velise Fm.	173.93	2.10	-26.93	-4.27	-	-23.02	-
DF15-216	Telychian	Velise Fm.	175.85	1.26	-27.85	-5.36	-	-20.15	-
DF15-214	Telychian	Velise Fm.	180.2	2.50	-26.75	-5.05	31.39	-20.64	52.03
DF15-212	Telychian	Velise Fm.	183.4	1.58	-26.37	-4.62	-	-2.71	-
DF15-211	Telychian	Rumba Fm.	185	1.55	-28.8	-5.07	20.58	4.14	16.44
DF15-209	Telychian	Rumba Fm.	188.7	0.34	-30.35	-4.99	23.18	9.01	14.17
DF15-208	Telychian	Rumba Fm.	190.57	0.30	-31.15	-5.97	8.20	18.41	-10.21
DF15-207	Aeronian?	Nurmekund Fm.	190.88	0.84	-28.33	-5.01	33.80	15.37	18.43

DF15-204	Rhuddanian?	Nurmekund Fm.	194.77	2.30	-29.42	-5.08	32.20	-16.86	49.06
DF15-203	Rhuddanian?	Nurmekund Fm.	196.65	1.62	-29.05	-5.08	35.55	11.52	24.03
DF15-202	Rhuddanian?	Nurmekund Fm.	198.84	1.29	-29.36	-5.26	32.40	11.52	20.88
DF15-201	Rhuddanian	Nurmekund Fm.	200.7	1.52	-26.89	-5.38	-	10.99	-
DF15-200	Rhuddanian	Nurmekund Fm.	202.55	1.87	-29.67	-5.67	35.67	9.77	25.90
DF15-199	Rhuddanian	Nurmekund Fm.	204.65	2.05	-29.22	-5.36	34.07	-1.65	35.72
DF15-198	Rhuddanian	Nurmekund Fm.	206.9	2.08	-29.11	-5.53	33.25	-1.64	34.89
DF15-197	Rhuddanian	Nurmekund Fm.	208.4	2.52	-29.49	-5.30	-	0.37	-
DF15-196	Rhuddanian	Nurmekund Fm.	210.68	4.85	-26.15	-4.37	34.99	-20.44	55.43
DF15-195	Rhuddanian	Nurmekund Fm.	212.6	2.34	-29.28	-5.48	-	-6.27	-
DF15-194	Rhuddanian	Nurmekund Fm.	214.65	2.28	-29.3	-5.33	34.77	-35.41	70.18
DF15-193	Rhuddanian	Nurmekund Fm.	216.6	1.77	-29.27	-5.90	37.04	-29.67	66.71
DF15-192	Rhuddanian	Nurmekund Fm.	218.75	1.71	-29.04	-5.62	-	14.89	-
DF15-191	Rhuddanian	Nurmekund Fm.	220.65	0.82	-29.3	-4.61	34.48	-	-
DF15-190	Rhuddanian	Tamsalu Fm.	222.75	0.13	-30.19	-4.75	31.83	-	-
DF15-189	Rhuddanian	Varbola Fm.	224.6	0.30	-30.1	-4.75	28.72	14.51	14.21
DF15-188	Rhuddanian	Varbola Fm.	226.6	0.02	-29.94	-4.99	24.79	-	-
DF15-187	Rhuddanian	Varbola Fm.	228.5	-0.78	-30.4	-4.94	-	-	-
DF15-186	Rhuddanian	Varbola Fm.	230.72	-0.52	-30.28	-4.84	27.00	-	-
DF15-185	Rhuddanian	Varbola Fm.	232.46	-0.90	-31.27	-4.96	27.41	-15.96	43.37
DF15-184	Rhuddanian	Varbola Fm.	234.2	-1.16	-30.64	-5.09	30.38	-7.02	37.40
DF15-183	Rhuddanian	Varbola Fm.	237.47	-1.31	-30.41	-5.07	28.91	-	-
DF15-181	Hirnantian?	Varbola Fm.	239.95	0.23	-29.27	-4.46	30.27	-18.38	48.65
DF15-180	Hirnantian?	Varbola Fm.	240.6	0.72	-30.47	-4.39	32.76	-27.08	59.84
DF15-179	Hirnantian?	Varbola Fm.	241.33	0.76	-29.82	-4.92	-	-28.02	28.02

Table S2.2 – lithologic data for the Viki drill core

Sample ID	Age	Stratigraphy	Depth (m)	% Carb	% TOC	CAS	% pyr
DF15-86	Sheinwoodian	Jaagarahu Fm.	49.9	70.70	0.26	368.18	0.01
DF15-85	Sheinwoodian	Jaagarahu Fm.	51.12	16.90	0.23	2505.11	1.40
DF15-84	Sheinwoodian	Jaagarahu Fm.	52.48	92.10	0.1	297.28	0.04
DF15-82	Sheinwoodian	Jaagarahu Fm.	54.7	74.80	0.07	395.62	0.00
DF15-77	Sheinwoodian	Jaagarahu Fm.	61.77	70.40	0.16	866.80	0.31
DF15-76	Sheinwoodian	Jaagarahu Fm.	63	71.30	0.13	905.78	0.00
DF15-75	Sheinwoodian	Jaagarahu Fm.	64.03	94.80	0.09	564.13	0.02
DF15-74	Sheinwoodian	Jaagarahu Fm.	64.9	71.50	0.16	1109.72	0.31
DF15-72	Sheinwoodian	Jaagarahu Fm.	67.02	64.40	0.05	138.61	0.06
DF15-70	Sheinwoodian	Jaagarahu Fm.	69.15	64.50	0.06	435.66	0.02
DF15-67	Sheinwoodian	Jaagarahu Fm.	73.5	77.36	0.06	182.26	0.00
DF15-65	Sheinwoodian	Jaagarahu Fm.	77.25	73.50	0.18	212.83	0.00
DF15-64	Sheinwoodian	Jaagarahu Fm.	78.4	75.20	0.07	296.75	0.12
DF15-63	Sheinwoodian	Jaagarahu Fm.	79.79	69.00	0.27	41.72	0.98
DF15-62	Sheinwoodian	Jaagarahu Fm.	80.82	73.30	0.17	127.94	0.09
DF15-61	Sheinwoodian	Jaagarahu Fm.	81.82	99.60	0.07	214.79	0.78
DF15-60	Sheinwoodian	Jaagarahu Fm.	82.82	97.20	0.23	97.35	0.01
DF15-59	Sheinwoodian	Jaagarahu Fm.	83.7	99.20	0.03	0.00	0.00
DF15-58	Sheinwoodian	Jaagarahu Fm.	84.7	69.30	0.28	477.40	0.37
DF15-57	Sheinwoodian	Jaagarahu Fm.	85.9	64.40	0.04	0.00	0.14
DF15-56	Sheinwoodian	Jaani Fm.	87.6	83.80	0.05	654.15	0.00
DF15-54	Sheinwoodian	Jaani Fm.	89.64	72.40	-	0.00	0.24
DF15-53	Sheinwoodian	Jaani Fm.	91	50.11	0.19	1079.21	0.39
DF15-52	Sheinwoodian	Jaani Fm.	92.15	72.90	0.05	395.50	0.48
DF15-47	Sheinwoodian	Jaani Fm.	96.82	67.00	0.04	910.74	0.28
DF15-46	Sheinwoodian	Jaani Fm.	97.73	25.60	0.11	1777.88	0.24
DF15-44	Sheinwoodian	Jaani Fm.	99.36	98.75	0.03	164.99	0.00
DF15-45	Sheinwoodian	Jaani Fm.	99.4	72.00	0.07	384.53	0.00

DF15-43	Sheinwoodian	Jaani Fm.	100.8	53.20	0.06	934.88	0.41
DF15-42	Sheinwoodian	Jaani Fm.	101.7	61.10	0.05	540.89	0.00
DF15-41	Sheinwoodian	Jaani Fm.	102.4	51.90	0.09	535.32	0.00
DF15-40	Sheinwoodian	Jaani Fm.	103.6	55.60	0.18	513.07	0.05
DF15-39	Sheinwoodian	Jaani Fm.	104.73	49.70	0.11	446.09	0.11
DF15-38	Sheinwoodian	Jaani Fm.	105.6	78.90	0.07	406.62	0.47
DF15-37	Sheinwoodian	Jaani Fm.	106.4	44.80	0.04	592.75	0.38
DF15-36	Sheinwoodian	Jaani Fm.	107.4	43.30	0.17	626.78	0.06
DF15-35	Sheinwoodian	Jaani Fm.	108.95	75.40	0.12	288.69	0.27
DF15-34	Sheinwoodian	Jaani Fm.	110.08	26.10	0.09	935.82	1.72
DF15-33	Sheinwoodian	Jaani Fm.	111.72	49.00	0.1	1814.56	0.71
DF15-32	Sheinwoodian	Jaani Fm.	112.65	49.00	0.09	0.00	0.00
DF15-31	Sheinwoodian	Jaani Fm.	112.94	35.60	0.06	490.35	0.00
DF15-30	Telychian	Jaani Fm.	114.43	57.20	0.12	370.78	0.22
DF15-29	Telychian	Jaani Fm.	115.45	60.90	0.1	535.65	0.02
DF15-28	Telychian	Jaani Fm.	116.23	57.60	0.07	370.19	1.66
DF15-27	Telychian	Jaani Fm.	116.81	45.60	0.09	375.32	0.15
DF15-26	Telychian	Jaani Fm.	117.81	17.80	0.09	0.00	0.57
DF15-25	Telychian	Jaani Fm.	118.78	22.30	0.11	900.37	0.00
DF15-24	Telychian	Jaani Fm.	120.14	24.90	0.1	679.33	0.27
DF15-23	Telychian	Jaani Fm.	121.04	27.00	0.06	747.60	0.22
DF15-22	Telychian	Velise Fm.	122.07	63.10	0.12	215.38	0.24
DF15-21	Telychian	Velise Fm.	124.06	17.36	0.1	1043.20	0.25
DF15-20	Telychian	Velise Fm.	125.35	12.70	0.18	1106.67	0.03
DF15-19	Telychian	Velise Fm.	126.59	42.70	0.06	576.17	0.16
DF15-18	Telychian	Velise Fm.	127.6	26.40	0.1	755.01	0.00
DF15-17	Telychian	Velise Fm.	129.09	20.90	0.08	733.03	0.10
DF15-16	Telychian	Velise Fm.	130	21.60	0.08	647.52	0.21
DF15-15	Telychian	Velise Fm.	131.2	26.70	0.06	166.48	0.68
DF15-14	Telychian	Velise Fm.	132.24	44.80	0.12	368.24	0.02
DF15-13	Telychian	Velise Fm.	133.08	20.96	0.09	781.82	0.04

DF15-12	Telychian	Velise Fm.	134.3	22.10	0.08	461.77	0.64
DF15-11	Telychian	Velise Fm.	135.48	0.00	0.1	-	1.59
DF15-10	Telychian	Velise Fm.	137.25	13.20	0.11	1312.12	3.21
DF15-9	Telychian	Velise Fm.	138.25	25.50	0.07	398.55	0.46
DF15-8	Telychian	Velise Fm.	139.32	38.80	0.11	325.41	0.75
DF15-7	Telychian	Velise Fm.	141.27	26.40	0.13	604.55	0.06
DF15-6	Telychian	Velise Fm.	142.46	10.20	0.1	1170.97	0.08
DF15-5	Telychian	Velise Fm.	143.8	0.00	0.12	-	0.08
DF15-4	Telychian	Velise Fm.	145.26	24.10	0.07	342.34	0.72
DF15-3	Telychian	Velise Fm.	146.65	8.77	0.06	600.42	0.00
DF15-2	Telychian	Velise Fm.	148.82	21.00	0.09	476.89	0.00
DF15-1	Telychian	Velise Fm.	151.17	5.50	0.08	2946.34	0.03
DF15-228	Telychian	Velise Fm.	151.68	28.00	0.16	499.72	0.04
DF15-227	Telychian	Velise Fm.	153.6	12.75	0.17	0.00	0.04
DF15-226	Telychian	Velise Fm.	155.65	46.40	-	165.04	0.27
DF15-224	Telychian	Velise Fm.	160.25	10.80	0.21	971.47	0.00
DF15-222	Telychian	Velise Fm.	164.07	6.50	0.07	996.00	0.02
DF15-221	Telychian	Velise Fm.	166.2	0.00	0.15	0.00	0.03
DF15-220	Telychian	Velise Fm.	168.35	50.80	0.15	209.65	1.09
DF15-218	Telychian	Velise Fm.	172.27	0.00	0.07	0.00	0.70
DF15-217	Telychian	Velise Fm.	173.93	6.00	0.16	0.00	0.04
DF15-216	Telychian	Velise Fm.	175.85	0.00	0.2	0.00	0.43
DF15-214	Telychian	Velise Fm.	180.2	35.77	0.1	592.92	0.03
DF15-212	Telychian	Velise Fm.	183.4	7.90	0.25	0.00	0.00
DF15-211	Telychian	Rumba Fm.	185	74.60	0.19	152.11	0.01
DF15-209	Telychian	Rumba Fm.	188.7	86.30	0.16	315.99	0.57
DF15-208	Telychian	Rumba Fm.	190.57	92.40	0.01	148.87	0.03
DF15-207	Aeronian?	Nurmekund Fm.	190.88	86.60	0.36	73.12	0.00
DF15-204	Rhuddanian?	Nurmekund Fm.	194.77	96.60	0.29	47.03	0.00
DF15-203	Rhuddanian?	Nurmekund Fm.	196.65	83.00	0.18	217.10	0.00
DF15-202	Rhuddanian?	Nurmekund Fm.	198.84	68.30	0.28	64.25	0.43

DF15-201	Rhuddanian	Nurmekund Fm.	200.7	70.20	0.36	0.00	0.24
DF15-200	Rhuddanian	Nurmekund Fm.	202.55	94.10	0.12	211.80	0.00
DF15-199	Rhuddanian	Nurmekund Fm.	204.65	91.90	0.45	10.87	0.12
DF15-198	Rhuddanian	Nurmekund Fm.	206.9	96.30	0.41	9.67	0.12
DF15-197	Rhuddanian	Nurmekund Fm.	208.4	64.70	0.35	121.05	0.04
DF15-196	Rhuddanian	Nurmekund Fm.	210.68	96.80	0.01	588.06	0.44
DF15-195	Rhuddanian	Nurmekund Fm.	212.6	71.40	0.01	0.00	0.14
DF15-194	Rhuddanian	Nurmekund Fm.	214.65	72.30	0.59	228.18	0.07
DF15-193	Rhuddanian	Nurmekund Fm.	216.6	68.80	0.43	38.60	0.55
DF15-192	Rhuddanian	Nurmekund Fm.	218.75	93.00	0.51	0.00	0.10
DF15-191	Rhuddanian	Nurmekund Fm.	220.65	62.50	0.41	446.49	0.01
DF15-190	Rhuddanian	Tamsalu Fm.	222.75	79.30	0.19	76.71	0.03
DF15-189	Rhuddanian	Varbola Fm.	224.6	76.40	0.24	50.35	0.01
DF15-188	Rhuddanian	Varbola Fm.	226.6	83.90	0.78	182.83	0.18
DF15-187	Rhuddanian	Varbola Fm.	228.5	55.80	0.39	0.00	0.87
DF15-186	Rhuddanian	Varbola Fm.	230.72	60.90	0.04	102.66	0.01
DF15-185	Rhuddanian	Varbola Fm.	232.46	44.80	0.47	140.73	0.81
DF15-184	Rhuddanian	Varbola Fm.	234.2	57.60	0.57	147.64	0.22
DF15-183	Rhuddanian	Varbola Fm.	237.47	79.30	0.38	138.27	0.17
DF15-181	Hirnantian?	Varbola Fm.	239.95	78.60	0.1	125.58	0.00
DF15-180	Hirnantian?	Varbola Fm.	240.6	54.30	0.9	278.67	0.00
DF15-179	Hirnantian?	Varbola Fm.	241.33	61.60	0.33	0.00	0.22

Table S2.3 – ICP-OES trace element data for the Viki drill core

Sample ID	Age	Stratigraphy	Depth (m)	Mg (ppm)	Ca (ppm)	Sr (ppm)	Fe (ppm)	Mn (ppm)
DF15-86	Sheinwoodian	Jaagarahu Fm.	49.9	26634.60	330494.56	297.13	125.83	108.74
DF15-85	Sheinwoodian	Jaagarahu Fm.	51.12	16649.64	327567.55	303.09	70.19	114.02
DF15-84	Sheinwoodian	Jaagarahu Fm.	52.48	27744.19	340251.20	310.72	120.90	112.32
DF15-82	Sheinwoodian	Jaagarahu Fm.	54.7	8005.34	293685.60	256.31	72.79	77.27
DF15-77	Sheinwoodian	Jaagarahu Fm.	61.77	53839.82	293137.90	183.09	250.67	146.37
DF15-76	Sheinwoodian	Jaagarahu Fm.	63	44929.80	186327.08	104.59	192.50	106.85
DF15-75	Sheinwoodian	Jaagarahu Fm.	64.03	21826.60	179381.88	124.40	114.27	76.83
DF15-74	Sheinwoodian	Jaagarahu Fm.	64.9	67956.07	161916.63	93.65	424.13	158.89
DF15-72	Sheinwoodian	Jaagarahu Fm.	67.02	43086.20	86691.63	25.44	197.91	89.21
DF15-70	Sheinwoodian	Jaagarahu Fm.	69.15	40787.76	80962.09	26.31	146.44	77.70
DF15-67	Sheinwoodian	Jaagarahu Fm.	73.5	60488.39	123135.22	39.19	275.52	119.26
DF15-65	Sheinwoodian	Jaagarahu Fm.	77.25	50336.31	100499.13	31.64	234.63	96.77
DF15-64	Sheinwoodian	Jaagarahu Fm.	78.4	36692.68	70302.91	21.11	217.13	76.02
DF15-63	Sheinwoodian	Jaagarahu Fm.	79.79	58932.65	117631.74	34.25	278.87	121.51
DF15-62	Sheinwoodian	Jaagarahu Fm.	80.82	70890.96	142518.05	39.74	371.64	149.78
DF15-61	Sheinwoodian	Jaagarahu Fm.	81.82	34182.95	65863.57	21.60	223.29	75.38
DF15-60	Sheinwoodian	Jaagarahu Fm.	82.82	33301.04	64005.89	20.46	169.97	71.33
DF15-59	Sheinwoodian	Jaagarahu Fm.	83.7	17396.48	32038.41	10.09	156.18	47.41
DF15-58	Sheinwoodian	Jaagarahu Fm.	84.7	31839.08	61724.67	16.36	464.26	96.48
DF15-57	Sheinwoodian	Jaagarahu Fm.	85.9	42322.82	82632.49	21.52	515.45	124.38
DF15-56	Sheinwoodian	Jaani Fm.	87.6	7907.18	181233.64	256.26	854.89	136.30
DF15-54	Sheinwoodian	Jaani Fm.	89.64	2181.32	16435.64	7.37	57.24	15.17
DF15-53	Sheinwoodian	Jaani Fm.	91	3590.43	8079.43	6.00	23.63	11.93
DF15-52	Sheinwoodian	Jaani Fm.	92.15	4181.93	25857.24	9.96	125.30	26.98
DF15-47	Sheinwoodian	Jaani Fm.	96.82	5627.05	28746.67	29.59	159.62	41.53
DF15-46	Sheinwoodian	Jaani Fm.	97.73	5526.36	63336.63	88.07	192.50	62.73
DF15-44	Sheinwoodian	Jaani Fm.	99.36	1872.23	40640.31	77.92	61.82	38.24
DF15-45	Sheinwoodian	Jaani Fm.	99.4	3952.54	55589.82	76.77	143.62	54.70

DF15-43	Sheinwoodian	Jaani Fm.	100.8	2172.50	30195.89	86.16	57.95	34.20
DF15-42	Sheinwoodian	Jaani Fm.	101.7	1134.39	27801.88	97.88	42.31	28.18
DF15-41	Sheinwoodian	Jaani Fm.	102.4	1266.99	26475.99	72.49	43.97	32.76
DF15-40	Sheinwoodian	Jaani Fm.	103.6	1826.64	50783.48	169.19	74.40	53.49
DF15-39	Sheinwoodian	Jaani Fm.	104.73	4991.61	83069.68	239.56	263.63	100.37
DF15-38	Sheinwoodian	Jaani Fm.	105.6	3564.26	69923.92	186.56	221.92	95.47
DF15-37	Sheinwoodian	Jaani Fm.	106.4	1642.10	27402.15	76.22	102.53	39.41
DF15-36	Sheinwoodian	Jaani Fm.	107.4	2303.68	43608.26	153.00	157.14	67.68
DF15-35	Sheinwoodian	Jaani Fm.	108.95	2572.16	62548.88	191.85	184.39	90.16
DF15-34	Sheinwoodian	Jaani Fm.	110.08	1117.45	25400.94	102.05	84.07	43.32
DF15-33	Sheinwoodian	Jaani Fm.	111.72	3008.68	54630.95	138.08	381.13	100.94
DF15-32	Sheinwoodian	Jaani Fm.	112.65	-	-	-	-	-
DF15-31	Sheinwoodian	Jaani Fm.	112.94	1460.53	22365.57	75.02	259.82	50.37
DF15-30	Telychian	Jaani Fm.	114.43	1397.19	30696.42	77.49	352.94	71.98
DF15-29	Telychian	Jaani Fm.	115.45	2298.67	41366.55	107.02	569.43	100.19
DF15-28	Telychian	Jaani Fm.	116.23	1938.64	41089.91	109.47	512.98	97.92
DF15-27	Telychian	Jaani Fm.	116.81	3236.59	36319.20	101.21	774.28	122.20
DF15-26	Telychian	Jaani Fm.	117.81	1127.06	26394.43	85.45	286.78	73.11
DF15-25	Telychian	Jaani Fm.	118.78	2920.48	35511.92	92.85	637.02	117.44
DF15-24	Telychian	Jaani Fm.	120.14	1139.23	23989.79	62.52	324.89	67.34
DF15-23	Telychian	Jaani Fm.	121.04	2425.95	38788.67	92.24	613.61	132.18
DF15-22	Telychian	Velise Fm.	122.07	867.47	37693.65	80.36	410.79	112.75
DF15-21	Telychian	Velise Fm.	124.06	1073.07	22815.53	60.88	281.95	73.72
DF15-20	Telychian	Velise Fm.	125.35	907.88	19253.40	55.55	183.65	60.17
DF15-19	Telychian	Velise Fm.	126.59	1538.61	26024.41	74.78	325.42	91.97
DF15-18	Telychian	Velise Fm.	127.6	1107.48	31166.85	77.85	367.38	105.27
DF15-17	Telychian	Velise Fm.	129.09	1518.41	26649.00	71.07	391.57	110.46
DF15-16	Telychian	Velise Fm.	130	701.75	32741.41	79.08	288.60	108.06
DF15-15	Telychian	Velise Fm.	131.2	982.61	36717.21	81.23	352.22	125.44
DF15-14	Telychian	Velise Fm.	132.24	863.14	44622.34	107.04	413.91	129.34
DF15-13	Telychian	Velise Fm.	133.08	647.13	24535.90	67.67	217.87	80.12

DF15-12	Telychian	Velise Fm.	134.3	839.41	34054.57	80.19	417.59	88.36
DF15-11	Telychian	Velise Fm.	135.48	1237.78	3182.26	21.17	91.97	29.77
DF15-10	Telychian	Velise Fm.	137.25	840.55	19821.94	59.67	335.28	66.02
DF15-9	Telychian	Velise Fm.	138.25	1011.86	46360.82	103.18	611.81	116.68
DF15-8	Telychian	Velise Fm.	139.32	881.20	36416.07	74.53	525.24	110.06
DF15-7	Telychian	Velise Fm.	141.27	868.12	34514.18	78.00	545.80	88.22
DF15-6	Telychian	Velise Fm.	142.46	1062.10	15542.19	55.66	305.99	56.79
DF15-5	Telychian	Velise Fm.	143.8	1306.35	7003.90	42.08	154.74	45.47
DF15-4	Telychian	Velise Fm.	145.26	869.67	11546.21	43.97	320.90	49.66
DF15-3	Telychian	Velise Fm.	146.65	718.11	21746.60	60.99	301.34	65.74
DF15-2	Telychian	Velise Fm.	148.82	942.33	46476.48	88.39	513.65	205.27
DF15-1	Telychian	Velise Fm.	151.17	1097.24	15045.04	54.16	309.52	75.10
DF15-228	Telychian	Velise Fm.	151.68	5545.19	40012.57	73.84	523.81	132.45
DF15-227	Telychian	Velise Fm.	153.6	5242.64	21664.63	59.93	365.49	107.07
DF15-226	Telychian	Velise Fm.	155.65	2051.68	75032.02	76.85	547.50	196.14
DF15-224	Telychian	Velise Fm.	160.25	2652.07	71577.72	95.31	777.93	205.86
DF15-222	Telychian	Velise Fm.	164.07	2888.67	42181.55	93.00	440.69	104.57
DF15-221	Telychian	Velise Fm.	166.2	4954.13	43136.63	99.00	395.04	116.55
DF15-220	Telychian	Velise Fm.	168.35	1527.83	127757.47	111.82	1187.69	406.84
DF15-218	Telychian	Velise Fm.	172.27	4921.16	19780.62	50.81	324.34	105.57
DF15-217	Telychian	Velise Fm.	173.93	4065.86	8625.50	24.52	190.64	71.00
DF15-216	Telychian	Velise Fm.	175.85	2728.86	16374.91	53.20	211.72	77.49
DF15-214	Telychian	Velise Fm.	180.2	7887.47	118369.06	99.92	1098.83	996.38
DF15-212	Telychian	Velise Fm.	183.4	5329.35	22390.17	40.45	321.00	175.71
DF15-211	Telychian	Rumba Fm.	185	2351.77	173244.24	134.42	526.08	637.80
DF15-209	Telychian	Rumba Fm.	188.7	1767.30	152947.59	134.30	142.94	230.01
DF15-208	Telychian	Rumba Fm.	190.57	1138.91	61300.22	117.19	93.21	107.10
DF15-207	Aeronian?	Nurmekund Fm.	190.88	2870.91	201365.29	147.05	195.18	161.99
DF15-204	Rhuddanian?	Nurmekund Fm.	194.77	5109.15	388596.06	860.39	223.42	83.75
DF15-203	Rhuddanian?	Nurmekund Fm.	196.65	5204.76	88144.59	109.70	337.74	65.07
DF15-202	Rhuddanian?	Nurmekund Fm.	198.84	2722.10	315785.57	247.66	172.25	112.94

DF15-201	Rhuddanian	Nurmekund Fm.	200.7	2221.62	153478.21	134.04	131.05	55.08
DF15-200	Rhuddanian	Nurmekund Fm.	202.55	6791.69	321478.88	486.08	415.20	108.33
DF15-199	Rhuddanian	Nurmekund Fm.	204.65	4219.86	157798.88	232.03	200.99	50.54
DF15-198	Rhuddanian	Nurmekund Fm.	206.9	3409.52	180791.31	305.39	159.10	49.39
DF15-197	Rhuddanian	Nurmekund Fm.	208.4	8663.23	202861.47	362.56	440.90	80.47
DF15-196	Rhuddanian	Nurmekund Fm.	210.68	22208.39	123607.52	54.73	239.46	91.80
DF15-195	Rhuddanian	Nurmekund Fm.	212.6	2508.38	114955.67	231.65	118.14	30.52
DF15-194	Rhuddanian	Nurmekund Fm.	214.65	1570.01	106328.50	270.68	78.74	22.41
DF15-193	Rhuddanian	Nurmekund Fm.	216.6	6605.72	367327.40	348.44	459.51	110.28
DF15-192	Rhuddanian	Nurmekund Fm.	218.75	2485.05	116137.20	168.04	162.01	31.95
DF15-191	Rhuddanian	Nurmekund Fm.	220.65	6606.13	114658.02	156.30	363.57	62.01
DF15-190	Rhuddanian	Tamsalu Fm.	222.75	2792.94	200032.24	166.83	162.03	88.76
DF15-189	Rhuddanian	Varbola Fm.	224.6	2064.49	107399.58	106.57	77.16	42.79
DF15-188	Rhuddanian	Varbola Fm.	226.6	1322.15	108033.75	96.43	95.87	50.33
DF15-187	Rhuddanian	Varbola Fm.	228.5	2772.54	220300.12	183.36	172.26	85.82
DF15-186	Rhuddanian	Varbola Fm.	230.72	3351.19	172007.06	175.50	99.45	63.86
DF15-185	Rhuddanian	Varbola Fm.	232.46	3005.37	109844.31	102.81	164.44	50.80
DF15-184	Rhuddanian	Varbola Fm.	234.2	2264.57	143648.30	122.91	131.67	58.91
DF15-183	Rhuddanian	Varbola Fm.	237.47	4394.63	319812.35	244.48	253.90	126.08
DF15-181	Hirnantian?	Varbola Fm.	239.95	5458.19	-	293.52	167.62	106.76
DF15-180	Hirnantian?	Varbola Fm.	240.6	5896.13	299766.02	396.22	131.72	97.21
DF15-179	Hirnantian?	Varbola Fm.	241.33	4027.94	362660.35	344.95	196.51	104.05

3. $\delta^{34}S_{CAS}$, $\delta^{34}S_{pyr}$ and $\delta^{18}O_{CAS}$ from Silurian carbonates provide insights on the impact of early marine diagenesis, recrystallization and site-specific depositional conditions on CAS

Jocelyn A. Richardson[1*], Aivo Lepland[2,3], Olle Hints[3], Anthony A. Prave[4], William P. Gilhooly[5], Alexander S. Bradley[1] and David A. Fike[1*]

[1]Department of Earth and Planetary Sciences, Washington University, St. Louis, MO 63130 USA
[2]Geological Survey of Norway, 7491 Trondheim, Norway
[3]Department of Geology, Tallinn University of Technology, Ehitajate 5, 19086 Tallinn, Estonia
[4]School of Earth and Environmental Sciences, University of St Andrews, Fife KY16 9AL, UK
[5] Department of Earth Sciences, Indiana University-Purdue University Indianapolis, Indianapolis, IN, USA

3.1 Abstract

New detailed bulk isotope data ($\delta^{13}C_{carb}$, $\delta^{13}C_{org}$, $\delta^{18}O_{carb}$, $\delta^{34}S_{CAS}$, $\delta^{34}S_{pyr}$ and $\delta^{18}O_{CAS}$) from the Paatsalu drill core, Estonia, in the Baltoscandian basin provide insights into the impact of basin-scale and platform-specific depositional processes on carbon, sulfur and oxygen isotopes during the early Silurian. Carbon isotopes record a large, globally correlative 5‰ positive isotope excursion coincident with the Ireviken bioevent. The expression of both $\delta^{13}C_{carb}$ and $\delta^{13}C_{org}$ is variable by, on average, 0.5 to 1‰ within the Baltoscandian basin between the Paatsalu drill core, previously published data from the Viki drill core (Estonia) and Gotland, Sweden. This variability could be a result of the depth at which the precipitating carbonate is sampling DIC across the basin, resulting in a site-specific depositional signal on top of a global trend. Paired $\delta^{34}S_{CAS}$-$\delta^{34}S_{pyr}$ from the Paatsalu drill core exhibit sample-to-sample variability of 7‰ and up to 20‰, respectively. This variability cannot be reconciled with changes to the global sulfur cycle, due to the short time-scale over which it occurs. The sample-to-sample variability is greatest in the shallow-water carbonate facies and is lessened in deeper-water carbonate facies. This trend is comparable to the trends in paired $\delta^{34}S_{CAS}$-$\delta^{34}S_{pyr}$ from the Viki drill core and is most likely a result of more closed-system (shallow facies) vs. more open-system (deeper facies) conditions, where increased and pulsed sedimentation rate in shallow-water environments generates greater variability in both $\delta^{34}S_{CAS}$ and $\delta^{34}S_{pyr}$ due to isotope distillation in pore fluid from progressive microbial sulfate reduction (MSR). Absolute sulfur isotope values, magnitude and direction of variability are different between Paatsalu and Viki. We suggest that this is due to the variable local sea level at each site during shallow- and deep-water carbonate deposition, such that the Paatsalu core reflects overall shallower conditions. Paired $\delta^{34}S_{CAS}$-$\delta^{18}O_{CAS}$ data show parallel variability, providing further evidence for closed system conditions in shallow-water carbonates. There are no co-

varying changes in $\delta^{34}S_{CAS}$, $\delta^{34}S_{pyr}$ and $\delta^{18}O_{CAS}$ between Paatsalu, Viki and Gotland implying that local depositional environment and early marine diagenesis has masked the large-scale sulfur cycle at these sites.

3.2 Introduction

Geochemical data (e.g. elemental abundances and isotopic ratios) from outcrop and/or core samples of marine sedimentary rocks are used to reconstruct the operation and evolution of global biogeochemical cycles over Earth history (Bartley and Kah, 2004; Canfield and Farquhar, 2009; Garrels and Lerman, 1981; Holser, 1997). This is common practice for reconstructing the carbon and sulfur cycles where both oxidized and reduced phases (carbonate and organic carbon; sulfate and sulfide, respectively) are preserved in carbonate successions throughout the rock record. Due to the relatively short residence time of carbon in the ocean-atmosphere system (10^5 years) with respect to the duration of carbon isotope excursions expressed within the rock record, many such excursions are understood to reflect perturbations to the global C-cycle due to changing organic carbon burial and/or the weathering input to the ocean (Kump and Arthur, 1999). A number of studies have found $\delta^{13}C_{carb}$ excursions in association with a facies change, usually marine regression. In such cases, the stratigraphic expression of the $\delta^{13}C_{carb}$ excursions can be variable in magnitude and/or duration between time correlative sections (Jones et al., 2011; Rose et al., 2019; Saltzman et al., 2000b; Samtleben et al., 2000). In contrast, the residence time for sulfate in the modern ocean (~ 13 Myr) is substantially longer and is thought to have been greater than 2 Myr (i.e., substantially longer than that for the marine DIC reservoir) for the entire Phanerozoic, as determined by estimates of the ocean sulfate reservoir (as low as 5 mM in the early Paleozoic and mid-Mesozoic to 28 mM today; Canfield, 2004; Horita et al., 2002; Lowenstein et al., 2003). As such, rapid (< 1 Myr duration) sulfur isotope excursions in the rock record cannot be as readily explained by perturbations to the global sulfur cycle (Richardson et al., 2019).

The sulfur cycle is fundamentally linked to the carbon cycle through microbial sulfate reduction (MSR), which remineralizes organic carbon (Jørgensen, 1982). MSR reduces dissolved sulfate to sulfide, and while some of this sulfide will be re-oxidized to sulfate or intermediate S species (Jørgensen, 1977), the rest will be scavenged by available reactive iron to form iron sulfide minerals (that convert to pyrite on geologic timescales) (Berner, 1984) and/or reacted with organic matter (Sinninghe-Damste and de Leeuw, 1990). MSR imparts a fractionation between sulfate and sulfide that leaves the resultant product sulfide depleted in ^{34}S relative to the sulfate pool by as much as 70‰, depending on sulfate reduction rates and organic carbon availability (Eldridge et al., 2016; Leavitt et al., 2013; Sim et al., 2011). As such, the operation of the sulfur cycle is recorded in marine sedimentary rocks as sulfide in pyrite and organic S compounds (Canfield, 2001b; Raven et al., 2015), and as sulfate in evaporite minerals (Kampschulte and Strauss, 2004), sedimentary barite (Paytan et al., 1998) and carbonate-associated sulfate (CAS; Burdett et al., 1989). Due to the spatial and temporal extent of carbonate rocks, sulfur isotope values (δ^{34}S) of co-occurring pyrite and CAS are measured to infer changes in the burial and/or the weathering flux of pyrite and sulfate, the size of the sulfate reservoir and/or the dominant microbial metabolic community (Canfield, 2001; Garrels and Lerman, 1981). However, recent studies aiming to reconstruct the ancient sulfur cycle have generated highly variable, in both magnitude and direction, sulfur isotope datasets ($\delta^{34}S_{CAS}$ and/or $\delta^{34}S_{pyr}$) from time-correlative sections worldwide (Jones and Fike, 2013; Kah et al., 2016; Thompson and Kah, 2012; Young et al., 2016b). Previous studies have incorrectly interpreted sample-to-sample variability that is characteristic of many $\delta^{34}S_{CAS}$-$\delta^{34}S_{pyr}$ datasets as apparent isotope excursions that reflect a local or global sulfur cycle perturbation (e.g. Kozik et al., 2019; Lyu et al., 2019; Stebbins et al., 2018). However, this variability has been interpreted by others as a result of depositional environment and early marine diagenesis on $\delta^{34}S_{CAS}$ and $\delta^{34}S_{pyr}$ (Liu et al., 2019; Pasquier et al., 2017; Richardson et al., 2019; Rose et al., 2019). Occurring in strata characterized by co-eval $\delta^{13}C$ excursions, this sample-to-sample $\delta^{34}S$ variability and apparent isotope excursions have been attributed to a small, rapidly changing marine sulfate reservoir that is perturbed by increases to organic carbon and pyrite burial (Adams et al., 2010; Gill et al., 2007; Owens et al., 2013; Thompson and Kah, 2012; Wotte et al., 2012b). Such observations of co-eval $\delta^{13}C$ excursions with variable $\delta^{34}S$ are often found during periods of rapid biological turnover (Hammarlund et al., 2012; John et al., 2010; Rose et al., 2019).

Oxygen isotopes of sulfate ($\delta^{18}O_{SO4}$) can act as an additional proxy for the sulfur cycle as, like $\delta^{34}S_{SO4}$, $\delta^{18}O_{SO4}$ reflects the major fluxes in the sulfur cycle. $\delta^{18}O_{SO4}$ changes in response to changing the source of sulfate into the ocean (i.e. sulfide oxidation or weathering of evaporites), burial ratio of pyrite to sulfate and MSR, where ^{18}O is enriched in the sulfate pool during ongoing sulfate reduction (Bottrell and Newton, 2006; Gilhooly et al., 2016). Oxygen isotopes in sulfate may exchange with oxygen isotopes in seawater, however, this relationship is temperature and pH dependent (Chiba and Sakai, 1985). It is not expected that oxygen isotopes between sulfate and seawater will equilibrate faster than 10 Myr at seawater temperatures and pH (Chiba and Sakai, 1985). If diagenetic alteration and overprinting of $\delta^{18}O_{SO4}$ has not occurred, $\delta^{18}O_{SO4}$ variability over short geologic timescales usually reflects changing amounts of microbial sulfur cycling including MSR, sulfur disproportionation, abiotic and biotic sulfide oxidation (Turchyn and Schrag, 2006). Although these reactions in oxidative sulfur cycling affect both $\delta^{34}S_{SO4}$ and $\delta^{18}O_{SO4}$, the magnitudes of the sulfur isotope fractionations during disproportionation and sulfide oxidation are small compared to sulfur fractionation occurring during MSR. In contrast, the oxygen isotope fractionations during these reactions are much greater (Gomes and Johnston, 2017). Thus, paired $\delta^{34}S_{SO4}$-$\delta^{18}O_{SO4}$ and $\delta^{34}S_{SO4}$-$\delta^{34}S_{pyr}$ can be a powerful tool to understand global vs. local signals in ancient carbonate successions (Rennie and Turchyn, 2014).

The Silurian is characterized by rapid environmental, oceanic and atmospheric change. Biological turnover was frequent and often associated with glaciation, sea level change and carbon cycle perturbations (Calner, 2008; Munnecke et al., 2010). Silurian strata are well-studied for their sedimentology, biodiversity, biostratigraphy and carbon isotope stratigraphy, particularly in the East Baltic region (Bickert et al., 1997; Calner, 2005; Hints et al., 2006; Kaljo and Martma, 2006; Kiipli et al., 2006, 2004; Lazauskiene et al., 2003; Lehnert et al., 2010; Loydell et al., 2010; Munnecke et al., 2003; Rose et al., 2019; Samtleben et al., 2000, 1996). In this study, we present $\delta^{13}C_{carb}$, $\delta^{13}C_{org}$, $\delta^{34}S_{CAS}$, $\delta^{34}S_{pyr}$ and $\delta^{18}O_{CAS}$ from the Paatsalu drill core, Estonia, which is temporally correlative with previously published geochemical datasets from the Viki drill core, Saaremaa Island, Estonia (Richardson et al., 2019) and Gotland, Sweden (Rose et al., 2019). We provide evidence for basin-wide sulfur isotope variability through the early Silurian within the Baltoscandian basin that cannot be explained by changes to the global or basinal sulfur cycle. The addition of $\delta^{18}O_{CAS}$ data helps to resolve the origin of the variability in $\delta^{34}S_{CAS}$ within the Paatsalu drill core, and corroborates previous interpretations that local depositional controls dominate the sulfur isotope signatures of the Baltoscandian basin (Richardson et al., 2019; Rose et al., 2019).

3.3 Geological Setting

The Paatsalu drill core site is located on the west coast of mainland Estonia (Figure 3.1) and is housed at the Särguaha field station and drill core repository (more information can be found at http://geokogud.info/drillcore/128). Samples in this study span the mid-Llandovery to the mid-

Wenlock. The section has experienced partial and variable dolomitization and recrystallization. The formation boundaries are constrained via biostratigraphy of chitinozoans, scolecodonts and conodonts (Hints et al., 2006), bentonites (Kallaste and Kiipli, 2006) and immobile trace elements (Kiipli et al., 2008).

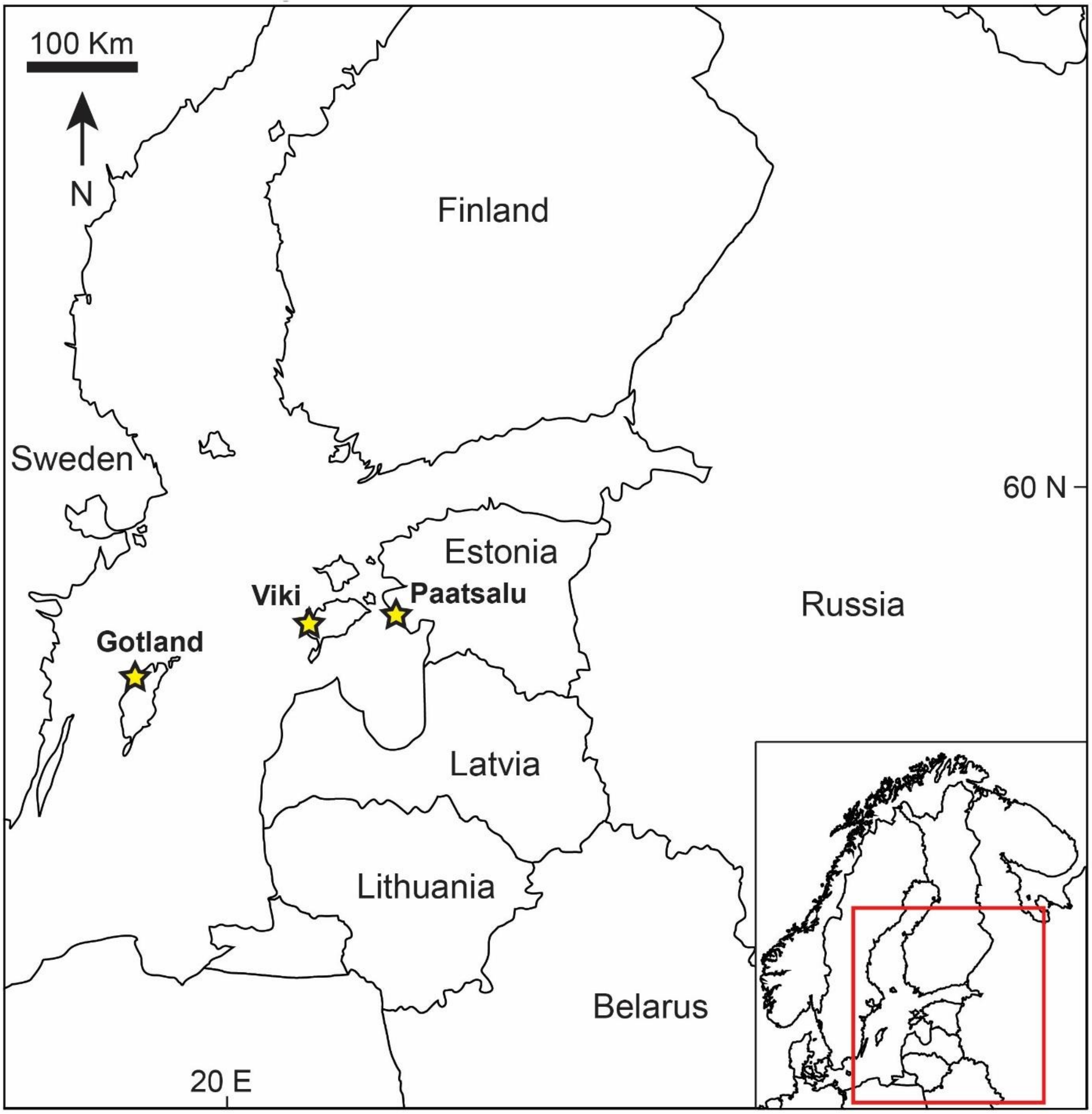

Figure 3.1 – Map of Eastern Europe with a close-up of the Baltic countries outlined in red (inset). Locations of the Paatsalu drill core (this study), the Viki drill core, Estonia (Richardson et al., 2019) and Gotland Island, Sweden (Rose et al., 2019).

The base of the studied section at 111.8 m is within the Nurmekund Fm. (part of the Raikküla regional stage) and likely correlates to the mid to late Rhuddanian global stage. In the Paatsalu drill core, the Nurmekund Fm. is a micritic mudstone with calcareous siliciclastic grainstone interbeds and varying abundances of bioclastic material. This is a vertical stacking of shoreline (grainstone) and lagoonal (micritic limestone) environments. At approximately 104 to 102 m, there is low-angle cross-bedding within the grainstones and a sharp erosive contact that represents the boundary between the Nurmekund and overlying Rumba Fms. The Rumba Fm. (83 to 102 m) is composed of interbedded wackestones and packstones with a bioclast assemblage dominated by echinoderms, brachiopods, and bryozoans indicative of reef and shoal facies, thus a deepening has occurred from the Nurmekund to the Rumba Fms. There is a bentonite bed at 88 m that has been correlated with the K-bentonite in the Rumba Fm. of the Viki drill core at 185.1 m (Kiipli et al., 2006).

The overlying Velise Fm., from 70 to 83 m, is composed of grey-green mudstone and marlstone interbeds with various pyrite morphologies. Burrows (common) and echinoderm fragments (rare) are visibly pyritized, there are abundant macroscopic euhedral pyrites ranging in size up to 12 mm in length across a face, and there are smaller pyrite aggregates. The Velise Fm. strata are the deepest facies within the Paatsalu core, representing a transition from open to deep shelf facies. These strata likely experienced late-stage fluid migration allowing for the growth of large pyrite. At 70.5 m there is an erosive contact where an oolitic packstone overlies the marlstone succession of the Velise Fm., marking the onset of the Jaani Fm. (70-34 m). This bed is approximately 1 m thick and represents a sequence boundary where inner shelf facies were placed on top of mid to outer shelf mudstones. The top of the oolitic packstone at 69.5 m is a flooding surface that places similar mud-marlstones of the underlying Velise Fm. on top of the packstone.

The mud-marlstone section of the Jaani Fm. has undergone partial dolomitization (unlike the Velise Fm.). Pyrite is abundant and macroscopic within the first meter of the Jaani mudstone, but the size and abundance decrease with increasing stratigraphic height in the Jaani Fm. Although bioclasts are rare in the mudstone-marlstone succession, their abundance increases with increasing height co-occurring with an increase in nodular micritic limestone to the top of the Jaani Fm. at 34 m. The Jaani Fm. records a shallowing from distal to proximal and mid shelf facies.

From 34 m to the top of the core, the Jaagarahu Fm. is dominated by shallow-water carbonate facies. Wackestone and packstone interbeds occur between 34 and 23 m, with an increasing abundance of mud drapes towards the mid-Jaagarahu Fm. The bioclast assemblage is similar to the Rumba Fm. This is overlain by repetitions of thinly interbedded dolomitic arenite with dolomitized mudstone and wackestone beds to the top of the core. The Jaagarahu Fm. is a continued shallowing from mid to inner-shelf reef and shoal facies to marginal marine and peritidal paleoshoreline facies.

3.4 Methods

3.4.1 Carbon Isotopes

To prepare samples for carbonate carbon and carbonate oxygen isotope analyses, ~100 μg of sample powder was dissolved in 100% phosphoric acid (H_3PO_4) for at least 4 hours at 70°C. Sample vials were flushed with He and the evolved CO_2 was measured on a Thermo Finnigan Gasbench II coupled to a Delta V Advantage Isotope Ratio Mass Spectrometer at Washington University. Organic carbon isotope analyses are performed on the organic residue left after acidifying 4–5 g of carbonate sample powder with 6M HCl. Acidifications were left for up to 20 minutes and were repeated until there was no visible reaction when HCl was added. Insoluble residues were analysed for organic carbon isotope composition on a Flash 2000 Organic Elemental Analyzer, coupled via a ConFlo IV to a Delta V Plus Isotope Ratio Mass Spectrometer at Washington University. Carbon and oxygen isotopes are expressed in standard delta notation ($\delta^{13}C$, $\delta^{18}O$) in permil (‰) as a deviation from the Vienna-Pee Dee Belemnite (V-PDB) standard. The 1σ error on $\delta^{13}C_{carb}$ $\delta^{18}O_{carb}$ and $\delta^{13}C_{org}$ is 0.15‰ based on standard and replicate samples.

3.4.2 Sulfur and Oxygen Isotopes

To prepare samples for sulfur and oxygen isotopes of CAS, and sulfur isotopes of pyrite, the methods follow Richardson et al., (2019), modified from Wotte et al., (2012a). Briefly, 30–50 g of sample powder was rinsed in a 10% brine (NaCl) solution for 30 minutes. This step aims to remove any free sulfur species that might be sorbed onto the carbonate (e.g. from in situ pyrite oxidation; Richardson et al., in review). After a total of three brine rinses, the supernatant was checked for sulfate by adding 1 ml of saturated $BaCl_2$ solution, and brine rinses were repeated if any precipitate formed in the supernatant. This was followed by 3 deionized H_2O rinses. Samples were acidified with 6M HCl and stirred for up to 3 hours (or until there is no visible reaction) to release CAS. The acidic supernatant containing the dissolved sulfate was filtered and reacted with an excess of $BaCl_2$ to precipitate $BaSO_4$ that was rinsed, weighed, and dried for subsequent use in the isotopic analyses. To extract pyrite as chromium-reducible sulfur (Canfield et al., 1986), insoluble residues from the CAS extraction were reacted with a 6M HCl and 2M chromium (II) chloride solution under constant N_2 gas and are left stirring for 4 hours at 186°C. The evolved gas from the sample reaction was passed through a water trap and bubbled into a test tube containing silver nitrate solution in deionized H_2O in order to precipitate silver sulfide.

Sulfur isotope analyses were performed at Washington University by combining ~350 μg of silver sulfide or barium sulfate with 1–3 mg of vanadium pentoxide and was combusted using a Costech ECS 4010 elemental analyzer coupled to a Thermo Finnigan Delta V Plus mass spectrometer. S-isotopes are expressed in standard delta notation ($\delta^{34}S$) in permil (‰) as a deviation from the Vienna-Canyon Diablo Troilite (V-CDT) standard. The same barium sulfate aliquots were analysed for oxygen isotopes of sulfate at IUPUI, measured by pyrolysis using a Thermo TC/EA coupled to a Thermo Delta V Plus mass spectrometer. The 1σ error on $\delta^{34}S_{CAS}$ is 0.3‰ and for $\delta^{18}O_{CAS}$ and $\delta^{34}S_{pyr}$ is 0.2‰ from standards and replicate samples.

3.5 Results

3.5.1 Carbon Isotopes

The Paatsalu drill core records a large $\delta^{13}C_{carb}$ isotope excursion (Figure 3.2) that corresponds to the Ireviken bioevent and carbon isotope excursion recorded in numerous sections worldwide (Munnecke et al., 2003; Richardson et al., 2019.; Rose et al., 2019). Although the base of the section has few datapoints, $\delta^{13}C_{carb}$ transiently increases from 0‰ at 111.8 m to 1.3‰ at 108.5m before declining to -1.3‰ at 98.2 m. A similar positive isotope excursion is observed in the Nurmekund Fm. in the Viki drill core (Richardson et al., 2019). $\delta^{13}C_{carb}$ values increase throughout the Rumba formation from -1.3‰ at 98.2 m to 0.4‰ at 86.2 m. There is a jump in $\delta^{13}C_{carb}$ to 2‰ at 83.4 m. Throughout the Velise Fm. values are stable around 2‰. Between 70 and 66 m, corresponding to the packstone unit at the base of the Jaani Fm., $\delta^{13}C_{carb}$ increases rapidly to 4‰. Values reach a maximum of 4.8‰ in the middle of the Jaani Fm. at 51 m and decrease to 3.8‰ at

33.8 m. $\delta^{13}C_{carb}$ continues to transiently decline into the Jaagarahu Fm., with a step-wise decrease from 2.6 to -0.2‰ between 16.5 and 9.6 m. Values remain at -0.2‰ to the top of the section.

Trends in $\delta^{13}C_{org}$ generally follow $\delta^{13}C_{carb}$ (Figure 3.2). $\delta^{13}C_{org}$ values vary around -29‰ at the bottom of the section in the Nurmekund Fm. At 98.2 m, there is a decrease in $\delta^{13}C_{org}$ to -31.2‰, coincident with the decrease in $\delta^{13}C_{carb}$. Throughout the Rumba and Velise Fms. $\delta^{13}C_{org}$ steadily increases from -32.1‰ at 96.5 m to -27.15‰ at 70 m. There is a step-wise increase up to -24.7‰ at 68.6 m across the lithologic change at the base of the Jaani Fm. In contrast to $\delta^{13}C_{carb}$ which increases and decreases throughout the Jaani Fm., $\delta^{13}C_{org}$ data has a small drawdown from -24.7‰ to -26.9‰ at 38 m but increases to -25.7‰ at the top of the Jaani Fm. $\delta^{13}C_{org}$ is variable from -26 and -24‰ between 33.8 and 16.5 m before decreasing to -30‰ at the top of the section.

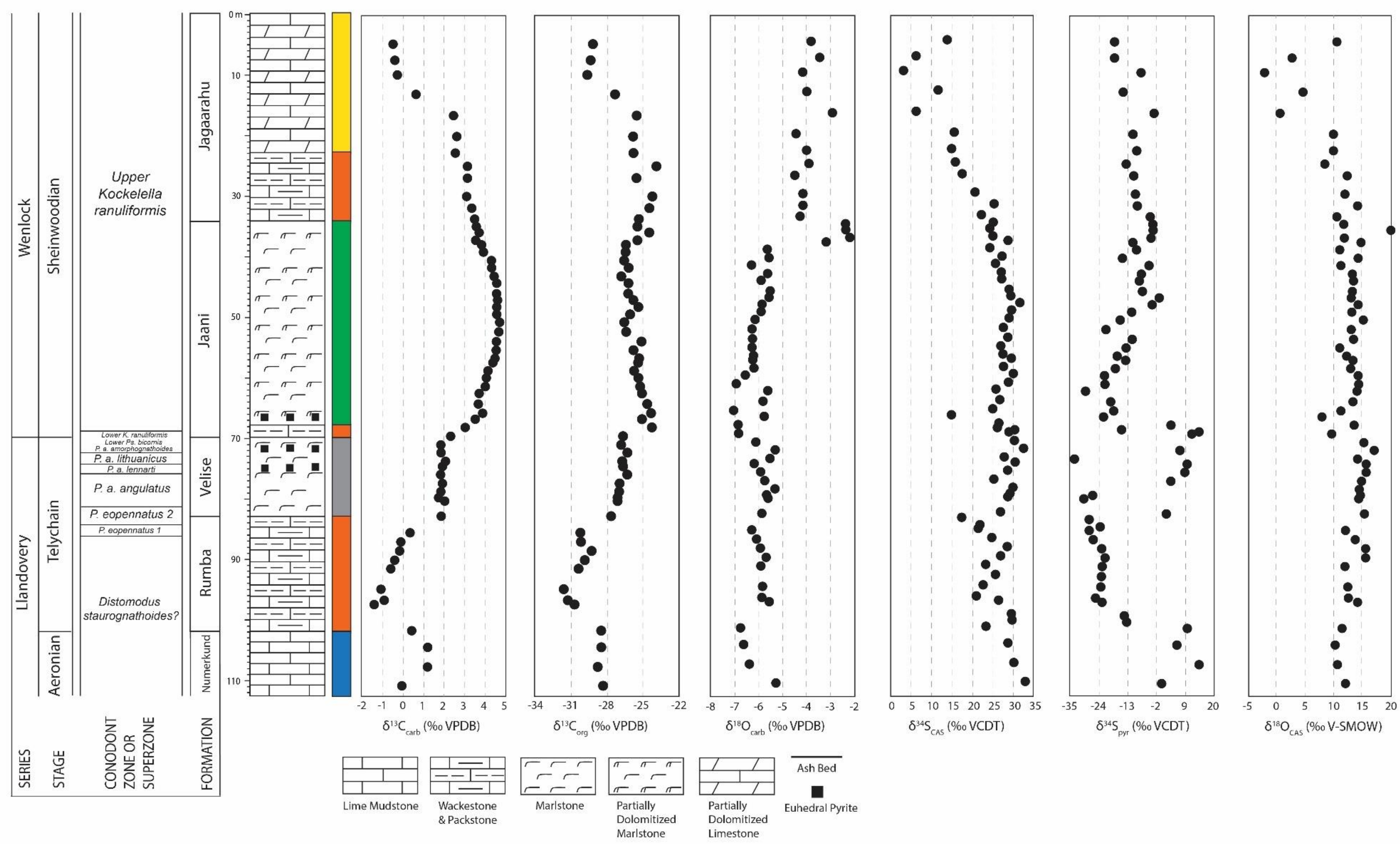

Figure 3.2 – Paatsalu drill core stratigraphy (left) and coeval isotope chemostratigraphy. Included beside the stratigraphy is the color key for the lithofacies used in subsequent figures. From left to right: $\delta^{13}C_{carb}$, $\delta^{13}C_{org}$, $\delta^{18}O_{carb}$, $\delta^{34}S_{CAS}$, $\delta^{34}S_{pyr}$ and $\delta^{18}O_{CAS}$.

3.5.2 Sulfur Isotopes

$\delta^{34}S_{CAS}$ data have a maximum sample-to-sample variability of 7‰ (Figure 3.2). At 111.8 m $\delta^{34}S_{CAS}$ is 33‰ and decreases to 23.4‰ over the next 10 m of core into the basal Rumba Fm. Within the Rumba Fm. $\delta^{34}S_{CAS}$ becomes more variable with an isotopic range of 12.2‰ (29.7‰ at 100.5 m to 17.5‰ at 84.3 m at the top of the Rumba Fm.). Within the overlying Velise Fm, $\delta^{34}S_{CAS}$ increases and becomes less variable (values between 25.4 and 32‰). From 65.6 to 46.2 m, values appear to steady around 27.5‰, with the exception of one outlier at 67.2 m of 15‰. $\delta^{34}S_{CAS}$ decreases into the overlying strata to 15.6‰ at 20 m, while values vary between 3.3 and 14‰ in the final few meters of the section.

Pyrite isotopes at the base of the core are relatively high, ranging from 1 to 15.4‰ in the first 10 m. Above 102.5 m there is a decrease in $\delta^{34}S_{pyr}$ from 10.9 to -21.8‰ over 4 m. Between 98.2 and 80.3, corresponding to a majority of the Rumba Fm., $\delta^{34}S_{pyr}$ varies between -20 and -30‰, with one outlier at 83.4 m of 2.8‰. At 78 m, $\delta^{34}S_{pyr}$ increases to positive values between 4.6 to 15.4‰. At the base of the Jaani Fm., values decrease again to -14.3‰, and continue to decrease to -21.1‰ at 62.9 m. Throughout the Jaani Fm., $\delta^{34}S_{pyr}$ increases to approximately -2‰ at 35 m. At 32 m, $\delta^{34}S_{pyr}$ stabilizes around -9‰. From 16.5 to the top of the section, $\delta^{34}S_{pyr}$ decreases from 16.5 to 4.5‰.

3.5.3 Oxygen Isotopes

Oxygen isotopes can be reported in two ways throughout this section; oxygen isotopes in carbonate (most commonly used as a diagenetic indicator and seawater temperature proxy; Banner and Hanson, 1990; Emiliani, 1966) and oxygen isotopes of sulfate in the barite that is precipitated during from bulk CAS extractions (used to assess changes to the sulfur cycle and oxidative sulfur cycling in sediments; Bottrell and Newton 2006).

$\delta^{18}O_{carb}$ has two major trends in the dataset; in the lower part of the core, between the Nurmekund and the base of the Jaagarahu Fm. (39.3 m) values vary between -5 and -7‰ (Figure 3.2). The lowermost datapoints decrease from -5.2 to -6.7‰ at 102.6 m. In the Rumba and lower Velise Fms. Values remain around -6‰ up to ~71.5 m, where values become increasingly variable between -5 and -7‰. At 59 m the variability decreases and $\delta^{18}O_{carb}$ again converge around -6‰ up to 39.3 m. Above this, there is a step-wise increase where $\delta^{18}O_{carb}$ vary between -4.5 and -2‰ up to the top of the section.

The trends in $\delta^{18}O_{CAS}$ are similar to the trends in $\delta^{34}S_{CAS}$ (Figure 3.2). At the base of the section, $\delta^{18}O_{CAS}$ is 12.4‰ and decreases to 10.6‰ at 105.34 m, following the decreasing trend in $\delta^{34}S_{CAS}$. Up to 71.5 m, at the top of the Velise Fm., $\delta^{18}O_{CAS}$ increases to 15.6‰, and although $\delta^{18}O_{CAS}$ is variable between 105.34 and 71.5 m, it is not as variable as its $\delta^{34}S_{CAS}$ counterpart. At base of the Jaani Fm. (67.2 m), $\delta^{18}O_{CAS}$ decreases to 8.3‰. Values increase to 14.5‰ by 63 m and remain relatively invariant for most of the Jaani Fm. Between 42 and 26.9 m, $\delta^{18}O_{CAS}$ becomes increasingly variable from 11.5 to 15‰ (with one outlier at 36 m of 20.3‰). Above 26.9 m, in the Jaagarahu Fm., $\delta^{18}O_{CAS}$ decreases to the lowest value of the core of -1.2 ‰ at 9.6 m. To the top of the section values return towards 11‰.

3.6 Discussion

3.6.1 Diagenesis

Dolomitization, burial and meteoric diagenesis

In order to ascertain the origin of the excursions and variability in the isotope proxies, it is essential to assess early- to late-stage, post-depositional alteration from fluid migration during burial or meteoric diagenesis, or dolomitization. Due to partial dolomitization and visible recrystallization throughout the core, we have plotted geochemical parameters associated with diagenesis against lithology. Common indicators of diagenesis include $\delta^{13}C_{carb}$ vs. $\delta^{18}O_{carb}$, Mn vs. Sr, and Fe vs. Sr, where $\delta^{13}C_{carb}$, $\delta^{18}O_{carb}$ and Sr are anticipated to decrease during recrystallization (e.g. associated with either meteoric or burial diagenesis) (Banner and Hanson, 1990). Although our data show increases in Mn and Fe with concomitant decreases in Sr, $\delta^{13}C_{carb}$ vs. $\delta^{18}O_{carb}$ does not show a correlation (Figs. 3A, B and C), indicating that the fluid affecting the trace elements was not appreciably depleted in $\delta^{13}C_{carb}$ and $\delta^{18}O_{carb}$ (see section 5.1.2). The Mn, Sr and Fe abundances here are lower than typically for many diagenetic carbonates recrystallized during meteoric alteration (Banner and Hanson, 1990; Brand and Veizer, 1980; Hood et al., 2018; Husson et al., 2015). Samples with the highest abundance of Sr, and lowest Mn and Fe abundance, come from the mudstone and wacke/packstone facies. Marlstone, dolomitized marlstone and limestone facies have lower Sr with increasing Mn and Fe abundances (Figure 3.3B and C). This likely reflects the proportion of components that formed and/or recrystallized in an anoxic fluid. Overall, we conclude that the geochemical data have not been substantially reset or overprinted by burial or meteoric diagenesis.

Samples above 20 m in the partially dolomitized limestone of the Jaagarahu Fm. have $\delta^{34}S_{CAS}$ and $\delta^{18}O_{CAS}$ values that are more variable and generally more depleted than the samples below. To assess the potential alteration of these uppermost samples, lithology-specific $\delta^{34}S_{CAS}$ is plotted against Mg/Ca ratio, CAS abundance (ppm) and pyrite abundance (Figs. 4A, B and C). Samples with a Mg/Ca ratio < 0.125 vary in $\delta^{34}S_{CAS}$ between 21 and 33‰. These $\delta^{34}S_{CAS}$ values are typical of ancient carbonates and are similar to the range observed in these strata from the Viki drill core (Richardson et al., 2019). At higher Mg/Ca ratios (above 0.35), $\delta^{34}S_{CAS}$ values span the entire range observed in Paatsalu from 3 to 32‰, where the depleted values from the Jaagarahu Fm. have slightly increased Mg/Ca ratios relative to all other samples (Figure 3.4A). This contrasts observations in the Viki drill core where lower $\delta^{34}S_{CAS}$ values have low Mg/Ca ratios (Richardson et al., 2019). However, there are other alteration processes, such as early diagenetic sulfide oxidation, that can complicate the trends observed from dolomitization. Plots of $\delta^{34}S_{CAS}$ vs. CAS and pyrite abundances can indicate the potential impact of pyrite oxidation, either during diagenesis or the bulk CAS extraction protocol (Figure 3.4B and C) (Marenco et al., 2008a). There is no correlation between either $\delta^{34}S_{CAS}$ vs. CAS and pyrite abundance, however the lightest $\delta^{34}S_{CAS}$ samples from the Jaagarahu Fm. contain the greatest abundance of sulfate. This correlation is not systematic but could reflect variable pyrite/sulfide oxidation and subsequent incorporation as CAS during, for example, dolomitization. Alternatively, the low and variable $\delta^{34}S_{CAS}$ and $\delta^{18}O_{CAS}$ values from the upper Jaagarahu Fm., could reflect a change in the oxidative sulfur cycling in these sediments, where sulfide with a low $\delta^{34}S$ was reoxidized during bioturbation and/or tidal reworking, or by different microbial metabolisms such as sulfide oxidizers or disproportionation.

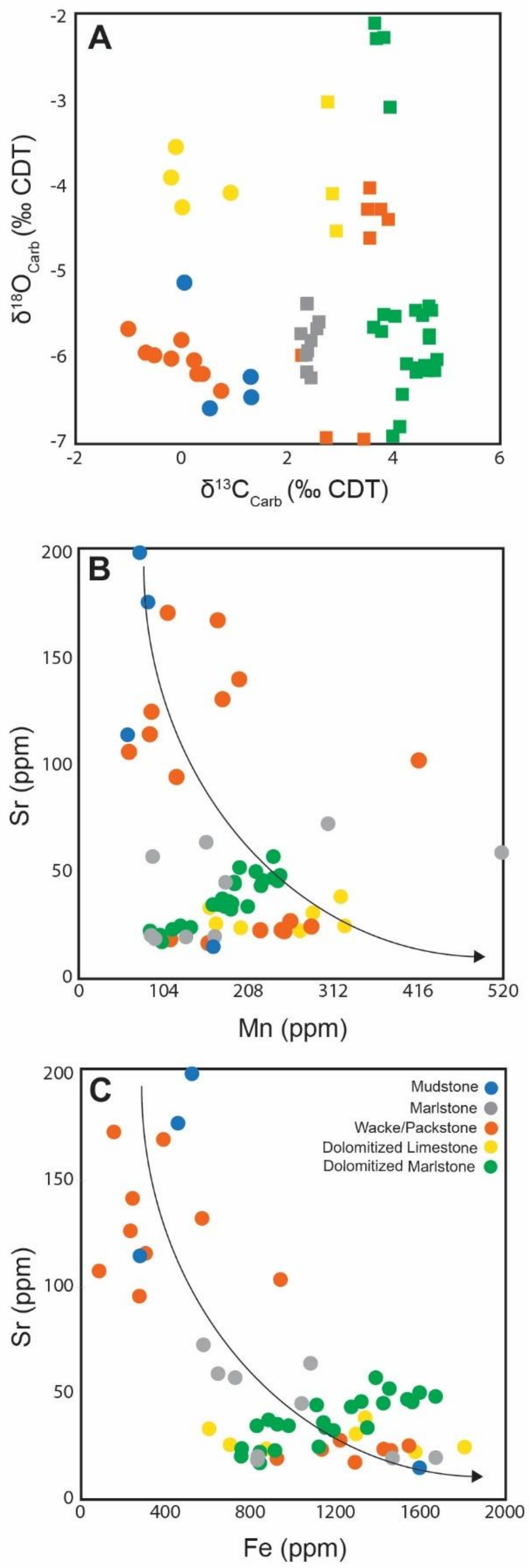

Figure 3.3 – Cross plots of indicators of diagenesis color-coded by lithology. (A) $\delta^{13}C_{carb}$ vs. $\delta^{18}O_{carb}$, square samples are those that span the IBE, (B) Sr vs. Mn abundance, (C) Sr vs. Fe abundance.

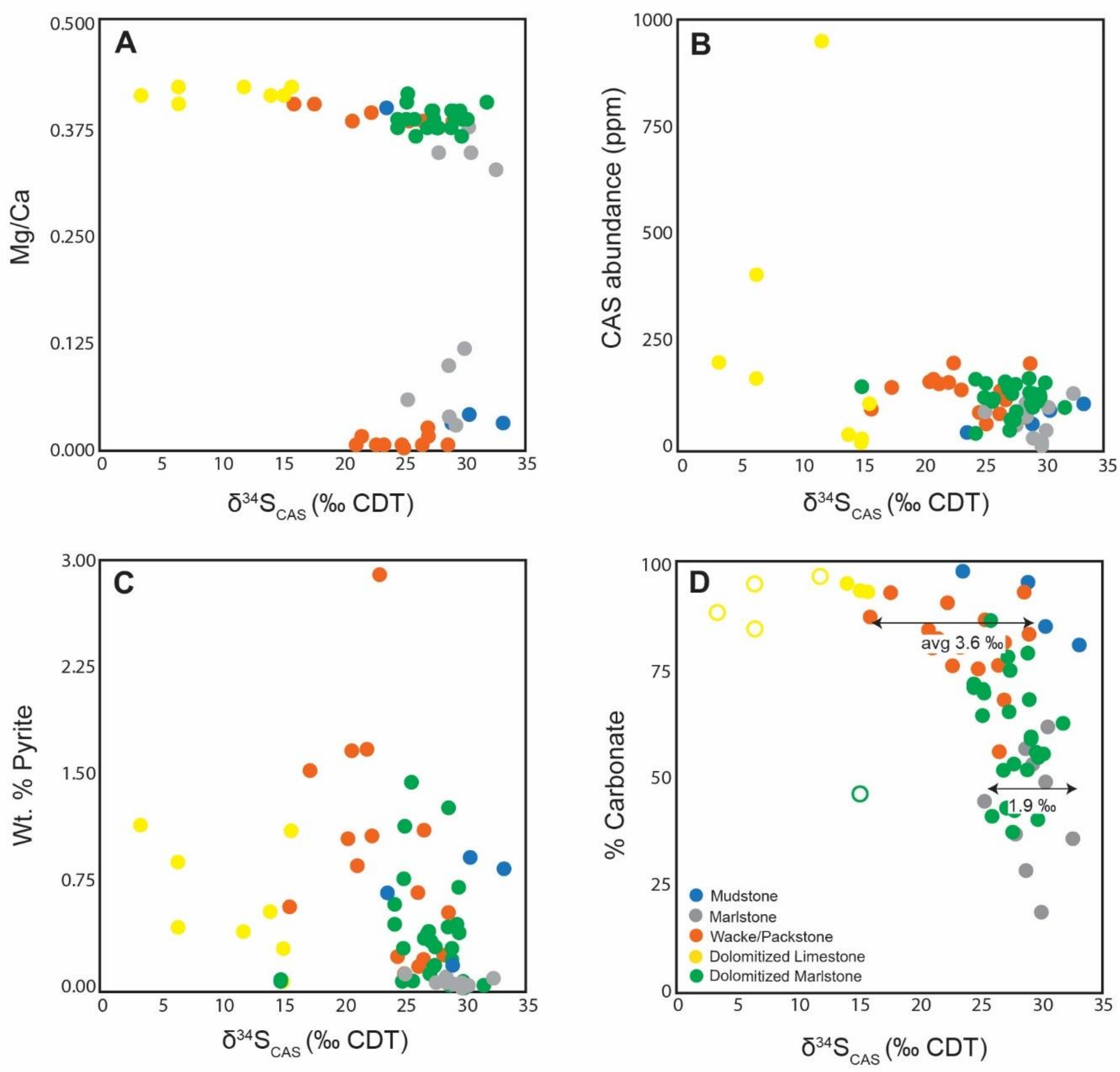

Figure 3.4 – Cross plots of $\delta^{34}S_{CAS}$ vs. (A) Mg/Ca molar ratio, (B) CAS abundance, (C) wt % S in pyrite and (D) carbonate abundance. Open symbols are samples thought to be altered and arrow represent the average sample-to-sample variability in shallow-water (3.6‰) and deep-water (1.9‰) facies. Plots are color-coded by lithology. Plots are color-coded by lithology.

Early marine diagenesis

Early marine diagenesis of carbonate includes the cementation and micritization of primary carbonate components (such as fossils), as well as subsequent dissolution-reprecipitation of cement (Bathurst, 1975). Cementation and recrystallization that occurs in the sediment below the chemocline could capture localized $\delta^{34}S_{CAS}$ and $\delta^{18}O_{CAS}$ values as a result of isotope distillation that occurs during MSR, where MSR drives the $\delta^{34}S$ and $\delta^{18}O$ of pore fluid sulfate higher as the lighter isotope is partitioned into the product sulfide. It has been suggested that this process occurs commonly in environments where increased sedimentation rate and organic carbon loading results in increased closed-system isotope behavior, preventing the exchange of pore fluid sulfate with overlying seawater (Gomes and Hurtgen, 2015; Pasquier et al., 2017; Richardson et al., 2019). In a similar vein, $\delta^{13}C_{carb}$ of early diagenetic cements precipitating from evolved pore fluid may have a signature distinct from seawater. Respiration of organic carbon decreases the $\delta^{13}C_{DIC}$ of pore fluid, generating a cement with a lower $\delta^{13}C_{carb}$ than coeval seawater. $\delta^{18}O_{carb}$ should be unchanging in this situation.

To determine if closed-system isotope behavior has affected the oxygen and sulfur isotopes of CAS here, a series of cross-plots of $\delta^{18}O_{CAS}$ vs. $\delta^{34}S_{CAS}$ together with other diagenetic indicators are shown (Figure 3.5). There is a strong positive correlation between $\delta^{34}S_{CAS}$ and $\delta^{18}O_{CAS}$ data (Figure 3.5A). This correlation is strengthened by the low $\delta^{34}S_{CAS}$-$\delta^{18}O_{CAS}$ samples that are deemed to be altered and are not expected to be a result of pore fluid isotope distillation. As such, these data are not considered when assessing potential enrichment of these isotopes during progressive MSR (Figure 3.5B). Wackestone and packstone facies, as well as partially dolomitic marlstone facies show a stronger $\delta^{34}S_{CAS}$-$\delta^{18}O_{CAS}$ correlation than mudstone and marlstone facies (Fig, 5C; although this could be due to under-sampling and/or limited availability of the later facies). However, $\delta^{34}S_{CAS}$ and $\delta^{18}O_{CAS}$ show greater variability in wackestone and packstone facies compared to the dolomitic marlstone (Figure 3.4D and 5C), potentially attributed to the increased yet pulsed nature of shallow-water sedimentation (Richardson et al., 2019). Differences in the slope of $\delta^{34}S_{CAS}$ vs. $\delta^{18}O_{CAS}$ may indicate changes in the cell-specific sulfate reduction rate (csSRR), where a shallower slope corresponds to faster csSRR (Antler et al., 2013; Gomes and Johnston, 2017). This may indicate that wackestone and packstone facies had higher csSRR than marlstone facies, in agreement with the increased availability of labile organic carbon in shallow-water environments.

Although Mn/Sr ratios are commonly used as indicators for meteoric diagenesis (e.g. Banner and Hanson, 1990), the ratio reflects precipitation or recrystallization in any anoxic fluid (Halverson et al., 2007). In the absence of correlations between other diagenetic indicators ($\delta^{13}C_{carb}$ vs. $\delta^{18}O_{carb}$), Mn/Sr can be an indication of precipitation or recrystallization in anoxic pore fluid during early marine diagenesis. Mn/Sr ratios greater than 2 are thought to be fully recrystallized (Halverson et al., 2007; Turchyn et al., 2009), where Mn/Sr in Paatsalu show a majority of samples have a recrystallized signature (Figure 3.5D). Using a Mn/Sr ratio of 2 as a threshold, $\delta^{34}S_{CAS}$ vs. $\delta^{18}O_{CAS}$ is replotted and a more significant correlation is created in the data with Mn/Sr > 2 (Figure 3.5E), compared to the entire dataset (Figure 3.5B) and to samples with Mn/Sr < 2 (Figure 3.5E). All of the deep-water carbonates have a Mn/Sr ratio > 2. To further substantiate that the $\delta^{18}O_{CAS}$ has not been influenced by meteoric diagenesis, $\delta^{18}O_{CAS}$ vs. $\delta^{18}O_{carb}$ shows no correlation (Figure 3.5F).

Although we do not have component-specific isotope data to assess the $\delta^{13}C_{carb}$ of early diagenetic cements, lithology-specific $\delta^{13}C_{carb}$ vs. $\delta^{18}O_{carb}$ could provide evidence of a closed-system (Figure 3.3A). Here, the dolomitic limestone and packstone facies have the highest abundance, and proportion, of pore-filling diagenetic cements. $\delta^{13}C_{carb}$ vs. $\delta^{18}O_{carb}$ shows that these facies have a wider range in $\delta^{13}C_{carb}$ than $\delta^{18}O_{carb}$ compared to the micrite dominated facies (Figure 3.3A). The wacke/packstone facies show a decreasing trend in $\delta^{13}C_{carb}$ below 1‰, with relatively invariant $\delta^{18}O_{carb}$. These samples are from the interbedded wackestone and packstone units of the

Rumba Fm. coincident with the most variable and most enriched $\delta^{34}S_{CAS}$-$\delta^{18}O_{CAS}$ values from wacke/packstone facies.

We infer that coeval variations in $\delta^{34}S_{CAS}$ and $\delta^{18}O_{CAS}$ in Paatsalu strata are recording progressive enrichment of sulfur and oxygen isotopes in the sediment during MSR in different paleoenvironments. The range in $\delta^{34}S_{CAS}$ and $\delta^{18}O_{CAS}$ is similar between shallow-water (wackestone and packstone) and deep-water (dolomitized marlstone) carbonate facies, indicating that deep-water carbonates can precipitate and/or recrystallize in the anoxic zone of the sediment and capture an enriched S and O isotopic signal (Rennie and Turchyn, 2014). In this framework, the most evolved pore water sulfate plots to the upper-right and the least evolved (and therefore most representative of seawater $\delta^{34}S_{SO4}$ and $\delta^{18}O_{SO4}$) samples are in the bottom-left quadrant in $\delta^{34}S_{CAS}$ vs. $\delta^{18}O_{CAS}$ (Figure 3.5B; excluding samples affected by alteration). We suggest that seawater $\delta^{34}S_{SO4}$ and $\delta^{18}O_{SO4}$ are closer to 25.2 and 12.2‰, respectively, based on clustering of $\delta^{34}S_{CAS}$-$\delta^{18}O_{CAS}$ datapoints in the dolomitic marlstone facies that likely formed in more open connectivity with seawater with respect to the shallow-water facies. This agrees with time-equivalent $\delta^{34}S_{CAS}$ values from brachiopods from Gotland (Present, 2018) and evaporite data (Kampschulte and Strauss, 2004). Based on the low-density of samples that have a $\delta^{34}S_{CAS}$ of ~15‰ and $\delta^{18}O_{CAS}$ of ~10‰, as well as suggested $\delta^{34}S_{SO4}$ from Silurian marine evaporite (Kampschulte and Strauss, 2004), these values are likely too low to represent seawater values and are likely impacted by oxidative sulfur cycling. It is important to highlight that MSR and oxidative, microbial sulfur cycling can both increase and decrease $\delta^{34}S_{SO4}$ and $\delta^{18}O_{SO4}$ relative to coeval seawater (e.g. Goldberg et al., 2005).

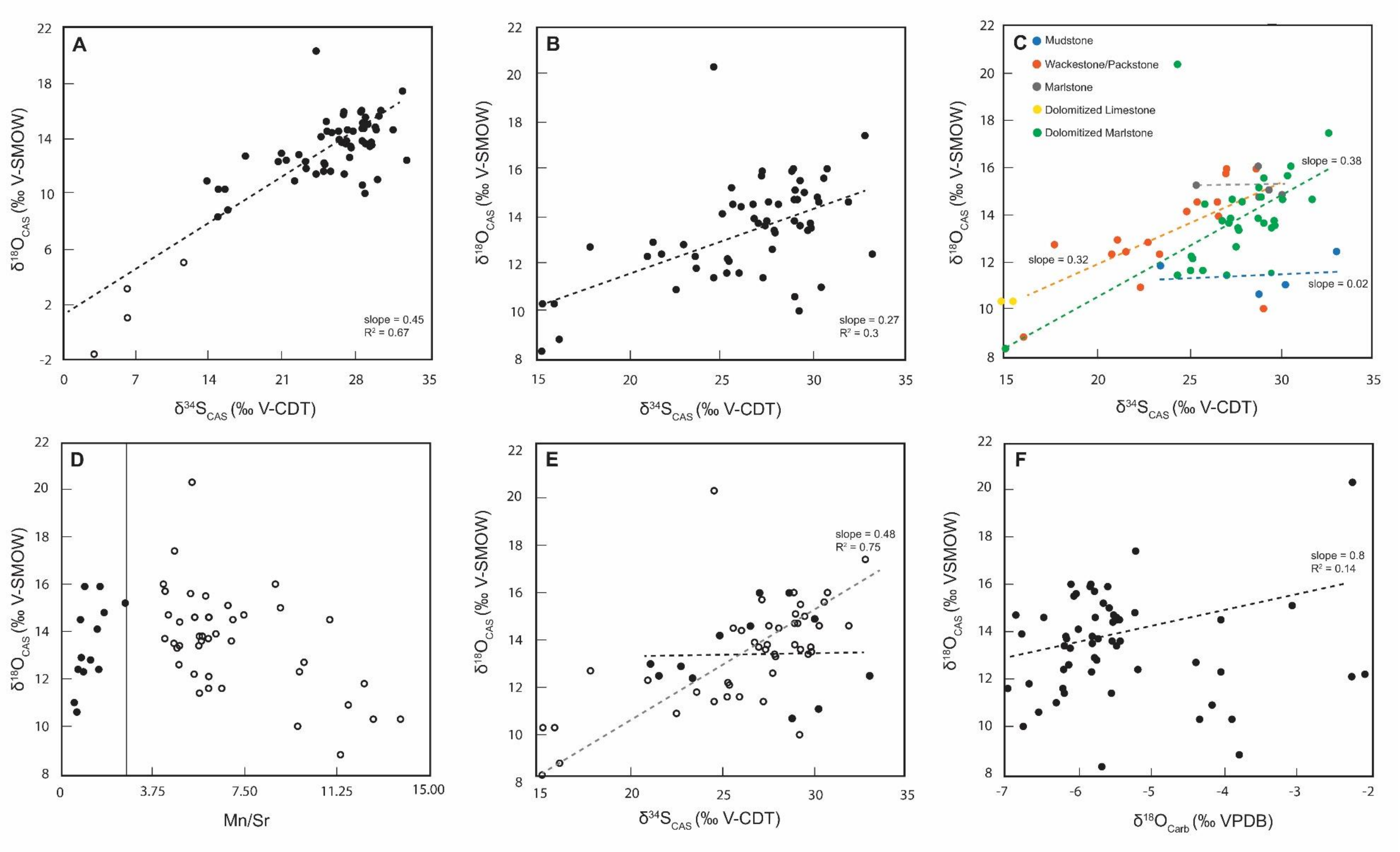

Figure 3.5 – Cross plots of $\delta^{18}O_{CAS}$ vs. (A) $\delta^{34}S_{CAS}$ with altered samples as open circles, (B) $\delta^{34}S_{CAS}$ with grey points in A removed, (C) $\delta^{34}S_{CAS}$ color-coded with lithologic information. The slope for dolomitized limestone is omitted due to the small number of sampls from this unit (n = 2) (D) Mn/Sr, black line is a ratio of 2. Open circles are samples with an Mn/Sr > 2 and solid circles are samples with Mn/Sr < 2. (E) $\delta^{34}S_{CAS}$ plotted as Mn/Sr greater than 2 (open circles, grey dashed line) and Mn/Sr less than 2 (solid circles, black dashed line), and, (F) $\delta^{18}O_{carb}$.

3.6.2 Intra-basin isotope variability

Carbon isotopes

Compared to the Viki drill core the carbon isotope record of Paatsalu is condensed in the lower to mid-Llandovery but is expanded in the upper Llandovery into the early-Wenlock due to differences in sedimentation rate. The trends in paired $\delta^{13}C_{carb}$-$\delta^{13}C_{org}$ are consistent between the two drill cores. The absolute $\delta^{13}C_{carb}$ and $\delta^{13}C_{org}$ values are offset by up to 1‰, with the Viki core mostly recording more positive $\delta^{13}C_{carb}$ but lower $\delta^{13}C_{org}$ (Figure 3.6). The magnitude of the C-isotope excursion during the Ireviken Event is the same between these Estonian drill cores but is 0.5‰ lower than the record on Gotland (Rose et al., 2019). These differences in magnitude could be due to variations in the local $\delta^{13}C_{DIC}$ (dissolved inorganic carbon) gradient generated by the biological pump, exporting ^{13}C-depleted carbon to deeper settings (Holser, 1997). Additionally, sampling gradients across a carbonate platform can generate $\delta^{13}C_{carb}$ variability of up to 5‰ due to the relative proportion of ^{13}C-enriched aragonite sediment from the platform, with ^{13}C-depleted pelagic material (Swart, 2008; Swart and Eberli, 2005), as well as fluid vs. sediment buffered lithification and early marine diagenesis (Higgins et al., 2018). Based on paleo-shoreline estimates (Cocks and Torsvik, 2005) and the stratigraphy, Paatsalu overall records shallower settings than Viki and therefore could record more positive $\delta^{13}C$ than Viki.

Early Silurian carbon isotope records from the Baltoscandian basin most likely represent a global record of the carbon cycle, evidenced by the number of sections worldwide that retain coeval C-isotope excursions coincident with the Ireviken bioevent and commonly a facies change, inferred to be controlled by global eustatic sea level (Azmy et al., 1998; Cramer and Saltzman, 2005; Munnecke et al., 2003; Richardson et al., 2019; Rose et al., 2019). The duration of the Ireviken event in the Paatsalu section (~ 1 to 2 Myr) is sufficiently long for the carbon cycle to respond to a perturbation (Kump and Arthur, 1999). Thus, the $\delta^{13}C$ signal in the Baltoscandian basin could be recording a perturbation to the carbon cycle (e.g., from increased organic carbon burial and/or increased weathering of carbonate rocks). Local depositional effects on $\delta^{13}C$ are superimposed on the global C-isotope signal between the sites, where the effects of depositional environment are not enough to mask or alter the globally correlative signal. It is important to note that the effect of mineralogy and fluid vs. sediment buffered early marine diagenesis across a platform cannot be discounted as a mechanism for the observed carbon isotope excursion in the Baltoscandian basin, and further assessment is required to determine if this is a perturbation to the global carbon cycle (e.g. $\delta^{44}Ca$ and $\delta^{26}Mg$) (Higgins et al., 2018).

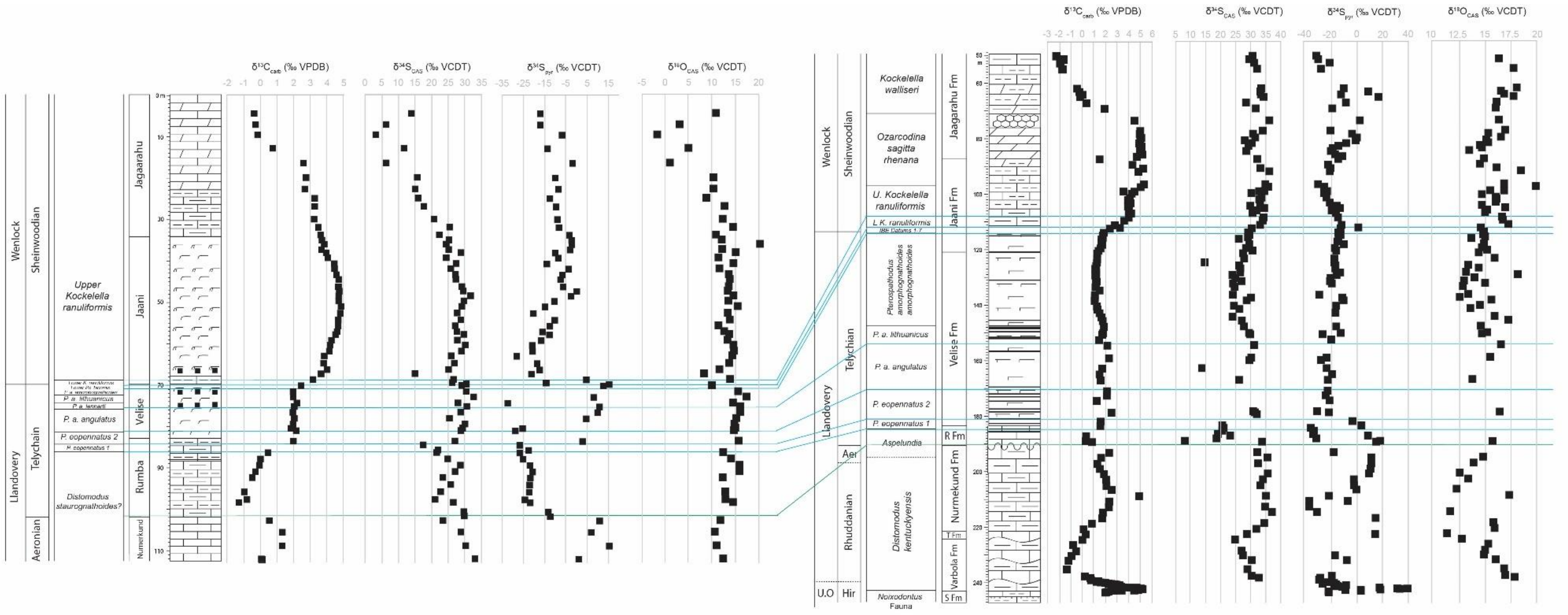

Figure 3.6 – Comparison of $\delta^{13}C_{carb}$, $\delta^{34}S_{CAS}$, $\delta^{34}S_{pyr}$ and $\delta^{18}O_{CAS}$, from Paatsalu (left) and Viki (right). Correlations made based on conodont biozones (blue lines) and the top of the *Conochitina alargada* chitinozoan biozone (green line).

Sulfur isotopes

An important finding of this research is the distinct sulfur isotopic records in the Paatsalu and Viki drill cores (Figure 3.6), and between these and the strata from Gotland (Richardson et al., 2019; Rose et al., 2019), particularly the absence in the Estonian sections of a paired $\delta^{34}S_{CAS}$-$\delta^{34}S_{pyr}$ excursion observed during the Ireviken event on Gotland (Rose et al., 2019). Additionally, the variability in paired $\delta^{34}S_{CAS}$-$\delta^{34}S_{pyr}$ at each site occurs too rapidly to be reconciled by changes to the global sulfur cycle (Richardson et al., 2019), thus an alternate explanation is required.

Overall, the range in $\delta^{34}S_{CAS}$ and $\delta^{34}S_{pyr}$ are consistent between Paatsalu and Viki (25 and 50‰, respectively). However, the average absolute magnitude in $\delta^{34}S_{CAS}$ and $\delta^{34}S_{pyr}$ is 5‰ lower and higher, respectively, in Paatsalu. It is expected that $\delta^{34}S_{pyr}$ should differ between sites since it inherently locally controlled (Aller et al., 2010; Claypool, 2004; Liu et al., 2019; Pasquier et al., 2017). In contrast, temporally-correlative $\delta^{34}S_{CAS}$ records are expected to record similar magnitudes and trends based on the assumption that $\delta^{34}S_{CAS}$ is a proxy for global seawater sulfate. The changes in $\delta^{34}S_{CAS}$ and $\delta^{34}S_{pyr}$ between the cores are not always coeval in timing and/or direction but, roughly similar trends are observed between the two drill cores. $\delta^{34}S_{CAS}$ and $\delta^{34}S_{pyr}$ are more variable in shallow-water carbonate facies, owing to higher sedimentation rate, increased labile organic carbon delivery and increased reactive iron availability. These parameters result in a more closed-system between pore fluid and seawater that generates distillation of isotopes during MSR (Aller et al., 2010; Fike et al., 2015; Richardson et al., 2019). The opposite occurs during high sea level (such as during the Jaani Fm.), resulting in more stable and lower $\delta^{34}S_{CAS}$ and $\delta^{34}S_{pyr}$. The similarities in $\delta^{34}S_{CAS}$ and $\delta^{34}S_{pyr}$ trends between the two cores occur in similar facies at slightly different times (and duration) in different places on the carbonate platform, rather than secular changes in $\delta^{34}S_{SO4}$.

Much like the variable magnitude of the C-isotope expression between Paatsalu, Viki and Gotland, sulfur isotopes will retain variable expressions between sites since they are inherently locally controlled. Although local controls on $\delta^{34}S_{pyr}$ is generally well-established, the effect of depositional environment and early marine diagenesis on $\delta^{34}S_{CAS}$ is less well constrained (Fike et al., 2015; Liu et al., 2019; Pasquier et al., 2017; Present, 2018; Richardson et al., 2019; Rose et al., 2019). The difference in absolute values of $\delta^{34}S_{CAS}$ (by an average of 5‰) between Paatsalu and Viki, as well as less pronounced trends between facies and paired $\delta^{34}S_{CAS}$-$\delta^{34}S_{pyr}$ in Paatsalu, may be due to the differential proximity of the sites to the paleoshoreline, such that, Paatsalu preserves a shallower record overall compared to Viki. For example, during the sea level low-stand in the early to mid-Llandovery, shallow-water carbonate facies (marginal marine to outer shelf) were deposited at both the Paatsalu and Viki sites. However, due to the proximity of the Paatsalu site to the shoreline, the shallow-water facies recorded here are vertical stacks of peritidal-lagoonal and paleoshoreline sequences (Nurmekund and Rumba Fms.). In contrast, the Nurmekund and Rumba Fms. in the Viki drill core reflect a deepening from backreef to proximal shelf facies (Richardson et al., 2019). The lower $\delta^{34}S_{CAS}$ values and the higher sample-to-sample variability in the Nurmekund and Rumba Fms. from Paatsalu compared to Viki may reflect the increased frequency of sediment reworking from wave-action and tidal processes in the peritidal environment. An increase in sediment reworking will disturb the stratification in anoxic sediments, including isotope distillation, and introduce seawater sulfate into pore space, as well as re-oxidizing available sulfide into sulfate, resulting in less distillative enrichment in $\delta^{34}S_{SO4}$ (Aller, 2004; Aller et al., 2010; Fike et al., 2015). The result is a fluid-buffered system where the $\delta^{34}S$ of the precipitating carbonate is moderated by the $\delta^{34}S$ pore fluid that is frequently replenished by seawater (Present, 2018). The average $\delta^{34}S_{CAS}$ of the Nurmekund and Rumba Fms. in Paatsalu is 25.4‰ which closely agrees with both evaporite (Kampschulte and Strauss, 2004) and brachiopod-only data (Present, 2018).

Differences in the shallow-water carbonate facies based on distance to the shoreline will also affect $\delta^{34}S_{pyr}$. The resultant $\delta^{34}S_{pyr}$ from the peritidal-shoreline environment will reflect a pore fluid signature that is less chemically evolved (due to the increase in system openness from frequent reworking and tidal influences) as is evidenced by lower and less variable $\delta^{34}S_{pyr}$ from the Nurmekund and Rumba Fms. in Paatsalu compared to Viki. The differences in absolute $\delta^{34}S_{CAS}$ and $\delta^{34}S_{pyr}$ values and the lack of pronounced coeval $\delta^{34}S_{CAS}$-$\delta^{34}S_{pyr}$ changes in both Viki and in Paatsalu, preclude identification of any clear basinal or global signature of S-cycling at this time. This further supports the notion that $\delta^{34}S_{pyr}$ and to some degree $\delta^{34}S_{CAS}$ are both controlled by local depositional processes, and that these signatures will vary depending on location on a carbonate shelf, relative local sea level at the given location, energy of the depositional system, and sedimentation rate. As such, the impact of depositional environment and early marine diagenesis should be assessed for all $\delta^{34}S_{CAS}$ and $\delta^{34}S_{pyr}$ sections, to determine whether local processes overprint and/or mask global trends.

Oxygen isotopes

Oxygen isotopes of sulfate substantiate our conclusion that sulfur isotope signatures in the Baltoscandian basin preserve a local, pore fluid signature, that can mask any changes to the global sulfur cycle. Absolute $\delta^{18}O_{CAS}$ values between the Paatsalu and Viki drill cores are similar (~ 10 to 20‰; Figure 3.6), however there is greater variability in the Viki drill core. Importantly, lithology-specific $\delta^{34}S_{CAS}$-$\delta^{18}O_{CAS}$ data show similar, positive correlations between the Paatsalu and Viki drill cores, where the shallow-water carbonate facies record the shallowest slopes in

$\delta^{34}S_{CAS}$-$\delta^{18}O_{CAS}$, attributed to faster sulfate reduction (Figure 3.7B and C). Mn/Sr ratios (Figure 3.7D and E) and $\delta^{18}O_{CAS}$ vs $\delta^{18}O_{carb}$ (Figure 3.7F) further support the idea that bulk isotope proxies from the Viki core have not been reset by post-depositional alteration (Richardson et al., 2019) and paired $\delta^{34}S_{CAS}$-$\delta^{18}O_{CAS}$ enrichments are recording a pore-water signature at these locations, as well as deep-water carbonate facies that precipitate and/or recrystallize at depth within the anoxic zone of the sediment.

From the marlstone facies, seawater-like $\delta^{34}S_{CAS}$ and $\delta^{18}O_{CAS}$ in the Viki core are 26 and 13.5‰ for $\delta^{34}S_{CAS}$ and $\delta^{18}O_{CAS}$, respectively, comparable with Paatsalu data (25.2 and 12.2‰). For $\delta^{34}S_{CAS}$, these suggested seawater sulfate values are similar to time-equivalent brachiopod and evaporite $\delta^{34}S$ (Kampschulte and Strauss 2004; Present, 2018). The $\delta^{18}O_{CAS}$ values are lighter than $\delta^{18}O_{SO4}$ from evaporite deposits by ~2‰ (Claypool et al., 1980). This could be a result of isotopic enrichment of $\delta^{18}O_{SO4}$ during basin restriction, or, due to a small sample set. More sections should be sampled for paired $\delta^{34}S_{CAS}$-$\delta^{18}O_{CAS}$ analyses to identify the least evolved values that best approximate seawater. In these sections, $\delta^{18}O_{CAS}$ is not generally an archive for changes to the sulfur cycle. Instead, $\delta^{18}O_{CAS}$ records an early marine diagenetic signal that varies based on depositional setting, responding similarly to $\delta^{34}S_{CAS}$.

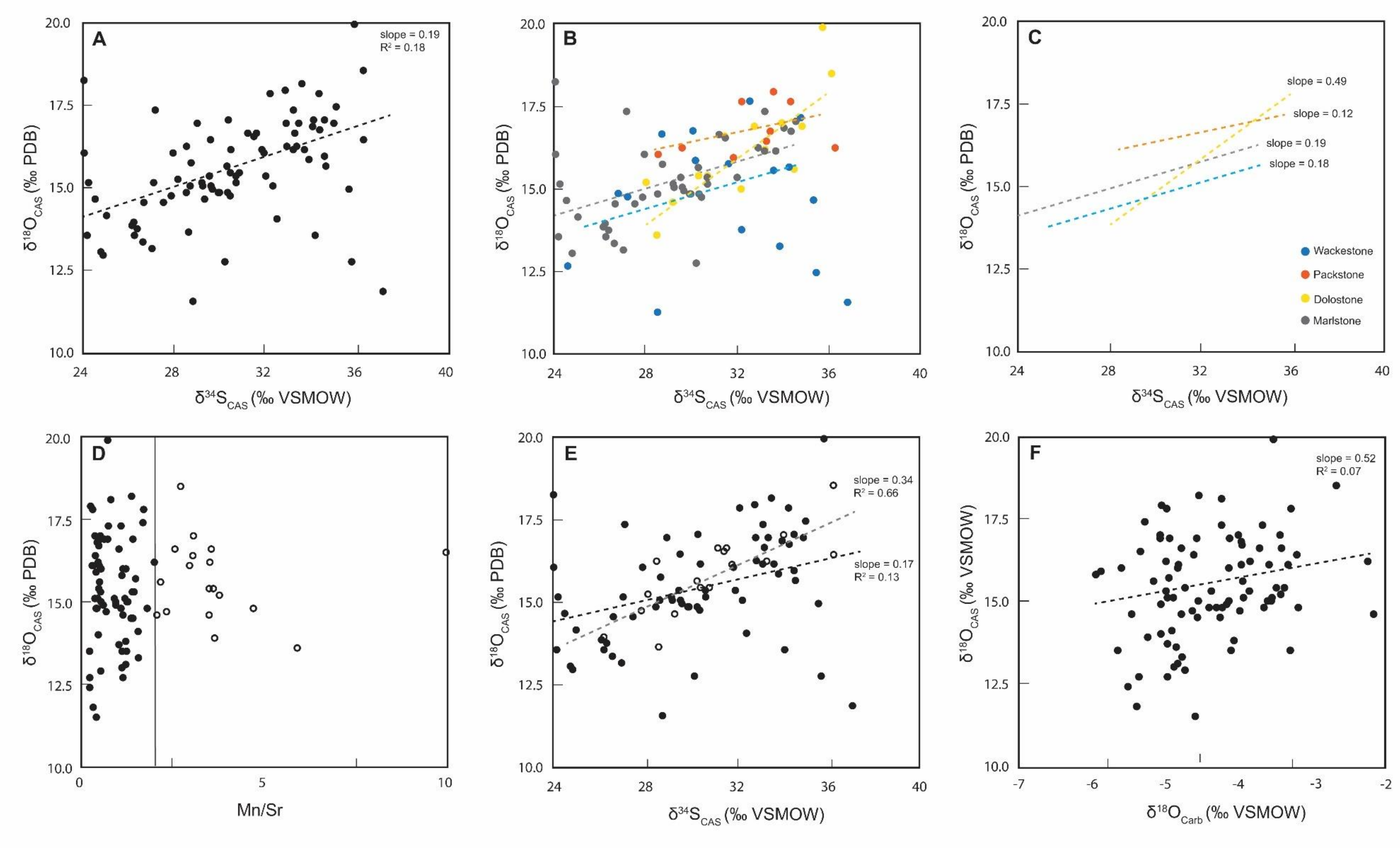

Figure 3.7 - Cross plots of $\delta^{18}O_{CAS}$ from the Viki drill core vs. (A) $\delta^{34}S_{CAS}$, (B) $\delta^{34}S_{CAS}$ color-coded with lithologic information, (C) the lines shown in B for clarity, (D) Mn/Sr, black line is a ratio of 2. Open circles are samples with an Mn/Sr > 2 and solid circles are samples with Mn/Sr < 2. (E) $\delta^{34}S_{CAS}$ plotted as Mn/Sr greater than 2 (open circles) and Mn/Sr less than 2 (solid circles), and, (F) $\delta^{18}O_{carb}$

3.7 Conclusions

Bulk stable isotope data from the Paatsalu drill core provide additional information on the effect of depositional environment on $\delta^{34}S_{CAS}$, $\delta^{34}S_{pyr}$ and $\delta^{18}O_{CAS}$ within the Baltoscandian basin during the Silurian and across a carbonate platform. Paired $\delta^{13}C_{carb}$-$\delta^{13}C_{org}$ record a positive carbon isotope excursion coincident with the Ireviken bioevent, but of different magnitudes to that preserved in the Viki drill core and Gotland, Sweden. The variability of the carbon isotopes is the expression of local depositional settings (due to depth gradients in $\delta^{13}C_{DIC}$ from the biological pump and/or mixing of different carbon mineralogies) on top of the global perturbation. Paired $\delta^{34}S_{CAS}$-$\delta^{34}S_{pyr}$ are variable in shallow-water carbonate facies and more stable in deep-water facies, similar to observations from paired $\delta^{34}S_{CAS}$-$\delta^{34}S_{pyr}$ in the Viki core. The magnitude, direction and timing of changes in $\delta^{34}S_{CAS}$-$\delta^{34}S_{pyr}$ are not synchronous between Paatsalu, Viki and Gotland. Additionally, paired $\delta^{34}S_{CAS}$-$\delta^{18}O_{CAS}$ data preserve pore fluid signatures of progressive porewater sulfur isotope distillation as a result of MSR. These data indicate that shallow-water carbonate deposition results in variable, often heavy $\delta^{34}S_{CAS}$, $\delta^{34}S_{pyr}$ and $\delta^{18}O_{CAS}$ due to high sedimentation rate and increased labile organic carbon availability causing distillation of pore fluid. However, proximity to the paleoshoreline will also affect shallow-water $\delta^{34}S_{CAS}$, $\delta^{34}S_{pyr}$ and $\delta^{18}O_{CAS}$ values due to tide and wave-action disrupting sediment stratification and isotope distillation. Similar patterns in paired $\delta^{34}S_{CAS}$-$\delta^{18}O_{CAS}$ data between shallow- and deep-water carbonate facies, combined with high Mn/Sr ratios in deep-water carbonate facies, suggest that, although deep-water carbonates may form in a more open-system, they precipitate and/or recrystallize at depth and ultimately capture evolved pore fluid $\delta^{34}S$ values. Local sea-water like values for $\delta^{34}S_{CAS}$ and $\delta^{18}O_{CAS}$ are approximately 25.5 and 13‰ based on clustering of the lowest values from marlstone units in $\delta^{34}S_{CAS}$ vs $\delta^{18}O_{CAS}$, in broad agreement with temporal evaporite records. Combined

$\delta^{34}S_{CAS}$, $\delta^{34}S_{pyr}$ and $\delta^{18}O_{CAS}$ from Paatsalu and Viki, compared to sulfur isotope data from Gotland do not show any apparent secular trend during the Ireviken bioevent. At these sites during the early Silurian, sulfur and oxygen isotopes were recording distinct depositional and early diagenetic processes, irrespective of basin or global sulfur cycling. Future studies aiming to interpret $\delta^{34}S_{CAS}$-$\delta^{34}S_{pyr}$ data in terms of sulfur cycling should include paired $\delta^{34}S_{CAS}$-$\delta^{18}O_{CAS}$ to assess the impact of isotope distillation on the samples.

3.8 Acknowledgements

Acknowledgment is made to the donors of the American Chemical Society Petroleum Research Fund (#57548-ND2) for partial support of this research and from the Estonian Research Council (#PUT611) to O.H. We thank the Geological Survey of Estonia, the Department of Geology at Tallinn University of Technology, and the Department of Geology at Tartu University. S. Moore conducted stable isotope and ICP-OES measurements at Washington University.

3.9 Supplementary Material

3.9.1 Methods

Lithologic Information

The abundance of carbonate in each sample was calculated gravimetrically via dissolution of carbonate during sample preparation for organic carbon isotope analyses. The area under the CO_2 peak from sample combustion in the EA provides total organic carbon abundance (% TOC) on the insoluble reside after carbonate dissolution. CAS abundance (given in ppm) was gravimetrically based on the final yield of $BaSO_4$ and the initial % carbonate of the sample. Similarly, whole rock pyrite abundance (wt % pyrite) was calculated from the final yield of silver sulfide and the initial mass of insoluble reside used in the extraction.

Elemental Abundance

Major and trace element analyses by inductively coupled plasma optical emission spectroscopy (ICP-OES) followed a sample preparation that ensures only the carbonate fraction is dissolved, avoiding contamination from clays (Husson et al., 2015). Analyses were conducted using a PerkinElmer Optima 7300DV ICP-OES at Washington University. Calcium, magnesium, iron, strontium and manganese (in ppm) were standardized to the Sigma Multi-element Standard Solution 5.

3.9.2 Results

Lithologic Information

Carbonate abundance (wt. % carbonate) is generally ≥ 75% in rocks from the deepest part of the section and the top of the section (Fig. S3.1; Nurmekund, Rumba and Jaagarahu Fms.). Carbonate content decreases below 70% at 83.4 m, the onset of the Velise Fm. and continues to decrease to a minimum of 18.7% at 79.3 m. Through the remainder of the Velise Fm. and into the base of the Jaani Fm., carbonate content is variable between 36% and 85%. From 55.6 m, the variability decreases, and carbonate content steadily increases to 71.6% at 36 m, before a step increase to ≥ 80% for the remainder of the section (Fig. S1). Total organic carbon (TOC, wt %), is < 0.25% for the entire section. TOC is variable between 0 and 0.16% throughout the Nurmekund and Rumba Fms. At 83.4 m TOC stabilizes around 0.05% until the onset of the Jaani Fm. at 68.6 m when TOC gradually increases up to 0.22% at 47.3 m. Up to the top of the section, TOC is the most variable between 0.03 and 0.2% (Fig. S3.1). Sulfate abundance (ppm in carbonate) is < 200 ppm for a majority of the section, with the exception of 2 outliers of 407 and 955 ppm at 16.5 and 12.9 m (Fig. S1). Pyrite abundance (measured as wt. % pyrite of whole rock) is the most variable in the Nurmekund, Rumba and Jaagarahu Fms. In the Nurmekund and Rumba Fms. Pyrite abundance varies between 0.15 and 1.6% except for the section maximum of 3% at 92.2 m. At 83.4m this variability decreases and up to 43.3m, pyrite abundance is generally < 0.5 wt. %. From 43.3 to the top of the section, wt. % pyrite varies up to 1.6% (Fig. S3.1).

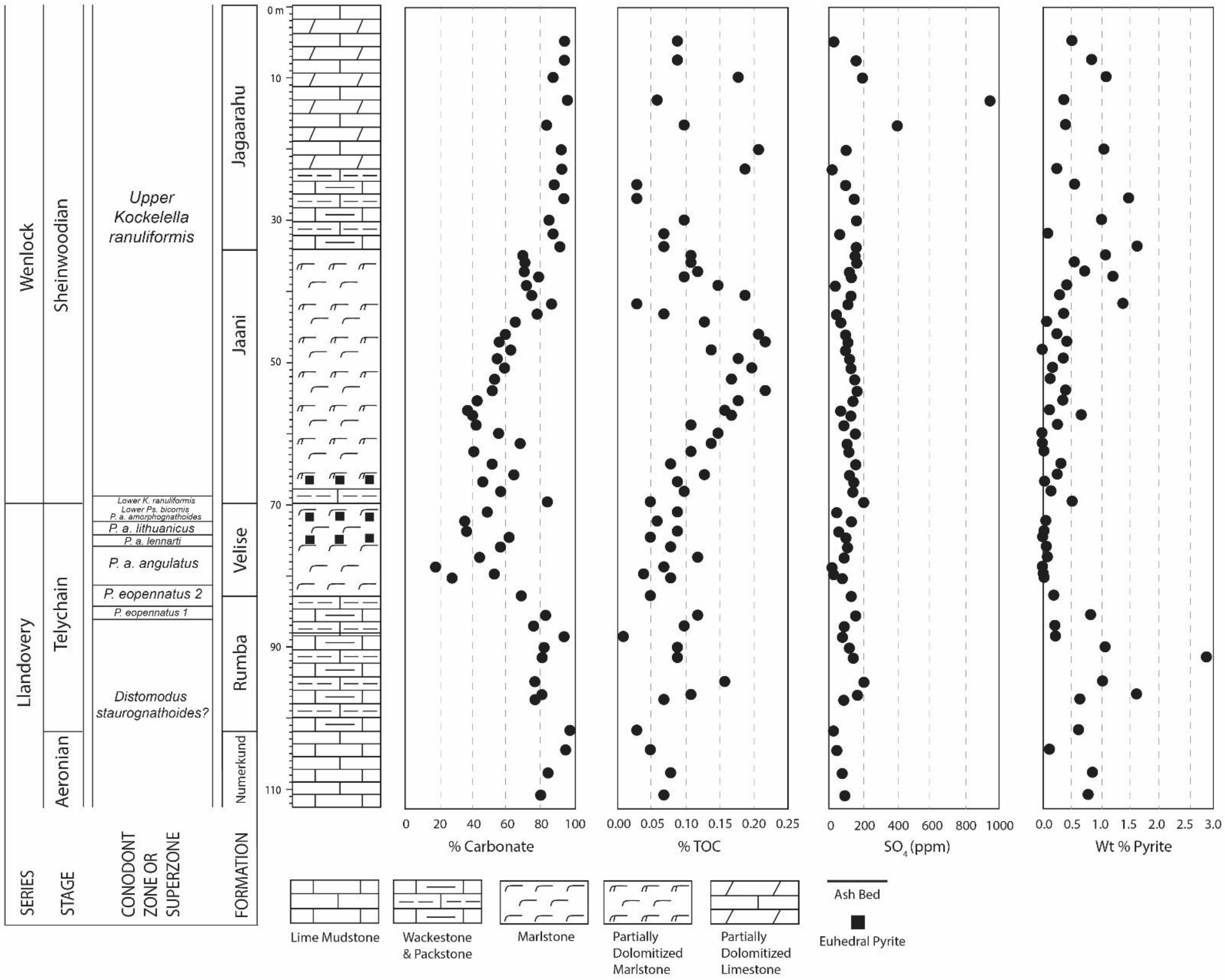

Figure S3.1 – Paatsalu drill core stratigraphy (left) and lithologic information (from left to right); carbonate abundance, TOC, CAS abundance and wt. % pyrite

Trace Elements

The Silurian carbonates of the Baltoscandian basin have experienced variable amounts of dolomitization (Hints et al., 2006; Põldvere, 2010; Richardson et al., 2019). The Paatsalu drill-core has two trends in Mg/Ca molar ratio; a ratio ≤ 0.1 in the lower section of the core corresponding to the end-Llandovery (Nurmekund, Rumba and Velise Fm.), with one notable sample at 102.6 m with a ratio of 0.4. In the upper Velise Fm. at 72.8 m there is a step increase to Mg/Ca ratios of ~ 0.4 for the rest of the section (Fig. S3.2). Sr/Ca ratio (in mmol/mol) show a decreasing trend from the base of the section to top. Ratios are more variable from the Nurmekund to the top of the Jaani Fm., generally varying between 0.9 and 0.3 until 35 m where ratios decrease and stabilize at 0.15 for the rest of the core (Fig. S3.2). Contrastingly, iron abundance shows an overall increase in abundance up-section. Up to 86.2 m, Fe abundance is generally < 500 ppm (apart from the sample at 102.5 that seems to be anomalous in many parameters). Above this, Fe abundance increases to 1670 ppm but decreases to 930 ppm at 60.3 m. There is a step increase to 1500 ppm at 54 m with a decrease back to 900 ppm at 36 m. From 33.8 m to the top of the section Fe abundance varies between 1800 and 600 ppm. Mn abundance is ≤ 500 ppm with an overall increasing abundance up-section from 60 ppm at the base to 120 ppm in the lower Jaani Fm. Mn abundance and variability increases to the top of the section between 120 and 320 ppm (Fig. S3.2).

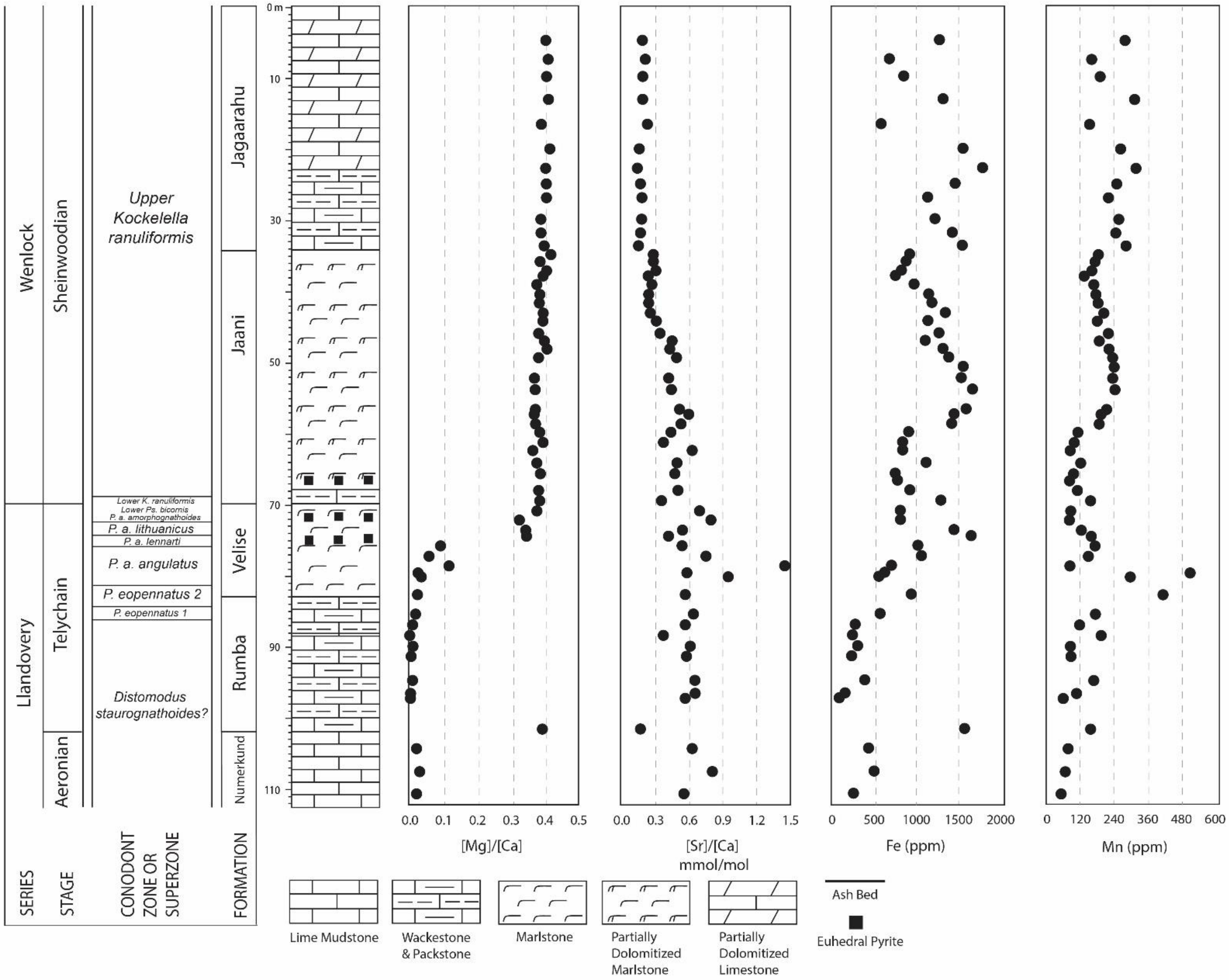

Figure S2 – Paatsalu drill core stratigraphy (left) and elemental abundance data (from left to right); molar Mg/Ca ratio, Sr/Ca (mmol/mol), iron abundance and manganese abundance.

3.9.3 Data tables

Table S3.1 – isotope data for Paatsalu drill core

Sample ID	**Depth (m)**	**Age**	**Stratigraphy**	$\delta^{13}C_{carb}$	$\delta^{18}O_{carb}$	$\delta^{13}C_{org}$	$\delta^{34}S_{CAS}$	$\delta^{34}S_{pyr}$	$\delta^{18}O_{CAS}$
DF-15-232	111.78	Aeronian	Nurmekund Fm.	0.05	-5.19	-28.82	33	1.03	12.4
DF-15-234	108.62	Aeronian	Nurmekund Fm.	1.3	-6.3	-29.27	30.22	15.39	11.0
DF-15-236	105.34	Aeronian	Nurmekund Fm.	1.31	-6.54	-28.97	28.78	6.88	10.6
DF-15-238	102.56	Aeronian	Nurmekund Fm.	0.53	-6.67	-28.98	23.42	10.87	11.8
DF-15-240	98.19	Telychian	Rumba Fm.	-1.3	-5.47	-31.21	26.51	-21.81	14.5
DF-15-241	97.48	Telychian	Rumba Fm.	-0.81	-5.78	-31.77	21.07	-24.3	12.9
DF-15-242	95.63	Telychian	Rumba Fm.	-0.97	-5.75	-32.11	22.73	-22.28	12.8
DF-15-244	92.21	Telychian	Rumba Fm.	-0.49	-5.82	-30.87	23.36	-21.74	12.3
DF-15-245	90.77	Telychian	Rumba Fm.	-0.3	-5.6	-30.35	27.01	-20.65	15.9
DF-15-246	89.23	Telychian	Rumba Fm.	-0.06	-5.84	-29.78	28.62	-21.93	15.9
DF-15-247	87.72	Telychian	Rumba Fm.	0	-6	-30.67	24.84	-25.17	14.1
DF-15-248	86.19	Telychian	Rumba Fm.	0.45	-6.2	-30.72	21.53	-26.73	12.4
DF-15-250	83.42	Telychian	Rumba Fm.	1.97	-5.78	-28.15	26.97	2.84	15.7
DF-15-252	80.89	Telychian	Velise Fm.	2.14	-5.52	-27.61	28.75	-28.79	14.7
DF-15-253	80.32	Telychian	Velise Fm.	1.84	-5.58	-27.61	29.3	-25.39	15.0
DF-15-254	79.32	Telychian	Velise Fm.	1.95	-5.23	-27.48	30.01		14.8
DF-15-255	77.95	Telychian	Velise Fm.	2.03	-5.66	-27.44	25.34	4.56	15.2
DF-15-256	76.47	Telychian	Velise Fm.	1.94	-5.83	-26.8	28.71	9.92	16.0
DF-15-257	75.10	Telychian	Velise Fm.	2.03	-6.1	-27.15	30.54	10.822	16.0
DF-15-258	74.24	Telychian	Velise Fm.	2.18	-5.44	-27.22	27.89	-32.383	14.5
DF-15-259	72.80	Telychian	Velise Fm.	1.96	-5.22	-26.79	32.6	8.05	17.4
DF-15-260	71.50	Telychian	Velise Fm.	1.95	-6.03	-27.31	30.36		15.6
DF-15-261	70.05	Telychian	Velise Fm.	2.43	-6.75	-27.15	29.02	12.614	10.0
DF-15-262	68.58	Sheinwoodian	Jaani Fm.	3.14	-6.77	-24.74	26.57	4.605	13.9

DF-15-263	67.20	Sheinwoodian	Jaani Fm.	3.63	-5.68	-25.57	15.01	-21.236	8.3
DF-15-264	66.20	Sheinwoodian	Jaani Fm.	3.99	-6.96	-24.81	25.08	-17.339	11.6
DF-15-265	64.67	Sheinwoodian	Jaani Fm.	3.78	-5.73	-25.13	26.8	-18.49	13.7
DF-15-266	62.90	Sheinwoodian	Jaani Fm.	3.82	-5.53	-25.57	25.86	-28.132	14.4
DF-15-267	61.75	Sheinwoodian	Jaani Fm.	4.12	-6.85	-25.72	28.92	-20.703	14.7
DF-15-268	60.30	Sheinwoodian	Jaani Fm.	4.17	-6.47	-25.87	30.09	-20.859	14.6
DF-15-269	59.12	Sheinwoodian	Jaani Fm.	4.25	-6.11	-26.23	27.71	-16.688	13.3
DF-15-270	57.75	Sheinwoodian	Jaani Fm.	4.49	-6.16	-25.89	29.63	-12.771	13.7
DF-15-271	57.04	Sheinwoodian	Jaani Fm.	4.59	-6.13	-25.81	27.56	-16.005	12.6
DF-15-272	55.67	Sheinwoodian	Jaani Fm.	4.65	-6.19	-26.28	27.05	-12.583	11.4
DF-15-273	54.23	Sheinwoodian	Jaani Fm.	4.66	-6.17	-25.61	28.76	-10.251	13.8
DF-15-274	52.60	Sheinwoodian	Jaani Fm.	4.78	-6.19	-26.89	27.66	-20.313	13.4
DF-15-275	51.00	Sheinwoodian	Jaani Fm.	4.82	-6.06	-27.05	29.07	-14.85	15.5
DF-15-276	49.68	Sheinwoodian	Jaani Fm.	4.68	-5.81	-26.56	29.67	-10.43	13.5
DF-15-277	48.45	Sheinwoodian	Jaani Fm.	4.68	-5.77	-25.87	31.7	-2.59	14.6
DF-15-278	47.30	Sheinwoodian	Jaani Fm.	4.72	-5.48	-26.29	29.49	0.12	13.4
DF-15-279	46.22	Sheinwoodian	Jaani Fm.	4.67	-5.43	-26.72	29.07	-6.32	13.6
DF-15-280	44.47	Sheinwoodian	Jaani Fm.	4.68	-5.81	-26.7	27.26	-7.52	13.8
DF-15-281	43.33	Sheinwoodian	Jaani Fm.	4.55	-5.54	-27.3	27.17	-6.73	13.6
DF-15-282	41.90	Sheinwoodian	Jaani Fm.	4.43	-6.21	-26.68	25.75	-3.79	11.6
DF-15-283	40.68	Sheinwoodian	Jaani Fm.	4.42	-5.48	-27.06	27.35	-13.97	14.6
DF-15-284	39.27	Sheinwoodian	Jaani Fm.	4.03	-5.55	-26.94	24.37	-8.6	11.4
DF-15-285	38.05	Sheinwoodian	Jaani Fm.	3.94	-3.09	-26.91	28.8	-10	15.1
DF-15-286	37.30	Sheinwoodian	Jaani Fm.	3.65	-2.1	-25.95	25.12	-3.02	12.2
DF-15-287	36.00	Sheinwoodian	Jaani Fm.	3.82	-2.27	-24.96	24.37	-2.22	20.3
DF-15-288	35.00	Sheinwoodian	Jaani Fm.	3.68	-2.28	-25.95	25.2	-2.32	12.1
DF-15-289	33.75	Sheinwoodian	Jaagarahu Fm.	3.6	-4.18	-25.83	22.32	-3.33	10.9
DF-15-290	31.92	Sheinwoodian	Jaagarahu Fm.	3.46	-4.06	-24.95	25.41	-8.27	14.5
DF-15-291	29.97	Sheinwoodian	Jaagarahu Fm.	3.21	-4.06	-24.7	20.76	-9.01	12.3

DF-15-292	26.90	Sheinwoodian	Jaagarahu Fm.	3.25	-4.4	-26.03	17.64	-9.65	12.7
DF-15-293	24.93	Sheinwoodian	Jaagarahu Fm.	3.25	-3.81	-24.36	15.96	-12.55	8.8
DF-15-294	22.71	Sheinwoodian	Jaagarahu Fm.	2.66	-3.91	-26.28	15.05	-8.5	10.3
DF-15-295	19.95	Sheinwoodian	Jaagarahu Fm.	2.73	-4.35	-26.31	15.69	-9.94	10.3
DF-15-296	16.45	Sheinwoodian	Jaagarahu Fm.	2.57	-2.83	-26.01	6.4	-1.86	1.0
DF-15-297	12.90	Sheinwoodian	Jaagarahu Fm.	0.74	-3.9	-27.82	11.76	-13.69	5.0
DF-15-298	9.65	Sheinwoodian	Jaagarahu Fm.	-0.17	-4.07	-30.14	3.31	-6.84	-1.7
DF-15-299	7.20	Sheinwoodian	Jaagarahu Fm.	-0.29	-3.36	-29.86	6.38	-17.01	3.1
DF-15-300	4.5	Sheinwoodian	Jaagarahu Fm.	-0.38	-3.72	-29.67	13.97	-17	10.9
DF-18-8	101.5	Aeronian	Rumba Fm.	-	-	-	29.80	-12.37	-
DF-18-9	100.45	Telychian	Rumba Fm.	-	-	-	29.63	-13.29	-
DF-18-10	93.89	Telychian	Rumba Fm.	-	-	-	25.74	-22.05	-
DF-18-11	85.58	Telychian	Rumba Fm.	-	-	-	21.95	-22.52	-
DF-18-12	84.35	Telychian	Rumba Fm.	-	-	-	17.51	-26.74	-
DF-18-13	69.7	Sheinwoodian	Velise Fm.	-	-	-	30.44	15.36	-
DF-18-14	69.34	Sheinwoodian	Velise Fm.	-	-	-	26.20	-14.31	-

Table S3.2 - ICP-OES data for Paatsalu drill core

Sample ID	Depth (m)	Age	Stratigraphy	Ca (ppm)	Mg (ppm)	Sr (ppm)	Fe (ppm)	Mn (ppm)
DF-15-232	111.78	Aeronian	Nurmekund Fm.	198194.88	5098.45	113.30	281.24	60.00
DF-15-234	108.62	Aeronian	Nurmekund Fm.	241423.76	8466.47	199.07	526.07	74.79
DF-15-236	105.34	Aeronian	Nurmekund Fm.	272312.26	7017.85	175.78	460.27	84.96
DF-15-238	102.56	Aeronian	Nurmekund Fm.	73042.74	29129.64	13.50	1598.32	164.93
DF-15-240	98.19	Telychian	Rumba Fm.	184180.41	1410.63	107.43	111.95	67.53
DF-15-241	97.48	Telychian	Rumba Fm.	257300.81	2074.52	172.91	181.53	114.85
DF-15-242	95.63	Telychian	Rumba Fm.	253001.53	3519.05	169.39	414.85	176.15
DF-15-244	92.21	Telychian	Rumba Fm.	212483.16	2062.47	126.34	259.50	95.07

DF-15-245	90.77	Telychian	Rumba Fm.	184231.99	2806.09	115.73	330.87	92.99
DF-15-246	89.23	Telychian	Rumba Fm.	364215.87	2052.72	141.62	269.66	202.49
DF-15-247	87.72	Telychian	Rumba Fm.	163820.18	2317.61	95.59	301.74	125.75
DF-15-248	86.19	Telychian	Rumba Fm.	201473.59	4598.02	132.22	596.95	182.03
DF-15-250	83.42	Telychian	Rumba Fm.	177145.16	5065.06	103.41	966.37	422.47
DF-15-252	80.89	Telychian	Velise Fm.	75201.56	3003.20	72.60	582.64	306.19
DF-15-253	80.32	Telychian	Velise Fm.	98669.67	2981.09	59.02	651.27	518.85
DF-15-254	79.32	Telychian	Velise Fm.	38905.80	4745.16	57.13	732.03	91.24
DF-15-255	77.95	Telychian	Velise Fm.	83171.32	5229.27	63.88	1087.33	156.92
DF-15-256	76.47	Telychian	Velise Fm.	81001.22	7845.59	44.99	1045.07	180.58
DF-15-257	75.10	Telychian	Velise Fm.	44816.19	15762.85	19.48	1676.86	167.28
DF-15-258	74.24	Telychian	Velise Fm.	34489.24	12048.54	19.27	1473.27	132.02
DF-15-259	72.80	Telychian	Velise Fm.	24631.50	8145.51	20.00	838.73	89.37
DF-15-260	71.50	Telychian	Velise Fm.	25874.76	9899.29	18.39	836.32	94.22
DF-15-261	70.05	Telychian	Velise Fm.	46621.98	18231.14	17.37	1317.83	164.89
DF-15-262	68.58	Sheinwoodian	Jaani Fm.	36921.29	14313.80	19.16	949.56	117.95
DF-15-263	67.20	Sheinwoodian	Jaani Fm.		10919.21		803.62	90.08
DF-15-264	66.20	Sheinwoodian	Jaani Fm.	36254.18	14243.37	17.79	776.54	104.38
DF-15-265	64.67	Sheinwoodian	Jaani Fm.	43441.88	16608.18	22.16	1142.49	129.64
DF-15-266	62.90	Sheinwoodian	Jaani Fm.	30556.60	11321.26	19.72	864.60	92.26
DF-15-267	61.75	Sheinwoodian	Jaani Fm.	37533.67	15045.18	14.62	863.81	106.73
DF-15-268	60.30	Sheinwoodian	Jaani Fm.	44757.27	17499.01	20.43	935.72	119.68
DF-15-269	59.12	Sheinwoodian	Jaani Fm.	78326.31	29652.61	42.75	1446.07	195.48
DF-15-270	57.75	Sheinwoodian	Jaani Fm.	80720.07	30231.00	49.60	1474.59	201.98
DF-15-271	57.04	Sheinwoodian	Jaani Fm.	89538.21	33860.63	47.71	1617.01	221.88
DF-15-272	55.67	Sheinwoodian	Jaani Fm.	54.49	32.19			
DF-15-273	54.23	Sheinwoodian	Jaani Fm.	99716.88	37638.41	45.90	1692.49	251.58
DF-15-274	52.60	Sheinwoodian	Jaani Fm.	102207.85	38364.43	44.58	1559.73	243.45
DF-15-275	51.00	Sheinwoodian	Jaani Fm.		40716.63	43.33	1582.61	248.71

DF-15-276	49.68	Sheinwoodian	Jaani Fm.	108115.27	41892.89	54.75	1410.83	243.31
DF-15-277	48.45	Sheinwoodian	Jaani Fm.	97632.89	40279.95	43.52	1342.31	230.35
DF-15-278	47.30	Sheinwoodian	Jaani Fm.	89788.15	36344.36	41.89	1132.02	195.73
DF-15-279	46.22	Sheinwoodian	Jaani Fm.	114090.18	44241.10	40.99	1295.01	228.14
DF-15-280	44.47	Sheinwoodian	Jaani Fm.	103032.95	41257.12	33.66	1163.97	188.55
DF-15-281	43.33	Sheinwoodian	Jaani Fm.	114414.94	45908.19	31.22	1370.73	211.98
DF-15-282	41.90	Sheinwoodian	Jaani Fm.	115747.37	45123.77	29.91	1211.21	191.35
DF-15-283	40.68	Sheinwoodian	Jaani Fm.	121039.26	47369.90	31.28	1173.20	183.78
DF-15-284	39.27	Sheinwoodian	Jaani Fm.	112047.61	42845.80	32.13	999.65	176.27
DF-15-285	38.05	Sheinwoodian	Jaani Fm.	84103.82	33729.08	21.37	778.77	142.08
DF-15-286	37.30	Sheinwoodian	Jaani Fm.	99531.91	40933.58	32.10	850.12	169.11
DF-15-287	36.00	Sheinwoodian	Jaani Fm.	116181.66	45554.84	34.87	905.46	180.76
DF-15-288	35.00	Sheinwoodian	Jaani Fm.	109593.79	46471.65	32.83	946.95	192.57
DF-15-289	33.75	Sheinwoodian	Jaagarahu Fm.	149866.72	60557.02	25.17	1571.72	290.94
DF-15-290	31.92	Sheinwoodian	Jaagarahu Fm.	126885.03	50094.79	23.55	1452.94	254.45
DF-15-291	29.97	Sheinwoodian	Jaagarahu Fm.	141484.28	55802.63	27.71	1247.73	265.16
DF-15-292	26.90	Sheinwoodian	Jaagarahu Fm.	118004.77	48490.10	23.41	1161.03	228.36
DF-15-293	24.93	Sheinwoodian	Jaagarahu Fm.	123969.00	50896.72	22.93	1486.79	257.84
DF-15-294	22.71	Sheinwoodian	Jaagarahu Fm.	151203.30	61765.27	23.84	1812.27	326.35
DF-15-295	19.95	Sheinwoodian	Jaagarahu Fm.	123407.86	51948.55	21.59	1579.88	271.72
DF-15-296	16.45	Sheinwoodian	Jaagarahu Fm.	131423.73	52008.24	32.47	608.62	161.21
DF-15-297	12.90	Sheinwoodian	Jaagarahu Fm.	184023.78	76720.62	37.69	1343.67	321.51
DF-15-298	9.65	Sheinwoodian	Jaagarahu Fm.	111729.49	45934.89	22.98	877.46	198.93
DF-15-299	7.20	Sheinwoodian	Jaagarahu Fm.	109162.88	45397.50	24.94	707.07	168.62
DF-15-300	4.5	Sheinwoodian	Jaagarahu Fm.	148471.11	60710.64	30.04	1300.69	287.43

Table S3.3 – lithologic data Paatsalu drill core

Sample ID	Depth (m)	Age	Stratigraphy	% Carbonate	% TOC	ppm SO4	Wt % pyrite
DF-15-232	111.78	Aeronian	Nurmekund Fm.	80.93	0.072	95.94	0.82
DF-15-234	108.62	Aeronian	Nurmekund Fm.	85.28	0.082	80.51	0.90
DF-15-236	105.34	Aeronian	Nurmekund Fm.	95.67	0.054	48.61	0.14
DF-15-238	102.56	Aeronian	Nurmekund Fm.	98.24	0.032	28.72	0.65
DF-15-240	98.19	Telychian	Rumba Fm.	77.58	0.067	89.67	0.68
DF-15-241	97.48	Telychian	Rumba Fm.	81.63	0.110	170.71	1.68
DF-15-242	95.63	Telychian	Rumba Fm.	77.46	0.165	208.94	1.08
DF-15-244	92.21	Telychian	Rumba Fm.	81.80	0.086	145.88	2.92
DF-15-245	90.77	Telychian	Rumba Fm.	82.94	0.085	122.56	1.12
DF-15-246	89.23	Telychian	Rumba Fm.	94.75	0.014	81.91	0.24
DF-15-247	87.72	Telychian	Rumba Fm.	76.74	0.102	92.84	0.23
DF-15-248	86.19	Telychian	Rumba Fm.	83.84	0.118	160.12	0.87
DF-15-250	83.42	Telychian	Rumba Fm.	69.45	0.052	134.11	0.21
DF-15-252	80.89	Telychian	Velise Fm.	28.51	0.079	81.30	0.04
DF-15-253	80.32	Telychian	Velise Fm.	53.47	0.037	30.12	0.03
DF-15-254	79.32	Telychian	Velise Fm.	18.74	0.065	20.28	0.01
DF-15-255	77.95	Telychian	Velise Fm.	44.77	0.116	91.84	0.10
DF-15-256	76.47	Telychian	Velise Fm.	57.11	0.077	112.00	0.08
DF-15-257	75.10	Telychian	Velise Fm.	62.23	0.053	102.67	0.02
DF-15-258	74.24	Telychian	Velise Fm.	37.07	0.088	60.23	0.04
DF-15-259	72.80	Telychian	Velise Fm.	35.99	0.058	135.10	0.07
DF-15-260	71.50	Telychian	Velise Fm.	49.32	0.086	48.08	
DF-15-261	70.05	Telychian	Velise Fm.	84.87	0.045	207.69	0.54
DF-15-262	68.58	Sheinwoodian	Jaani Fm.	57.29	0.098	143.58	0.16
DF-15-263	67.20	Sheinwoodian	Jaani Fm.	46.65	0.091	149.00	0.05
DF-15-264	66.20	Sheinwoodian	Jaani Fm.	65.04	0.126	123.58	0.27

DF-15-265	64.67	Sheinwoodian	Jaani Fm.	52.19	0.081	160.63	0.34
DF-15-266	62.90	Sheinwoodian	Jaani Fm.	41.39	0.111	120.47	0.04
DF-15-267	61.75	Sheinwoodian	Jaani Fm.	68.79	0.140	109.28	0.01
DF-15-268	60.30	Sheinwoodian	Jaani Fm.	56.03	0.145	158.31	0.00
DF-15-269	59.12	Sheinwoodian	Jaani Fm.	42.73	0.109	90.57	0.28
DF-15-270	57.75	Sheinwoodian	Jaani Fm.	40.63	0.172	131.47	0.70
DF-15-271	57.04	Sheinwoodian	Jaani Fm.	37.67	0.156	71.14	0.14
DF-15-272	55.67	Sheinwoodian	Jaani Fm.	43.32	0.181	144.06	0.37
DF-15-273	54.23	Sheinwoodian	Jaani Fm.	52.29	0.224	168.43	0.42
DF-15-274	52.60	Sheinwoodian	Jaani Fm.	53.66	0.171	154.35	0.15
DF-15-275	51.00	Sheinwoodian	Jaani Fm.	59.54	0.202	132.78	0.19
DF-15-276	49.68	Sheinwoodian	Jaani Fm.	55.22	0.184	124.41	0.38
DF-15-277	48.45	Sheinwoodian	Jaani Fm.	63.22	0.140	100.20	0.01
DF-15-278	47.30	Sheinwoodian	Jaani Fm.	56.42	0.222	114.60	0.44
DF-15-279	46.22	Sheinwoodian	Jaani Fm.	60.04	0.208	100.64	0.27
DF-15-280	44.47	Sheinwoodian	Jaani Fm.	65.93	0.129	72.21	0.09
DF-15-281	43.33	Sheinwoodian	Jaani Fm.	78.81	0.070	46.64	0.39
DF-15-282	41.90	Sheinwoodian	Jaani Fm.	87.36	0.032	114.33	1.44
DF-15-283	40.68	Sheinwoodian	Jaani Fm.	75.63	0.190	132.45	0.32
DF-15-284	39.27	Sheinwoodian	Jaani Fm.	72.48	0.151	39.48	0.44
DF-15-285	38.05	Sheinwoodian	Jaani Fm.	79.70	0.099	134.95	1.26
DF-15-286	37.30	Sheinwoodian	Jaani Fm.	71.19	0.121	123.17	0.76
DF-15-287	36.00	Sheinwoodian	Jaani Fm.	71.59	0.108	166.60	0.58
DF-15-288	35.00	Sheinwoodian	Jaani Fm.	70.33	0.113	156.89	1.13
DF-15-289	33.75	Sheinwoodian	Jaagarahu Fm.	92.26	0.067	163.42	1.69
DF-15-290	31.92	Sheinwoodian	Jaagarahu Fm.	88.25	0.072	65.86	0.11
DF-15-291	29.97	Sheinwoodian	Jaagarahu Fm.	85.87	0.102	165.05	1.06
DF-15-292	26.90	Sheinwoodian	Jaagarahu Fm.	94.63	0.028	151.70	1.54
DF-15-293	24.93	Sheinwoodian	Jaagarahu Fm.	88.92	0.028	100.64	0.58

DF-15-294	22.71	Sheinwoodian	Jaagarahu Fm.	93.40	0.189	21.16	0.27
DF-15-295	19.95	Sheinwoodian	Jaagarahu Fm.	93.08	0.207	103.68	1.10
DF-15-296	16.45	Sheinwoodian	Jaagarahu Fm.	84.40	0.097	406.39	0.42
DF-15-297	12.90	Sheinwoodian	Jaagarahu Fm.	96.72	0.059	954.75	0.39
DF-15-298	9.65	Sheinwoodian	Jaagarahu Fm.	88.25	0.177	200.52	1.14
DF-15-299	7.20	Sheinwoodian	Jaagarahu Fm.	94.95	0.089	162.73	0.88
DF-15-300	4.5	Sheinwoodian	Jaagarahu Fm.	95.06	0.089	30.79	0.53

4. Depositional and Diagenetic Constraints on the Abundance and Spatial Variability of Carbonate-Associated Sulfate

Jocelyn A. Richardson[1*], Matthew Newville[2], Antonio Lanzirotti[2], Samuel M. Webb[3], Catherine V. Rose[4], Jeffrey G. Catalano[1] and David A. Fike[1*]

[1]Department of Earth and Planetary Sciences, Washington University, St. Louis, MO 63130 USA
[2]Consortium for Advanced Radiation Sources University of Chicago, Chicago, IL 60637, USA
[3]Stanford Synchrotron Radiation Lightsource, Menlo Park, CA 94025, USA
[4] School of Earth and Environmental Sciences, University of St Andrews, Fife KY16 9AL, UK

In review:
Richardson, J.A., Newville, M., Lanzirotti, A., Webb, S.M., Rose C. V., Catalano, J. G., Fike, D. A., Depositional and diagenetic constraints on the abundance and spatial variability of carbonate-associated sulfate. *Chem. Geo.*

4.1 Abstract

Marine carbonate rocks are composed, in varying abundance, of cement, micrite, abiotic grains and fossils, that can provide information about the physical and chemical environments in which they formed. Geochemical analyses of these carbonates are not always interpreted alongside the wealth of geologic (including petrographic) information available, resulting in potentially faulty reconstructions of biogeochemical and environmental conditions. These concerns have prompted closer scrutiny of the effect of depositional lithofacies and diagenesis on carbonate proxies. Here, we have combined X-ray Absorption Near Edge Structure (XANES) spectroscopy and μ-X-ray Fluorescence (μ-XRF) imaging to map the speciation and abundance of sulfur in carbonate petrographic thin sections in Upper Ordovician carbonates from Anticosti Island, Canada and early Silurian carbonates from Gotland, Sweden, across multiple depositional facies. Lithofacies and fossil communities between Anticosti Island and Gotland are similar, which allows for comparison of changes in the dominant S species and their abundance in separate basins, associated with variations in (glacio)eustatic sea level. Sulfide abundance is greatest in mudstone, wackestone and packstone facies, where interstitial micrite hosts abundant pyrite. Sulfate abundance, as carbonate-associated sulfate (CAS), varies within individual fossil fragments, as well as within the same fossil phylum and is particularly high in unaltered brachiopods. In contrast, sulfate abundance is generally very low in micrite (near the detection limit) and generally arises in situ from sulfide that has been oxidized as opposed to true CAS. In different cement fabrics, sulfate abundance is greatest in drusy, pore-filling cements. Organic sulfur compounds are also detected and, although low in abundance, are mostly found within micrite. The detection and characterization of both inorganic sulfur and organic sulfur compounds provides a platform to understand early processes of biomineralization. This approach will broaden our understanding of the source of inorganically

bound sulfate in ancient carbonates, as well as the effect of depositional setting and diagenesis on CAS incorporation, (re)mobilization, and ultimate abundance in sedimentary carbonates. Additionally, this work has implications for the CAS isotopic value of individual carbonate components that may affect interpretations of stratigraphic variability of numerous CAS sections throughout Earth history.

4.2 Introduction

Over geologic timescales, the marine sulfur cycle is closely linked to the redox state of the Earth's surface environments due to the relative burial ratio between the redox-sensitive sulfur species (i.e. sulfide and sulfate) (Berner and Raiswell, 1983). As a result, carbonate rocks are frequently analysed for the abundance and isotopic composition ($\delta^{34}S$) of their S-bearing phases, primarily pyrite and carbonate-associated sulfate (CAS), to understand long-term trends in sulfur cycling(Canfield, 2004; Fike and Grotzinger, 2008). CAS is used as a proxy for the composition of ancient seawater sulfate, understood to reflect the ambient incorporation and substitution of a sulfate ion for a carbonate ion during carbonate precipitation (Burdett et al., 1989). Given the large extent of carbonate precipitation throughout Earth history, many studies have used CAS to generate high-resolution datasets to constrain the operation and temporal evolution of the marine S-cycle from the Archean to the Cenozoic (Burdett et al., 1989; Crowe et al., 2014; Fike and Grotzinger, 2008; Kampschulte and Strauss, 2004; Ries et al., 2009; Turchyn et al., 2009).

Unlike many other geochemical proxies that are a major component of carbonates (such as $\delta^{13}C_{carb}$), CAS is a trace component, where abundances typically range from tens to hundreds of ppm in ancient carbonates and hundreds to thousands of ppm in modern carbonates (Staudt and Schoonen, 1995). These low abundances in ancient rocks indicate CAS may be more susceptible to alteration than other proxies (e.g., $\delta^{13}C$), which may contribute to the characteristic sample-to-sample isotopic variability (as much as 10‰; e.g. Edwards et al., 2018; Jones and Fike, 2013; Riccardi et al., 2006) observed in $\delta^{34}S_{CAS}$ in many deep-time records (Kampschulte and Strauss, 2004; Osburn et al., 2015; Rose et al., 2019). Such high-frequency stratigraphic variability cannot be accounted for by changes to the global marine sulfate reservoir, due to the multi-million-year residence time of seawater sulfate (Berner, 2001).

Carbonates can be composed, in varying abundances, of four major components; micrite (microcrystalline calcite or ‘lime mud’), cement, fossils and abiotic grains, all of which can be differentially affected by diagenesis. Diagenesis of carbonates includes any process occurring after the precipitation/sedimentation of carbonate, including lithification. Examples of diagenetic fluids that may affect marine carbonates are: (chemically evolved) porewaters, meteoric fluids, dolomitizing fluids, and basinal brine fluids. Several studies have assessed the effect of diagenesis on CAS of bulk rock samples (Fichtner et al., 2017; Gill et al., 2008; Hurtgen et al., 2006; Rennie and Turchyn, 2014; Richardson et al., 2019). Others have attempted to reduce the effect of secondary CAS signals by selecting for individual carbonate phases (e.g. micrite and brachiopods in Kampschulte and Strauss, 2004; Wotte et al., 2012a; fossils in Gill et al., 2011; Kampschulte et al., 2001; Present et al., 2015), and/or by reducing sample size to minimize the number of altered components homogenized into the sample (Paris et al., 2014; Present et al., 2015; Rennie et al., 2018). Additionally, an increasing number of studies are emphasising the potential impact that sedimentary facies, and therefore relative local sea level, have on CAS abundance, $\delta^{34}S_{CAS}$, and $\delta^{34}S_{pyr}$ preserved in the rock record (Fike et al., 2015; Pasquier et al., 2017; Richardson et al., 2019; Rose et al., 2019; Strauss, 1997). Depositional environments can affect the relative abundance of carbonate components, producing lithofacies (outcrop and hand sample observations) and microfacies (petrographic observations) that likely have their own imprint on the initial composition of CAS.

Until recently, it was unknown how CAS abundance varied spatially within an individual hand sample (Present et al., 2015; Rose et al., in review). Due to the low abundance of CAS in the rock record, there have been few techniques that can determine the CAS abundance of individual components within a petrographic context. Micro X-Ray Fluorescence (μ-XRF) imaging and X-Ray Absorption Near Edge Structure (XANES) spectroscopy make possible the non-destructive detection of low abundance S-species at micrometer-scale spatial resolution within a petrographic context. S-species have a wide range of oxidation states that corresponds to ~14 eV range of absorption edge energies in XANES spectroscopy (Hedman et al., 1986), providing an ideal platform for multi-energy μ-XRF imaging that an distinguish among the various S species. Coordination with petrographic observations allows for identification of primary and diagenetic components. Initial investigations by Rose et al. (in review) indicate sulfate abundance is spatially variable within an individual Ordovician carbonate thin section, with CAS abundance ranging from ~10 to 200 ppm. The study identified multiple sulfate moieties using XANES spectroscopy, showing that sulfate is present both as organic esters and in two inorganic phases, each likely associated with distinct carbonate lattice structures. The present study expands on this earlier work by combining petrographic observations, μ-XRF imaging, and XANES spectroscopy on multiple samples from a range of lithofacies from Anticosti Island, Canada and Gotland, Sweden (Figure 4.1). The samples from these localities were chosen as they span critical periods of Earth history with known biological turnover (End-Ordovician mass extinction and the mid-Silurian Ireviken Bioevent; IBE), climate change, glacioeustatic sea level change and well-documented perturbations to the global carbon cycle. These samples are well characterized in terms of broad sedimentology and stratigraphy, geochemistry and bulk carbon and sulfur isotopes (Jones and Fike, 2013; Present et al., 2015; Rose et al., 2019). This approach assesses the dominant sulfur species and how they vary among lithofacies and between primary and diagenetic carbonate phases. We present a subset of μ-XRF images and XANES spectra from Ordovician and Silurian carbonate samples that we have generated.

Here we show a model for the source, incorporation and preservation of S-species in primary carbonate (fossils), the source and preservation of sulfur during lithification and early diagenesis (formation of cement and micrite), and the fate of the S-species during post-depositional, late-stage alteration (e.g., replacement of fossils, carbonate mineral neomorphism). Such insights at the micron scale will aid our understanding and interpretations of bulk chemostratigraphic data, where biogeochemical proxies ultimately may reflect local, facies-dependent controls superimposed on any basinal or global signatures.

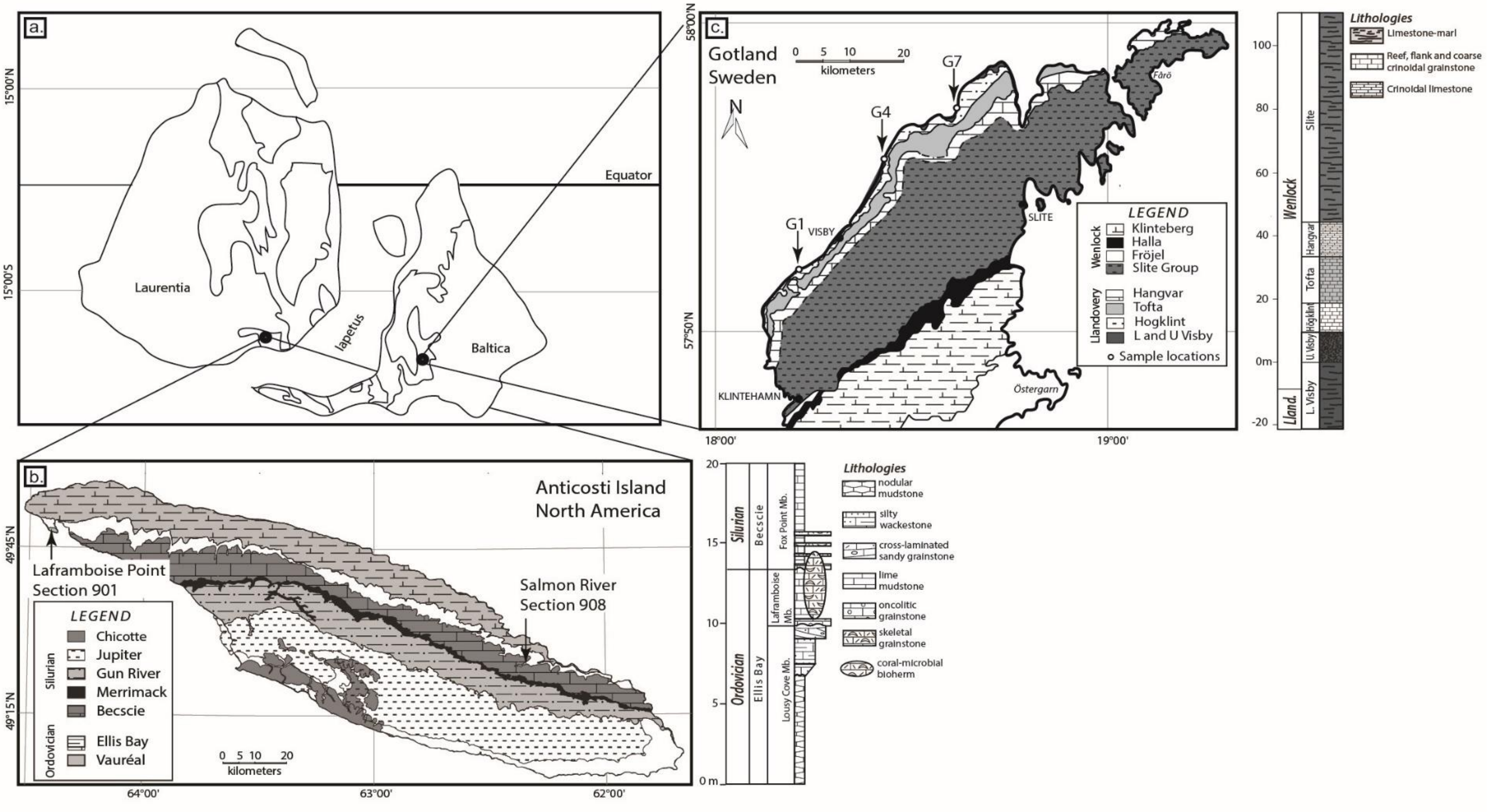

Figure 4.1 – a.) Paleogeographic reconstruction of Laurentia and Baltica at the Ordovician-Silurian boundary (~ 440 Ma) including locations of Anticosti Island and Gotland. Modified from Cocks and Torsvik, (2002) b.) geologic map of Anticosti Island with sample locations annotated. A generalized stratigraphic section is shown on the left (modified from Jones et al., 2011 and Jones and Fike 2013) and c.) geologic map of Gotland with sample locations annotated including a generalized stratigraphic section on the left (modified from Rose et al., 2019).

4.3 Materials and Methods

4.3.1 Samples

Anticosti Island, Quebec, Canada (Figure 4.1), represents a storm-dominated carbonate platform, with 200 km of E-W trending, well-exposed strata that has experienced minimal structural deformation. Strata on the north of Anticosti are Hirnantian, ~ 444 Ma, and young to the south (Desrochers et al., 2010; Long and Copper, 1987). The Ordovician and Silurian carbonate rocks on Anticosti Island dip to the south west and have been buried to depths within the oil window (Desrochers et al., 2010; Jones et al., 2011; Pinet and Lavoie, 2007). Late-stage diagenesis and fluid migration has not appreciably affected the abundance and isotopes of sulfate or sulfide (Jones and Fike, 2013). Samples in this study from Anticosti span a range of shallow-water carbonate lithofacies corresponding to the latest Hirnantian, associated with the end-Ordovician mass extinction, a well-documented global C-isotope excursion, and glaciation that is expressed as a shallowing-upward facies transition (Jones et al., 2011; Jones and Fike, 2013). The samples presented are sourced from the Lousy Cove and Laframboise members of the Ellis Bay Formation, from Laframboise point (section 901) and Salmon River (section 908) (Fig 1b; Jones et al., 2011).

Gotland, Sweden (Figure 4.1), represents numerous stacked carbonate platforms that formed in the Baltoscandian basin during the Silurian. Strata are the oldest in the northwest of Gotland, with progressively younger strata to the south. The carbonate strata on Gotland are minimally thermally and tectonically altered (Jeppsson, 1983) and bulk geochemistry shows little broad-scale resetting of isotope proxies (Rose et al., 2019). Here, Gotland samples are from the early Wenlock (~ 428 Ma) and consist of shallow-water carbonates that span the Ireviken Bioevent (IBE) and a well-defined global C-isotope excursion coincident with a facies change that represents marine regression and a cooling climate (Lehnert et al., 2010; Munnecke et al., 2010, 2003). The samples were sourced from numerous sections along the northern edge of Gotland from the Lower Visby, Upper Visby and Tofa formations (sections G1, G4 and G7; Figure 4.1c; Rose et al., 2019).

4.3.2 Methods

Synchrotron analyses were performed around the S K-edge (2472 eV) at the GeoSoilEnviroCARS (GSECARS) beamline 13-ID-E at the Advanced Photon Source (APS) at Argonne National Laboratory and beamline 14-3 at the Stanford Synchrotron Radiation Lightsource (SSRL), SLAC National Accelerator Laboratory. Detailed beamline configurations and measurement approaches have been described previously (Rose et al., in review). Both the APS 13-ID-E and SSRL 14-3 beamlines utilize Kirkpatrick-Baez mirror focusing for μ-XRF and XANES data collection. At both facilities, the sample environment is a helium-purged chamber. The apparent S K-edge differs slightly between APS and SSRL due to monochromator calibration and, as such, the energy scales for XANES spectra were adjusted to the SSRL reference line. There were also differences in data collection because of distinct facility characteristics. At APS, the energy was calibrated using an anhydrite standard that provides a maximum intensity white line at ~ 2481.5 eV. For the APS analyses, the pitch of the focusing mirrors was slightly decreased, thus, the monochromatized X-ray beam contained a small component of 3rd order harmonic (i.e., X-ray photons with energies near 7500 eV). This adjustment allowed for the ability to generate spatial distribution maps of elements with absorption edges higher than that of the S K-edge at ~2472 eV (e.g. Mn, Fe). At the APS, maps representative of the distribution of sulfide and sulfate were generated by collecting data at energies corresponding to the highest absorption for each species (2471 eV and 2482 eV respectively; Figure 4.2). Maps of total sulfur were also generated at 2550 eV, well above the absorption edge energy. As part of the data correction, sulfide fluorescence that occurred when mapping at the sulfate excitation energy has been removed from all of the sulfate energy maps presented here (using the MicroAnalysis Toolkit (Webb et al., 2011)) and GSE Mapviewer (Newville, 2013)). All maps are normalized to the edge-step and are scaled to the same total S counts, such that the white pixels on each map that represent maximum counts, correspond to the same number of counts across each map. XANES spectra were collected at the APS to verify sulfur speciation at locations identified during mapping.

The optics at SSRL BL 14-3 were tuned to reduce higher-order harmonics, so only S-species were imaged. The energy was calibrated to the S K-edge at 2472.2 eV using a sodium thiosulfate powder. Maps were collected at more energies to allow for detection and differentiation of less abundant S-species and structural changes to the sulfate ion. Multi-energy maps were collected at 2472.0, 2476.3, 2482.1, 2482.3, 2482.5, 2482.65, 2482.8 and 2483.2 eV in order to distinguish subtle differences in the K-edge spectra of sulfate moieties. A greater number of XANES spectra were collected on each mapped region at SSRL. A principal component analysis was performed on the XANES dataset from each region (Sixpack; Webb, 2005). Using these analyses, component score plots (where one component is plotted against another component) were used to identify the XANES spectra that are the most different from one another, but together encompass the entire variation of the XANES dataset for the given region. Spatial distribution maps of the energy of maximum intensity in the end-member XANES spectra, such as co-occurring sulfide and sulfate or organic sulfur compounds (OSCs), are generated by performing a least-squares XANES fitting of the end-member spectra to the original multi-energy maps (Farfan et al., 2018; Mayhew et al., 2011). That is, the normalized fluorescence intensity of a given end-member spectra is determined for each of the multi-energies that was mapped. A least-squares fitting of the normalized fluorescence intensity is applied to each pixel using the data collected at the same pixel in the multi-energy map, generating an abundance map of the given end-member spectrum.

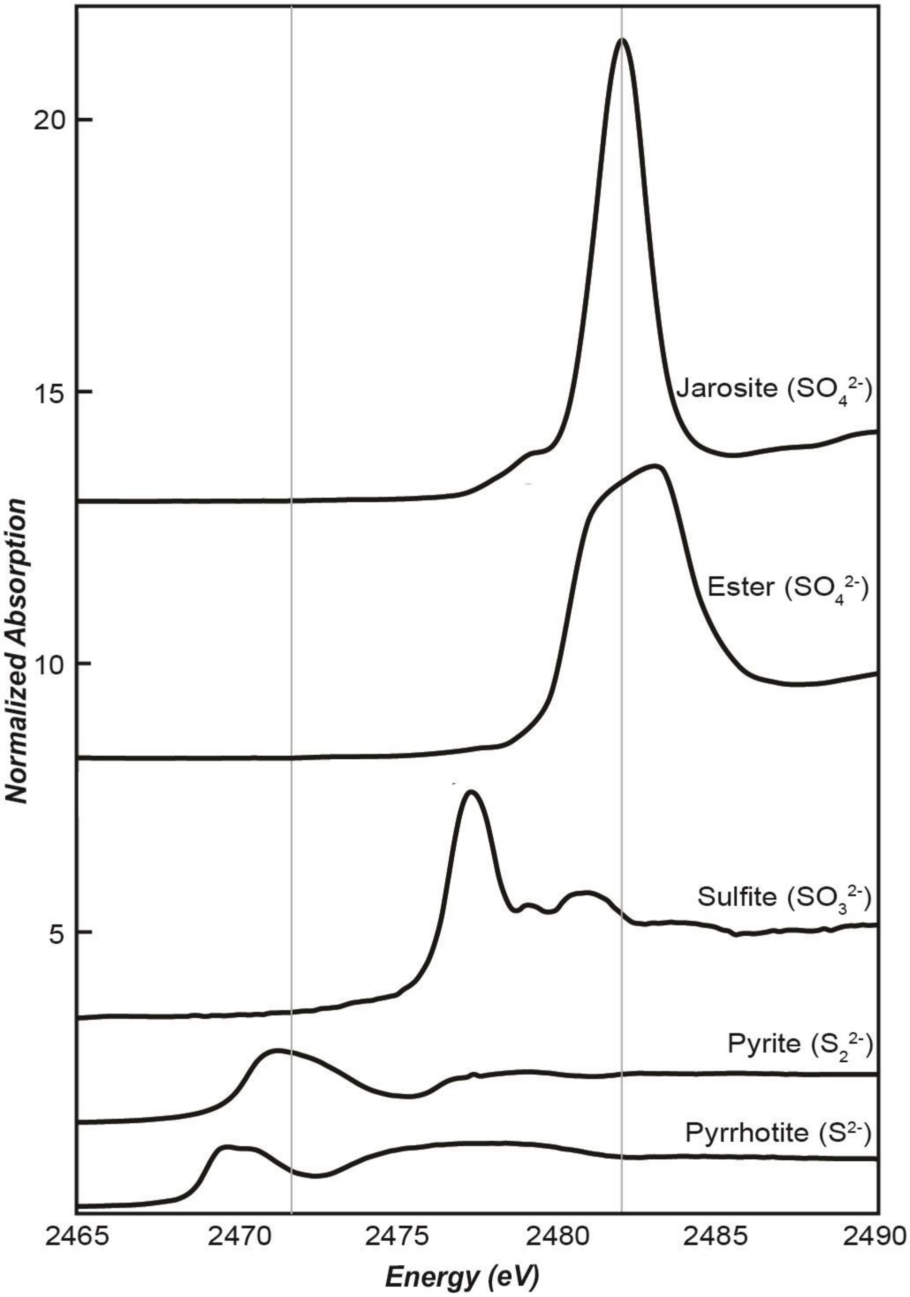

Figure 4.2 – Standard XANES of common sulfur species in the S K-edge region obtained at BL 13-ID-E. Pyrite standard from Konecke et al. (2017) and chondroitin sulfate (ester) standard from the ESRF ID-21 S XANES spectra database (Cuif et al., 2003).

4.4 Results

4.4.1 Fossils and Grains

Fossils show variation in sulfate abundance between different phyla or classes (Figure 4.3), as well as within certain phyla (e.g. brachiopods, Figure 4.4c and 4d). Abiotic grains also differ in sulfate abundance between grains as seen in Figures 4.3b and 4.3c, which correspond to different locations within the same thin section. These regions were mapped consecutively during the same analytical session so there were no differences in beam characteristics. During the Ordovician and Silurian, the major reef builders were tabulate (e.g. *Coenites sp.*, C in Figure 4.3a) and rugose corals (RU; Figure 4.3c), and stromatoporoids. Other important biomineralizers include brachiopods (B; Figure 4.4d), bryozoans (BRY; Figure 4.4a), crinoids (Figure 4.5a) and ostracods (Scholle and Ulmer-Scholle, 2003). Bivalves and gastropods make up a large proportion of unidentified fossil fragments throughout the Phanerozoic, evident in the Ordovician grainstone samples studied here (Figure 4.3b and 3.3c).

Tabulate and rugose corals are present in all studied packstone and grainstone facies from Anticosti Island and Gotland. Corals in these samples always consist of both micrite, from infilling or micritization, and recrystallized calcite. *Coenites sp.* (Figure 4.3a) is a branching tabulate coral that makes up the centre of oncoids in a poorly washed fossiliferous grainstone from the Upper Visby Formation on Gotland (platform interior shoal facies). In this sample, *Coenites sp.* is associated with *Allonema sp.*, a calcareous encrusting problematica (Jarochowska and Munnecke, 2014) (Figure 4.3a, inset), forming an oncoid. *Allonema sp.* is predominantly preserved as micrite, with small recrystallized vesicles of the original *Allonema* structure. The main S-species in the micrite of *Allonema sp.* is sulfide (Figure 4.3d, XANES spectrum 5) as well as the detection of thiol (XANES spectrum 4), determined by peak shape and position. The recrystallized vesicles within the micrite show localized increases in sulfate content (Figure 4.3a and 4.3d, XANES spectrum 1). These vesicles lack sulfide but do contain low abundances of thiol/thioether and sulfite (2473.2 and 2477.8 eV respectively) (Almkvist et al., 2010). Variation in the intensity of the thiol/thioether and sulfite peak occurs within the micrite in the centre of *Coenites sp.* (Figure 4.3a and 3.3d, XANES spectra 2 and 3).

The oncolite grainstone from the La Framboise Member on Anticosti Island (Figure 4.1b), deposited in the platform interior as coarse reef-debris facies, contains high proportions of bioclast fragments and lithoclasts that show strong variations in sulfate abundance across the sample (Figure 4.3b and 3.3c). Bioclasts are commonly recrystallized (RC), surrounded by micritic envelopes (ME), or fully micritized (MB; Figure 4.3b and 3.3c). Micritic lithoclasts (M), micrite envelopes, and micritized bioclasts frequently contain signals from both sulfide and sulfate within a given location (Figure 4.3d XANES spectra 8 and 11). Additionally, XANES spectroscopy detects a subtle shift in the maximum energy of the inorganic sulfate peak from 2482.3 to 2482.6 eV between different bioclast fragments in the oncolite grainstone (Figures 4.3b and 4.3d, XANES spectra 6, 7 and 9). Figure 4.3c hosts a large solitary rugose coral (RU) where the fossilized calyx and septa are micrite, and the dissepiments are filled with recrystallized calcite. The sulfate abundance is greatest in the preserved skeleton, now micrite, whereas sulfate abundance is very low in the recrystallized dissepiments. The micrite in the mold of the rugose coral contains strong signals for inorganic sulfate, consistent with CAS, with no interference from sulfide. Brachiopods contain the highest concentration of sulfate of all fossils studied (Figures 4.4c and 4.4d), whereas well-preserved bryozoans also contain high abundances of sulfate (Figure 4.4a).

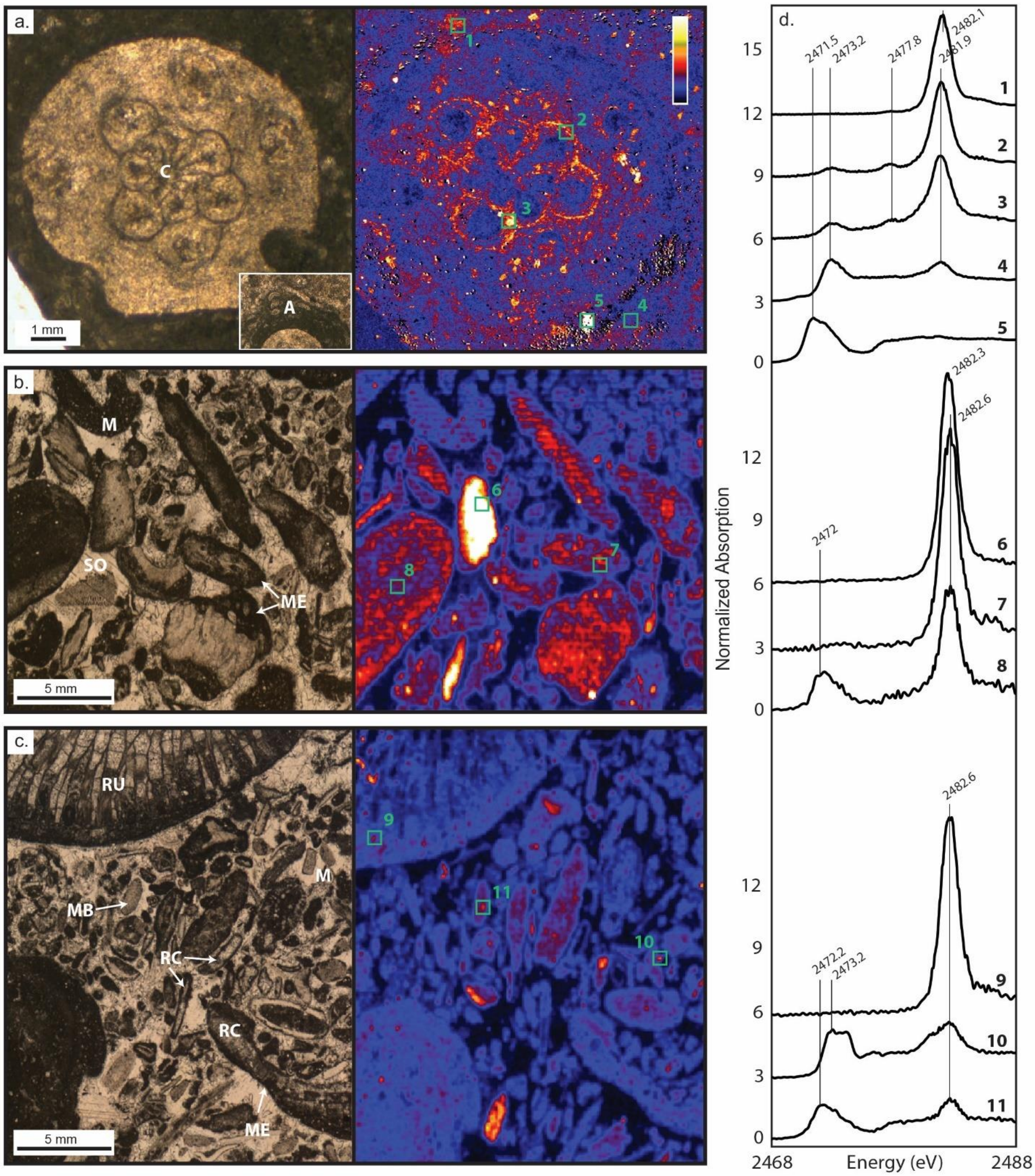

Figure 4.3 – Photomicrographs showing a variety of fossils, fossil fragments and grains with corresponding sulfate energy map (sulfide subtracted) on the right. A = *Allonema*, C = *Coenites sp*., M = micrite infilling, ME = micrite envelope, SO = syntaxial overgrowth, MB = micritized bioclast, RU = Rugose, RC = recrystallized centre. Map colors correspond to abundance where black is minimum and white is maximum abundance (applies to all maps) a.) *Coenites sp*., with *Allonema* (inset) from a coral grainstone from the Upper Visby Formation, Gotland b.) Fossiliferous grainstone from an oncolite platform, Lousy Cove Member, Anticosti Island c.) another region of sample in b. where the high sulfate bioclasts are similar to

the high sulfate bioclast in b, and d.) XANES of locations numbered in a-c with important peak energies annotated.

4.4.2 Cement

Sulfides are generally less abundant in cement when compared to micrite (Figure 4.4 vs. Figure 4.5). Figure 4.4 depicts a variety of cements from packstone and grainstone facies. The microfacies of the Lousy Cove Member of the Hirnantian-aged Ellis Bay Formation on Anticosti Island (Figure 4.1b and 4a; Jones et al., 2011) indicate formation on the platform interior in an open marine environment. Similarly, the Lower Visby, Tofta and Hogklint formations of Gotland during the early Wenlock have platform interior (reef) and margin microfacies (Figures 3.1c, 3.4b, c and d). These samples (both Anticosti and Gotland) are from the rising limb of the C-isotope excursions at each locality, coincident with a lithofacies change reflecting marine regression.

Sulfate abundance in equant, blocky cement (BL) is usually near the detection limit (Figure 4.4a), although abundance is sometimes observed to increase at crystal boundaries. Syntaxial calcite overgrowths (SO), single calcite crystal overgrowths around a pre-existing grain (Figure 4.4b), are commonly formed over echinoderm fragments (here crinoid fragments) of high-Mg calcite (Christ et al., 2015; Flügel and Munnecke, 2010). The sulfate abundance in syntaxial cement varies relative to the crinoid fragment underneath (Figure 4.4b showing both lower abundance (right) and similar or greater abundance (left) of sulfate). Drusy cements (DR) are characteristically pore-filling cements where the crystal size of the cement increases towards the center of the pore (Flügel and Munnecke, 2010; Figures 3.4c and 3.4d). Drusy cements are observed here to have higher sulfate concentrations than blocky cements; further, the CAS abundances increase toward the center of these cements.

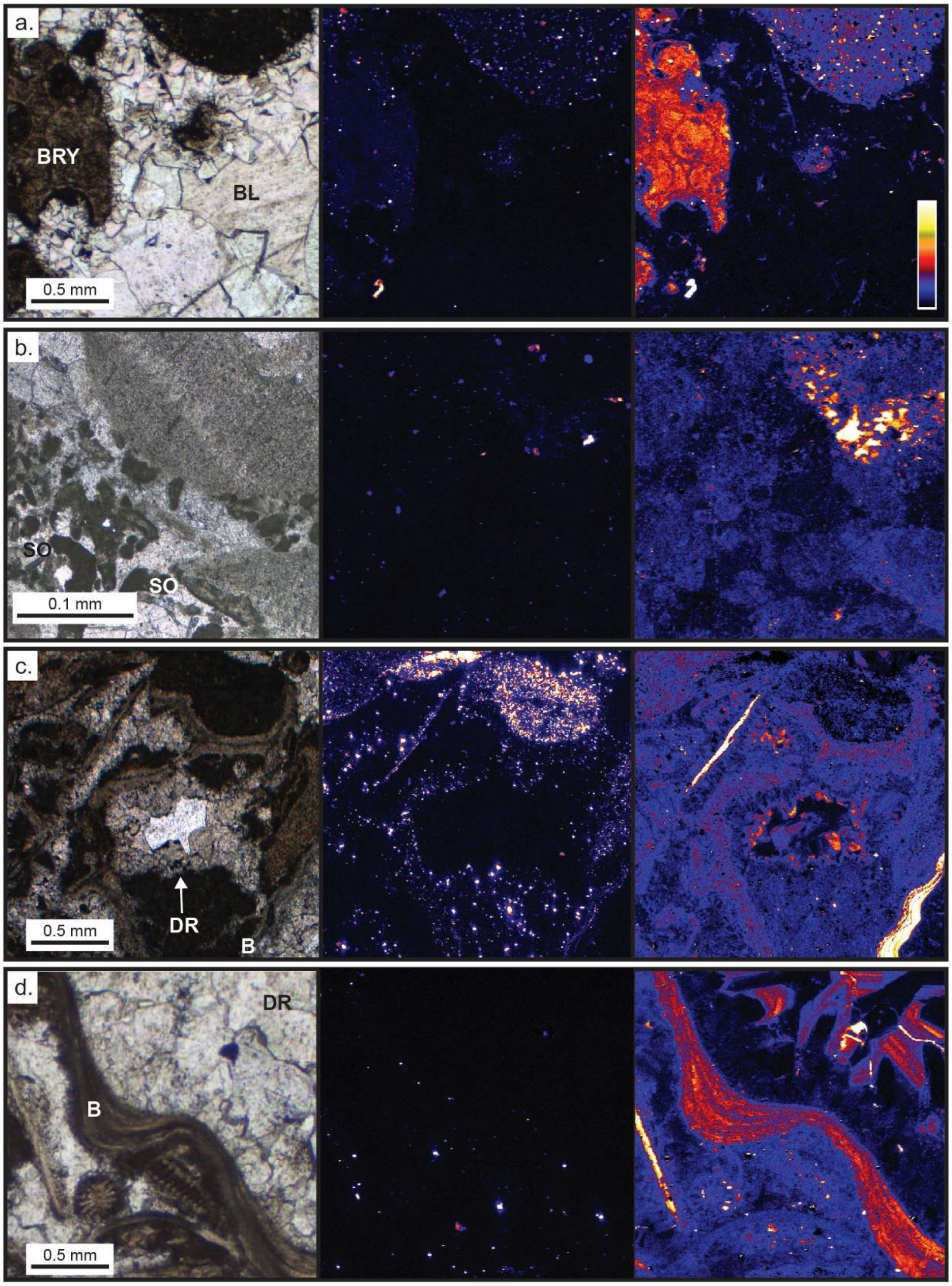

Figure 4.4 – Photomicrographs (left) showing a variety of cement fabrics as interstitial cement and diagenetic features with corresponding sulfide (centre) and sulfate (right; sulfide removed) energy maps for each panel. BL = blocky, DR = drusy, SO = syntaxial overgrowth, B = brachiopod and BRY = bryozoan a.) petrographic thin section image of intra-hermal sample, Lousy Cove Member, Anticosti Island, b.) bioclastic grainstone from the Lower Tofta Formation, Gotland, c.) poorly washed fossiliferous grainstone from the Upper Visby Formation, Gotland, d.) brachiopodal grainstone from Gotland.

4.4.3 Micrite

Micrite is fine-grained carbonate and is a major interstitial component of mudstone, wackestone, and packstone facies. Micrite contains the highest abundance of sulfide compared to the other carbonate components. Figure 4.5a is a wackestone from the Lousy Cove Member on Anticosti Island (Fig 1b). Microfacies observations indicate that the depositional environment was a shallow platform-margin reef. The sulfide map (Figure 4.5b) shows finely disseminated sulfide throughout the micrite, and to a lesser extent within the micritized crinoid fragments. This sulfide is observed in all samples analysed that have interstitial and micritized fossil fragments, and is mostly pyrite, determined through a correlation with Fe abundance maps and XANES spectra. In addition, there are isolated sulfate phases within the micrite (Figure 4.5c). Moreover, a majority of the sulfides have been partially oxidized, contributing to the sulfate signal (Figure 4.5d), which is confirmed by XANES spectroscopy, showing both sulfide and sulfate peaks present at one location (Figure 4.5e). The intensity of co-occuring sulfide and sulfate peaks vary, indicative of differing amounts of oxidation across the sample. There are few spectra from this region with a sulfate signal without accompanying sulfide, and, where they do occur, they are associated with a low sulfate background within crinoid fragments (Figure 4.5e, location 5). Micrite is also present in grainstone samples, where it is observed in lithoclasts, oncolitic and cortoid grains as micritic envelopes, and calcareous algae and cyanobacteria, where again sulfides are abundant.

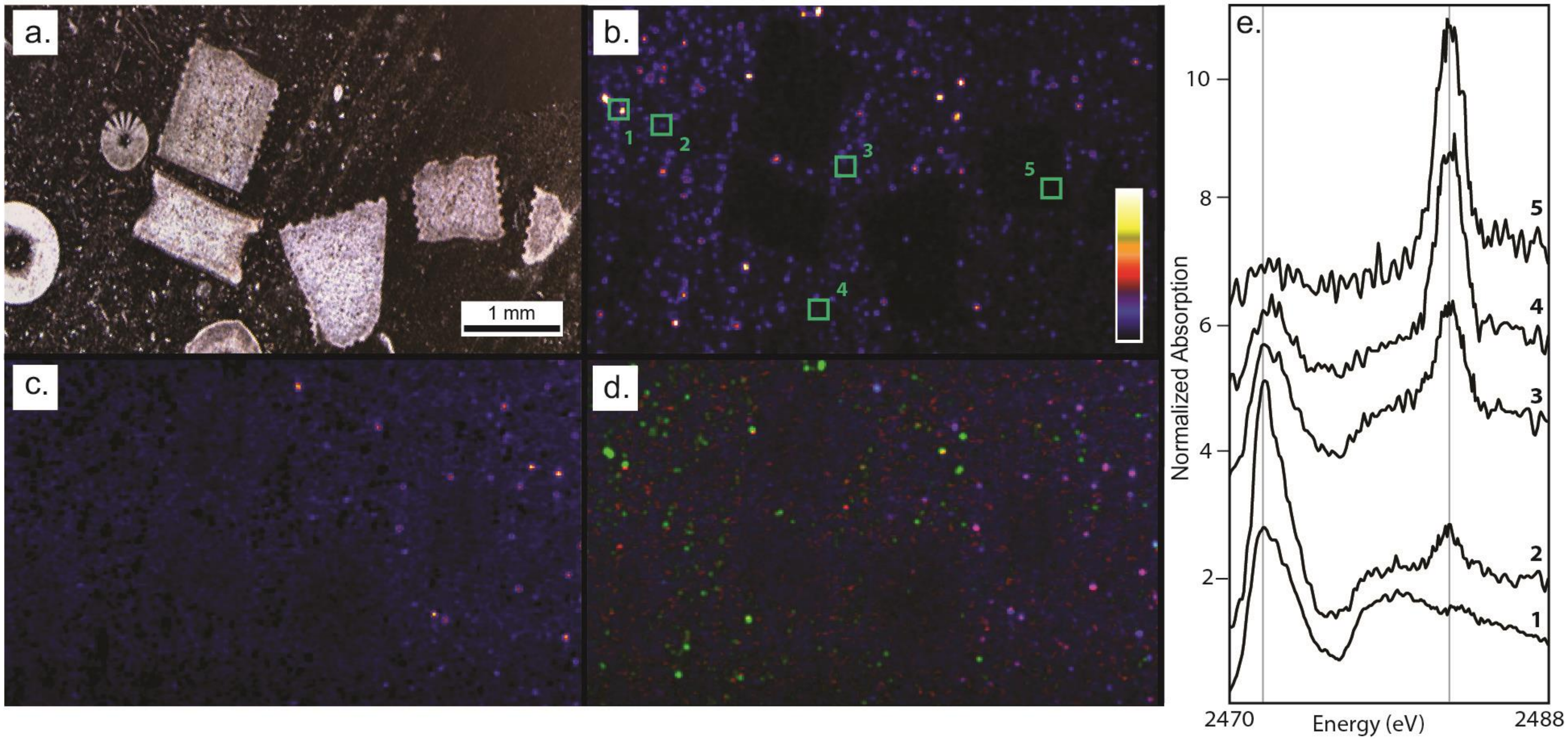

Figure 4.5 – a.) Photomicrograph of a crinoidal wackestone Lousy Cove Member, Anticosti Island. b.) sulfide energy map (2472.0 eV) of (a); numbers depict representative XANES spectra. c) map of sulfate energy (2482.3 eV with sulfide interference removed), d.) tricolor map where red = oxidized sulfide, blue = sulfate, and green = sulfide, purple is where both sulfate and oxidized sulfide co-occur; e.) XANES of micrite and crinoid fragments labelled in b. XANES 1, 3 and 5 are the end-member XANES used to perform fitting, generating maps at the exact energies corresponding to the maximum intensity. Dashed lines at 2472 and 2482 represent the approximate white line of sulfide and sulfate, respectively.

4.5 Discussion

4.5.1 Preservation of primary seawater sulfate signal in fossils

Primary carbonate components are those that precipitate within seawater, or within sediment that is in open connectivity with seawater (e.g. deep-water facies; Claypool, 2004; Richardson et al., 2019). Relatively little is known about the biological incorporation of sulfate into carbonate, and whether the mechanism is ambient incorporation, akin to that for inorganic carbonate (Busenberg and Plummer, 1985; Staudt et al., 1994), or if there is a biological control and/or source during incorporation (Burdett et al., 1989; Cuif et al., 2003; Cusack et al., 2008; Yoshimura et al., 2013). The majority of carbonate cementation occurs in the subsurface, usually within the first few mm (Flügel and Munnecke, 2010) and are not considered primary. Although some carbonate may precipitate directly on the seafloor, there is no evidence for seafloor encrustations in these samples. The origin and formation of micrite can occur via multiple pathways: authigenic precipitation within the water column or in the sediment (automicrite), physical or chemical breakdown of skeletal fragments or calcareous algae (allomicrite), and diagenetically through recrystallization (diagenetic micrite and microspar; Flügel and Munnecke, 2010). As such, fossils are the only component derived directly from local ambient seawater in these samples and we, thus, focus our discussion of sulfate variability in preserved primary fossil fabrics. The fate of sulfate during diagenesis of primary carbonate (e.g. micritization of fossils) is discussed in sections 3.5.2 and 3.5.3.

Few fossils retain their primary carbonate mineralogy and fabric over geologic time. Brachiopods, however, are commonly robust to recrystallization owing to the multi-layered low-Mg calcite shell of articulate brachiopods (Lowenstam, 1961). The abundance of sulfate within brachiopod shells is the highest of all components analysed. The sulfate abundance appears banded, correlating to the primary brachiopod structure (Figures 3.4c and 3.4d) where calcite crystals are oriented obliquely to the shell edge. Such high-resolution mapping of sulfate within brachiopods has not been shown before. In the extant brachiopod *Terebratulina retusa*, sulfate abundance is greatest in the primary (outer) layer of the shell coincident with increased Mg abundance and, although sulfate is present in the secondary fibrous layer, it is lower in abundance and is surrounded by thiols (Cusack et al., 2008). This prior work was unable to determine if sulfate-bearing polysaccharides were the source of the sulfate in the primary layer or what contributed to differences in the sulfate abundance between the primary and secondary layers. Here, we are unable to differentiate between the primary and secondary layers in the petrographic thin sections. However, the μ-XRF maps do not show gradients across the shell in sulfate abundance, implying that these species do not contain obvious differences between the primary and secondary layers and differences are not resolvable at this scale, or that the primary layer in these specimens was not preserved. XANES spectra within the brachiopods indicate that inorganic sulfate comprises the vast majority of sulfate. It has been suggested that brachiopods may preserve a more faithful record of CAS abundance and $\delta^{34}S_{CAS}$ due to the resistance of the primary brachiopod shell structure to recrystallization (Kampschulte and Strauss, 2004; Present et al., 2015). The detailed preservation of brachiopods here, combined with the maps showing sulfate variability within the shell fabric and XANES spectra characteristic of inorganic sulfate, indicate that brachiopods could be an archive of primary CAS.

Like brachiopods, well-preserved bryozoans contain a high abundance of sulfate (Figure 4.4a). There are few previous studies of CAS in bryozoans, but extant bryozoans contain > 5000 ppm sulfate (Staudt and Schoonen, 1995) and micro-drilling of Ordovician-aged bryozoans from Anticosti Island indicates that their sulfate content is ~500 ppm, within a similar range of coeval brachiopods (Present et al., 2015). The detailed preservation of the bryozoan, and its sulfate content, suggests this may also be a potentially primary sulfate signal (Figure 4.4a). Fossil bryozoa, especially those from the family Stenolaemata (common in Ordovician and Silurian carbonate strata; Ernst and Munnecke, 2009) form their exoskeleton from low-Mg calcite. This could mean that fossil bryozoan, like brachiopods, are similarly robust to diagenetic recrystallization (Smith et al., 2006). However, the observed difference in magnitude in concentration between extant and fossil bryozoans could indicate partial loss of sulfate during diagenesis, perhaps pertaining to greater porosity and permeability of bryozoan exoskeletons when compared to brachiopods. This difference in sulfate requires further investigation, including isotopic studies, to determine whether bryozoans may be a faithful archive of CAS, that can corroborate brachiopod evidence, or provide data where brachiopods are absent. Generally, all other fossils in these samples have been replaced by micrite and/or cement, where the sulfate abundance may be compromised by post-depositional alteration.

4.5.2 Lithification and Early Marine Diagenesis

Carbonate cementation is an essential part in lithification and studying the resulting cements can be informative about their history of formation and subsequent diagenesis due to the variety of morphologies and fabrics formed. Equant blocky fabrics (Figure 4.4a) suggest there was recrystallization of pre-existing cement in meteoric or burial environments (Flügel and Munnecke, 2010). The low sulfate concentration in the cement in Figure 4.4a indicates that the diagenetic fluid causing recrystallization must also have been low in sulfate, such as meteoric or sulfate-poor porewaters, likely precluding a basinal fluid. Fe and Mn abundance maps do not show elevated abundance in the cements (Figure 4.6), which are anticipated to increase during recrystallization in contact with anoxic fluids (Brand and Veizer, 1980). Sedimentary porewaters may evolve under closed-system conditions, where sulfate in the porewater is used up by microbial sulfate reduction

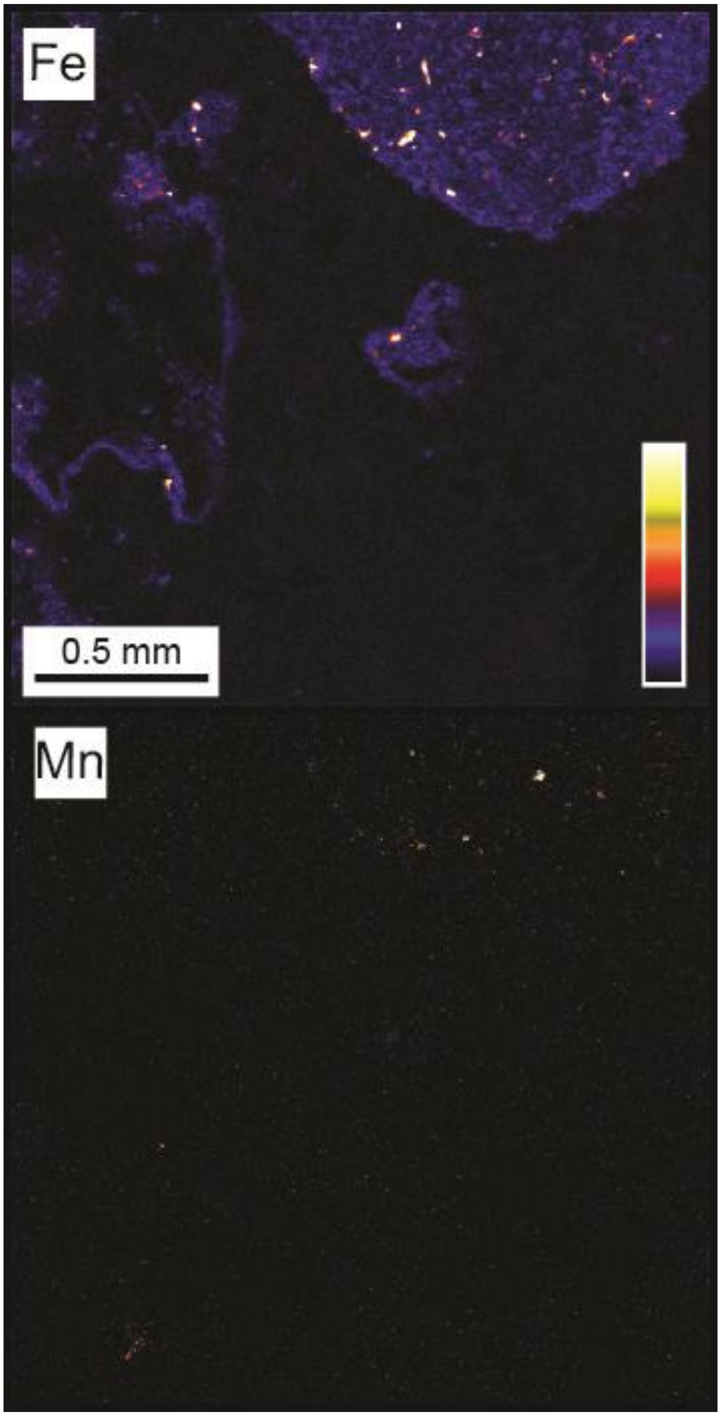

Figure 4.6 – Fe (left) and Mn (right) energy maps of intra-hermal sample, Lousy Cove Member, Anticosti Island in Figure 4.4a.

(MSR) more rapidly than it is replenished by diffusion from the overlying seawater. Such closed-system conditions occur preferentially in shallow-water environments due to increased sedimentation rates and increased labile organic carbon and Fe abundance (Aller et al., 2010; Fike et al., 2015; Toth and Lerman, 1977). Together these observations indicate that equant cements formed below the region where porewaters retained substantial sulfate or precipitated at a slow enough rate that resulted in inefficient incorporation of sulfate into the carbonate lattice (Busenberg and Plummer, 1985; Kile et al., 2000).

‘Cloudy’ syntaxial cement (Figure 4.4b) is indicative of meteoric or early, shallow marine diagenesis (Walker et al., 1990). Due to the moderate abundance of sulfate, meteoric diagenesis is deemed unlikely, thus the formation of the syntaxial overgrowth is likely early diagenetic. Sulfate abundance in the syntaxial cement is usually greater than the blocky cement in Figure 4.4a. The higher abundance of sulfate in the syntaxial overgrowth could reflect the resupply of porewater sulfate for example, by tidal pumping (Aller et al., 2010) and/or faster rates of crystal growth . A tidal influence is consistent with thin-section observations of a change to smaller and more abundant fossil fragments and an increase in lithoclasts associated with the presence of syntaxial overgrowths.

During the Ordovician and Silurian, drusy pore-filling cements are commonly of early marine origin (Figures 4.4c and 4.4d) (Christ et al., 2015) due to the lower Mg/Ca ratio of seawater causing more rapid growth along the *a* and *b* crystallographic axes, resulting in complex polyhedral crystal habits (Folk, 1965). Evolution of the sulfate concentration in porewater is likely to occur as a result of progressive MSR, where [SO_4^{2-}] decreases with increasing depth in the sediment (Figure 4.7). MSR increases alkalinity, and ultimately encourages carbonate precipitation in pore spaces with depth in the sediment (Baumgartner et al., 2006; Berner et al., 1970). Increased carbonate supersaturation in turn causes an increase in the rate of carbonate precipitation (Langdon et al., 2000). Busenberg and Plummer (1985) found that the rate of carbonate growth increases the distribution coefficient of sulfate into calcite, i.e. as the rate of crystal growth increases, so does the amount of sulfate substituted into the mineral. Thus, in a setting of increased and more rapid calcite precipitation, CAS abundance should increase (in accordance with Busenberg and Plummer, 1985). However, CAS abundance should also scale with SO_4^{2-}:CO_3^{2-} ratio. As such, for CAS abundance to increase as MSR decreases SO_4^{2-} availability, the rate of precipitation would need to be sufficient to offset the decreasing SO_4^{2-}:CO_3^{2-} ratio.

The variability in CAS within single crystals of drusy cements can be explained by sector zoning. It has been demonstrated that surface topography of calcite can induce SO_4^{2-} sectoral and intra-sectoral zoning within the mineral structure (Staudt et al., 1994). The effective partition co-efficient of sulfate into calcite depends on mechanistic properties of incorporation and surface structural controls (spiral growth vs. linear attachment) (Staudt et al., 1994). Thus, it is possible that cements in these thin sections have recorded and preserved structural properties during precipitation that may have affected the effective partition co-efficient within a given crystal, resulting in the observed CAS variability in a single cement crystal. Although it is uncommon for studies to target only cement components, these findings have implications for bulk $\delta^{34}S_{CAS}$ records that will homogenize variable amounts of different cement morphologies based on the lithofacies, ultimately masking and/or muting the primary $\delta^{34}S_{CAS}$ signal. This is likely to contribute to the inherent variability in most ancient $\delta^{34}S_{CAS}$ records, where the changes occur too rapidly with respect to the residence time of seawater sulfate and thus cannot reflect changes to the global sulfur cycle. Although such variability may sometimes be interpreted as transient perturbations to the local sulfur cycle, our findings suggest this may also be explained by changes in the carbonate lithofacies. We anticipate such phase-specific sulfate variability is found in all carbonate rocks and the unique micron-scale environmental signatures are lost by averaging components.

Allomicrite, common in shallow-water carbonates studied here (Figure 4.5), has a higher proportion of pyrite than automicrite (e.g. micrite clasts in Figure 4.4b). This increase may result from an influx of organic matter during fossil breakdown, promoting MSR by increasing the availability of labile organic carbon (Leavitt et al., 2013; Sim et al., 2011). Any newly produced sulfide could form pyrite if the environment is not Fe limited. Sulfate abundance is low (< 100 ppm) in all micrite analyzed. This observation could be due to the sulfate-limited environment resulting from increased MSR and/or a result of the generally high abundance of silicate minerals and Fe within micrite (Rose et al., in review), essentially diluting the abundance of sulfate contained within the fine-grained fossil fragments. The high abundance of sulfide present in micrite is most likely an observation that will apply to micrite precipitated in various locations throughout Earth History. We suggest this high abundance of sulfide is due to the increased surface area where there may be increased availability of iron and organic carbon (to fuel MSR) due to surface sorption.

4.5.3 Preservation of organic sulfur compounds

XANES spectroscopy has previously been used to assess the occurrence of organic sulfur compounds (OSCs) in ancient carbonates. For example, Rose et al. (in review) document the presence of sulfate esters within a series of Upper Ordovician carbonates. Cuif et al. (2003) measure sulfate within corals and infer these to be in the form of sulfate esters. Because this sulfate dominated in the calcification centres and fibres within the septa of Scleractinian corals

Montastrea, *Favia* and *Lophelia*, Cuif et al. (2003) infer that sulfate esters (chondroitin sulfate) are very important in the biomineralization process of these genera. However, XANES spectra in each of the Scleractinia lack the characteristic ‘shoulder’ (additional peak) of a sulfate ester (Almkvist et al., 2010) and look strikingly similar to XANES spectrum herein determined to be inorganic sulfate. Dauphin et al., (2003) similarly conclude that chondroitin sulfate is present in the mollusc shells *Pinna* and *Pinctada* despite the XANES spectra lacking the shoulder of an ester sulfate. In contrast, XANES investigations of *Corallium* (Tamenori et al., 2014; Perrin et al., 2017), a deep-water coral, show inorganic sulfate and a weak sulfite signal within the calcite skeleton. XANES spectra of co-occurring organic tissue in the calcite skeleton of *Corallium* contained multiple organic S species including disulfide, thioether, sulfoxide, sulfone, and sulfate, while Mg-calcite sclerites from within the tissue contain thioether and sulfate (Tamenori et al., 2014; Perrin et al., 2017). The similarity between XANES spectra in multiple species of *Corallium* and *Coenites sp.*, measured here (Figure 4.3d, spectra 1-5), indicate that the biomineralization pathway of some extinct tabulate corals may be comparable to that of *Corallium*. Understanding the biomineralization pathway of fossil species is extremely important to interpreting geochemical signals from carbonates, especially CAS. Insights from these modern and ancient coral species indicate numerous sources of S (beyond seawater sulfate) that may be incorporated into carbonate skeletons during growth and/or recrystallization. Other OSCs are found within micrite and micritic envelopes seldom associated with specific fossil groups (e.g. Figures 4.3a, c and d, XANES spectra 4 and 10) for the samples given here. This spatial independence makes it difficult to constrain early biomineralization pathways for all fossil groups. Additionally, upon traditional laboratory CAS extraction these compounds could be released, potentially contributing sulfate from multiple sources to the resulting bulk CAS signal and affecting geochemical proxies typically assumed to be sourced directly from seawater (e.g., [CAS] and $\delta^{34}S_{CAS}$).

4.5.4 Post-depositional Alteration

Unfortunately, there are currently no good constraints to determine the exact timing of formation of interstitial micrite and cements. As such, we limit discussion of post-depositional alteration to fossil micritization and recrystallization, replacement fabrics of cements, and oxidation of sulfide. Primary carbonate fabrics are commonly replaced in many bioclast fragments via micritization by algae or dissolution and re-precipitation of cement. Multiple secondary textures may be found within a single fossil: for example, the fossilized calyx and septa of the rugose coral in the Anticosti Island oncolite grainstone are micrite and the dissepiments contain recrystallized calcite (Figure 4.3c). Sulfate concentrations are highest in the micrite and very low in the recrystallized dissepiments, indicating this latter cement formed from meteoric fluid or evolved porewater lacking substantial residual sulfate. Additional peaks in the XANES spectra of the rugose coral (and *Coenites sp.* from Gotland; Figures 4.3a, c and d) indicate the presence of thiol/thioether and sulfite. This may suggest that low abundances of primary S-species were retained during dissolution of the primary carbonate due to the similarity of these spectra with prior reports (Perrin et al., 2017a; Tamenori et al., 2014). However, it is possible to generate intermediate valence S compounds as the result of X-ray irradiance. Specifically, there is evidence for beam-induced reduction of sulfate to sulfite within silicate glass (Wilke et al., 2008). Due to the low intensity of the sulfite peak, photoreduction of sulfate cannot be precluded as the source of the sulfite here. Sulfite in carbonates has been detected previously, thus, the samples here are not anomalous (Frisia et al., 2005; Perrin et al., 2017a). Additionally, the intensity of the sulfite peak varies within the given location (Figure 4.3d XANES 1-3) and is only rarely observed. Together these observations argue that the detection of sulfite is not an artefact (Perrin et al., 2017).

All bioclast fragments in Figure 4.3b (likely molluscs, corals and echinoderms, due to age, lack of preserved primary structure, and presence of syntaxial overgrowths) have a sulfate abundance greater than that of the surrounding cement, but the abundance is variable between the bioclasts. Two different sulfate phases are observed between the moderate sulfate-containing bioclasts and the highest sulfate-containing bioclast (center, Figure 4.3b); the energy of maximum intensity for the sulfate within the high-sulfate bioclast is at 2482.3 eV, which is downshifted from the sulfate contained within the other bioclasts in this region by 0.3 eV. This downshifting may correspond to differences in the lattice of the carbonate, i.e. the sulfate ion must change shape and lose symmetry in order to fit into the carbonate mineral phase (for primary aragonite or high-Mg calcite, Fernández-Díaz et al., 2010) resulting in a lower degeneracy of the sulfate orbital and therefore a slightly lower excitation energy relative to that for calcite (Cotton and Wilkinson, 1972; Pin et al., 2013). Although molluscs in this sample (predominantly gastropods and bivalves) may have made their shell structure out of aragonite, no aragonite is preserved. Echinoderms, however, generate their exoskeleton exclusively from high-Mg calcite (Flügel and Munnecke, 2010). Generally, high-Mg calcite will convert to low-Mg calcite over geologic time (due to diagenetic fluids removing Mg from the carbonate lattice), but the signal observed here indicates high-Mg calcite is preserved, likely in echinoderm fragments. The high sulfate abundance could reflect the amount of Mg in the calcite lattice, where increasing wt % Mg results in increased ability to incorporate sulfate, due to the smaller size of an Mg atom compared to Ca (Takano, 1985). The observation of sulfate abundance differences between high-Mg and low-Mg calcite bioclasts is an important finding as it indicates that the conversion from high- to low-Mg calcite on geologic timescales also results in the loss of primary sulfate.

As mentioned, sulfide is the dominant signal in all micrite components (interstitial, envelopes, clasts etc.). In all samples, numerous XANES spectra of sulfides within micrite show both sulfide and sulfate peaks (e.g. Figure 4.3d locations 8 and 11 and Figure 4.5e locations 2, 3 and 4), where the intensity of the sulfide and sulfate peaks vary between locations within a given sample. This observation is strong evidence for the pervasive impact of oxidation of sulfide on the abundance of sulfate in micritic components. Oxidation of sulfide may occur at any stage after early diagenetic pyrite formation in the presence of an oxic fluid. These observations are in agreement with micro-drilled data from micrites that show low, yet variable, concentrations of sulfate with large isotopic variation from Anticosti Island samples (Present et al., 2015). These findings indicate that apparent CAS in micrite from ancient shallow-water carbonates may not be a faithful archive of original seawater sulfate and, instead, is likely a mixture of early and late diagenetic sources of sulfate, potentially including a high proportion of sulfate sourced from the oxidation of local pyrite. These results potentially call into question studies that target micrite as a more faithful recorder of CAS (e.g. Kampschulte and Strauss 2004; Wotte et al., 2012), but corroborate the need for multiple salt rinses to remove secondary sulfate phases prior to bulk CAS extraction (Wotte et al., 2012) and also highlight the importance of a petrographic context.

4.5.5 Correlating micron-scale observations with bulk data

The spatial variability of sulfide and sulfate abundance within a given sample, and between samples of different lithofacies, correlates with the changing proportions of carbonate components, shallow-water deposition, and early marine diagenesis. This correlation agrees with interpretations of bulk S abundance and isotope data from Anticosti Island and Gotland that are interpreted to reflect local, depositional-dependent processes (Jones and Fike, 2013; Rose et al., 2019). The bulk S-isotope datasets exhibit large samples-to-sample variability (up to 9‰ on Anticosti Island and 6 to 7‰ on Gotland; Jones and Fike, 2013 and Rose et al., 2019, respectively), characteristic of many bulk deep-time CAS datasets (Edwards et al., 2018; Hurtgen et al., 2002; Kampschulte and Strauss, 2004; Osburn et al., 2015; Richardson et al., 2019; Ries et al., 2009; Thompson and Kah, 2012; Wotte et al., 2012b; Young et al., 2016). The carbonate strata from both localities record a paired $\delta^{13}C_{carb}$-$\delta^{13}C_{org}$ excursion, and where there is a coeval paired $\delta^{34}S_{CAS}$-$\delta^{34}S_{pyr}$ excursion on Gotland, a $\delta^{34}S_{CAS}$ excursion is absent on Anticosti Island. Commonly, a paired $\delta^{13}C_{carb}$-$\delta^{13}C_{org}$ and $\delta^{34}S_{CAS}$-$\delta^{34}S_{pyr}$ excursion in the rock record are explained by changes to the global sulfur cycle, such as increased pyrite burial. Time-correlative carbonates from within the same paleo-basin as Gotland do not show the same $\delta^{34}S_{CAS}$-$\delta^{34}S_{pyr}$ excursion (Richardson et al., 2019), indicating that the Gotland S-isotope data is locally controlled. Since the bulk sulfur isotopes from Anticosti Island and Gotland are not dominated by a global signal, we anticipate that variations in sulfate abundance in these samples is also not controlled by a changing sulfate concentration at this time. This study helps explain the origin of the stratigraphic scatter in bulk $\delta^{34}S_{CAS}$ data from Anticosti Island and Gotland by demonstrating the impact that depositional environment has on the abundance of CAS and pyrite at the micron scale within each carbonate component, and between the same carbonate components under changing litho- and microfacies.

The identification of variable sulfate abundance within a single sample can be explained by processes during lithification, early marine diagenesis, and post-depositional alteration (Figure 4.7). Initially, primary carbonate (as marine fauna) forms at the sediment water interface. During lithification, both blocky and drusy cement will form interstitial and pore-filling cements, and pyrite will form in the zone of sulfate reduction, provided a source of iron availability (Figure 4.7, panel a). These cements will precipitate anywhere below the sediment-water interface, however drusy cements tend to have a higher precipitation rate, and, as such may form in the zone of sulfate reduction where carbonate precipitation is promoted. The difference in precipitation rate between equant and drusy cements could result in increased incorporation of sulfate in drusy cement, or, equant cement could be forming below this region, where sulfate is less abundant or essentially absent as the result of progressive MSR. The difference in precipitation location between fossils and inorganic carbonate cements results in differences in the sulfate content of these components. This result is exemplified in the sulfate excitation map of a brachiopod and drusy cement from Gotland, where the brachiopod likely retains a primary seawater sulfate signature (Figure 4.7, panel b, left hand side).

During early marine diagenesis (Figure 4.7, panel b, right hand side), syntaxial cements may form when echinoderm fragments are within shallow depths of the sediment. Oxidation of pyrite may occur at any time after its formation, specifically in the presence of an oxic fluid and can occur syndepositionally (e.g., such as during early diagenetic reworking events that introduce oxygenated seawater deeper into the sediment; Figure 4.7, panel b) as well as during late-stage diagenesis after lithification and burial. Any time after lithification, bioclasts and older cements may dissolve, generating new pores which may be infilled with drusy or equant cement at any time, ultimately forming from a different source fluid (Figure 4.7, panel b, right hand side). This model has variable and changing abundance and δ^{34}S of SO_4^{2-} and H_2S within the sediment, due to the fractionation occurring during MSR and relative depth in the sediment (Fike et al., 2015). As MSR progresses in the sediment, $\delta^{34}S_{SO4}$ moves towards heavier values as the lighter isotope is consumed preferentially during MSR. As such, $\delta^{34}S_{H2S}$ follows this trend towards heavier values (offset by the microbial fractionation) as the source pool continues to become enriched in ^{34}S. In shallow-water environments where sedimentation rate is high, and labile organic carbon and Fe are available, S-isotopes may evolve under more closed-system conditions (Claypool, 2004) as described above. The frequency of sediment reworking events in shallow-water environments introduces new sulfate into the sediment, essentially resetting the distillation process of isotopes. These processes should be reflected in both $\delta^{34}S_{CAS}$ and $\delta^{34}S_{pyr}$ at the bulk (Richardson et al., 2019) and micron scales. Ultimately this model for different CAS content of individual carbonate components within a given sample may contribute to the elevated sample-to-sample variability in bulk-rock $\delta^{34}S_{CAS}$ datasets throughout Earth history (e.g., Kampschulte and Strauss 2004; Jones and Fike 2013; Osburn et al., 2015), where changes in this variability in a stratigraphic section may relate to changes in the relative proportions of the different cements or other carbonate components resulting from varying depositional conditions. Future work characterizing the S-isotopic composition of each component is imperative to understanding the degree to which marine diagenesis is the cause of the inherent variability in all bulk $\delta^{34}S_{CAS}$ datasets.

Figure 4.7 – Schematic of lithification and early marine diagenesis. a.) water column and sediment with redox zones, concentration of sulfide (yellow) and sulfate (red) in the sediment, and locations of carbonate and pyrite precipitation (modified from Fike et al., (2015). b.) thin sections depict the evolution of carbonate components at each location shown in (a) and an example of sulfate abundance within carbonate components that we anticipate are being formed in each time interval. Abbreviations as in previous figures, PYR = pyrite, CR = crinoid, BC = bioclast, M = micrite, RU = Rugose, B = brachiopod, DR= drusy cement, BL = blocky cement, SO = syntaxial overgrowth, ME = micrite envelope, MB = micritized bioclast. Thin section 1 illustrates lithification around primary biogenic calcite and micrite lithoclasts, with initial drusy cement forming in the high SO_4^{2-} region of the sediment. An example of the anticipated high CAS abundance primary carbonate and cement is shown in a brachiopod and drusy cement from the Hogklint Formation, Gotland. Thin section 2 shows the formation of drusy and syntaxial cements and pyrite, as well as recrystallization and micritization of fossils during early marine diagenesis. An example of low CAS abundance cement is shown in a fossilized rugose coral and micritic bioclasts from the Lousy Cove Member, Anticosti Island.

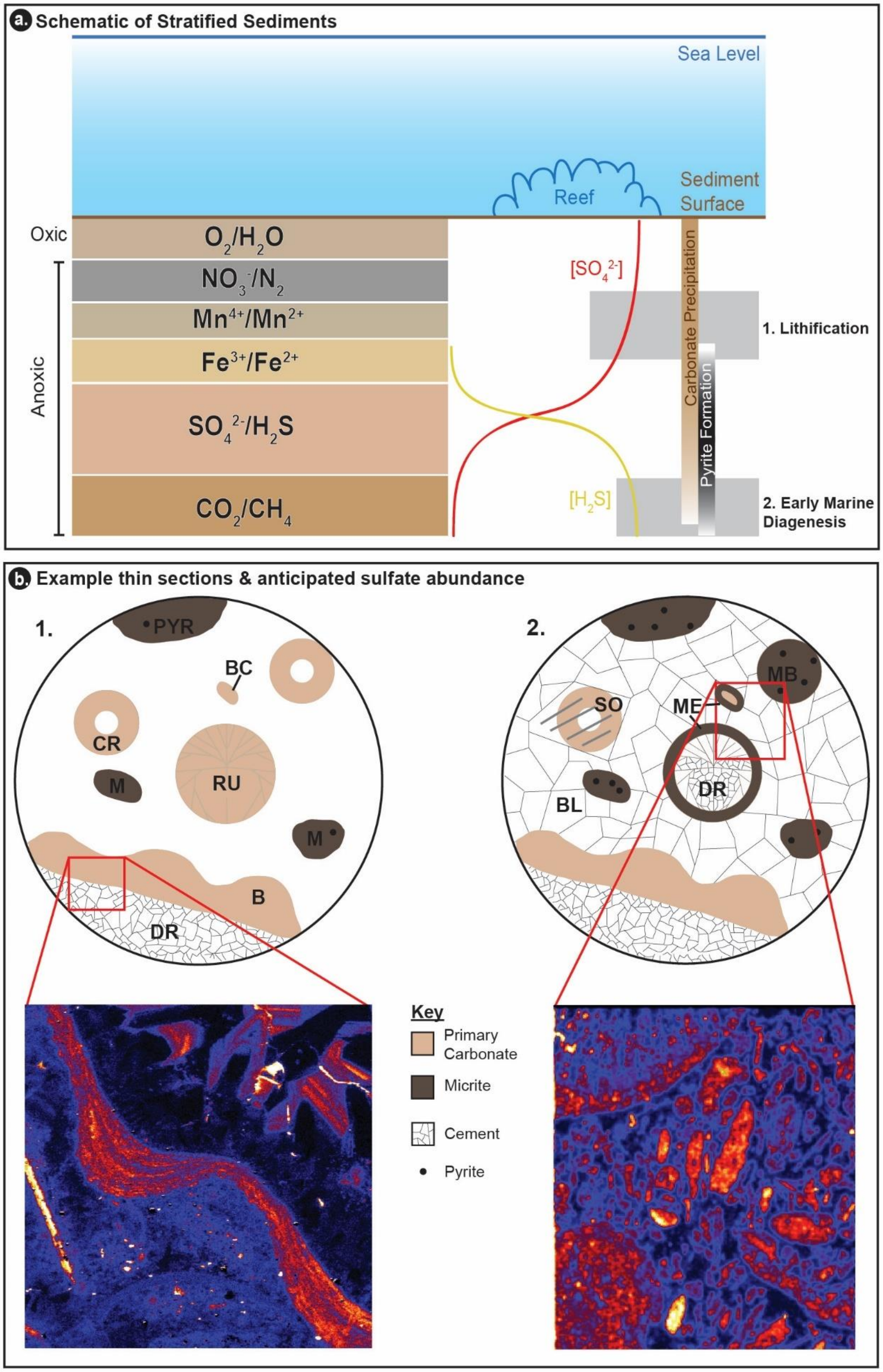
a.
Schematic of Stratified Sediments
Sea Level
Reef
Sediment Surface
Oxic
Anoxic
O_2/H_2O
NO_3^-/N_2
Mn^{4+}/Mn^{2+}
Fe^{3+}/Fe^{2+}
SO_4^{2-}/H_2S
CO_2/CH_4
$[SO_4^{2-}]$
$[H_2S]$
Carbonate Precipitation
Pyrite Formation
1. Lithification
2. Early Marine Diagenesis
b.
Example thin sections & anticipated sulfate abundance
1.
PYR
BC
CR
RU
M
M
B
DR
2.
MB
SO
ME
DR
BL
Key
Primary Carbonate
Micrite
Cement
Pyrite

As mentioned, we expect that disseminated sulfides are likely to be a major component in all forms of micrite present in carbonate sections throughout Earth history. It has been shown that laboratory oxidation of granular sulfide (< 300 μm) during acid extraction can appreciably affect bulk CAS at sulfide abundances greater than 1 weight % (Marenco et al., 2008a). In studied carbonate sections however, pyrite generally occurs at less than 1 weight % (e.g. Jones and Fike 2013; Richardson et al., 2019; Rose et al., 2019) and thus it is assumed that pyrite oxidation during laboratory extractions does not greatly affect bulk CAS measurements, especially in the absence of a correlation between, wt. % pyrite and CAS abundance, as well as CAS abundance and $\delta^{34}S_{CAS}$. However, this does not preclude an impact on CAS from sulfides that have already undergone (partial) oxidation during post-depositional diagenesis. Such partial oxidation of pyrites has been demonstrated to exist in all samples containing micrite here using XANES spectroscopy (Figure 4.5e). This sulfate (originally sourced form pyrite) may be sorbed onto the micrite surface and may be incorporated as CAS during carbonate recrystallization and/or during an extraction, ultimately driving the isotopic value of the sample towards lighter values. As such, it is important that CAS extraction protocols incorporate multiple brine rinses to remove any sulfate that is not lattice bound (Wotte et al., 2012). In the case that sulfate sourced from the oxidation of sulfide is incorporated into the carbonate during recrystallization, brine rinses will not amend this issue and samples will show a high CAS abundance and lower $\delta^{34}S_{CAS}$.

The extremely low abundance of preserved OSCs in corals and in micrite observed here are not anticipated to affect bulk CAS measurements. However, the role of OSCs during biotic carbonate growth is unknown; as such, CAS in well-preserved fossils could reflect a complex mixture of inorganic and organic S sources, resulting in a $\delta^{34}S_{CAS}$ signal distinct from that of coeval seawater. A majority of fossils preserved in ancient carbonates are commonly recrystallized or micritized, and sulfate abundance is variable. Thus, we anticipate that, unless the fossils preserve original mineralogy and structure, the sulfate signal is unlikely to be completely primary. Differences in sulfate abundance between fossil fragments may record the relative difference in primary CAS, as it is assumed all fossils of a given group within a petrographic thin section should be (approximately) affected equally by diagenesis. Since the primary CAS content of extinct fossil groups is largely unknown, it is difficult to infer the source of diagenetic fluids that they may have been exposed to. Moving forward, it will be important to gain a greater understanding of the source of sulfate in modern biomineralizers from abundance and isotope studies of single species. This knowledge will provide a platform to assess sulfate variability within a given species (and perhaps genus), and how this may result in variable sulfate abundance after diagenesis. Broad-scale meteoric diagenesis can be precluded from both localities due to the variability of sulfate in a given sample, heterogeneity that would be lost during wholesale meteoric diagenesis. Thus, we anticipate that marine or evolved marine waters are the dominant source of diagenetic sulfate in fossils observed in the present study. The addition of isotope data to the regions mapped in this study will provide a more robust understanding of primary and secondary signals, and the source of secondary signals. Further, component-specific isotope analyses will aid our understanding and interpretation of highly variable bulk $\delta^{34}S_{CAS}$ datasets.

4.6 Conclusions

High resolution μ-XRF imaging and XANES spectroscopy at the S K-edge in ancient carbonates reveals the presence and variable abundance of multiple S-species (predominantly sulfide and sulfate) in a range of lithofacies from shallow water marine carbonates. Investigation of fossils, cement, micrite, and abiotic grains across multiple lithofacies indicates that shallow-water depositional environments and early marine diagenesis are strong controls on the abundance and spatial variability of S-species, agreeing with recent studies on bulk S-isotopes that suggest depositional environment (e.g. sediment reworking, iron availability, and sedimentation rate) contributes to S-isotope variability. Well-preserved brachiopods and bryozoans have the highest sulfate abundance of all fossil groups studied, indicating these components might serve as two potential archives for robust $\delta^{34}S_{CAS}$. measurements. The identification of multiple OSCs in fossil tabulate corals, similar to OSCs inferred to be present in modern, deep-water corals, points towards a similar biomineralization pathway in extinct fossil groups. Elucidating such biomineralization pathways will aid our understanding of the source(s) of CAS in ancient carbonates and future interpretations of other geochemical proxies obtained from extinct fossil groups. In this sample set, cements contain inorganic sulfate, where variability in abundance reflects changes in pore fluid composition and precipitation rates during early marine diagenesis. We anticipate that such variation in sulfate abundance is not limited to the samples here and will occur in most other cements forming at various depths with carbonate sediment. Inorganic sulfate in bioclast fragments is observed to have two excitation energies ~0.3 eV apart. This shifting of the sulfate excitation energy reflects changes in the carbonate mineralogy (low- vs. high-Mg calcite). Sulfides, and sulfate sourced from the oxidation of sulfides, is dominant in micritic components and facies. The high abundance of sulfide reflects the availability of Fe and labile organic matter (thereby promoting MSR) in fine-grained sediments from shallow-water carbonate environments, with the oxidation of sulfide occurring progressively over time in contact with oxic diagenetic fluids. Together, these observations suggest that CAS sourced from shallow-water micrite components in carbonate rocks is not inherently a reliable recorder of ancient seawater sulfate during deposition and highlights the μ-scale sulfate variability that bulk CAS records are masking. Future studies aiming to reconstruct the operation of the sulfur cycle during key intervals of Earth history should exercise caution when homogenizing shallow-water carbonates that mix variable abundances of different carbonate components that formed throughout lithification and early marine diagenesis, particularly shallow-water facies that are micrite dominated. We recommend that studies target unaltered fossil fragments that retain primary mineralogy and fabric, or deep-water carbonate facies where porewater is more connected to the overlying seawater, reducing any signal from isotope distillation during early marine diagenesis.

4.7 Acknowledgements

We thank R. Nickerson and C. Roach for help and discussion during beam time and A. Munnecke for useful comments on carbonate petrography. We would also like to thank M. Böttcher and two anonymous reviewers for helping to improve this manuscript. Acknowledgment is made to the donors of the American Chemical Society Petroleum Research Fund (#57548-ND2) for partial support of this research. Use of the Stanford Synchrotron Radiation Lightsource, SLAC National Accelerator Laboratory, is supported by the U.S. Department of Energy, Office of Science, Office of Basic Energy Sciences under Contract No. DE-AC02-76SF00515. The SSRL Structural Molecular Biology Program is supported by the DOE Office of Biological and Environmental Research, and by the National Institutes of Health, National Institute of General Medical Sciences (including P41GM103393). The contents of this publication are solely the responsibility of the authors and do not necessarily represent the official views of NIGMS or NIH. This research used resources of the Advanced Photon Source, a U.S. Department of Energy (DOE) Office of Science User Facility operated for the DOE Office of Science by Argonne National Laboratory under Contract No. DE-AC02-06CH11357.

5. The source of sulfate in brachiopod calcite: Insights from μ-XRF imaging and XANES spectroscopy

Jocelyn A. Richardson[1*], Matthew Newville[2], Anthonio Lanzirotti[2], Samuel M. Webb[3], Catherine V. Rose[4], Jeffrey G. Catalano[1] and David A. Fike[1*]

[1]Department of Earth & Planetary Sciences, Washington University, St. Louis, MO 63130 USA
[2]Consortium for Advanced Radiation Sources University of Chicago, Chicago, Illinois, 60637, U.S.A
[3]Stanford Synchrotron Radiation Lightsource, Menlo Park, CA 94025, USA.
[4] School of Earth and Environmental Sciences, University of St Andrews, Fife KY16 9AL, UK

In review:
Richardson, J.A., Newville, M., Lanzirotti, A., Webb, S.M., Rose C. V., Catalano, J. G., Fike, D. A., The source of sulfate in brachiopod calcite: Insights from μ-XRF imaging and XANES spectroscopy. *Chem. Geo.*

5.1 Abstract

Geochemical signatures preserved in sedimentary carbonate strata are often used as archives for paleoenvironmental reconstructions. However, diagenetic overprinting and/or muting of primary geochemical signatures complicates the interpretation of these data. To avoid this issue, geochemical techniques strive to target unaltered (or minimally altered) carbonate components. The multi-layer low-Mg calcite shell composition of articulate brachiopods are often the target in such studies because they are commonly more robust to recrystallization than the shells of other biomineralizers. Here, we have combined S K-edge μ-XRF imaging, XANES spectroscopy and petrography to determine the source of sulfate in the calcite lattice of ancient and extant brachiopods, in order to establish their suitability for use in reconstructing seawater sulfate $\delta^{34}S$ throughout the Phanerozoic. Both the extant brachiopod *Terebratalia transversa* and fossil brachiopods display intra-specimen variability in sulfate abundance parallel to the primary fabric, likely corresponding to variations in growth rate. XANES spectroscopy identifies a majority of the sulfate as inorganic (carbonate-associated sulfate; CAS). Additionally, XANES spectroscopy detected low abundances of both reduced and oxidized organic sulfur species (thiol, thioether, sulfoxide and sulfate esters) in all *T. transversa* samples and lesser abundances in a few of the fossil brachiopods. In *T. transversa*, inorganic sulfate and sulfate ester abundance increase towards the hinge of the valves. Bulk $\delta^{34}S_{CAS}$ of the samples containing the fossil brachiopods are consistently higher than time-equivalent brachiopod-only values, likely reflecting a mixture of CAS signals from homogenization of carbonate components differentially affected by depositional environment and diagenesis. In contrast, bulk $\delta^{34}S_{CAS}$ of modern *T. transversa* is approximately 1‰ heavier than coeval seawater. Although organic sulfate esters are found within the brachiopod shells, they are only ever present as trace components. Our findings indicate that the vast majority

of sulfate in brachiopod exoskeletons is inorganic, sourced from coeval seawater. This result provides a potential archive for a faithful $\delta^{34}S_{CAS}$ record throughout the Phanerozoic and the detailed characterization of organic sulfur compounds in extant and fossil brachiopods aids in our understanding of the evolution of biomineralization pathways.

5.2 Introduction

The shells of biomineralizing organisms can leave behind in sediments a direct record of evolution, ontogeny, and physiology and can passively record variations in local seawater chemistry, particularly those composed of calcium carbonate minerals. Articulate brachiopods are an archive commonly exploited for a range of geochemical proxies including $\delta^{13}C_{carb}$, $\delta^{18}O_{carb}$, and trace element abundances (Brand et al., 2003; Kampschulte et al., 2001; Lowenstam, 1961; Popp et al., 1986b; Present et al., 2015; Veizer et al., 1986). A large amount of research has focused on protocols for the determination of minimally altered brachiopod fragments (Popp et al., 1986a, 1986b; Rush and Chafetz, 1990) and their associated $\delta^{13}C_{carb}$, $\delta^{18}O_{carb}$ and carbonate clumped isotope records (Azmy et al., 1998; Cummins et al., 2014; Lowenstam, 1961; Qing and Veizer, 1994). The shells of articulate brachiopods are accepted to be one of the most faithful archives of geochemical information, as they are constructed from low-Mg calcite forming two layers (primary and secondary); this makes brachiopods more robust to recrystallization during diagenesis (Brand and Veizer, 1980; Lowenstam, 1961). The original fabric of brachiopod shells is usually visible in petrographic thin section as fibrous calcite, where calcite crystallites in the secondary layer are oriented parallel or obliquely to the outer structure.

Similar to inorganic carbonate components, biogenic carbonates incorporate trace amounts of sulfate into the crystal lattice, substituting for the carbonate ion, termed carbonate-associated sulfate (CAS) (Burdett et al., 1989). Generally, biogenic carbonate components contain greater abundances of sulfate than inorganic precipitates, such as early to late diagenetic cement (Staudt and Schoonen, 1995; Present et al., 2015; Richardson et al., in review). In marine carbonate, the stable isotopic signature of CAS ($\delta^{34}S_{CAS}$) is generally considered as a proxy for the isotopic value of ancient seawater sulfate. Due to the temporal and spatial extent of marine carbonates, and the other geochemical information they retain, bulk $\delta^{34}S_{CAS}$ records have been generated to constrain the operation and evolution of the biogeochemical sulfur cycle over Earth history (Gill et al., 2011; Hurtgen et al., 2009, 2005; Luo et al., 2010; Rennie et al., 2018). However, bulk $\delta^{34}S_{CAS}$ records often display large stratigraphic variability over timescales considered too short to reflect changes to the global ocean sulfate reservoir (Jones and Fike, 2013; Kampschulte and Strauss, 2004; Osburn et al., 2015; Ries et al., 2009; Thompson and Kah, 2012) due to the expected (>> 1 Myr) residence time of seawater sulfate at least for much of the Phanerozoic (Berner, 2001; Bottrell and Newton, 2006). It has been suggested that the characteristic variability in many deep-time $\delta^{34}S_{CAS}$ datasets is a result of both local depositional and diagenetic processes (Fike et al., 2015; Jones and Fike, 2013; Present et al., 2015; Richardson et al., accepted, in review; Rose et al., 2019). In order to use CAS to its fullest potential as a proxy, the source and incorporation of sulfate in primary carbonate must be investigated.

In recent years, two different communities have been investigating sulfate in a variety of carbonate components for different purposes: those measuring CAS abundance and $\delta^{34}S_{CAS}$ in the rock record for paleoenvironmental and biogeochemical S-cycle reconstructions (e.g. Fike and Grotzinger, 2008; Kampschulte and Strauss, 2004; Osburn et al., 2015); and those investigating the role of sulfates (potentially both organic and inorganic) in the biomineralization and subsequent fossilization of modern biomineralizers, as well as the suitability of biominerals for paleoenvironment reconstructions (e.g., Cuif et al., 2003; Cusack et al., 2008; Perrin et al., 2017). It was first recognized that CAS was lattice-bound sulfate, as opposed to micro-inclusions of sulfate minerals, using Raman spectroscopy (Takano et al., 1980) and later by X-ray Absorption Near Edge Structure (XANES) spectroscopy (Pingitore et al., 1995). This development resulted in an increased number of studies utilizing $\delta^{34}S_{CAS}$ in the rock record, where ~ 40 g of homogenized rock powder are typically used during sample preparation (e.g. Burdett et al., 1989; Wotte et al., 2012). To decrease the amount of scatter in $\delta^{34}S_{CAS}$ sections, assumed to be sourced from incorporating late-stage diagenetic carbonate components, studies have targeted specific components such as micrite (Kampschulte and Strauss, 2004; Wotte et al., 2012a) or fossils (Gill et al., 2011; Kampschulte et al., 2001; Present et al., 2015) and/or reduced the sample size (Paris et al., 2014; Rennie et al., 2018). Brachiopods frequently retain some of the highest abundances of sulfate in biogenic calcite from the rock record (Staudt and Schoonen, 1995). Due to the robust nature of brachiopod exoskeletons to recrystallization, some have suggested they may be a faithful record for $\delta^{34}S_{CAS}$ (Kampschulte and Strauss, 2004; Present et al., 2015).

In addition to the potential as an archive for primary seawater $\delta^{34}S_{SO4}$ values, sulfate in brachiopods may provide a platform to assess the evolution of biomineralization processes and fossilization pathways. Previous work to determine the source of sulfate in biogenic calcite using micro-X-ray Fluorescence (μ-XRF) imaging and XANES spectroscopy has focused on modern corals (Cuif et al., 2003; Perrin et al., 2017b; Tamenori et al., 2014), mollusks (Dauphin et al., 2005, 2003; Tamenori and Yoshimura, 2018; Yoshimura et al., 2013) and, to a lesser extent, brachiopods (Cusack et al., 2008). These XANES studies have shown that sulfate is present within these biogenic carbonates; however, the interpretations of these results has varied as to whether the sulfate represents chondroitin sulfate (i.e., as sulfate esters; Cuif et al., 2003; Dauphin et al., 2003, 2005; Cusack et al 2008; Yoshimura et al., 2013; Tamenori and Yoshimura, 2018) or inorganic sulfate (Tamenori et al., 2014; Perrin et al., 2017). However, none of these studies observe the diagnostic fingerprint (lower energy shoulder; Almvist, 2010) of ester sulfate. As such, the existence, relative abundance, and role of organic sulfates in biomineralization within biogenic carbonates remains poorly constrained. In addition to sulfate, reduced organic sulfur species were found in organic matrices, including thiols and sulfite (Dauphin et al., 2005; Tamenori et al., 2014; Perrin et al., 2017; Tamenori and Yoshimura, 2018).

This study aims to answer questions pertinent to both communities investigating CAS by determining if sulfate is predominantly organically or inorganically bonded within brachiopod exoskeletons. Specifically, we report the spatial variation in sulfate abundance within individual extant *Terebratalia transversa* (Sowerby, 1846) and within individual Ordovician- and Silurian-aged fossil brachiopods using high resolution μ-XRF imaging and XANES spectroscopy. Previous work has shown the first occurrences of organic sulfur compounds (OSCs) preserved within a petrographic context in Ordovician and Silurian carbonates (including sulfate esters, thioethers and sulfite) co-occurring with inorganic sulfate determined to represent CAS (Richardson et al., (in review); Rose et al., (in review)). This study aims to assess the reliability of sulfate in brachiopods as a proxy for seawater sulfate by determining the abundance and role of organic sulfur species present within modern and fossil brachiopod exoskeletons.

5.3 Materials and Methods

5.3.1 Samples

Living *T. transversa* samples were obtained by dredging around the San Juan Islands, Washington, USA, by a research vessel from Friday Harbor Labs in March 2017. These samples were subsequently left out of water to open and dry out. The brachiopods were sonicated and then impregnated in an epoxy mold, cut along the plane of symmetry and mounted on a glass slide to make a thin section. Sample TT01 is approximately 2.7 cm along the plane of symmetry with shell thickness of 1 mm (Figure 5.1A). Sample TT02 is smaller at 1.7 cm along the plane of symmetry and has a shell thickness of ~ 0.3 mm (Figure 5.1B). Additionally, the shell of TT02 is much darker in colour than TT01.

Fossil brachiopods are from Hirnantian-aged strata of Anticosti Island, Canada, and Wenlock-aged strata of Gotland, Sweden. The fossil brachiopod thin sections from Anticosti Island were within a bioturbated packstone from the Fox Point Member of the Becscie Formation (Figure 5.1C) and a crinoidal wackestone from the Lousy Cove Member of the Ellis Bay Formation (Fig 1D; Jones et al., 2011). Samples from Gotland are from a poorly washed fossiliferous grainstone (Figure 5.1E) and a brachiopodal grainstone (Figure 5.1F) from the Upper Visby Formation (Rose et al., 2019). Calcite containing inorganic sulfate (acting as CAS standards for XANES spectroscopy) were precipitated in the laboratory following the free drift method (Gruzensky, 1967; Paquette and Reeder, 1990) as described in Rose et al., (in review). The CAS standard is a low Mg-calcite containing ~ 4000 ppm sulfate, determined by ion chromatography.

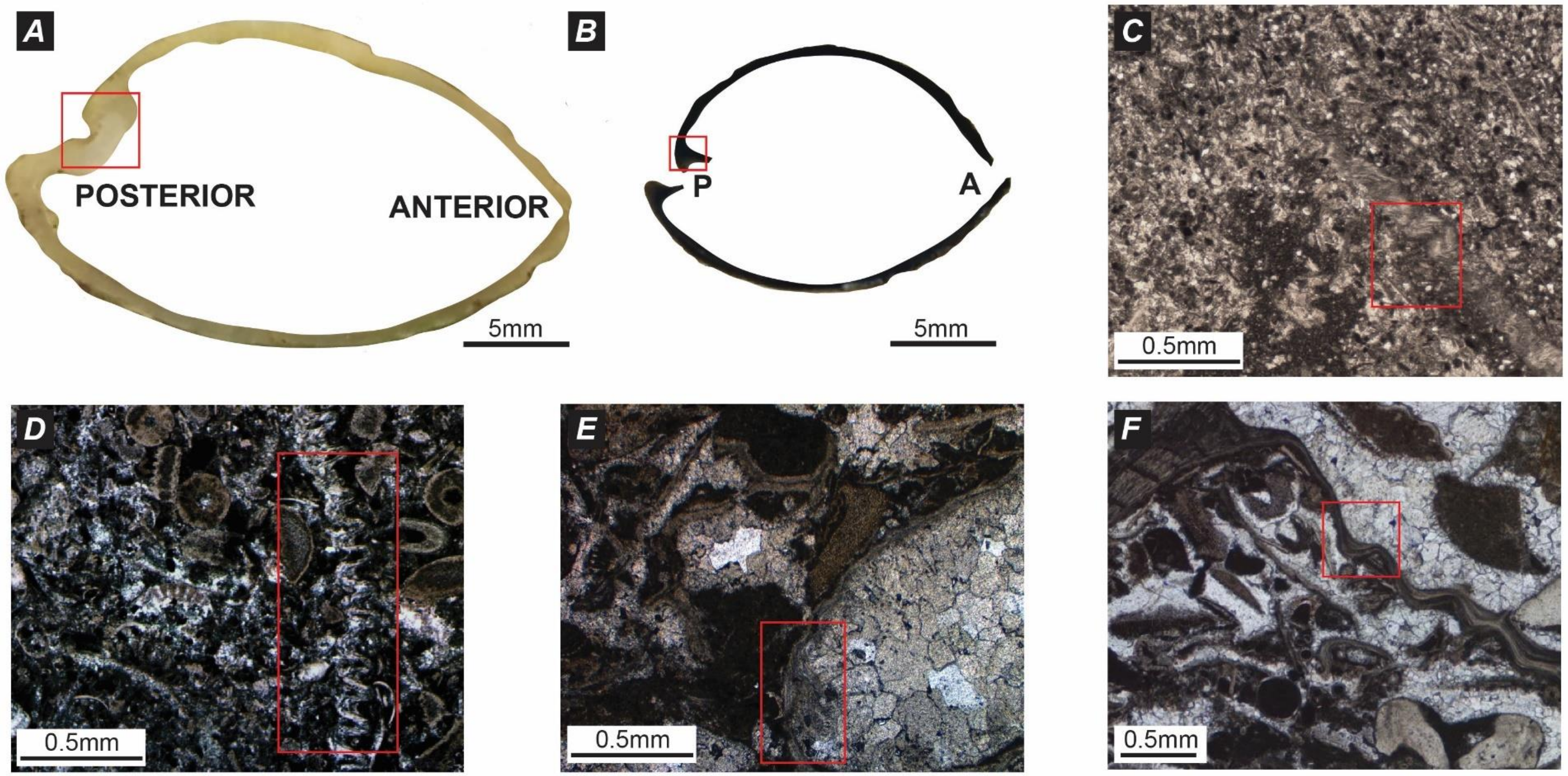

Figure 5.1 – images of extant and fossil brachiopods with outlined areas that correspond to mapped regions in later figures. A) *T. transversa* sample TT01, B) *T. transversa* sample TT02, C) ORD1; Bioturbated packstone from the Fox Point Member of the Becscie Formation, Anticosti Island, D) ORD2; Crinoidal wackestone from the Lousy Cove Member of the Ellis Bay Formation, Anticosti Island, E) SIL1; Poorly washed fossiliferous grainstone from the Upper Visby Formation, Gotland, F) SIL2; Brachiopodal grainstone from the Upper Visby Formation, Gotland.

5.3.2 SEM

Scanning Electron Microscopy (SEM) was performed using a FEI Nova Nano SEM at the Nano Research Facility, Washington University. Extant *T. transvera* samples were gold coated with ~20 μm to create a conductive surface in order to reduce charging effects and improve the secondary electron image. Analyses were performed under high vacuum at 10 kV.

5.3.3 μ-XRF and XANES

Analyses were performed around the sulfur K-edge (2472 eV) at the GeoSoilEnviroCARS microprobe beamline 13-ID-E, the Advanced Photon Source (APS), Argonne National Laboratory, and beamline 14-3 at the Stanford Synchrotron Radiation Lightsource (SSRL), Stanford Linear Accelerator Center. APS uses a liquid-N_2 cooled and SSRL uses a water cooled double Si (111) crystal monochromator to select the desired X-ray energy and Kirkpatrick-Baez mirrors to focus to a ~2 to 5 μm spot size. The sample environment is a helium-purged chamber to reduce X-ray attenuation in air. For detailed descriptions of each beamline and measurement approach see Rose et al. (in review). At the APS, an anhydrite standard provides the white line for sulfate (around 2481.5 eV) and maps were collected at the sulfide and sulfate excitation energies (2472.0 and 2481.5). At SSRL, a sodium thiosulfate powder calibrates the S K-edge to 2472.2 eV and maps were collected at the sulfide, sulfoxide, and multiple sulfate energies to detect differences in organic and inorganic species (2472.0, 2476.3, 2482.1, 2482.3, 2482.6 and 2482.8 eV). μ-XRF maps were processed using the MicroAnalysis Toolkit (Webb et al., 2011) and GSEMapViewer (Newville, 2013). At the sulfate excitation energy, reduced S-species contribute to the fluorescence signal, complicating accurate reconstruction of sulfate abundances. To correct for this, the fluorescence component from such species is subtracted from every sulfate excitation map.

Locations for XANES analyses were determined based on the fluorescence maps. XANES spectra from both the APS and SSRL were processed using SIXPACK (Webb, 2005). At the APS, S K-edge XANES spectroscopy was used to verify speciation. A greater number of XANES spectra were collected at SSRL in order to perform a XANES fitting of the map data. Spectra were corrected for detector deadtime and normalized using a background subtraction of the linearized pre- and post-edge region (2165 and 2510 eV, respectively). Subsequently, a principal component analysis (PCA) of the spectra for a given map region generated components that were cross-plotted. ‘End-member’ spectra that are at the edge of the cross-plot are the most dissimilar to one another. A least-squares fitting of these end-member spectra to the original multi-energy maps creates spatial distribution maps of the species detected as the end-members (Mayhew et al., 2011; Richardson et al., in review). Comparisons of the XANES spectra of the standards at each beamline demonstrated that the SSRL data were shifted to higher energies by 0.5 eV due to calibration differences that can be corrected. For clarity in reporting the results between the different beamlines, APS data were moved by + 0.5 eV to align with the SSRL energy calibration before further analysis.

5.3.4 Bulk Isotopes

Samples for bulk $\delta^{34}S_{CAS}$ are prepared by the method described in Richardson et al., (2019) (adapted from Wotte et al., 2012). Briefly, CAS was extracted from samples by rinsing up to 60g of sample powder in a 10% brine for a minimum of 3 rinses. This step was followed by 3 deionized water rinses, where the supernatant was checked for sulfate after the third rinse by adding $BaCl_2$. DI rinses were repeated until no precipitate formed in the supernatant on the addition of $BaCl_2$. Samples were then reacted with gradual addition of 6M HCl to reach a pH of 2 and stirred for no longer than 3 hours. The supernatant was then filtered and left to react with $BaCl_2$ for up to 5 days to form $BaSO_4$. *T. transversa* was prepared by homogenising 4 specimens, generating 5.6 g of carbonate powder and followed the same extraction protocol outlined above. Less sample for CAS extraction from *T. transversa* was required based on estimates of CAS abundance from synchrotron data. Approximately 350 μg of the resulting barium sulfate was combined with 1–3 mg of vanadium pentoxide and combusted using a Costech ECS 4010 elemental analyzer coupled to a Thermo Finnigan Delta V Plus isotope ratio mass spectrometer at Washington University. S-isotopes ($\delta^{34}S$) are expressed in standard delta notation in per mil (‰) as a deviation from V-CDT.

5.4 Results

5.4.1 Imaging of Calcite Textures

SEM of TT02 depicts two distinct fabrics or textures (Figure 5.2). The two textures are fibrous, bladed calcite crystallites, generating layers (Figure 5.2 A-C), and an indistinct texture that is likely a different orientation of the calcite crystallites (Figure 5.2B, D-E). A majority of the mapped region has the indistinct texture, with the fibrous texture limited to the region below the socket.

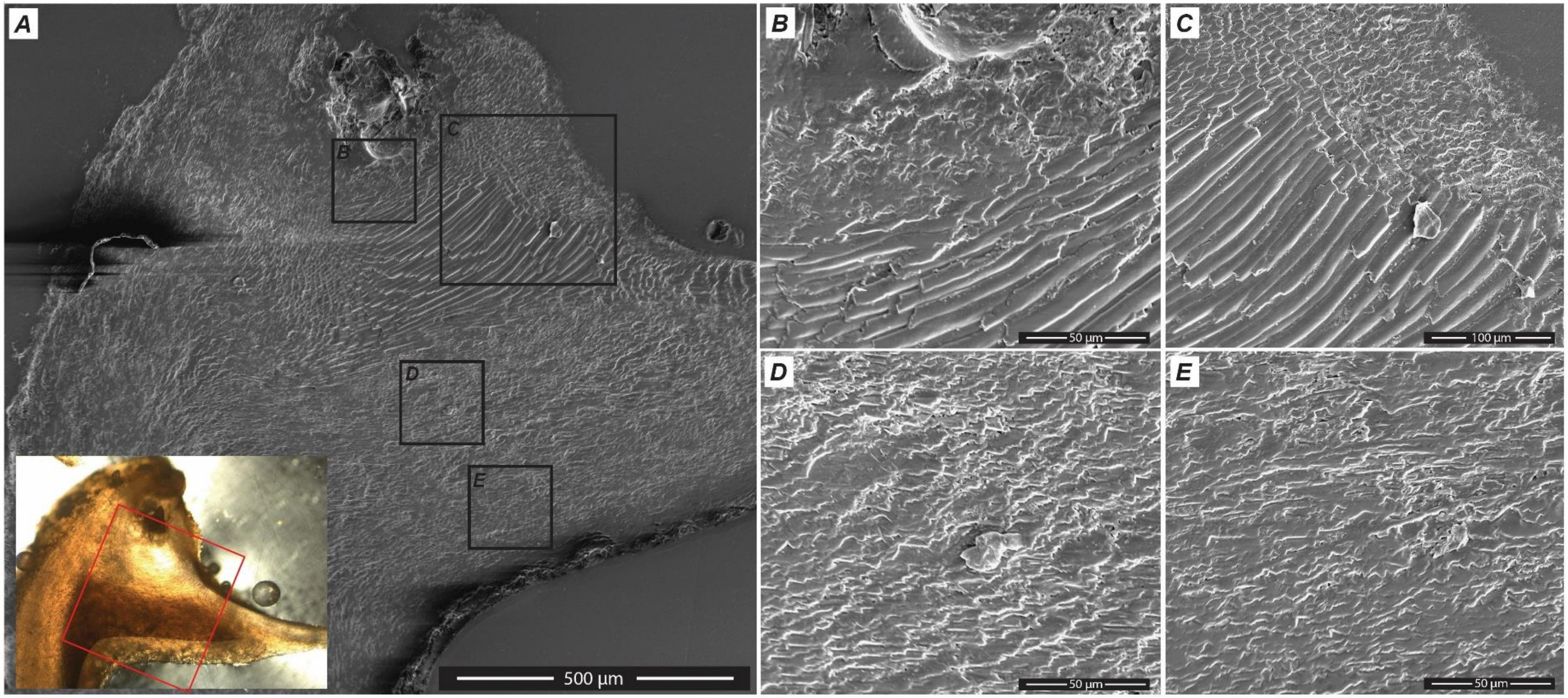

Figure 5.2 – SEM images of TT02. A) Large image corresponding to the mapped region in TT02, with transmitted light image inset. Areas outlined and labelled in black correspond to the higher resolution images in B to E.

5.4.2 μ-XRF and XANES of Extant Brachiopods

To observe differences between reduced and oxidized sulfur species, excitation maps for sample TT01 are shown for 2476.3 eV and 2482.3 eV, corresponding to the sulfoxide and sulfate excitation energy respectively (Almkvist et al., 2010) (Figure 5.3A and B). Numerous reduced sulfur species will fluoresce at 2476.3 eV, including sulfide. At the hinge line between the two brachiopod valves, the highest abundance of reduced sulfur species is observed and co-occurs with the highest abundance of inorganic sulfate and sulfate esters (Figure 5.3A, B and C). Smaller, less intense regions of increased reduced sulfur moieties occur along the edge of the shell (Figure 5.3A). Sulfate abundance decreases along the fibrous calcite layers (Figure 5.3B). Reduced sulfur species that co-occur with inorganic sulfate are common throughout the rest of the sample with no clear pattern as to where they are present (yellow Figure 5.3C). XANES spectra confirm the presence of thiol, sulfoxide, sulfate esters and inorganic sulfate (Figure 5.3D, 1-3, 2 and 4, respectively). The organic species have maximum intensities at 2473, 2476.3 and 2481 eV, and co-occur with sulfate peaks in a single region.

In contrast, due to the differences in calibration between APS and SSRL, the reduced-S excitation map obtained for TT02 corresponds to the sulfide energy at 2472 eV (Figure 5.4A). Around the socket, sulfate abundance is high and co-occurs with a low abundance of reduced-S species (Figure 5.4A and B). Inorganic sulfate abundance is the greatest along the top right edge of the shell. The sulfate abundance decreases towards the inner fibrous calcite but there is an increase in the frequency of the high abundance sulfate layers towards the inner portion of the shell (Figure 5.4B), which co-occurs with reduced-S species along one calcite layer towards the inner shell (Figure 5.4A). Additionally, in the fibrous calcite, sulfate abundance increases around the edge of individual calcite crystallites. XANES spectra are indicative of inorganic sulfate in a majority of the sample, with sulfate esters present around the socket (Figure 5.4C, 1 and 5 respectively). In many locations, a low-intensity thiol peak of variable intensity co-occurs with sulfate (Figure 5.4C, 2-5).

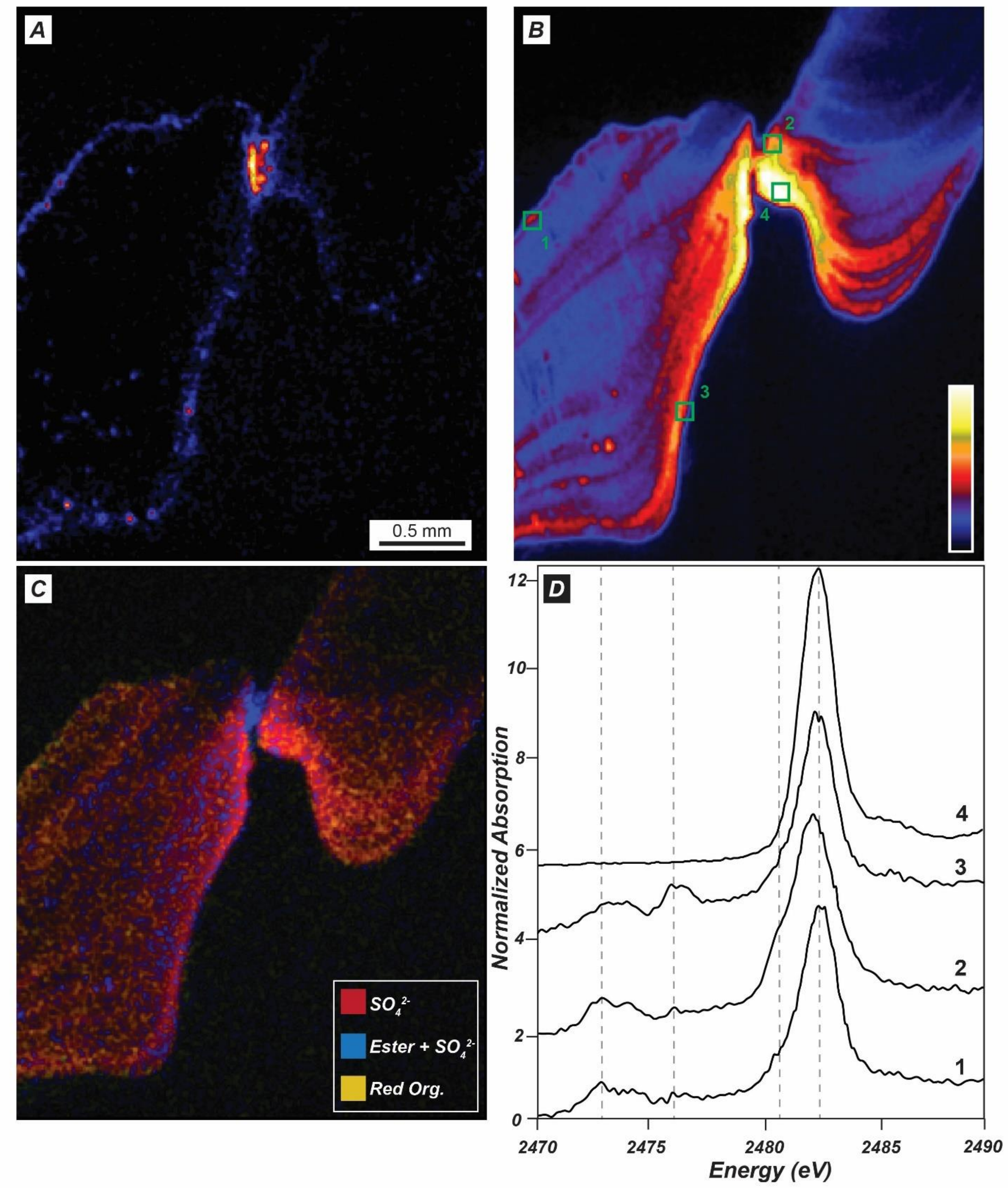

Figure 5.3 – Sample TT01 A) sulfoxide excitation energy map at 2476.3 eV B) Sulfate excitation energy map at 2482.3 eV with green boxes showing spot locations for representative XANES. C) tricolour plot using data from XANES fitting where red corresponds to inorganic sulfate, blue is sulfate with an ester and yellow is the location of sulfate combined with a reduced organic sulfur compound. D) XANES of spot locations numbered in B. Dashed lines at 2473.2 eV, 2476.6 eV, 2481 eV and 2482.6 eV.

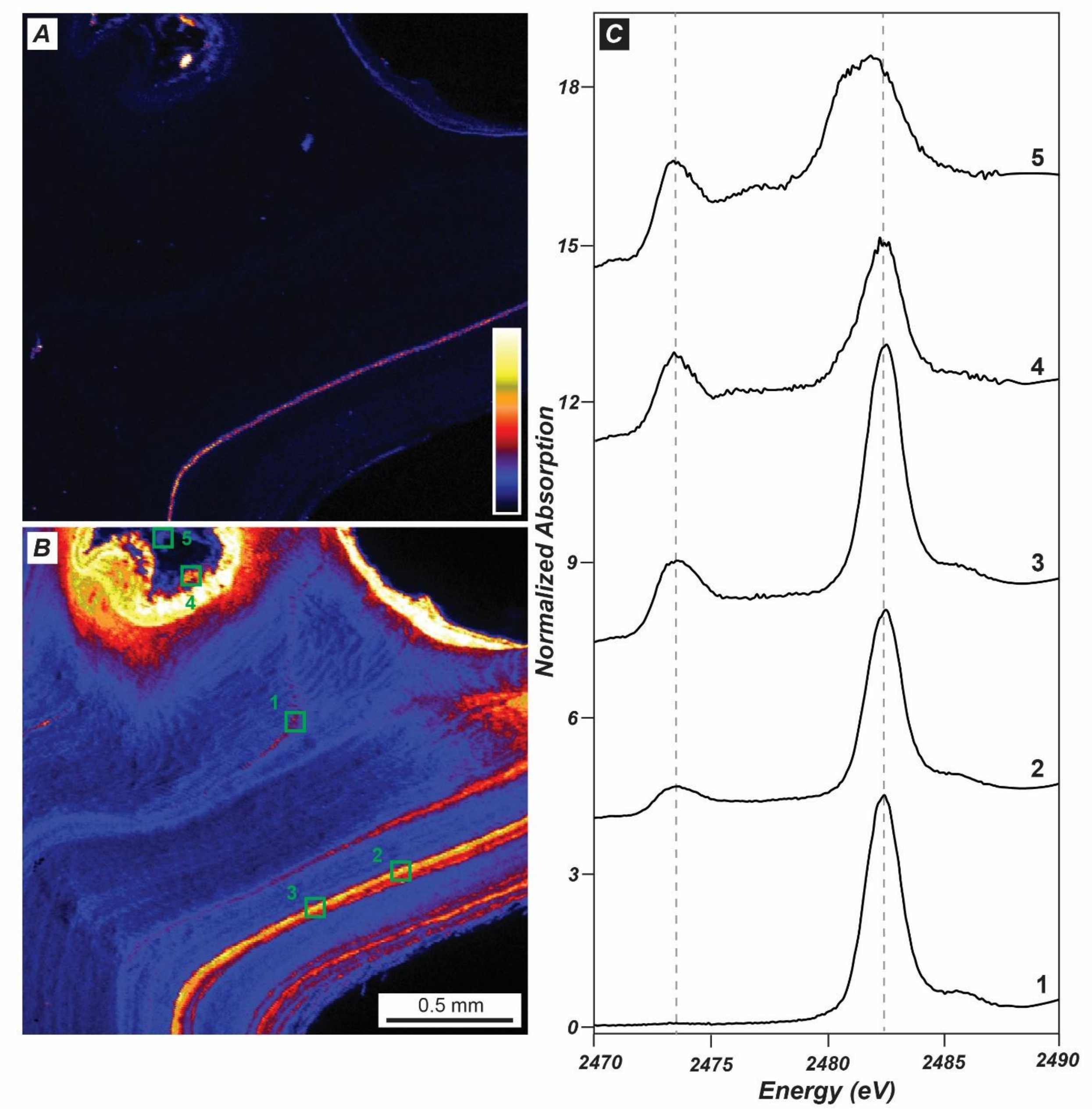

Figure 5.4 – Sample TT02 A) sulfide excitation energy map at 2472 eV. B) sulfate excitation energy map at 2481.5 eV with green boxes showing spot locations for representative XANES. C) XANES of spot locations in B. Dashed lines at 2473.5 eV and 2482.4 eV. Sample TT01 and fossil brachiopods are all scaled to the same S (quantitative) counts for comparison. Sample TT02, however, contains higher sulfate abundance, thus, for variation within the shell structure to be visible, the scale is 3 times that of TT01 and fossil brachiopods (i.e., sulfur counts corresponding to white on TT02 map is three times greater than all other maps).

5.4.3 μ-XRF and XANES of Fossil Brachiopods

Fossil brachiopods have some of the highest abundances of sulfate compared to fossils of equivalent age such as bivalves, crinoids and corals (Present et al., 2015; Richardson et al., in review). All fossil brachiopods analyzed contain intra-specimen variability in sulfate abundance (Figure 5.5). Within ORD1 sulfate abundance is variable along the original fibrous fabric of the secondary shell layer (Figure 5.5A). Although the original fibrous texture of the secondary layer is not visible in ORD2 (Figure 5.5B), the original ribs are preserved, indicating this cross-section is perpendicular to the plane of symmetry (unlike Figure 5.5A and 5C that are subparallel to symmetry), crosscutting fewer lines of growth than the other samples. As such, variability is muted in ORD2 compared to other samples. Sample SIL1 is the only fossil sample to preserve both valves of a single specimen (Figure 5.5C). The two valves display strong differences in sulfate abundance, while also recording variability along the original fabric in the ventral valve (top valve Figure 5.5C). Comparatively, SIL2 is an oblique cross-section. Again, sulfate abundance follows the original fabric and is of comparable abundance to the sulfate zoning within the surrounding abiotic calcite cement (Figure 5.5D). Organic sulfur compounds are detected only in ORD1, with a broadened sulfate peak, corresponding to the shoulder of a sulfate ester at 2481.1 eV at location 1, and peaks at 2473.5 and 2478 eV corresponding to thiol and sulfite respectively (Almkvist et al., 2010). XANES spectra indicate that inorganic, lattice-bound sulfate is the only species present in all other fossil brachiopods and is directly comparable to the spectra within abiotic cement (Figure 5.5E spectra 3-6 where spectra 5 is within abiotic cement).

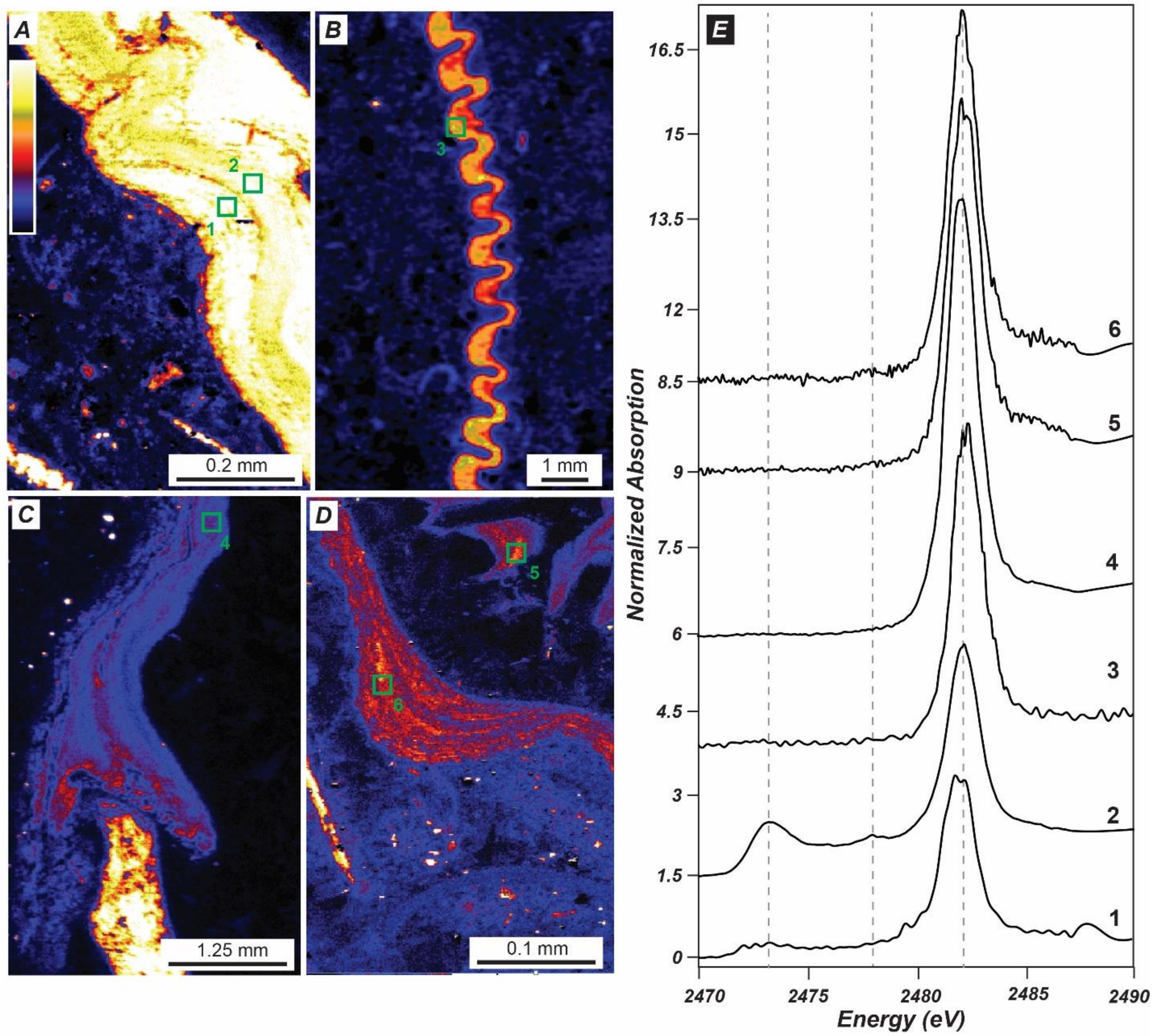

Figure 5.5 – Fossil brachiopod sulfate energy excitation maps and XANES. Green boxes and numbers correspond to a spectra number A) ORD1. B) ORD2. C) SIL1. D) SIL2. E) XANES of spot locations numbered on each map. Dashed lines at 2473.5 eV, 2478 eV and 2482.3 eV.

5.4.4 Bulk Isotopes

Bulk $\delta^{34}S_{CAS}$ for Anticosti Island samples ORD1 and ORD2 are 27.4‰ and 25‰ (± 0.23‰; duplicate analyses), respectively (Jones and Fike, 2013). Bulk $\delta^{34}S_{CAS}$ for Gotland samples SIL1 and SIL2 are 33.6 and 29.6‰ (± 0.2‰; duplicate analyses), respectively (Rose et al., 2019). Bulk

T. transversa have a $\delta^{34}S_{CAS}$ of 22.4‰ (± 0.3‰; triplicate analyses), while local seawater from which they were sourced has a $\delta^{34}S_{SO4}$ of 21.0‰ (± 0.3‰; Oduro et al., 2012).

5.5 Discussion

5.5.1 Role of Organic Sulfur Compounds (OSCs)

The detection of co-occurring reduced and oxidized OSCs and the generation of spatially explicit abundance maps of these species within a petrographic context can provide valuable new insights into biomineralization in extant brachiopod exoskeletons and diagenetic processes in fossil brachiopods. The presence of co-occurring reduced and putative oxidized OSCs has been reported previously within modern coral calcite (Perrin et al., 2017), and within concentrated modern brachiopod organic matrices (Cusack et al., 2008), specifically as thiols, sulfoxides, and presumed esters. However, one outstanding question in numerous XAS studies of biogenic carbonate is the nature of the lattice-bound sulfate (inorganic vs. organic; Cuif et al., 2003; Dauphin et al., 2003; Cusack et al., 2008; Tamenori et al., 2014; Perrin et al., 2017; Tamenori and Yoshimura, 2018). XANES spectra can differentiate between inorganic and organic sulfate by an additional feature, a shoulder on the low-energy side of the main sulfate peak that represents an organic sulfate ester (Almkvist et al., 2010; Rose et al., in review). There are visible differences in the spectra obtained here, indicative of organic sulfate esters with the characteristic shoulder versus those lacking a distinct shoulder (e.g. Figure 5.3D spot 2 vs. spot 4). The spectra that do not have an ester shoulder on the sulfate peak are akin to spectra within abiotic calcite (e.g. Figure 5.5D and E, spots 5 and 6) and are similar to S K-edge XANES of other carbonate components (Rose et al., in review; Richardson et al., in review). This characteristic shoulder of an organic sulfate ester in XANES spectra has seldom been observed within carbonates, suggesting that previous studies did not detect organic sulfate using XANES spectroscopy (Cuif et al., 2003; Dauphin et al., 2003; Dauphin et al., 2005; Yoshimura and Tamenori 2018).

To more definitively identify the nature of the sulfate that comprises a majority of the fossil and extant brachiopods investigated (i.e., those with XANES spectra lacking an ester shoulder), post-edge features can be used to further differentiate among sulfate species (Figure 5.6; Fleet, 2005). Many discrete sulfate minerals exhibit three fine-structure features at approximately 2484.9, 2491.3 and 2498 eV (Fleet et al., 2005) on top of the large, broad feature in all spectra occurring between ~2490 and ~2505 eV. Such fine-structure features originate from photoelectron scattering from ordered sulfur and cation neighbors, whereas the larger, broad feature originates from the first tetrahedral oxygen shell. The majority of samples, including those from abiotic carbonate cements, have a XANES spectrum that includes a post-edge feature at 2484.9 eV (Figure 5.6, orange arrows). However, while some spectra also display higher-energy fine-structure features in the post-edge region (e.g., TT02 1), these are weak or absent in the spectra of many samples.

Previous work has interpreted the absence of features beyond 2485 eV to indicate that organic sulfate compounds were present (Yoshimura and Tamenori, 2018). However, the synthetic inorganic CAS sample presented here also shows no evidence of substantial fine-structure features (Figure 5.6). In addition, other oxoanions substituting in calcite (CrO_4^{2-}, AsO_4^{3-}, SeO_3^{2-}, and SeO_4^{2-}) have weak fine-structure features in the X-ay absorption spectra (Alexandratos et al., 2007; Aurelio et al., 2010; Reeder et al., 1994; Tang et al., 2007). Both tetrahedral (CrO_4^{2-}) and trigonal pyramidal (SeO_3^{2-}, AsO_3^{3-}) oxoanions have been shown using X-ray standing waves to occupy the carbonate group site in calcite, but with the central atom of the oxoanion offset from the carbon position in the structure (Bedzyk and Cheng, 2002; Cheng, 1998; Cheng et al., 1999, 1997). Such a shift produces a distribution of oxoanion-Ca interatomic distances, creating a disordered Ca shell and weak to negligible fine-structure features in the post-edge region of XANES spectra. The consistent, systematic behaviour of oxoanions in the calcite lattice indicates that sulfate will behave similarly. The absence of fine-structure features above 2485 eV thus only indicates the absence of crystalline sulfate salt (e.g., gypsum) and alone is not diagnostic of organic versus inorganic sulfate. This conclusion is consistent with the original interpretation of the XANES spectra of sulfate in natural calcium carbonates (Pingitore et al., 1995).

Further evaluation of the XANES spectra, including the post-edge region, suggests that the presence or absence of the features at 2484.9 eV does provide information regarding the form of sulfate present. Post-edge features fall into different categories based on valency and crystallinity (as seen in the standard XANES spectra Figure 5.6). The shoulder at 2484.9 eV indicates divalency of the sulfate ion and the two post-edge oscillations at 2491.3 and 2498 eV correspond to crystalline structures. Using this the sulfate can be classed as: gypsum like (crystalline and divalent showing all three features), monovalent sulfate minerals like Na_2SO_4 (crystalline and monovalent, lacking the shoulder at 2484.9 eV), CAS (poorly crystalline and divalent, in some cases showing the shoulder at 2484.9 eV) and organic sulfate compounds (poorly crystalline and monovalent, showing one broad feature at 2498 eV). Samples TT01, spot 2 and ORD 2 that show the diagnostic ester sulfate shoulder near 2481 eV have post-edge features most similar to the ester standard. In contrast, samples lacking an ester sulfate component contain the 2484.9 eV feature but lack a large fine-structure feature at higher energy that would indicate crystalline sulfate minerals. This set of spectral properties is thus indicative of inorganic sulfate contained in a calcite lattice.

The detection and characterization of reduced and oxidized organic S-species in small regions of individual specimens is novel, especially within fossil brachiopods, due to the low abundance of the organic matrix within brachiopods (< 3 wt. %; Cusack et al., 2008). It is clear, however, that most of the sulfate in both extant and fossil brachiopods is predominantly inorganic, lattice-bound sulfate. This observation does not rule out the possibility that some of this sulfate may originally be sourced from organic compounds, through desulfurization of esters or oxidation of reduced organic moieties, and some localized occurrence of diagnostic organic sulfate esters was observed, albeit in trace amounts (e.g., Figure 5.3C). However, considering the size of the sulfate reservoir has been > 5 mM for most of the Phanerozoic (Lowenstein et al., 2003), the relatively high abundance of sulfate in brachiopods and the relatively low abundance of OSCs in comparison, it is highly likely that the vast majority of brachiopod-sourced CAS is inorganic and derived directly from ambient seawater sulfate.

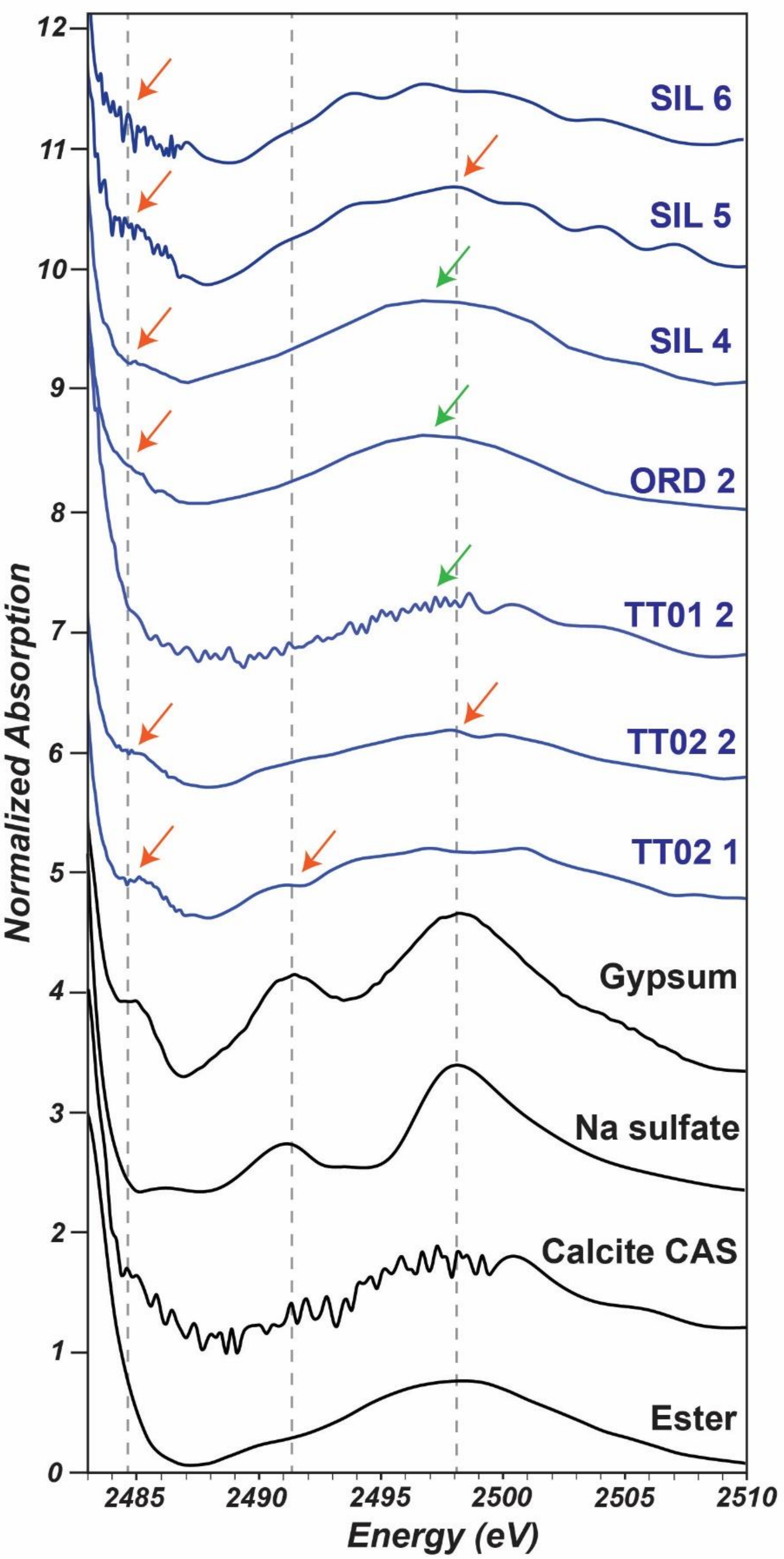

Figure 5.6 – XANES spectra post-edge features. Standards are outlined in black and sample points are outlined in blue. Sample SIL5 is a spectrum obtained from abiotic cement that is not a sulfate ester but represents inorganic, lattice-bound sulfate. Dashed lines at 2484.9, 2491.3 and 2498 that correspond to features in sulfate mineral post-edge.

5.5.2 Sulfate abundance and variability

Each brachiopod displays internal variation in sulfate abundance that appears to follow the original fabric of the secondary layer. The source samples for the fossil brachiopods have not experienced broad-scale post-depositional alteration (see Jones et al., 2011; Jones and Fike 2013; Rose et al., 2019), which is important in determining the fidelity of CAS to original marine sulfate. Diagenetic recrystallization would result in homogenisation of sulfate abundance. Additionally, all brachiopods retain unaltered original carbonate fabrics. As such, we anticipate that this variation in sulfate abundance does not reflect a diagenetic component. Further, since most articulate brachiopods are epifaunal, sessile benthos (Ager, 1967) and therefore in good contact with overlying seawater, it is not likely that changes in sulfate concentration, such as would be found within the sediment due to microbial sulfate reduction, are the source of the observed sulfate variability in the brachiopods.

The rate of shell growth is not constant throughout the lifespan of a brachiopod. Growth rate is faster in the juvenile stage and decreases after maturation. Additionally, growth rates may differ or shell may be resorbed (Carlson, 1989), between the ventral and dorsal valves (Buesing and Carison, 1992; Pérez-Huerta et al., 2014). In abiotic carbonate precipitation, the likelihood of sulfate substitution into the carbonate lattice is kinetically controlled and is anticipated to increase proportionally with growth rate (Busenberg and Plummer, 1985). Thus, sulfate abundance in brachiopods could be an important recorder of growth rate irrespective of any local variation in seawater sulfate abundance. Based on the linear relationship between length and width during brachiopod growth, and the size to shell thickness relationship, TT01 is considered a fully mature sample while TT02 is not yet fully mature but is developed beyond the juvenile stage (Endo, 1987; Pérez-Huerta et al., 2014). The difference in total sulfate abundance between TT01 and TT02 could be due to different juvenile growth rates (Figure 5.3 and Figure 5.4). While ontogeny cannot be determined for the fossil brachiopod species, the preservation of both valves in SIL1 indicates that growth rate was faster in the dorsal valve (Figure 5.5C). Further, amorphous calcium carbonate (ACC) is a common precursor to biomineral precipitation (Cusack and Freer, 2008) and has been detected in modern Terebratulida as a precursor to calcite during shell repair, indicating it is likely a precursor during original growth (Griesshaber et al., 2009). An ACC precursor may allow for greater amounts of sulfate to substitute into the carbonate structure, since the ACC structure may be more susceptible to incorporating the larger sulfate ion.

Comparisons of sulfate abundance and SEM images of TT02 (Figure 5.2) indicate that sulfate abundance increases on the outer edge of individual crystallites within the fibrous calcite. It is important to consider potential crystal orientation effects (i.e. calcite anisotropy) and/or changes in excitation volume that may contribute to this apparent increase in abundance. It has been demonstrated that Sr and Mg K-edge XANES spectroscopy can be affected by calcite crystal orientation, due to calcite anisotropy, based on both corals and brachiopods (Allison et al., 2005; Pérez-Huerta et al., 2008). This orientation effect, however, results mostly in slightly variable pre- and post-edge features, as opposed to differences in the normalised absorption intensity (Pérez-Huerta et al., 2008). There are no differences in the sulfate absorption peaks in XANES spectra across TT02 (the only difference is the variable abundance of the reduced S species). Due to this, we anticipate that calcite orientation has no appreciable effect on the observed sulfate abundance (fluorescence yield) in the µ-XRF images of TT02. Comparisons of calcium and sulfate excitation maps indicate that calcium abundance increases to the edge of some crystals in this region, meaning these increases in abundance could reflect surface topography of the sample, where changes in excitation volume create an apparent abundance increase (Figure 5.7). It is important that the difference in energy of fluorescence between calcium and sulfate can make it difficult to deconvolve fluorescence response vs. surface roughness. However, there are increases in sulfate abundance in this region that show no associated increase in calcium abundance, indicating that some of this variation in sulfate abundance to the edge of crystals may be real.

If the increase in abundance around individual crystals is not an artefact caused by changes in excitation volume, it may reflect the original organic template. Although the sulfate is not an ester (Figure 5.4C), it could be sourced from desulfurized esters or oxidation of reduced-S moieties from the organic template, resulting in an apparent increase in CAS abundance around the fibrous calcite. Intra-crystalline organic matrix (IOM) has been recognised as a template, or framework, for carbonate nucleation in biomineralizers (Pérez-Huerta et al., 2018). IOM can include a protein and polysaccharide-rich template or sheath that may often contain both reduced and oxidized sulfur groups (Addadi et al., 1987; Cusack et al., 2008). A covariation of phosphorus and reduced OSCs has been observed around individual calcite crystals in *T. retusa* that suggests this template can be preserved (Cusack et al., 2008). However, the absence of any OSCs where sulfate abundance increases to the edge of individual crystals of TT02 (Figure 5.4B and C) suggests that the variations in sulfate abundance here is not due to the presence of preserved IOM but is the result of changing excitation volume.

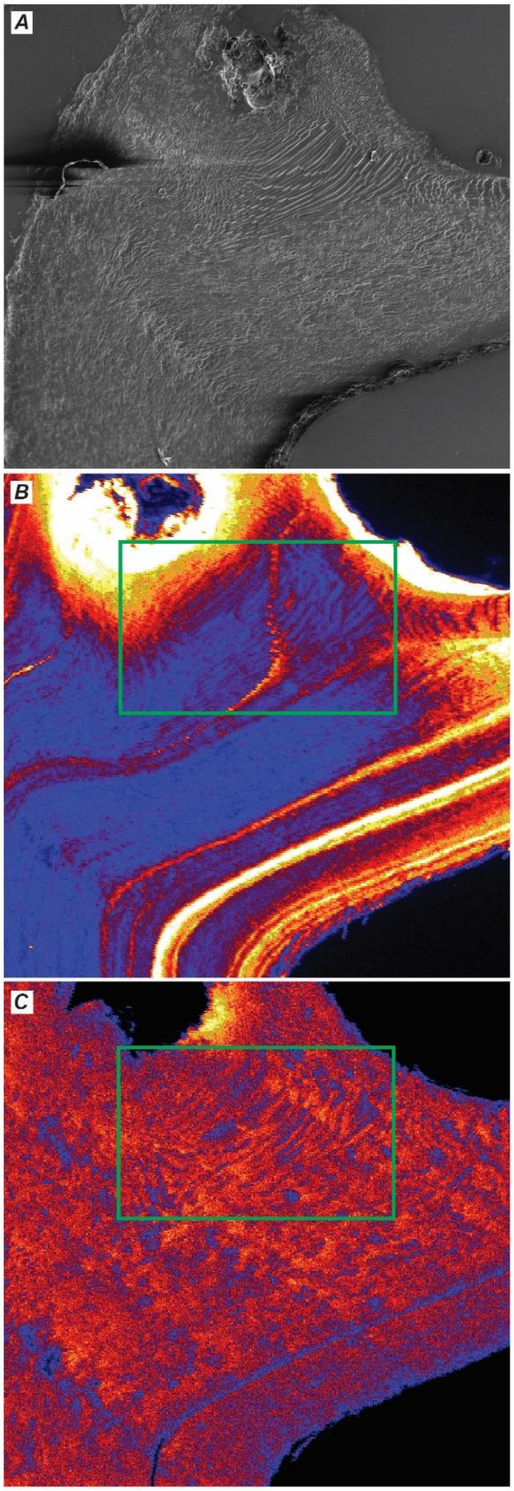

Figure 5.7 – Sample TT02 A) SEM image shown in Figure 5.2 for crystal fabric context. B) Calcium abundance map where the color scale is reduced in order to better observe internal variation for comparisons with sulfate. C) sulfate abundance map (also shown in Figure 5.4) where the color scale is stretched to show similar color within the fibrous region for ease of comparison with calcium.

5.5.3 Implications for Biomineralization

IOM takes part in numerous roles during biomineralization including nucleation, determination of mineralogy, and crystal orientation (Pérez-Huerta et al., 2018). The interplay of IOM on the resultant mineral composition and structure can affect the biomechanics of the exoskeletons and, ultimately, how biominerals respond during diagenesis. However, IOM is not well preserved on geologic timescales. In the absence of abundant IOM here, the presence (although in low abundance) of similar OSCs in extant and fossil brachiopods is promising for understanding the evolution of brachiopod biomineralization. Sulfate esters, in conjunction with carboxylates, can influence the orientation of calcite crystals (Addadi et al., 1987). Their presence in brachiopods could give rise to the orientated fibrous calcite in the secondary layer that ultimately contributes to brachiopod preservation potential. Additionally, the presence of chondroitin sulfate in solution favors calcite precipitation (Kitano and Hood, 1965) and L-Cysteine, containing thiols, generates hydrogen bonds between calcium or carbonate ions in solution, promoting calcite formation (Xie et al., 2005). Together, one or both of these OSCs may play a role in the calcite mineralogy of articulate brachiopods and are detected in extant and fossil brachiopods here using XANES spectroscopy. Similar observations of low abundances of reduced OSCs corresponding to amino acids within IOM has been shown in modern mollusks, corals and brachiopods (Dauphin et al., 2003; Cuif et al., 2003; Cusack et al., 2008), as well as within fossil corals and micrite (Richardson et al., in review).

5.5.4 Implications for Isotope Studies

Global ocean chemistries have dramatically changed throughout the Phanerozoic. For example, the seawater sulfate reservoir has increased in size from approximately 5-12 mM to 28 mM (Horita et al., 2002b; Lowenstein et al., 2003). Despite these changes, seawater sulfate has remained the largest reservoir of sulfur in the biogeochemical sulfur cycle for the Phanerozoic and the residence time of Phanerozoic seawater sulfate is on the multi-million-year time-scale (Berner, 2001). *T. transversa* are anticipated to live for approximately 10 years (Paine, 1969), growing continually throughout their lifetime via accretionary growth, adding carbonate marginally to the exoskeleton (Auclair et al., 2003). The lifespan of Ordovician and Silurian brachiopods is relatively unknown, since growth lines of brachiopods do not necessarily correlate with age (Auclair et al., 2003; Paine, 1969). However, it is not expected that fossil brachiopods would have had a lifespan wildly divergent from those of extant brachiopods. If brachiopods are recording global or basinal $\delta^{34}S_{SO4}$ then it is unlikely that $\delta^{34}S_{CAS}$ of their shells should exhibit much, if any, variation, due to the magnitude of difference between the lifespan of brachiopods and seawater sulfate residence time. Thus, if variability does exist it is likely recording local $\delta^{34}S_{SO4}$, as opposed to global ocean variability.

Bulk $\delta^{34}S_{CAS}$ of *T. transversa* is greater than local seawater sulfate by ~ 1‰ (Puget Sound $\delta^{34}S_{SO4}$ of 21 (± 0.3‰); (Oduro et al., 2012)). This value could be accounted for by the small fractionation that can occur during sulfate incorporation and substitution for the carbonate ion, which has been shown to be ≤ 0.8 ‰ in foraminifera (Burdett et al., 1989; Rennie et al., 2018). Comparatively, bulk $\delta^{34}S_{CAS}$ of the whole rock from which the fossil samples were sourced are heavier than time-correlative brachiopod-only samples for both the end-Ordovician and Silurian. Whole rock $\delta^{34}S_{CAS}$ from ORD 1 and ORD1 are approximately 2‰ greater than brachiopod-only values (Present et al., 2015), while whole rock $\delta^{34}S_{CAS}$ from SIL1 and SIL2 are between 4.5 and 5.1 ‰ greater (Present, 2018). We attribute this to the relatively low abundance of brachiopods in these specific ancient carbonate samples relative to other carbonate components. These other components likely record a mixture of $\delta^{34}S_{CAS}$ signals from water column components, early syn-sedimentary diagenesis, and post-depositional alteration (Richardson et al., accepted; Richardson et al., in review). We anticipate that micron-scale analysis of $\delta^{34}S_{CAS}$ within the fossil brachiopods (e.g., using secondary ion mass spectrometry or laser-ablation MC-ICP-MS) would agree more closely with other records, and any variability will reflect local seawater (and potentially pore-water for infaunal species) chemistry during brachiopod growth.

5.6 Conclusion

We have demonstrated the differences between organic sulfate esters and inorganic sulfate in extant and fossil brachiopod shells using XANES spectroscopy. Our results show that inorganic sulfate (as CAS) is the dominant signal in both extant and fossil brachiopods, and accounts for a majority of the intra-specimen sulfate variability. Sulfate abundance maps of individual brachiopods show variability parallel to the original fabric of the secondary layer. Sulfate abundance likely changes with varying growth rate throughout the brachiopod lifespan. Organic sulfate esters are present, albeit in low abundance, and often co-occur with reduced S-amino acids where they appear to be preferentially located near the hinge line. The presence of oxidized and reduced OSCs in both extant and fossil brachiopods suggests that these compounds may influence mineralogy and crystal orientation during biomineralization. These findings are important for researchers in paleoenvironmental reconstructions and biomineralization and we suggest (1) brachiopods are likely a more faithful archive for seawater sulfate isotopic values and (2) OSCs may play a role in brachiopod mineralogy and crystal orientation, therefore influencing biomineralization and ultimately affecting fossilization and preservation pathways.

5.7 Acknowledgements

We thank M. Dethier and others at Friday Harbor labs for obtaining *T. transversa* for this project specifically and S. Moore at Washington University in St. Louis for sulfur isotope analysis. Acknowledgment is made to the donors of the American Chemical Society Petroleum Research Fund (#57548-ND2) for partial support of this research. Use of the Stanford Synchrotron Radiation Lightsource, SLAC National Accelerator Laboratory, is supported by the U.S. Department of Energy, Office of Science, Office of Basic Energy Sciences under Contract No. DE-AC02-76SF00515. The SSRL Structural Molecular Biology Program is supported by the DOE Office of Biological and Environmental Research, and by the National Institutes of Health, National Institute of General Medical Sciences (including P41GM103393). The contents of this publication are solely the responsibility of the authors and do not necessarily represent the official views of NIGMS or NIH. Portions of this work were performed at GeoSoilEnviroCARS (The University of Chicago, Sector 13), Advanced Photon Source (APS), Argonne National Laboratory. GeoSoilEnviroCARS is supported by the National Science Foundation - Earth Sciences (EAR - 1634415) and Department of Energy- GeoSciences (DE-FG02-94ER14466). This research used resources of the Advanced Photon Source, a U.S. Department of Energy (DOE) Office of Science User Facility operated for the DOE Office of Science by Argonne National Laboratory under Contract No. DE-AC02-06CH11357.

6. Conclusions

The findings of this research bring to light the variable impact of depositional environment and early- to late-stage marine diagenesis on carbonate-associated sulfate that was previously relatively unconstrained. Individual carbonate platforms exert local, site-specific controls on $\delta^{34}S_{CAS}$ and $\delta^{34}S_{pyr}$ based on: sedimentation rate, availability of labile organic carbon and iron, and energy of the environment (i.e. tidal, wave- or storm-influenced). Together, these parameters impact the connectivity of pore fluids to seawater. For example, shallow-water, mid-platform facies that experience high, pulsed sedimentation rates with available carbon and iron have pore fluids that are the least connected to seawater. This results in a (variably) closed-system, where pore fluid $\delta^{34}S_{SO4}$ and $\delta^{34}S_{H2S}$ evolve to heavier values during ongoing microbial sulfate reduction (MSR). In contrast, shallow-water peritidal environments are continually impacted by tide and wave action that rework the sediment and introduce seawater sulfate into the pore fluid. This results in less evolved $\delta^{34}S_{SO4}$ and $\delta^{34}S_{H2S}$, although still variable, and the final $\delta^{34}S_{CAS}$ should more closely approximate seawater. In the case of deep-water carbonate deposition, low sedimentation rate and low depositional energy create a more open system between pore fluid and seawater, preventing isotope distillation through the replenishment of sulfate from seawater, generating more stable, and generally lower, $\delta^{34}S_{CAS}$ and $\delta^{34}S_{pyr}$.

Depositional environment controls the composition of carbonate rocks; the relative proportions of fossils, grains, cement (including cement morphology) and micrite vary between depositional settings and cement morphology is controlled by diagenetic processes. We found that the abundance and speciation of sulfur varies between these different components and between different facies. In these Ordovician and Silurian strata, shallow-water facies have a greater proportion of fossils and cements compared to deep-water facies that are dominated by micrite. Our results show that sulfate abundance is controlled by precipitation location (within seawater or in the sediment), growth rate and most likely the local SO_4^{2-}:CO_3^{2-} ratio. Sulfide abundance is dependent upon the proportion of micrite. Ultimately, these factors are influenced by depositional environment and early marine diagenesis in pore fluids where MSR (and other anaerobic metabolisms) change the SO_4^{2-}:CO_3^{2-} ratio, promoting carbonate precipitation. The detection and improved characterization of inorganic sulfate vs. organic sulfur compounds in ancient carbonates, fossil brachiopods and extant brachiopods provides evidence for brachiopods as a robust archive for $\delta^{34}S_{SO4}$ reconstructions in the Phanerozoic and points towards consistent biomineralization pathways over time. Understanding the processes of biomineralization and its effect on trace ion incorporation could reveal more archives for CAS where brachiopods are limited.

To fully understand the signatures that $\delta^{34}S_{CAS}$ represents, future research should focus on method-development for determining $\delta^{34}S_{CAS}$ values of individual components, with complementary sulfate abundance images, using secondary ion mass spectrometry (SIMS). Combined $\delta^{34}S_{CAS}$ and abundance data will constrain the fluid composition from which each component precipitated. However, this method will be time-intensive, expensive, not widely accessible and cannot provide high-resolution chemostratigraphy that bulk isotope ratio mass spectrometry (IRMS) approaches can. Researchers that continue to use traditional bulk methods should be cautious of over-interpreting variably heavy $\delta^{34}S_{CAS}$ from shallow-water carbonates and, where possible, should obtain time-correlative brachiopod $\delta^{34}S_{CAS}$ values and coeval $\delta^{18}O_{CAS}$ to determine the most primary CAS values. Studies should avoid shallow-water micrite that is dominated by sulfide due to *in situ* oxidation. Pre-Cambrian carbonate studies should focus on paired $\delta^{34}S_{CAS}$-$\delta^{18}O_{CAS}$ and diagenetic indicators of various cement morphologies to assess if they formed in contact with seawater or in the sediment in the zone of sulfate reduction or have experienced recrystallization and diagenesis in meteoric or burial conditions.

References

Adams, D.D., Hurtgen, M.T., Sageman, B.B., 2010. Volcanic triggering of a biogeochemical cascade during Oceanic Anoxic Event 2. Nat. Geosci. 3, 201–204. https://doi.org/10.1038/ngeo743

Addadi, L., Moradian, J., Shay, E., Maroudas, N.G., Weiner, S., 1987. A chemical model for the cooperation of sulfates and carboxylates in calcite crystal nucleation: Relevance to biomineralization. Proc. Natl. Acad. Sci. U. S. A. 84, 2732–6. https://doi.org/10.1073/PNAS.84.9.2732

Ager, D.V., 1967. Brachiopod palaeoecology. Earth-Science Rev. 3, 157–179. https://doi.org/10.1016/0012-8252(67)90375-3

Alexandratos, V.G., Elzinga, E.J., Reeder, R.J., 2007. Arsenate uptake by calcite: Macroscopic and spectroscopic characterization of adsorption and incorporation mechanisms. Geochim. Cosmochim. Acta 71, 4172–4187. https://doi.org/10.1016/J.GCA.2007.06.055

Aller, R.C., 2004. Conceptual models of early diagenetic processes: The muddy seafloor as an unsteady, batch reactor. J. Mar. Res. 62, 815–835. https://doi.org/10.1357/0022240042880837

Aller, R.C., Madrid, V., Chistoserdov, A., Aller, J.Y., Heilbrun, C., 2010. Unsteady diagenetic processes and sulfur biogeochemistry in tropical deltaic muds: Implications for oceanic isotope cycles and the sedimentary record. Geochim. Cosmochim. Acta 74, 4671–4692. https://doi.org/10.1016/j.gca.2010.05.008

Allison, N., Finch, A.A., Newville, M., Sutton, S.R., 2005. Strontium in coral aragonite: 3. Sr coordination and geochemistry in relation to skeletal architecture. Geochim. Cosmochim. Acta 69, 3801–3811. https://doi.org/10.1016/J.GCA.2005.01.026

Almkvist, G., Boye, K., Persson, I., 2010. K-edge XANES analysis of sulfur compounds: An investigation of the relative intensities using internal calibration. J. Synchrotron Radiat. 17, 683–688. https://doi.org/10.1107/S0909049510022946

Antler, G., Turchyn, A. V., Rennie, V., Herut, B., Sivan, O., 2013. Coupled sulfur and oxygen isotope insight into bacterial sulfate reduction in the natural environment. Geochim. Cosmochim. Acta 118, 98–117. https://doi.org/10.1016/J.GCA.2013.05.005

Auclair, A.-C., Joachimski, M.M., Lécuyer, C., 2003. Deciphering kinetic, metabolic and environmental controls on stable isotope fractionations between seawater and the shell of Terebratalia transversa (Brachiopoda). Chem. Geol. 202, 59–78. https://doi.org/10.1016/S0009-2541(03)00233-X

Aurelio, G., Fernández-Martínez, A., Cuello, G.J., Román-Ross, G., Alliot, I., Charlet, L., 2010. Structural study of selenium(IV) substitutions in calcite. Chem. Geol. 270, 249–256. https://doi.org/10.1016/J.CHEMGEO.2009.12.004

Azmy, K., Veizer, J., Bassett, M.G., Copper, P., 1998. Oxygen and carbon isotopic composition of Silurian brachiopods: Implications for coeval seawater and glaciations. Geol. Soc. Am. Bull. 110, 1499. https://doi.org/10.1130/0016-7606(1998)110<1499:OACICO>2.3.CO;2

Balan, E., Blanchard, M., Pinilla, C., Lazzeri, M., 2014. First-principles modeling of sulfate incorporation and 34S/32S isotopic fractionation in different calcium carbonates. Chem. Geol. 374–375, 84–91. https://doi.org/10.1016/J.CHEMGEO.2014.03.004

Banner, J.L., Hanson, G.N., 1990. Calculation of simultaneous isotopic and trace element variations during water-rock interaction with applications to carbonate diagenesis. Geochim. Cosmochim. Acta 54, 3123–3137. https://doi.org/10.1016/0016-7037(90)90128-8

Bartley, J.K., Kah, L.C., 2004. Marine carbon reservoir, Corg-Ccarb coupling, and the evolution of the Proterozoic carbon cycle. Geology 32, 129. https://doi.org/10.1130/G19939.1

Bathurst, R.G.C., 1975. Carbonate sediments and their diagenesis. Elsevier.

Baumgartner, L.K., Reid, R.P., Dupraz, C., Decho, A.W., Buckley, D.H., Spear, J.R., Przekop, K.M., Visscher, P.T., 2006. Sulfate reducing bacteria in microbial mats: Changing paradigms, new discoveries. Sediment. Geol. 185, 131–145. https://doi.org/10.1016/J.SEDGEO.2005.12.008

Bedzyk, M.J., Cheng, L., 2002. X-ray Standing Wave Studies of Minerals and Mineral Surfaces: Principles and Applications. Rev. Mineral. Geochemistry 49, 221–266. https://doi.org/10.2138/gsrmg.49.1.221

Berner, R.A., 2001. Modeling atmospheric O2 over Phanerozoic time. Geochim. Cosmochim. Acta 65, 685–694. https://doi.org/10.1016/S0016-7037(00)00572-X

Berner, R.A., 1989. Biogeochemical cycles of carbon and sulfur and their effect on atmospheric oxygen over phanerozoic time. Palaeogeogr. Palaeoclimatol. Palaeoecol. 75, 97–122. https://doi.org/10.1016/0031-0182(89)90186-7

Berner, R.A., 1984. Sedimentary pyrite formation: An update. Geochim. Cosmochim. Acta 48, 605–615. https://doi.org/10.1016/0016-7037(84)90089-9

Berner, R.A., Canfield, D.E., 1989. A new model for atmospheric oxygen over Phanerozoic time. Am. J. Sci. 289, 333–61.

Berner, R.A., Raiswell, R., 1983. Burial of organic carbon and pyrite sulfur in sediments over phanerozoic time: a new theory. Geochim. Cosmochim. Acta 47, 855–862. https://doi.org/10.1016/0016-7037(83)90151-5

Berner, R.A., Scott, M.R., Thomlinson, C., 1970. Carbonate alkalinity in the pore waters of anoxic marine sediments. Limnol. Oceanogr. 15, 544–549. https://doi.org/10.4319/lo.1970.15.4.0544

Bickert, T., Pätzold, J., Samtleben, C., Munnecke, A., 1997. Paleoenvironmental changes in the Silurian indicated by stable isotopes in brachiopod shells from Gotland, Sweden. Geochim. Cosmochim. Acta 61, 2717–2730. https://doi.org/10.1016/S0016-7037(97)00136-1

Bottrell, S.H., Newton, R.J., 2006. Reconstruction of changes in global sulfur cycling from marine sulfate isotopes. Earth-Science Rev. 75, 59–83. https://doi.org/10.1016/J.EARSCIREV.2005.10.004

Brand, U., Logan, A., Hiller, N., Richardson, J., 2003. Geochemistry of modern brachiopods: applications and implications for oceanography and paleoceanography. Chem. Geol. 198, 305–334. https://doi.org/10.1016/S0009-2541(03)00032-9

Brand, U., Veizer, J., 1980. Chemical Diagenesis of a Multicomponent Carbonate System--1: Trace Elements. SEPM J. Sediment. Res. Vol. 50, 1219–1236. https://doi.org/10.1306/212F7BB7-2B24-11D7-8648000102C1865D

Buesing, N., Carison, S.J., 1992. Geochemical investigation of growth in selected Recent articulate brachiopods. Lethaia 25, 331–345. https://doi.org/10.1111/j.1502-3931.1992.tb01402.x

Burdett, J.W., Arthur, M.A., Richardson, M., 1989. A Neogene seawater sulfur isotope age curve from calcareous pelagic microfossils. Earth Planet. Sci. Lett. 94, 189–198. https://doi.org/10.1016/0012-821X(89)90138-6

Busenberg, E., Plummer, N.L., 1985. Kinetic and thermodynamic factors controlling the distribution of SO32− and Na+ in calcites and selected aragonites. Geochim. Cosmochim. Acta 49, 713–725. https://doi.org/10.1016/0016-7037(85)90166-8

Calner, M., 2008. Silurian global events – at the tipping point of climate change, in: Mass Extinction. Springer Berlin Heidelberg, Berlin, Heidelberg, pp. 21–57. https://doi.org/10.1007/978-3-540-75916-4_4

Calner, M., 2005. Silurian carbonate platforms and extinction events—ecosystem changes exemplified from Gotland, Sweden. Facies 51, 584–591. https://doi.org/10.1007/s10347-005-0050-0

Canfield, D.E., 2004. The evolution of the Earth surface sulfur reservoir. Am. J. Sci. 304, 839–861. https://doi.org/10.2475/ajs.304.10.839

Canfield, D.E., 2001a. Biogeochemistry of Sulfur Isotopes. Rev. Mineral. Geochemistry 43.

Canfield, D.E., 2001b. Biogeochemistry of Sulfur Isotopes. Rev. Mineral. Geochemistry 43, 607–636. https://doi.org/10.2138/gsrmg.43.1.607

Canfield, D.E., Farquhar, J., 2009. Animal evolution, bioturbation, and the sulfate concentration of the oceans. Proc. Natl. Acad. Sci. U. S. A. 106, 8123–7. https://doi.org/10.1073/pnas.0902037106

Canfield, D.E., Raiswell, R., Westrich, J.T., Reaves, C.M., Berner, R.A., 1986. The use of chromium reduction in the analysis of reduced inorganic sulfur in sediments and shales. Chem. Geol. 54, 149–155. https://doi.org/10.1016/0009-2541(86)90078-1

Canfield, D.E., Teske, A., 1996. Late Proterozoic rise in atmospheric oxygen concentration inferred from phylogenetic and sulphur-isotope studies. Nature 382, 127–132.

https://doi.org/10.1038/382127a0

Carlson, S.J., 1989. The articulate brachiopod hinge mechanism: morphological and functional variation. Paleobiology 15, 364–386. https://doi.org/10.1017/S0094837300009568

Cecile, M.P., Shakur, M.A., Krouse, H.R., 1983. The isotopic composition of western Canadian barites and the possible derivation of oceanic sulphate δ^{34} S and δ^{18} O age curves. Can. J. Earth Sci. 20, 1528–1535. https://doi.org/10.1139/e83-142

Cheng, L., 1998. Atomic-scale study of ion incorporation at calcite surface using synchrotron X-ray methods. Northwestern University.

Cheng, L., Fenter, P., Sturchio, N.C., Zhong, Z., Bedzyk, M.J., 1999. X-ray standing wave study of arsenite incorporation at the calcite surface. Geochim. Cosmochim. Acta 63, 3153–3157. https://doi.org/10.1016/S0016-7037(99)00242-2

Cheng, L., Lyman, P.F., Sturchio, N.C., Bedzyk, M.J., 1997. X-ray standing wave investigation of the surface structure of selenite anions adsorbed on calcite. Surf. Sci. 382, L690–L695. https://doi.org/10.1016/S0039-6028(97)00167-2

Chiba, H., Sakai, H., 1985. Oxygen isotope exchange rate between dissolved sulfate and water at hydrothermal temperatures. Geochim. Cosmochim. Acta 49, 993–1000. https://doi.org/10.1016/0016-7037(85)90314-X

Christ, N., Immenhauser, A., Wood, R.A., Darwich, K., Niedermayr, A., 2015. Petrography and environmental controls on the formation of Phanerozoic marine carbonate hardgrounds. Earth-Science Rev. 151, 176–226. https://doi.org/10.1016/J.EARSCIREV.2015.10.002

Claypool, G.E., 2004. Ventilation of marine sediments indicated by depth profiles of pore water sulfate and δ34S. Geochemical Soc. Spec. Publ. 9, 59–65. https://doi.org/10.1016/S1873-9881(04)80007-5

Claypool, G.E., Holser, W.T., Kaplan, I.R., Sakai, H., Zak, I., 1980. The age curves of sulfur and oxygen isotopes in marine sulfate and their mutual interpretation. Chem. Geol. 28, 199–260. https://doi.org/10.1016/0009-2541(80)90047-9

Cocks, L.R.M., Torsvik, T.H., 2005. Baltica from the late Precambrian to mid-Palaeozoic times: The gain and loss of a terrane’s identity. Earth-Science Rev. 72, 39–66. https://doi.org/10.1016/J.EARSCIREV.2005.04.001

Cocks, L.R.M., Torsvik, T.H., 2002. Earth geography from 500 to 400 million years ago: a faunal and palaeomagnetic review. J. Geol. Soc. London. 159, 631–644. https://doi.org/10.1144/0016-764901-118

Cotton, F.A., Wilkinson, G., 1972. Advanced Inorganic Chemistry, 3rd ed. Wiley.

Cramer, B.D., Saltzman, M.R., 2005. Sequestration of 12C in the deep ocean during the early Wenlock (Silurian) positive carbon isotope excursion. Palaeogeogr. Palaeoclimatol. Palaeoecol. 219, 333–349. https://doi.org/10.1016/J.PALAEO.2005.01.009

Crowe, S.A., Paris, G., Katsev, S., Jones, C., Kim, S.-T., Zerkle, A.L., Nomosatryo, S., Fowle, D.A., Adkins, J.F., Sessions, A.L., Farquhar, J., Canfield, D.E., 2014. Sulfate was a trace constituent of Archean seawater. Science 346, 735–9. https://doi.org/10.1126/science.1258966

Cuif, J.-P., Dauphin, Y., Doucet, J., Salome, M., Susini, J., 2003. XANES mapping of organic sulfate in three scleractinian coral skeletons. Geochim. Cosmochim. Acta 67, 75–83. https://doi.org/10.1016/S0016-7037(02)01041-4

Cummins, R.C., Finnegan, S., Fike, D.A., Eiler, J.M., Fischer, W.W., 2014. Carbonate clumped isotope constraints on Silurian ocean temperature and seawater δ18O. Geochim. Cosmochim. Acta 140, 241–258. https://doi.org/10.1016/J.GCA.2014.05.024

Cusack, M., Dauphin, Y., Cuif, J.-P., Salomé, M., Freer, A., Yin, H., 2008. Micro-XANES mapping of sulphur and its association with magnesium and phosphorus in the shell of the brachiopod, Terebratulina retusa. Chem. Geol. 253, 172–179. https://doi.org/10.1016/J.CHEMGEO.2008.05.007

Cusack, M., Freer, A., 2008. Biomineralization: Elemental and Organic Influence in Carbonate Systems. Chem. Rev. 108, 4433–4454. https://doi.org/10.1021/cr078270o

Dauphin, Y., Cuif, J.-P., Doucet, J., Salomé, M., Susini, J., Terry Willams, C., 2003. In situ chemical speciation of sulfur in calcitic biominerals and the simple prism concept. J. Struct. Biol. 142, 272–280. https://doi.org/10.1016/S1047-8477(03)00054-6

Dauphin, Y., Cuif, J.-P., Salomé, M., Susini, J., 2005. Speciation and distribution of sulfur in a mollusk shell as revealed by in situ maps using X-ray absorption near-edge structure (XANES) spectroscopy at the S K-edge. Am. Mineral. 90, 1748–1758. https://doi.org/10.2138/am.2005.1640

Desrochers, A., Farley, C., Achab, A., Asselin, E., Riva, J.F., 2010. A far-field record of the end Ordovician glaciation: The Ellis Bay Formation, Anticosti Island, Eastern Canada. Palaeogeogr. Palaeoclimatol. Palaeoecol. 296, 248–263. https://doi.org/10.1016/j.palaeo.2010.02.017

Edwards, C.T., Fike, D.A., Saltzman, M.R., Lu, W., Lu, Z., 2018. Evidence for local and global redox conditions at an Early Ordovician (Tremadocian) mass extinction. Earth Planet. Sci. Lett. 481, 125–135. https://doi.org/10.1016/J.EPSL.2017.10.002

Eldridge, D.L., Guo, W., Farquhar, J., 2016. Theoretical estimates of equilibrium sulfur isotope effects in aqueous sulfur systems: Highlighting the role of isomers in the sulfite and sulfoxylate systems. Geochim. Cosmochim. Acta 195, 171–200. https://doi.org/10.1016/J.GCA.2016.09.021

Emiliani, C., 1966. Isotopic paleotemperatures. Science 154, 851–7. https://doi.org/10.1126/science.154.3751.851

Endo, K., 1987. Life habit and relative growth of some laqueid brachiopods from Japan. Nihon Koseibutsu Gakkai hokoku, kiji 180–194.

Ernst, A., Munnecke, A., 2009. A Hirnantian (latest Ordovician) reefal bryozoan fauna from Anticosti Island, eastern Canada: taxonomy and chemostratigraphy. Can. J. Earth Sci. 46, 207–229. https://doi.org/10.1139/E09-017

Farfan, G.A., Apprill, A., Webb, S.M., Hansel, C.M., 2018. Coupled X-ray Fluorescence and X-ray Absorption Spectroscopy for Microscale Imaging and Identification of Sulfur Species within Tissues and Skeletons of Scleractinian Corals. Anal. Chem. 90, 12559–12566. https://doi.org/10.1021/acs.analchem.8b02638

Fernández-Díaz, L., Fernández-González, Á., Prieto, M., 2010. The role of sulfate groups in controlling CaCO3 polymorphism. Geochim. Cosmochim. Acta 74, 6064–6076. https://doi.org/10.1016/J.GCA.2010.08.010

Fichtner, V., Strauss, H., Immenhauser, A., Buhl, D., Neuser, R.D., Niedermayr, A., 2017. Diagenesis of carbonate associated sulfate. Chem. Geol. 463, 61–75. https://doi.org/10.1016/J.CHEMGEO.2017.05.008

Fike, D.A., Bradley, A.S., Rose, C. V., 2015. Rethinking the Ancient Sulfur Cycle. Annu. Rev. Earth Planet. Sci. 43, 593–622. https://doi.org/10.1146/annurev-earth-060313-054802

Fike, D.A., Grotzinger, J.P., 2008. A paired sulfate–pyrite δ34S approach to understanding the evolution of the Ediacaran–Cambrian sulfur cycle. Geochim. Cosmochim. Acta 72, 2636–2648. https://doi.org/10.1016/j.gca.2008.03.021

Fleet, M.E., 2005. XANES spectroscopy of sulfur in earth materials. Can. Mineral. 43, 1811–1838. https://doi.org/10.2113/gscanmin.43.6.1811

Flügel, E., Munnecke, A., 2010. Microfacies of carbonate rocks : analysis, interpretation and application. Springer.

Folk, R.L., 1965. Some Aspects of Recrystallization in Ancient Limestones.

Frisia, S., Borsato, A., Fairchild, I.J., Susini, J., 2005. Variations in atmospheric sulphate recorded in stalagmites by synchrotron micro-XRF and XANES analyses. Earth Planet. Sci. Lett. 235, 729–740. https://doi.org/10.1016/J.EPSL.2005.03.026

Fry, B., Ruf, W., Gest, H., Hayes, J.M., 1988. Sulfur isotope effects associated with oxidation of sulfide by O2 in aqueous solution. Chem. Geol. Isot. Geosci. Sect. 73, 205–210. https://doi.org/10.1016/0168-9622(88)90001-2

Garrels, R.M., Lerman, A., 1981. Phanerozoic cycles of sedimentary carbon and sulfur (isotopes/sediment cycles/natural oxygen reservoirs). Geology 78, 4652–4656.

Gellatly, A.M., Lyons, T.W., 2005. Trace sulfate in mid-Proterozoic carbonates and the sulfur isotope record of biospheric evolution. Geochim. Cosmochim. Acta 69, 3813–3829. https://doi.org/10.1016/J.GCA.2005.01.019

Gilhooly, W.P., Reinhard, C.T., Lyons, T.W., 2016. A comprehensive sulfur and oxygen isotope study of sulfur cycling in a shallow, hyper-euxinic meromictic lake. Geochim. Cosmochim. Acta 189, 1–23. https://doi.org/10.1016/J.GCA.2016.05.044

Gill, B.C., Lyons, T.W., Frank, T.D., 2008. Behavior of carbonate-associated sulfate during meteoric diagenesis and implications for the sulfur isotope paleoproxy. Geochim. Cosmochim. Acta 72, 4699–4711. https://doi.org/10.1016/J.GCA.2008.07.001

Gill, B.C., Lyons, T.W., Jenkyns, H.C., 2011. A global perturbation to the sulfur cycle during the Toarcian Oceanic Anoxic Event. Earth Planet. Sci. Lett. 312, 484–496. https://doi.org/10.1016/J.EPSL.2011.10.030

Gill, B.C., Lyons, T.W., Saltzman, M.R., 2007. Parallel, high-resolution carbon and sulfur isotope records of the evolving Paleozoic marine sulfur reservoir. Palaeogeogr. Palaeoclimatol. Palaeoecol. 256, 156–173. https://doi.org/10.1016/J.PALAEO.2007.02.030

Goldberg, T., Poulton, S.W., Strauss, H., 2005. Sulphur and oxygen isotope signatures of late Neoproterozoic to early Cambrian sulphate, Yangtze Platform, China: Diagenetic constraints and seawater evolution. Precambrian Res. 137, 223–241. https://doi.org/10.1016/J.PRECAMRES.2005.03.003

Gomes, M.L., Hurtgen, M.T., 2015. Sulfur isotope fractionation in modern euxinic systems: Implications for paleoenvironmental reconstructions of paired sulfate–sulfide isotope records. Geochim. Cosmochim. Acta 157, 39–55. https://doi.org/10.1016/J.GCA.2015.02.031

Gomes, M.L., Johnston, D.T., 2017. Oxygen and sulfur isotopes in sulfate in modern euxinic systems with implications for evaluating the extent of euxinia in ancient oceans. Geochim. Cosmochim. Acta 205, 331–359. https://doi.org/10.1016/J.GCA.2017.02.020

Griesshaber, E., Kelm, K., Sehrbrock, A., Mader, W., Mutterlose, J., Brand, U., Schmahl, W.W., 2009. Amorphous calcium carbonate in the shell material of the brachiopod Megerlia truncata. Eur. J. Mineral. 21, 715–723. https://doi.org/10.1127/0935-1221/2009/0021-1950

Gruzensky, P.., 1967. Growth of calcite crystals. Cryst. Growth 365–367.

Habicht, K.S., Gade, M., Thamdrup, B., Berg, P., Canfield, D.E., 2000. The Archean sulfur cycle and the early history of atmospheric oxygen. Science (80-.). 288, 658–661. https://doi.org/10.1126/science.288.5466.658

Halevy, I., Peters, S.E., Fischer, W.W., 2012. Sulfate Burial Constraints on the Phanerozoic Sulfur Cycle. Science (80-.). 337, 331–334. https://doi.org/10.1126/science.1220224

Halverson, G.P., Dudás, F.Ö., Maloof, A.C., Bowring, S.A., 2007. Evolution of the 87Sr/86Sr composition of Neoproterozoic seawater. Palaeogeogr. Palaeoclimatol. Palaeoecol. 256, 103–129. https://doi.org/10.1016/J.PALAEO.2007.02.028

Hammarlund, E.U., Dahl, T.W., Harper, D.A.T., Bond, D.P.G., Nielsen, A.T., Bjerrum, C.J., Schovsbo, N.H., Schönlaub, H.P., Zalasiewicz, J.A., Canfield, D.E., 2012. A sulfidic driver for the end-Ordovician mass extinction. Earth Planet. Sci. Lett. 331–332, 128–139. https://doi.org/10.1016/j.epsl.2012.02.024

Harrison, A.G., Thode, H.G., 1958. Mechanism of the bacterial reduction of sulphate from isotope fractionation studies. Trans. Faraday Soc. 54, 84. https://doi.org/10.1039/tf9585400084

Hedman, B., Frank, P., Penner-Hahn, J.E., Roe, A.L., Hodgson, K.O., Carlson, R.M.K., Brown, G., Cerino, J., Hettel, R., Troxel, T., Winick, H., Yang, J., 1986. Sulfur K-edge X-ray absorption studies using the 54-pole wiggler at SSRL in undulator mode. Nucl. Instruments Methods Phys. Res. Sect. A Accel. Spectrometers, Detect. Assoc. Equip. 246, 797–800. https://doi.org/10.1016/0168-9002(86)90196-8

Higgins, J.A., Blättler, C.L., Lundstrom, E.A., Santiago-Ramos, D.P., Akhtar, A.A., Crüger Ahm, A.-S., Bialik, O., Holmden, C., Bradbury, H., Murray, S.T., Swart, P.K., 2018. Mineralogy, early marine diagenesis, and the chemistry of shallow-water carbonate sediments. Geochim. Cosmochim. Acta 220, 512–534. https://doi.org/10.1016/J.GCA.2017.09.046

Hints, O., Killing, M., Männik, P., Nestor, V., 2006. Frequency patterns of chitinozoans, scolecodonts, and conodonts in the upper Llandovery and lower Wenlock of the Paatsalu core, western Estonia, Proc. Estonian Acad. Sci. Geol.

Hints, O., Martma, T., Männik, P., Nõlvak, J., Põldvere, A., Shen, Y., Viira, V., 2014. New data on Ordovician stable isotope record and conodont biostratigraphy from the Viki reference drill core, Saaremaa Island, western Estonia. GFF 136, 100–104. https://doi.org/10.1080/11035897.2013.873989

Holser, W.., 1997. Geochemical events documented in inorganic carbon isotopes. Palaeogeogr. Palaeoclimatol. Palaeoecol. 132, 173–182. https://doi.org/10.1016/S0031-0182(97)00070-9

Holser, W.T., Kaplan, I.R., 1966. Isotope geochemistry of sedimentary sulfates. Chem. Geol. 1, 93–135. https://doi.org/10.1016/0009-2541(66)90011-8

Hood, A. v. S., Planavsky, N.J., Wallace, M.W., Wang, X., 2018. The effects of diagenesis on geochemical paleoredox proxies in sedimentary carbonates. Geochim. Cosmochim. Acta 232, 265–287. https://doi.org/10.1016/J.GCA.2018.04.022

Horita, J., Zimmermann, H., Holland, H.D., 2002a. Chemical evolution of seawater during the Phanerozoic. Geochim. Cosmochim. Acta 66, 3733–3756. https://doi.org/10.1016/S0016-7037(01)00884-5

Horita, J., Zimmermann, H., Holland, H.D., 2002b. Chemical evolution of seawater during the Phanerozoic: Implications from the record of marine evaporites. Geochim. Cosmochim. Acta 66, 3733–3756. https://doi.org/10.1016/S0016-7037(01)00884-5

Hurtgen, M.T., Arthur, M.A., Halverson, G.P., 2005. Neoproterozoic sulfur isotopes, the evolution of microbial sulfur species, and the burial efficiency of sulfide as sedimentary pyrite. Geology 33, 41–44. https://doi.org/10.1130/G20923.1

Hurtgen, M.T., Arthur, M.A., Suits, N.S., Kaufman, A.J., 2002. The sulfur isotopic composition of Neoproterozoic seawater sulfate: implications for a snowball Earth? Earth Planet. Sci. Lett. 203, 413–429. https://doi.org/10.1016/S0012-821X(02)00804-X

Hurtgen, M.T., Halverson, G.P., Arthur, M.A., Hoffman, P.F., 2006. Sulfur cycling in the aftermath of a 635-Ma snowball glaciation: Evidence for a syn-glacial sulfidic deep ocean. Earth Planet. Sci. Lett. 245, 551–570. https://doi.org/10.1016/j.epsl.2006.03.026

Hurtgen, M.T., Pruss, S.B., Knoll, A.H., 2009. Evaluating the relationship between the carbon and sulfur cycles in the later Cambrian ocean: An example from the Port au Port Group, western Newfoundland, Canada. Earth Planet. Sci. Lett. 281, 288–297. https://doi.org/10.1016/J.EPSL.2009.02.033

Husson, J.M., Higgins, J.A., Maloof, A.C., Schoene, B., 2015. Ca and Mg isotope constraints on the origin of Earth's deepest δ13C excursion. Geochim. Cosmochim. Acta 160, 243–266. https://doi.org/10.1016/J.GCA.2015.03.012

Jarochowska, E., Munnecke, A., 2014. The Paleozoic problematica Wetheredella and Allonema are two aspects of the same organism. Facies 60, 651–662. https://doi.org/10.1007/s10347-014-0399-z

Jeppsson, L., 1983. Silurian conodont faunas from Gotland. Foss. Strat. 15, 121–144.

Jeppsson, L., Männik, P., 1993. High-resolution correlations between Gotland and Estonia near the base of the Wenlock. Terra Nov. 5, 348–358. https://doi.org/10.1111/j.1365-3121.1993.tb00268.x

John, E.H., Wignall, P.B., Newton, R.J., Bottrell, S.H., 2010. δ34SCAS and δ18OCAS records during the Frasnian–Famennian (Late Devonian) transition and their bearing on mass extinction models. Chem. Geol. 275, 221–234. https://doi.org/10.1016/J.CHEMGEO.2010.05.012

Jones, D.S., Fike, D.A., 2013. Dynamic sulfur and carbon cycling through the end-Ordovician extinction revealed by paired sulfate–pyrite δ34S. Earth Planet. Sci. Lett. 363, 144–155. https://doi.org/10.1016/j.epsl.2012.12.015

Jones, D.S., Fike, D.A., Finnegan, S., Fischer, W.W., Schrag, D.P., McCay, D., 2011. Terminal Ordovician carbon isotope stratigraphy and glacioeustatic sea-level change across Anticosti Island (Québec, Canada). Bull. Geol. Soc. Am. 123, 1645–1664. https://doi.org/10.1130/B30323.1

Jørgensen, B.B., 1982. Mineralization of organic matter in the sea bed—the role of sulphate reduction. Nature 296, 643–645. https://doi.org/10.1038/296643a0

Jørgensen, B.B., 1977. The sulfur cycle of a coastal marine sediment (Limfjorden, Denmark)1. Limnol. Oceanogr. 22, 814–832. https://doi.org/10.4319/lo.1977.22.5.0814

Kah, L.C., Lyons, T.W., Frank, T.D., 2004. Low marine sulphate and protracted oxygenation of the Proterozoic biosphere. Nature 431, 834–838. https://doi.org/10.1038/nature02974

Kah, L.C., Thompson, C.K., Henderson, M.A., Zhan, R., 2016. Behavior of marine sulfur in the Ordovician. https://doi.org/10.1016/j.palaeo.2015.12.028

Kaljo, D., Martma, T., 2006. Application of carbon isotope stratigraphy to dating the Baltic

Silurian rocks. GFF 128, 123–129. https://doi.org/10.1080/11035890601282123

Kaljo, D., Martma, T., 2000. Proceedings of the Estonian Academy of Sciences, Geology - Google Books, 49th ed.

Kallaste, T., Kiipli, T., 2006. New correlations of Telychian (Silurian) bentonites in Estonia, in: Proceedings of the Estonian Academy of Sciences, Geology. pp. 241–251.

Kampschulte, A., Bruckschen, P., Strauss, H., 2001. The sulphur isotopic composition of trace sulphates in Carboniferous brachiopods: implications for coeval seawater, correlation with other geochemical cycles and isotope stratigraphy. Chem. Geol. 175, 149–173. https://doi.org/10.1016/S0009-2541(00)00367-3

Kampschulte, A., Strauss, H., 2004. The sulfur isotopic evolution of Phanerozoic seawater based on the analysis of structurally substituted sulfate in carbonates. Chem. Geol. 204, 255–286. https://doi.org/10.1016/J.CHEMGEO.2003.11.013

Kampschulte, A., Strauss, H., 1998. The Isotopic Composition of Trace Sulphates in Palaeozoic Biogenic Carbonates: Implications for Coeval Seawater and Geochemical Cycles, Mineralogical Magazine. https://doi.org/10.1180/minmag.1998.62a.2.59

Kiipli, E., Kiipli, T., Kallaste, T., 2006. Identification of the O-bentonite in the deep shelf sections with implication on stratigraphy and lithofacies, East Baltic Silurian. GFF 128, 255–260. https://doi.org/10.1080/11035890601283255

Kiipli, E., Kiipli, T., Kallaste, T., 2004. Bioproductivity rise in the East Baltic epicontinental sea in the Aeronian (Early Silurian). Palaeogeogr. Palaeoclimatol. Palaeoecol. 205, 255–272. https://doi.org/10.1016/J.PALAEO.2003.12.011

Kiipli, T., Mannik, P., Batchelor, R.A., Kiipli, E., Kallaste, T., Perens, H., 2001. Correlation of Telychian (Silurian) altered volcanic ash beds in Estonia, Sweden and Norway Conodonts from the Silurian and Ordovician of Oman, Saudi Arabia and Iran View project Studies on Silurian conodonts from eastern Qinling and the related strata Vi.

Kiipli, T., Orlova, K., Kiipli, E., Kallaste, T., 2008. Use of immobile trace elements for the correlation of Telychian bentonites on Saaremaa Island, Estonia, and mapping of volcanic ash clouds. Est. J. Earth Sci. 57, 39–52. https://doi.org/10.3176/earth.2008.1.04

Kile, D.., Eberl, D.., Hoch, A.., Reddy, M.., 2000. An assessment of calcite crystal growth mechanisms based on crystal size distributions. Geochim. Cosmochim. Acta 64, 2937–2950. https://doi.org/10.1016/S0016-7037(00)00394-X

Kitano, Y., Hood, D.W., 1965. The influence of organic material on the polymorphic crystallization of calcium carbonate. Geochim. Cosmochim. Acta 29, 29–41. https://doi.org/10.1016/0016-7037(65)90075-X

Kitano, Y., Okumura, M., Idogaki, M., 1975. Incorporation of sodium, chloride and sulfate with calcium carbonate. Geochem. J. 9, 75–84. https://doi.org/10.2343/geochemj.9.75

Kozik, N.P., Young, S.A., Bowman, C.N., Saltzman, M.R., Them, T.R., 2019. Middle–Upper

Ordovician (Darriwilian–Sandbian) paired carbon and sulfur isotope stratigraphy from the Appalachian Basin, USA: Implications for dynamic redox conditions spanning the peak of the Great Ordovician Biodiversification Event. Palaeogeogr. Palaeoclimatol. Palaeoecol. 520, 188–202. https://doi.org/10.1016/j.palaeo.2019.01.032

Kump, L.., Arthur, M.., Patzkowsky, M.., Gibbs, M.., Pinkus, D.., Sheehan, P.., 1999. A weathering hypothesis for glaciation at high atmospheric pCO2 during the Late Ordovician. Palaeogeogr. Palaeoclimatol. Palaeoecol. 152, 173–187. https://doi.org/10.1016/S0031-0182(99)00046-2

Kump, L.R., Arthur, M.A., 1999. Interpreting carbon-isotope excursions: carbonates and organic matter. Chem. Geol. 161, 181–198. https://doi.org/10.1016/S0009-2541(99)00086-8

Langdon, C., Takahashi, T., Sweeney, C., Chipman, D., Goddard, J., Marubini, F., Aceves, H., Barnett, H., Atkinson, M.J., 2000. Effect of calcium carbonate saturation state on the calcification rate of an experimental coral reef. Global Biogeochem. Cycles 14, 639–654. https://doi.org/10.1029/1999GB001195

Lazauskiene, J., Sliaupa, S., Brazauskas, A., Musteikis, P., 2003. Sequence stratigraphy of the Baltic Silurian succession: tectonic control on the foreland infill. Geol. Soc. London, Spec. Publ. 208, 95–115. https://doi.org/10.1144/GSL.SP.2003.208.01.05

Leavitt, W.D., Halevy, I., Bradley, A.S., Johnston, D.T., 2013. Influence of sulfate reduction rates on the Phanerozoic sulfur isotope record. Proc. Natl. Acad. Sci. U. S. A. 110, 11244–9. https://doi.org/10.1073/pnas.1218874110

Lehnert, O., Männik, P., Joachimski, M.M., Calner, M., Frýda, J., 2010. Palaeoclimate perturbations before the Sheinwoodian glaciation: A trigger for extinctions during the 'Ireviken Event.' Palaeogeogr. Palaeoclimatol. Palaeoecol. 296, 320–331. https://doi.org/10.1016/j.palaeo.2010.01.009

Liu, X., Fike, D., Li, A., Dong, J., Xu, F., Zhuang, G., Rendle-Bühring, R., Wan, S., 2019. Pyrite sulfur isotopes constrained by sedimentation rates: Evidence from sediments on the East China Sea inner shelf since the late Pleistocene. Chem. Geol. 505, 66–75. https://doi.org/10.1016/J.CHEMGEO.2018.12.014

Long, D.G.F., Copper, P., 1987. Stratigraphy of the Upper Ordovician upper Vaureal and Ellis Bay formations, eastern Anticosti Island, Quebec. Can. J. Earth Sci. 24, 1807–1820. https://doi.org/10.1139/e87-172

Lowenstam, H.A., 1961. Mineralogy, O ^{18} /O ^{16} Ratios, and Strontium and Magnesium Contents of Recent and Fossil Brachiopods and Their Bearing on the History of the Oceans. J. Geol. 69, 241–260. https://doi.org/10.1086/626740

Lowenstein, T.K., Hardie, L.A., Timofeeff, M.N., Demicco, R. V., 2003. Secular variation in seawater chemistry and the origin of calcium chloride basinal brines. Geology 31, 857. https://doi.org/10.1130/G19728R.1

Loyd, S.J., Berelson, W.M., Lyons, T.W., Hammond, D.E., Corsetti, F.A., 2012. Constraining pathways of microbial mediation for carbonate concretions of the Miocene Monterey Formation using carbonate-associated sulfate. Geochim. Cosmochim. Acta 78, 77–98. https://doi.org/10.1016/J.GCA.2011.11.028

Loydell, D.K., Nestor, V., Mnnik, P., 2010. Integrated biostratigraphy of the lower silurian of the Kolka-54 core, Latvia. Geol. Mag. 147, 253–280. https://doi.org/10.1017/S0016756809990574

Luo, G., Kump, L.R., Wang, Y., Tong, J., Arthur, M.A., Yang, H., Huang, J., Yin, H., Xie, S., 2010. Isotopic evidence for an anomalously low oceanic sulfate concentration following end-Permian mass extinction. Earth Planet. Sci. Lett. 300, 101–111. https://doi.org/10.1016/J.EPSL.2010.09.041

Lyons, T.W., Walter, L.M., Gellatly, A.M., Martini, A.M., Blake, R.E., 2004a. Sites of anomalous organic remineralization in the carbonate sediments of South Florida, USA: The sulfur cycle and carbonate-associated sulfate, in: Special Paper 379: Sulfur Biogeochemistry - Past and Present. Geological Society of America, pp. 161–176. https://doi.org/10.1130/0-8137-2379-5.161

Lyons, T.W., Walter, L.M., Gellatly, A.M., Martini, A.M., Blake, R.E., 2004b. Sites of anomalous organic remineralization in the carbonate sediments of South Florida, USA: The sulfur cycle and carbonate-associated sulfate, in: Special Paper 379: Sulfur Biogeochemistry - Past and Present. Geological Society of America, pp. 161–176. https://doi.org/10.1130/0-8137-2379-5.161

Lyu, Z., Zhang, L., Algeo, T.J., Zhao, L., Chen, Z.-Q., Li, C., Ma, B., Ye, F., 2019. Global-ocean circulation changes during the Smithian–Spathian transition inferred from carbon-sulfur cycle records. Earth-Science Rev. https://doi.org/10.1016/j.earscirev.2019.01.010

Marenco, P.J., Corsetti, F.A., Hammond, D.E., Kaufman, A.J., Bottjer, D.J., 2008a. Oxidation of pyrite during extraction of carbonate associated sulfate. Chem. Geol. 247, 124–132. https://doi.org/10.1016/j.chemgeo.2007.10.006

Marenco, P.J., Corsetti, F.A., Kaufman, A.J., Bottjer, D.J., 2008b. Environmental and diagenetic variations in carbonate associated sulfate: An investigation of CAS in the Lower Triassic of the western USA. Geochim. Cosmochim. Acta 72, 1570–1582. https://doi.org/10.1016/j.gca.2007.10.033

Marshall, J.D., Brenchley, P.J., Mason, P., Wolff, G.A., Astini, R.A., Hints, L., Meidla, T., 1997. Global carbon isotopic events associated with mass extinction and glaciation in the late Ordovician. Palaeogeogr. Palaeoclimatol. Palaeoecol. 132, 195–210. https://doi.org/10.1016/S0031-0182(97)00063-1

Mayhew, L.E., Webb, S.M., Templeton, A.S., 2011. Microscale Imaging and Identification of Fe Speciation and Distribution during Fluid–Mineral Reactions under Highly Reducing Conditions. Environ. Sci. Technol. 45, 4468–4474. https://doi.org/10.1021/es104292n

Munnecke, A., Calner, M., Harper, D.A.T., Servais, T., 2010. Ordovician and Silurian sea–water chemistry, sea level, and climate: A synopsis. Palaeogeogr. Palaeoclimatol. Palaeoecol. 296, 389–413. https://doi.org/10.1016/j.palaeo.2010.08.001

Munnecke, A., Männik, P., 2009. New biostratigraphic and chemostratigraphic data from the Chicotte Formation (Llandovery, Anticosti Island, Laurentia) compared with the Viki core (Estonia, Baltica). Est. J. Earth Sci. 58, 159. https://doi.org/10.3176/earth.2009.3.01

Munnecke, A., Samtleben, C., Bickert, T., 2003. The Ireviken Event in the lower Silurian of Gotland, Sweden – relation to similar Palaeozoic and Proterozoic events. Palaeogeogr. Palaeoclimatol. Palaeoecol. 195, 99–124. https://doi.org/10.1016/S0031-0182(03)00304-3

Nestor, H., Einasto, R., 1997. Ordovician and Silurian Carbonate sedimentation basin, in: Geology and Mineral Resources of Estonia. Estonian Academy Publishers, Tallinn, pp. 192–204.

Nestor, V., 2010. Distribution of Silurian chitinozoans. Viki Drill Core. Est. Geol. Sect. Bulletin 1, 19–20.

Newville, M., 2013. Larch: An Analysis Package for XAFS And Related Spectroscopies, Journal of Physics. J. Phys. Conf. Ser. 430.

Oduro, H., Van Alstyne, K.L., Farquhar, J., 2012. Sulfur isotope variability of oceanic DMSP generation and its contributions to marine biogenic sulfur emissions. Proc. Natl. Acad. Sci. 109, 9012–9016. https://doi.org/10.1073/pnas.1117691109

Osburn, M.R., Owens, J., Bergmann, K.D., Lyons, T.W., Grotzinger, J.P., 2015. Dynamic changes in sulfate sulfur isotopes preceding the Ediacaran Shuram Excursion. Geochim. Cosmochim. Acta 170, 204–224. https://doi.org/10.1016/J.GCA.2015.07.039

Owens, J.D., Gill, B.C., Jenkyns, H.C., Bates, S.M., Severmann, S., Kuypers, M.M.M., Woodfine, R.G., Lyons, T.W., 2013. Sulfur isotopes track the global extent and dynamics of euxinia during Cretaceous Oceanic Anoxic Event 2. Proc. Natl. Acad. Sci. 110, 18407–18412. https://doi.org/10.1073/PNAS.1305304110

Paine, R.T., 1969. Growth and Size Distribution of the Brachiopod Terebratalia transversa Sowerby, Pacific Science.

Paquette, J., Reeder, R.J., 1990. New type of compositional zoning in calcite : Insights into crystal-growth mechanisms. https://doi.org/10.1130/0091-7613(1990)018<1244

Paris, G., Adkins, J.F., Sessions, A.L., Webb, S.M., Fischer, W.W., 2014. Neoarchean carbonate-associated sulfate records positive Δ^{33}S anomalies. Science 346, 739–41. https://doi.org/10.1126/science.1258211

Paris, G., Sessions, A.L., Subhas, A. V., Adkins, J.F., 2013. MC-ICP-MS measurement of δ34S and Δ33S in small amounts of dissolved sulfate. Chem. Geol. 345, 50–61. https://doi.org/10.1016/J.CHEMGEO.2013.02.022

Pasquier, V., Sansjofre, P., Rabineau, M., Revillon, S., Houghton, J., Fike, D.A., 2017. Pyrite sulfur isotopes reveal glacial−interglacial environmental changes. Proc. Natl. Acad. Sci. 114, 5941–5945. https://doi.org/10.1073/pnas.1618245114

Paytan, A., 1998. Sulfur Isotopic Composition of Cenozoic Seawater Sulfate. Science (80-.). 282, 1459–1462. https://doi.org/10.1126/science.282.5393.1459

Paytan, A., Kastner, M., Campbell, D., Thiemens, M.H., 2004. Seawater sulfur isotope fluctuations in the Cretaceous. Science 304, 1663–5. https://doi.org/10.1126/science.1095258

Paytan, A., Kastner, M., Campbell, D., Thiemens, M.H., 1998. Sulfur isotopic composition of cenozoic seawater sulfate. Science 282, 1459–62. https://doi.org/10.1126/SCIENCE.282.5393.1459

Paytan, A., Kastner, M., Martin, E.E., Macdougall, J.D., Herbert, T., 1993. Marine barite as a monitor of seawater strontium isotope composition. Nature 366, 445–449. https://doi.org/10.1038/366445a0

Pérez-Huerta, A., Aldridge, A.E., Endo, K., Jeffries, T.E., 2014. Brachiopod shell spiral deviations (SSD): Implications for trace element proxies. Chem. Geol. 374–375, 13–24. https://doi.org/10.1016/J.CHEMGEO.2014.03.002

Pérez-Huerta, A., Coronado, I., Hegna, T.A., 2018. Understanding biomineralization in the fossil record. Earth-Science Rev. 179, 95–122. https://doi.org/10.1016/J.EARSCIREV.2018.02.015

Pérez-Huerta, A., Cusack, M., Janousch, M., Finch, A.A., IUCr, 2008. Influence of crystallographic orientation of biogenic calcite on *in situ* Mg XANES analyses. J. Synchrotron Radiat. 15, 572–575. https://doi.org/10.1107/S0909049508026484

Perrin, J., Rivard, C., Vielzeuf, D., Laporte, D., Fonquernie, C., Ricolleau, A., Cotte, M., Floquet, N., 2017a. The coordination of sulfur in synthetic and biogenic Mg calcites: The red coral case. Geochim. Cosmochim. Acta 197, 226–244. https://doi.org/10.1016/J.GCA.2016.10.017

Perrin, J., Rivard, C., Vielzeuf, D., Laporte, D., Fonquernie, C., Ricolleau, A., Cotte, M., Floquet, N., 2017b. The coordination of sulfur in synthetic and biogenic Mg calcites: The red coral case. Geochim. Cosmochim. Acta 197, 226–244. https://doi.org/10.1016/J.GCA.2016.10.017

Pin, S., Huthwelker, T., Brown, M.A., Vogel, F., 2013. Combined Sulfur K-Edge XANES–EXAFS Study of the Effect of Protonation on the Sulfate Tetrahedron in Solids and Solutions. J. Phys. Chem. A 117, 8368–8376. https://doi.org/10.1021/jp404272e

Pinet, N., Lavoie, D., 2007. The Offshore Part of the Anticosti Basin: A Major Gap in the Understanding of Early to Middle Paleozoic Basins of Eastern Canada in a Promising Hydrocarbon Setting, Convention Extended Abstracts: Calgary, Canadian Society of Petroleum and Geology.

Pingitore, N.E., Meitzner, G., Love, K.M., 1995. Identification of sulfate in natural carbonates by x-ray absorption spectroscopy. Geochim. Cosmochim. Acta 59, 2477–2483. https://doi.org/10.1016/0016-7037(95)00142-5

Põldvere, A., 2010. Viki Drill Core, Estonian Geological Sections, Bulletin 10. Geological Survey of Estonia.

Popp, B.N., Anderson, T.F., Sandberg, P. a., 1986a. Textural, elemental, and isotopic variations among constituents in middle Devonian Limestones, North America. J. Sediment. Res. 56, 715–727. https://doi.org/10.1306/212F8A26-2B24-11D7-8648000102C1865D

Popp, B.N., Anderson, T.F., Sandberg, P.A., 1986b. Brachiopods as indicators of original isotopic compositions in some Paleozoic limestones. Geol. Soc. Am. Bull. 97, 1262–1269. https://doi.org/10.1130/0016-7606(1986)97<1262:BAIOOI>2.0.CO;2

Present, T.M., 2018. Controls on the Sulfur Isotopic Composition of Carbonate-Associated Sulfate. California Institute of Technology.

Present, T.M., Paris, G., Burke, A., Fischer, W.W., Adkins, J.F., 2015. Large Carbonate Associated Sulfate isotopic variability between brachiopods, micrite, and other sedimentary components in Late Ordovician strata. Earth Planet. Sci. Lett. 432, 187–198. https://doi.org/10.1016/J.EPSL.2015.10.005

Qing, H., Veizer, J., 1994. Oxygen and carbon isotopic composition of Ordovician brachiopods: Implications for coeval seawater. Geochim. Cosmochim. Acta 58, 4429–4442. https://doi.org/10.1016/0016-7037(94)90345-X

Raab, M., Spiro, B., 1991. Sulfur isotopic variations during seawater evaporation with fractional crystallization. Chem. Geol. Isot. Geosci. Sect. 86, 323–333. https://doi.org/10.1016/0168-9622(91)90014-N

Raven, M.R., Adkins, J.F., Werne, J.P., Lyons, T.W., Sessions, A.L., 2015. Sulfur isotopic composition of individual organic compounds from Cariaco Basin sediments. Org. Geochem. 80, 53–59. https://doi.org/10.1016/j.orggeochem.2015.01.002

Reeder, R.J., Lamble, G.M., Lee, J.-F., Staudt, W.J., 1994. Mechanism of SeO42− substitution in calcite: An XAFS study. Geochim. Cosmochim. Acta 58, 5639–5646. https://doi.org/10.1016/0016-7037(94)90256-9

Rennie, V.C.F., Paris, G., Sessions, A.L., Abramovich, S., Turchyn, A. V., Adkins, J.F., 2018. Cenozoic record of δ34S in foraminiferal calcite implies an early Eocene shift to deep-ocean sulfide burial. Nat. Geosci. 1. https://doi.org/10.1038/s41561-018-0200-y

Rennie, V.C.F., Turchyn, A. V., 2014. The preservation of δSSO434 and δOSO418 in carbonate-associated sulfate during marine diagenesis: A 25 Myr test case using marine sediments. Earth Planet. Sci. Lett. 395, 13–23. https://doi.org/10.1016/J.EPSL.2014.03.025

Riccardi, A.L., Arthur, M.A., Kump, L.R., 2006. Sulfur isotopic evidence for chemocline upward excursions during the end-Permian mass extinction. Geochim. Cosmochim. Acta 70, 5740–5752. https://doi.org/10.1016/J.GCA.2006.08.005

Richardson, J.A., Keating, C., Lepland, A., Hints, O., Bradley, A.S., Fike, D.A., 2019. Silurian records of carbon and sulfur cycling from Estonia: The importance of depositional environment on isotopic trends. Earth Planet. Sci. Lett. 512, 71–82. https://doi.org/10.1016/J.EPSL.2019.01.055

Richardson, J.A., Newville, M., Lanzirotti, A., Webb, S.M., Rose, C. V, Catalano, J.G., Fike, D.A., n.d. Depositional and Diagenetic Constrains on the Abundance and Spatial Variability of Carbonate-Associated Sulfate.

Ries, J.B., Fike, D.A., Pratt, L.M., Lyons, T.W., Grotzinger, J.P., 2009. Superheavy pyrite (34Spyr > 34SCAS) in the terminal Proterozoic Nama Group, southern Namibia: A consequence of low seawater sulfate at the dawn of animal life. Geology 37, 743–746. https://doi.org/10.1130/G25775A.1

Rose, C. V., Fischer, W.W., Finnegan, S., Fike, D.A., 2019. Records of carbon and sulfur cycling during the Silurian Ireviken Event in Gotland, Sweden. Geochim. Cosmochim. Acta 246, 299–316. https://doi.org/10.1016/J.GCA.2018.11.030

Rose, C. V, Webb, S.M., Newville, M., Lanzirotti, A., Richardson, J.A., Tosca, N.J., Catalano, J.G., Bradley, A.S., Fike, D.A., n.d. Insights into Past Ocean Proxies from Micron-scale Mapping of Sulfur Species in Carbonates.

Rush, P.F., Chafetz, H.S., 1990. Fabric-retentive, non-luminescent brachiopods as indicators of original delta 13 C and delta 18 O composition; a test. J. Sediment. Res. 60, 968–981. https://doi.org/10.1306/D4267659-2B26-11D7-8648000102C1865D

Saltzman, M.R., Ripperdan, R.L., Brasier, M.D., Lohmann, K.C., Robison, R.A., Chang, W.T., Peng, S., Ergaliev, E.K., Runnegar, B., 2000a. A global carbon isotope excursion (SPICE) during the Late Cambrian: relation to trilobite extinctions, organic-matter burial and sea level. Palaeogeogr. Palaeoclimatol. Palaeoecol. 162, 211–223. https://doi.org/10.1016/S0031-0182(00)00128-0

Saltzman, M.R., Ripperdan, R.L., Brasier, M.D., Lohmann, K.C., Robison, R.A., Chang, W.T., Peng, S., Ergaliev, E.K., Runnegar, B., 2000b. A global carbon isotope excursion (SPICE) during the Late Cambrian: Relation to trilobite extinctions, organic-matter burial and sea level. Palaeogeogr. Palaeoclimatol. Palaeoecol. 162, 211–223. https://doi.org/10.1016/S0031-0182(00)00128-0

Samtleben, C., Munnecke, A., Bickert, T., 2000. Development of facies and C/O-isotopes in transects through the Ludlow of Gotland: Evidence for global and local influences on a shallow-marine environment. Facies 43, 1–38. https://doi.org/10.1007/BF02536983

Samtleben, C., Munnecke, A., Bickert, T., Pätzold, J., 1996. The Silurian of Gotland (Sweden): facies interpretation based on stable isotopes in brachiopod shells. Geol. Rundschau 85, 278–292. https://doi.org/10.1007/BF02422234

Schidlowski, M., Junge, C.E., Pietrek, H., 1977. Sulfur isotope variations in marine sulfate evaporites and the phanerozoic oxygen budget, Journal of Geophysical Research. https://doi.org/10.1029/jc082i018p02557

Scholle, P.A., Ulmer-Scholle, D.S., 2003. A Color Guide to the Petrography of Carbonate Rocks:

Grains, textures, porosity, diagenesis, Aapg Memoir. https://doi.org/10.1306/m77973

Shields, G.A., Strauss, H., Howe, S.S., Siegmund, H., 1999. Sulphur isotope compositions of sedimentary phosphorites from the basal Cambrian of China: implications for Neoproterozoic-Cambrian biogeochemical cycling. J. Geol. Soc. London. 156, 943–955. https://doi.org/10.1144/gsjgs.156.5.0943

Sim, M.S., Bosak, T., Ono, S., 2011. Large sulfur isotope fractionation does not require disproportionation. Science 333, 74–7. https://doi.org/10.1126/science.1205103

Sim, M.S., Ono, S., Hurtgen, M.T., 2015. Sulfur isotope evidence for low and fluctuating sulfate levels in the Late Devonian ocean and the potential link with the mass extinction event. Earth Planet. Sci. Lett. 419, 52–62. https://doi.org/10.1016/J.EPSL.2015.03.009

Sinninghe-Damste, J.S., de Leeuw, J.W., 1990. Analysis, structure and geochemical significance of organically- bound sulphur in the geosphere: state of the art and future research. Org. Geochem. 16, 1077–1103.

Smith, A.M., Key, M.M., Gordon, D.P., 2006. Skeletal mineralogy of bryozoans: Taxonomic and temporal patterns. Earth-Science Rev. 78, 287–306. https://doi.org/10.1016/J.EARSCIREV.2006.06.001

Sowerby, G.B., 1846. Descriptions of thirteen new species of brachiopods. Proc. Zool. Soc. London. 14.

Staudt, W.J., Oswald, E.J., Schoonen, M.A.A., 1993. Determination of sodium, chloride and sulfate in dolomites: a new technique to constrain the composition of dolomitizing fluids. Chem. Geol. 107, 97–109. https://doi.org/10.1016/0009-2541(93)90104-Q

Staudt, W.J., Reeder, R.J., Schoonen, M.A.A., 1994. Surface structural controls on compositional zoning of SO2−4 and SeO2−4 in synthetic calcite single crystals. Geochim. Cosmochim. Acta 58, 2087–2098. https://doi.org/10.1016/0016-7037(94)90287-9

Staudt, W.J., Schoonen, M.A.A., 1995. Sulfate Incorporation into Sedimentary Carbonates. pp. 332–345. https://doi.org/10.1021/bk-1995-0612.ch018

Stebbins, A., Algeo, T.J., Olsen, C., Sano, H., Rowe, H., Hannigan, R., 2018. Sulfur-isotope evidence for recovery of seawater sulfate concentrations from a PTB minimum by the Smithian-Spathian transition. Earth-Science Rev. https://doi.org/10.1016/J.EARSCIREV.2018.08.010

Strauss, H., 1997a. The isotopic composition of sedimentary sulfur through time. Palaeogeogr. Palaeoclimatol. Palaeoecol. 132, 97–118. https://doi.org/10.1016/S0031-0182(97)00067-9

Strauss, H., 1997b. The isotopic composition of sedimentary sulfur through time. Palaeogeogr. Palaeoclimatol. Palaeoecol. 132, 97–118. https://doi.org/10.1016/S0031-0182(97)00067-9

Swart, P.K., 2008. Global synchronous changes in the carbon isotopic composition of carbonate sediments unrelated to changes in the global carbon cycle. Proc. Natl. Acad. Sci. U. S. A. 105, 13741–5. https://doi.org/10.1073/pnas.0802841105

Swart, P.K., Eberli, G., 2005. The nature of the δ13C of periplatform sediments: Implications for stratigraphy and the global carbon cycle. Sediment. Geol. 175, 115–129. https://doi.org/10.1016/J.SEDGEO.2004.12.029

Takano, B., 1985. Geochemical implications of sulfate in sedimentary carbonates. Chem. Geol. 49, 393–403. https://doi.org/10.1016/0009-2541(85)90001-4

Takano, B., Asano, Y., Watanuki, K., 1980. Characterization of sulfate ion in travertine. Contrib. to Mineral. Petrol. 72, 197–203. https://doi.org/10.1007/BF00399480

Tamenori, Y., Yoshimura, T., 2018. Sulfur speciation in growth layers of shell cross section of the long-lived bivalve Margaritifera laevis using synchrotron spectromicroscopy analysis. Geochim. Cosmochim. Acta 237, 357–369. https://doi.org/10.1016/J.GCA.2018.07.002

Tamenori, Y., Yoshimura, T., Luan, N.T., Hasegawa, H., Suzuki, A., Kawahata, H., Iwasaki, N., 2014. Identification of the chemical form of sulfur compounds in the Japanese pink coral (Corallium elatius) skeleton using μ-XRF/XAS speciation mapping. J. Struct. Biol. 186, 214–223. https://doi.org/10.1016/J.JSB.2014.04.001

Tang, Y., Elzinga, E.J., Jae Lee, Y., Reeder, R.J., 2007. Coprecipitation of chromate with calcite: Batch experiments and X-ray absorption spectroscopy. Geochim. Cosmochim. Acta 71, 1480–1493. https://doi.org/10.1016/J.GCA.2006.12.010

Thode, H.G., Monster, J., Dunford, H.B., 1974. Sulphur Isotope Abundances in Petroleum and Associated Materials. Am. Assoc. Pet. Geol. Bull. 42, 2619–2641.

Thompson, C.K., Kah, L.C., 2012. Sulfur isotope evidence for widespread euxinia and a fluctuating oxycline in Early to Middle Ordovician greenhouse oceans. Palaeogeogr. Palaeoclimatol. Palaeoecol. 313–314, 189–214. https://doi.org/10.1016/J.PALAEO.2011.10.020

Toth, D.J., Lerman, A., 1977. Organic matter reactivity and sedimentation rates in the ocean. Am. J. Sci. 277, 465–485. https://doi.org/10.2475/ajs.277.4.465

Turchyn, A. V., Schrag, D.P., 2006. Cenozoic evolution of the sulfur cycle: Insight from oxygen isotopes in marine sulfate. Earth Planet. Sci. Lett. 241, 763–779. https://doi.org/10.1016/J.EPSL.2005.11.007

Turchyn, A. V., Schrag, D.P., Coccioni, R., Montanari, A., 2009. Stable isotope analysis of the Cretaceous sulfur cycle. Earth Planet. Sci. Lett. 285, 115–123. https://doi.org/10.1016/J.EPSL.2009.06.002

Veizer, J., Fritz, P., Jones, B., 1986. Geochemistry of brachiopods: Oxygen and carbon isotopic records of Paleozoic oceans. Geochim. Cosmochim. Acta 50, 1679–1696. https://doi.org/10.1016/0016-7037(86)90130-4

Walker, K.R., Jernigan, D.G., Weber, L.J., 1990. Petrographic criteria for the recognition of marine, syntaxial overgrowths, and their distribution in geologic time. Carbonates and Evaporites 5, 141–152. https://doi.org/10.1007/BF03174845

Webb, S.M., 2005. SIXPack a Graphical User Interface for XAS Analysis Using IFEFFIT. Phys. Scr. 2005, 1011. https://doi.org/10.1238/Physica.Topical.115a01011

Webb, S.M., McNulty, I., Eyberger, C., Lai, B., 2011. The MicroAnalysis Toolkit: X-ray Fluorescence Image Processing Software, in: AIP Conference Proceedings. American Institute of Physics, pp. 196–199. https://doi.org/10.1063/1.3625338

Wilke, M., Jugo, P.J., Klimm, K., Susini, J., Botcharnikov, R., Kohn, S.C., Janousch, M., 2008. The origin of S4+ detected in silicate glasses by XANES. Am. Mineral. 93, 235–240. https://doi.org/10.2138/am.2008.2765

Wing, B.A., Halevy, I., 2014. Intracellular metabolite levels shape sulfur isotope fractionation during microbial sulfate respiration. Proc. Natl. Acad. Sci. U. S. A. 111, 18116–25. https://doi.org/10.1073/pnas.1407502111

Wotte, T., Shields-Zhou, G.A., Strauss, H., 2012a. Carbonate-associated sulfate: Experimental comparisons of common extraction methods and recommendations toward a standard analytical protocol. Chem. Geol. 326–327, 132–144. https://doi.org/10.1016/J.CHEMGEO.2012.07.020

Wotte, T., Strauss, H., Fugmann, A., Garbe-Schönberg, D., 2012b. Paired δ34S data from carbonate-associated sulfate and chromium-reducible sulfur across the traditional Lower–Middle Cambrian boundary of W-Gondwana. Geochim. Cosmochim. Acta 85, 228–253. https://doi.org/10.1016/J.GCA.2012.02.013

Xie, A.-J., Shen, Y.-H., Zhang, C.-Y., Yuan, Z.-W., Zhu, X.-M., Yang, Y.-M., 2005. Crystal growth of calcium carbonate with various morphologies in different amino acid systems. J. Cryst. Growth 285, 436–443. https://doi.org/10.1016/J.JCRYSGRO.2005.08.039

Yan, D., Chen, D., Wang, Q., Wang, J., Wang, Z., 2009. Carbon and sulfur isotopic anomalies across the Ordovician-Silurian boundary on the Yangtze Platform, South China. Palaeogeogr. Palaeoclimatol. Palaeoecol. 274, 32–39. https://doi.org/10.1016/j.palaeo.2008.12.016

Yoshimura, T., Tamenori, Y., Suzuki, A., Nakashima, R., Iwasaki, N., Hasegawa, H., Kawahata, H., 2013. Element profile and chemical environment of sulfur in a giant clam shell: Insights from μ-XRF and X-ray absorption near-edge structure. Chem. Geol. 352, 170–175. https://doi.org/10.1016/J.CHEMGEO.2013.05.035

Young, S.A., Gill, B.C., Edwards, C.T., Leslie, S.A., 2016a. Middle–Late Ordovician (Darriwilian–Sandbian) decoupling of global sulfur and carbon cycles: Isotopic evidence from eastern and southern Laurentia. Palaeogeogr. Palaeoclimatol. Palaeoecol. 458, 118–132. https://doi.org/10.1016/J.PALAEO.2015.09.040

Young, S.A., Gill, B.C., Edwards, C.T., Saltzman, M.R., Leslie, S.A., 2016b. Middle–Late Ordovician (Darriwilian–Sandbian) decoupling of global sulfur and carbon cycles: Isotopic evidence from eastern and southern Laurentia. Palaeogeogr. Palaeoclimatol. Palaeoecol. 458, 118–132. https://doi.org/10.1016/j.palaeo.2015.09.040